

**Editors:**

**Assoc. Dr. Tran Ngoc Long**

**Dr. Nguyen Trong Ha - Dr. Nguyen Duy Duan**

# **ADVANCES IN CIVIL ENGINEERING**

**Proceedings of the 1<sup>st</sup> Conference on Advances  
in Civil Engineering (ICACE 2022)**

**May 21<sup>st</sup>, Vinh University, Vietnam**



**SCIENCE AND TECHNICS PUBLISHING HOUSE**

**Hanoi - 2022**



## ICACE-2022 Scientific Committee

---

### **Chairs**

Prof. TRAN Minh Tu, Hanoi University Civil Engineering, Vietnam

Prof. TRAN The Truyen, University of Transport and Communications, Vietnam

---

### **Members**

Prof. LEE Tae-Hyung, Konkuk University, Korea

Prof. BUI Quoc Tinh, Tokyo Institute of Technology, Japan

Prof. HA Dong-Ho, Konkuk University, Korea

Prof. PARK Duhee, Hanyang University, Korea

Prof. THAI Huu Tai, The University of Melbourne, Australia

Prof. LY Quang Viet, Tianjin Polytechnic University, China

Prof. KIM Seung-Eock, Sejong University, Korea

Dr. CHANA Sinsabvarodom, NTNU, Norway

Dr. DO Trong Nhan, National Cheng Kung University, Taiwan

Dr. GAUTAM Dipendra, Interdisciplinary Research Institute for Sustainability (IRIS), Nepal

Prof. SADIQ Shamsher, Ghulam Ishaq Khan Institute of Engineering Sciences and Technology, Pakistan

Prof. HO Huu Loc, Asian Institute of Technology, Thailand

Prof. NGUYEN Ngoc Tan, Sejong University, Korea

Prof. TRINH Minh Chien, Chonbuk National University, Korea

Dr. HO Sy Lanh, Hiroshima University, Japan

Dr. NGUYEN Van Dong, Chonnam National University, Korea

Dr. NGUYEN Duc Hai, Sejong University, Korea

Dr. PHAM Luong, RMIT University, Australia

Prof. LE Thang, California State University, Northridge, USA

Dr. TRAN Vinh Loc, Ton Duc Thang University, Vietnam

Dr. PHAM Thai Hoan, National University Civil Engineering, Vietnam

Dr. NGUYEN Van Quang, Vinh University, Vietnam

Dr. TRAN Viet Linh, Vinh University, Vietnam

## **ICACE-2022 Organizing Committee**

---

### **Chairs**

Prof. NGUYEN Huy Bang, Vinh University, Vietnam (Chair)

Dr. TRAN Ba Tien, Vinh University, Vietnam (Co-Chair)

Dr. TRAN Ngoc Long, Vinh University, Vietnam (Co-Chair)

---

### **Members**

Assoc. Prof. MAI Van Chung, Vinh University, Vietnam

Mr. NGUYEN Hong Soa, Vinh University, Vietnam

Mr. HOANG Viet Dung, Vinh University, Vietnam

Mr. NGUYEN Van Hai, Vinh University, Vietnam

Prof. DINH Xuan Khoa, Vinh University, Vietnam

Dr. PHAN Van Tien, Vinh University, Vietnam

Dr. LE Thanh Hai, Vinh University, Vietnam

Dr. PHAM Hong Son, Vinh University, Vietnam

Dr. PHAN Van Phuc, Vinh University, Vietnam

Dr. NGUYEN Trong Kien, Vinh University, Vietnam

---

### **Secretariats**

Dr. NGUYEN Trong Ha, Vinh University, Vietnam

Dr. NGUYEN Duy Duan, Vinh University, Vietnam

Mr. TRAN Xuan Vinh, Vinh University, Vietnam

Mr. NGUYEN Tien Hong, Vinh University, Vietnam

Mr. NGUYEN Duy Khanh, Vinh University, Vietnam

Mr. NGUYEN Manh Hung, Vinh University, Vietnam

## PREFACE

---

On the occasion of celebrating the 20-year anniversary of the Department of Civil Engineering, Vinh University, the International Conference on Advances in Civil Engineering (ICACE-2022) was organized to connect the faculties of the Department of Civil Engineering research professionals, scholars, and scientists from different institutions both in Vietnam and abroad. ICACE-2022 was organized on May 21<sup>st</sup>, 2022, at Vinh University, Vietnam. This event was a good opportunity to discuss new research findings in the civil engineering field. We believe that those updated studies will contribute to solving the practical problems. The main topics of the conference included Structural and mechanics engineering, Construction and building materials, Smart and sustainable infrastructure, Geotechnical engineering, Hydraulic, pavement, costal and offshore engineering, and Construction engineering and project management. This proceeding includes the full papers selected from the accepted submissions, which were presented at ICACE-2022.

On behalf of the Organizing Committee, we are sincerely thankful for the contribution of two keynote lectures, which are presented by Prof. Tran Minh Tu (Hanoi University of Civil Engineering, Vietnam) and Assoc. Prof. Tran The Truyen (University of Transportation and Communication, Vietnam). Additionally, a great appreciation is to all authors who submitted papers and presented at the parallel sessions. We also want to give our sincere thanks to companies and Vinh University for their support. Their contributions made the conference a success.

**Assoc. Prof. Tran Ngoc Long**

*On behalf of the Organizing Committee of ICACE-2022*

*Dean of Department of Civil Engineering, Vinh University*



## CONTENTS

---

	<i>Page</i>
1. The effect of earthquake frequency content on seismic response of horseshoe tunnels <i>Van-Quang Nguyen, Muhammad Umair Ashfaq, Muhammad Irslan Khalid, Ngoc-Long Tran, Trong-Cuong Vo, Van-Long Phan, Huu-Cuong Nguyen</i>	1
2. Damage simulation of reinforced concrete beams relating to corrosion of reinforcement in concrete <i>Vu Ba Thanh, Tran The Truyen, Vo Van Nam, Pham Duc Manh</i>	8
3. Experimental study concrete shrinkage at high temperature due to climate changes <i>Ngoc-Long Tran, Tien-Hong Nguyen, Xuan-Hieu Nguyen, Chung-Bao Nguyen</i>	17
4. Stress-strain state of a short reinforced concrete column cross-section subjected to biaxial compression <i>Phan Van-Phuc, Tran Van-Hoan, Nguyen Van-Thanh</i>	23
5. Exploring the shear strength characteristics and CBR value of an expansive soil by using brick dust and coir fiber <i>Muhammad Umair Ashfaq, Muhammad Irslan Khalid, Muhammad Shahroz Khalid and Van-Quang Nguyen</i>	38
6. Classification of concrete grade using machine learning methods <i>Viet-Linh Tran, Duc-Kien Thai, Huy-Khanh Dang, Trong-Cuong Vo</i>	43
7. Research and application of Tuned mass dampers - type vibration absorber devices for buildings <i>Nguyen Trong Kien, Nguyen Duy Khanh, Nguyen Thi Thu Hang</i>	51
8. Reality and difficulties in applying Building Information Modeling (BIM) in Vietnam <i>Pham Ngoc Minh</i>	60
9. Analysis of randomness and fuzziness of parameters related to corrosion of reinforcement in reinforced concrete structures <i>Thu Minh Tran, Duc Manh Tran, The Truyen Tran</i>	66
10. Prediction of the CBL of the SDTC with tubular cross-section using Rayleigh-Ritz method <i>Thi-Quynh Nguyen, and Thanh-Tung Nguyen Thi</i>	75
11. Causal Diagram of Project Management Knowledge Areas in Construction Projects <i>Le Dinh Thuc, Nguyen Quang Huy and Nguyen Minh-Thu</i>	81
12. Overview of causes of wheel rutting on some national highways in Viet Nam <i>Trong Cuong Vo and Thu Hien Nguyen Thi</i>	87
13. Study the procedure of compensation of differential shortening for super-high-rise buildings by the method of moving optimal compensation for construction projects in Vietnam <i>Nguyen Duc Xuan, Nguyen Sy Hung, Ho Ngoc Khoa, Nguyen Thi Thanh Tung</i>	96

14. Characterizations of sugarcane bagasse ash and its use in blended mortar <i>Duc-Hien Le and Minh-Tung Tran</i>	105
15. Nonlinear static analysis of functionally graded porous thin plates resting on elastic foundations <i>Thanh-Hai Le, Van-Long Nguyen, Minh-Tu Tran, Tuan-Anh Nguyen</i>	111
16. Experimental Study on Engineered Cementitious Composites Reinforced with Polypropylene Fiber <i>Xuan-Vinh Tran, Manh-Hung Nguyen, Tien-Hong Nguyen, Van-Thuc Luu</i>	122
17. A Study on Elastic Critical Buckling Strength of Continuous Steel Beams Subjected to Uniformly Distributed Load <i>Xuan-Tung Nguyen, Minh-Thu Nguyen and Xuan-Ba Ho</i>	129
18. Analyzing the causes and proposed some solutions to minimize water inflation during the rainy season in Vinh City, Nghe An <i>Thu-Hang Nguyen Thi</i>	135
19. Prediction of ground surface settlements of deep excavations in Vietnam <i>Nguyen Van-Hoa and Nguyen Tien-Hong, Phan Dinh-Quoc</i>	145
20. Vibration analysis of functionally graded porous plates resting on Kerr elastic foundations <i>Van-Long Nguyen, Minh-Tu Tran, Thanh-Hai Le, Xuan-Thuc Phan</i>	150
21. Analysis of the role of parameters in 16MND5 steel model considering the radiation effects <i>Can-Ngon Nguyen</i>	159
22. Using crater eco-city in Op village, Gia Lai Province as a model of planning and developing eco-urban areas in the direction of sustainable development <i>Kieu-Vinh Thi Nguyen, Thuy-Huong Thi Doan</i>	165
23. Research solutions to improve the quality of survey, design and construction of private housing works in Ha Tinh <i>Tran Van Binh and Luu Thi Thuy</i>	177

# The effect of earthquake frequency content on seismic response of horseshoe tunnels

Van-Quang Nguyen<sup>1,2</sup>, Muhammad Umair Ashfaq<sup>3</sup>, Muhammad Irslan Khalid<sup>3</sup>, Ngoc-Long Tran<sup>2</sup>, Trong-Cuong Vo<sup>2</sup>, Van-Long Phan<sup>2</sup>, Huu-Cuong Nguyen<sup>2,4</sup>

<sup>1</sup> Department of Civil & Environmental Engineering, Hanyang University, Seoul, Korea

<sup>2</sup> Department of Civil Engineering, Vinh University, Vinh, Vietnam

<sup>3</sup> Department of Civil Engineering, NFC Institute of Engineering and Fertilizer Research, Faisalabad, Punjab, Pakistan

<sup>4</sup> Department of Civil & Environmental Engineering, Sejong University, Seoul, Korea

*Email: nguyenvanquang240484@gmail.com*

**Abstract.** Two-dimensional finite difference element analyses are performed to evaluate the tunnel response under earthquakes with different frequency content. The nonlinear model is used to consider the behavior of soil elements, while the elastic model is used to simulate the structure element response. The elastic base is applied at the bottom to absorb propagating waves, and the free-field column is used at the lateral boundary to consider the free-field motion in the soil medium. This study also comprehensively investigates the effect of soil-structure relative stiffness and soil-structure contact. The numerical results are validated with analytical solutions. The parametric study results show that the earthquake frequency content significantly affects the tunnel response. The higher frequency content of the earthquake results in a lower lining response. The effect of earthquake frequency content is more evident when the intensity level of input motion is increased. A similar trend is observed with the effect of soil-tunnel contact. The tunnel response decreases with increasing soil stiffness.

**Keywords:** Dynamic FDM analysis, nonlinear analysis, horseshoe, earthquake, internal forces, earthquake frequency content.

## 1 Introduction

Tunnels are essential components of metropolitan transportation and utility networks. The seismic performance of underground structures is typically thought to perform better than aboveground structures during past earthquakes. However, the recent strong earthquake demonstrates that underground structures may undergo extensive damage. For example, the collapse of the Daikai station was observed during the 1995 Kobe earthquake [1]; damage of tunnels was documented during the 1999 Chi-Chi earthquake [2], 1999 Kocaeli earthquake [3], and 2008 Wenchuan earthquake [4]. Therefore, it is needed to effectively evaluate the seismic performance of the underground structure, especially the horseshoe tunnels.

The earthquake frequency content is an important characteristic of the seismic analysis. There are many parameters used to evaluate the frequency content of an earthquake motion, such as predominant period, mean period, power spectrum intensity, and the ratio between peak ground acceleration (PGA) to peak ground velocity (PGV) [5-7]. Among those, PGA/PGV ratio is a simple and useful parameter to provide information on earthquake frequency. Usually, earthquake motions are divided into three types based on the ratio of PGA/PGV [8]: (i) high frequency (HF) content when  $PGA/PGV > 1.2$ , (ii) intermediate frequency content when  $1.2 \geq PGA/PGV \geq 0.8$ , and (iii) low frequency (LF) content when  $PGA/PGV < 0.8$ .

There are some studies on the effect of earthquake frequency content on different structures considering soil-structure interaction, such as storage tanks [9] and retaining walls [10]. However,

to the knowledge of the authors, the specific study of the effect of the earthquake frequency content on the seismic soil-structure interaction problem of horseshoe tunnels with the nonlinear analysis is still limited. Due to the importance of the problem, a study is necessary to investigate the soil-structure interaction and earthquake frequency content effects on tunnel lining behavior in an accurate analysis.

In this study, two uniform soil types with different properties and twenty earthquake records with different frequency contents are used to evaluate the responses of a horseshoe tunnel. The investigation leads to some new findings useful for practical applications in terms of soil-structure interaction and earthquake frequency content.

## 2 Numerical simulation

Numerical analyses were performed using the FLAC<sup>2D</sup> software [11]. This software, a two-dimensional (2D) explicit finite difference code, was implemented because it is capable of modeling the nonlinear behavior of the soil and soil-structure interaction.

### 2.1 Structural modeling

The tunnel structure modeled in the numerical simulation was chosen from an existing road tunnel in Korea, as presented in Fig. 1(a). The tunnel is located 29 m below the ground surface. The cross-section of the tunnel has a total width of 11.8 m and a maximum height of 8.05 m. The lining thickness is 0.3 m. The tunnel structure was modeled as an elastic behavior material using beam elements with an element size of 0.5 m. The input properties used for structural elements are listed in Table 1.

**Table 1.** Properties of tunnel elements.

Parameter	Value
Density (kg/m <sup>3</sup> )	2500
Young's modulus (GPa)	22.8
Poisson's ratio	0.2

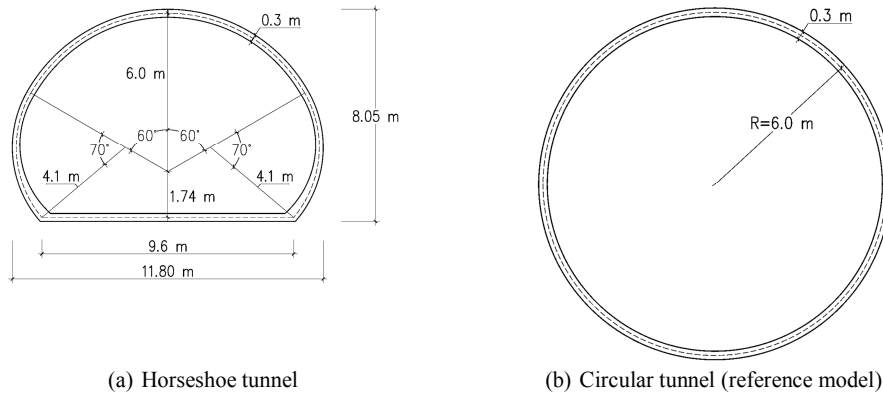


**Fig. 1.** The geometry of the (a) horseshoe tunnel and (b) circular tunnel cross-section.

### 2.2 Soil modeling

Two uniform soil profiles, shear wave velocity ( $V_s$ ) of 200 m/s and 400 m/s, were used in this study. Properties of the soil are summarized in Table 2.

**Table 2.** Properties of the soil material.

Parameter	Value
Density (kg/m <sup>3</sup> )	1800
Shear wave velocity, $V_S$ (m/s)	200, 400
Poisson's ratio	0.3
Small strain damping (%)	1

The numerical model of the tunnel and soil profile is displayed in Fig. 2. The dimensions of the 2D soil model were set to 120 m x 60 m (width x height). The width of the soil model was selected based on a sensitivity study conducted such that the waves reflected from the lateral boundaries do not influence the seismic response of the tunnel. The height of the soil domain is the depth from the ground surface to the bedrock at the investigated site. The soil medium was modeled using plane-strain quadrilateral elements. The element size of 0.5 m was selected based on the recommendation of Kuhlemeyer and Lysmer [12]:

$$\Delta l = \frac{\lambda}{10} \div \frac{\lambda}{8} \quad (1)$$

where  $\lambda$  is the wavelength of propagated wave corresponding to maximum frequency interested. The *Sig3* model, which is available in FLAC<sup>2D</sup>, was employed to simulate the nonlinear behavior of soil.

The Rayleigh damping was used to model small strain damping, is expressed as follows [13]:

$$[C] = \alpha[M] + \beta[K] \quad (2)$$

where  $[C]$  is the damping matrix,  $[M]$  is the mass matrix,  $[K]$  is the stiffness matrix,  $\alpha$  and  $\beta$  are the Rayleigh coefficients.

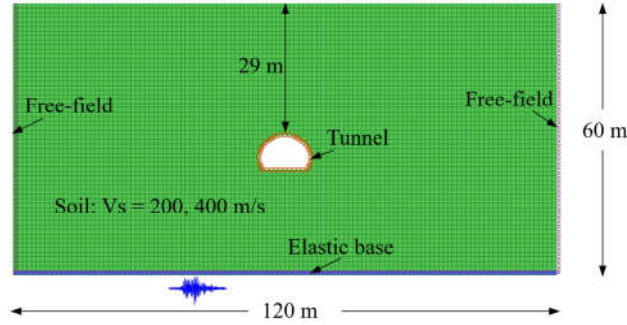


**Fig. 2.** Numerical model of the tunnel and soil domain.

### 2.3 Soil-tunnel contact and boundary conditions

The soil-structure contact was simulated using the interface elements. The interface option UNBONED in the FLAC<sup>2D</sup> software was used in this study. This contact interface can model a realistic partial-slip condition, considering the gapping and the slipping phenomena between soil and tunnel under loading.

The bottom boundaries are used elastic boundary (a quiet boundary) to absorb reflected waves. The input motion was applied as a stress-time history at the base of the numerical model. Lateral boundaries of the numerical models were simulated using the free-field boundary. The free-field boundary aims to create an infinite soil domain in the horizontal direction, as the actual condition. It thus avoids the wave reflections at the boundaries.

## 2.4 Earthquake motions

For this study, 20 motion records were selected from worldwide earthquakes provided by the NGA-West2 database (<https://ngawest2.berkeley.edu>). Two groups of ground motions, including low and high frequency content, are classified separately. Each group contains ten ground motions. The input ground motions are then scaled to 0.1 g and 0.6 g PGA. The response spectra of the 0.1 g input ground motion are shown in Fig. 3.

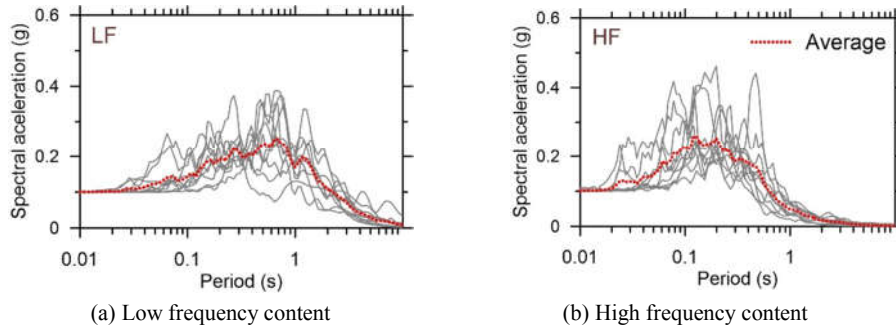


Fig. 3. Response spectra of input ground motions.

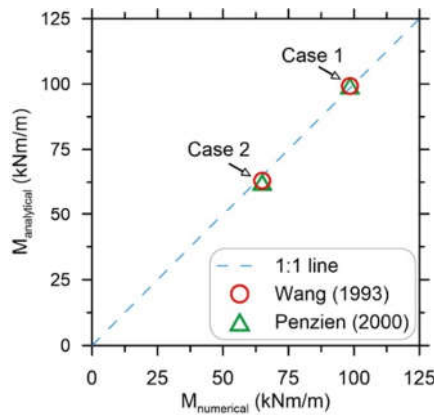


Fig. 4. Comparisons of the bending moment between numerical and analytical solution methods.

## 3 Model validation

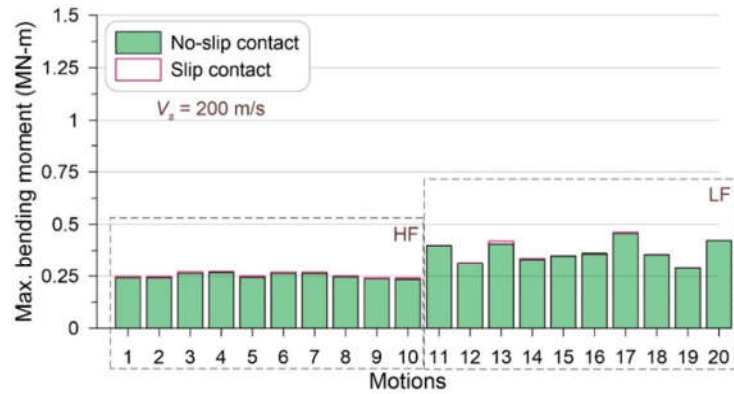
Before the parametric study step, the numerical model is first needed to validate. This research focuses on the parametric study of an unconventional shape to evaluate the tunnel lining response. As studied for the first time, it lacks analytical solutions or experimental tests. A reference model was developed and compared the results with available analytical solutions of Wang [14] and Penzien [15] to validate the numerical modeling method. The reference model has a circular section with an equivalent diameter of a horseshoe tunnel. The detail of circular section geometry is presented in Fig. 1(b). The material properties, boundary conditions, and soil domain size of the reference model are identical to those of the baseline numerical model mentioned earlier. Notably, one soil profile, which has  $V_S = 200$  m/s, was employed in the validation step. Two 0.6 g ground motions, one was selected from low frequency content (case 1), and the other was selected from

high frequency content (case 2), were used as input loading in the reference model. Moreover, the no-slip condition was adopted to be consistent with analytical solutions.

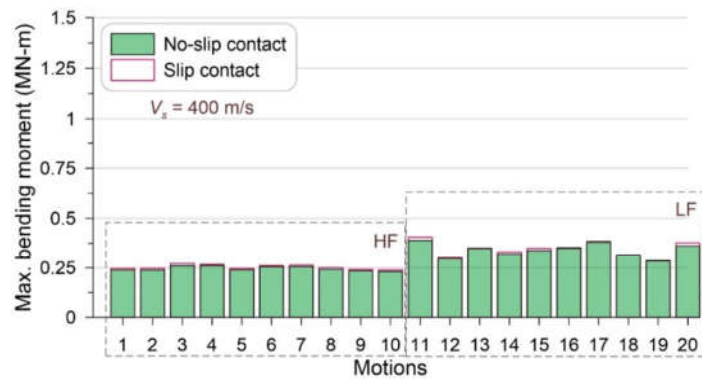
Fig. 4 shows the comparisons of the bending moment calculated from numerical simulation and analytical solutions for two cases. The dashed line (i.e., the 1:1 line) indicates target values. The closer scattering to the 1:1 line, the lower difference between numerical and analytical methods. As can be seen from the figure, the bending moment from numerical results is an almost perfect match with analytical solutions. It proves that the numerical model is reliable for further parametric studies.

#### 4 Results and discussions

A total of 160 analyses were performed in the parametric study step. The numerical results are presented in Fig. 5 and Fig. 6. The bending responses of the tunnel lining in the case of 0.1 g input motions are shown in Fig. 5. The effect of earthquake frequency content is evident for both  $V_S = 200$  m/s and  $V_S = 400$  m/s. The lower frequency content of earthquake causes a higher tunnel response (i.e. bending moment) compared to that of higher frequency content. However, the effect of soil-tunnel contact seems to be negligible in this case.



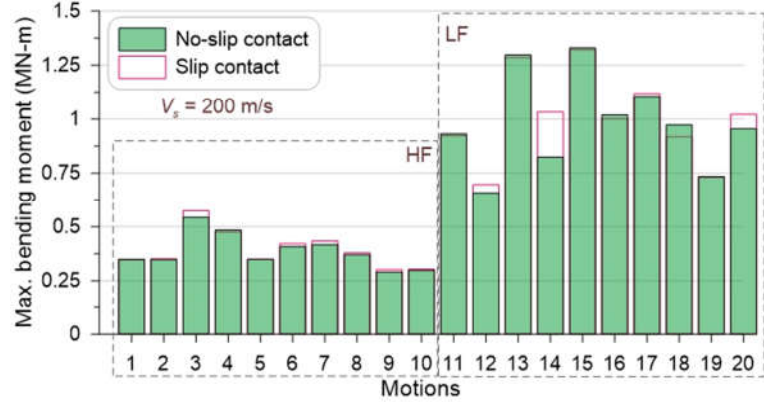
(a)  $V_S = 200$  m/s



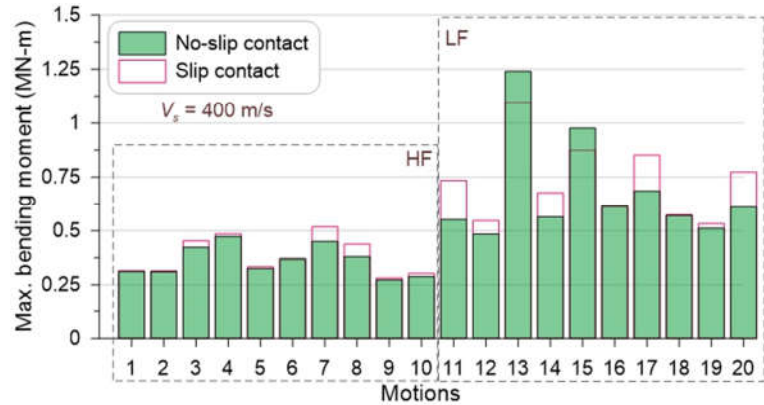
(b)  $V_S = 400$  m/s

Fig. 5. Tunnel responses in the case of 0.1 g input ground motions.

Fig. 6 presents the lining bending moment response in the case of 0.6 g input motions. The difference of bending moment between LH and HF is more obvious compared to that of the lower intensity of input motions (i.e., 0.1 g PGA). The effect of soil-tunnel contact is also more apparent. This is because the nonlinearity of soil increases when the increasing intensity of the input motion. It results in higher flexibility of tunnel lining. The tunnel located in the case of  $V_S = 400$  m/s generally causes a lower lining response compared to that of  $V_S = 200$  m/s. It indicates that tunnel embedded in stiff soil would be safer than soft soil when subjected to a seismic loading.



(a)  $V_S = 200$  m/s



(b)  $V_S = 400$  m/s

Fig. 6. Tunnel responses in the case of 0.6 g input ground motions.

## 5 Conclusions

This study presents the effect of earthquake frequency content on the seismic response of horseshoe tunnels. Effect of the soil-tunnel contact, the intensity of input motions, and the soil stiffness are also investigated. The numerical simulation models were developed and validated with analytical solutions. A nonlinear constitutive model was used for the surrounding soil. A total of 160 analyses were performed for parametric studies. The following conclusions are drawn.

- (1) The earthquake frequency content has a significant effect on the tunnel response. With the increase of ground motion intensity, the difference in tunnel response between LF and HF is increased.
- (2) The effect of soil-tunnel contact rises with increasing intensity levels. In the case of 0.1 g input motions, that effect is small and can be ignored. However, in the case of 0.6 g input motions, the effect is noticeable.
- (3) The higher soil stiffness, the lower the tunnel response is observed. It indicates that the tunnel located in stiff soil would be less vulnerable than soft soil when subjected to seismic loading.

## References

1. Iida H, Hiroto T, Yoshida N, Iwafuji M. Damage to Daikai subway station. *Soils and Foundations*.36(Special), 283-300 (1996).
2. Wang W, Wang T, Su J, Lin C, Seng C, Huang T. Assessment of damage in mountain tunnels due to the Taiwan Chi-Chi earthquake. *Tunnelling and Underground Space Technology*.16(3), 133-50 (2001).
3. Ghasemi H, Cooper JD, Imbsen R, Piskin H, Inal F, Tiras A. The November 1999 Duzce Earthquake: post-earthquake investigation of the structures on the TEM. Rep No FHWA-RD-00.146, 00-146 (2000).
4. Li T. Damage to mountain tunnels related to the Wenchuan earthquake and some suggestions for aseismic tunnel construction. *Bulletin of Engineering Geology and the Environment*.71(2), 297-308 (2012).
5. McGuire RK. Seismic ground motion parameter relations. *Journal of the Geotechnical Engineering Division*.104(4), 481-90 (1978).
6. Rathje EM, Faraj F, Russell S, Bray JD. Empirical relationships for frequency content parameters of earthquake ground motions. *Earthquake Spectra*.20(1), 119-44 (2004).
7. Newmark NM, Hall W, Mohraz B. A study of vertical and horizontal earthquake spectra. Report WASH-1255, Directorate of Licensing, US Atomic Energy Commission. 28-48 (1973).
8. Tso W, Zhu T, Heidebrecht A. Engineering implication of ground motion A/V ratio. *Soil Dynamics and Earthquake Engineering*.11(3), 133-44 (1992).
9. Kianoush M, Ghaemmaghami A. The effect of earthquake frequency content on the seismic behavior of concrete rectangular liquid tanks using the finite element method incorporating soil-structure interaction. *Engineering Structures*.33(7), 2186-200 (2011).
10. Cakir T. Evaluation of the effect of earthquake frequency content on seismic behavior of cantilever retaining wall including soil-structure interaction. *Soil Dynamics and Earthquake Engineering*.45, 96-111 (2013).
11. Itasca Consulting Group. *FLAC - Fast Lagrange Analysis of Continua; Version7.0. In: User Manual*. 2011.
12. Kuhlemeyer RL, Lysmer J. Finite element method accuracy for wave propagation problems. *Journal of Soil Mechanics & Foundations Div*.99(Tech Rpt), (1973).
13. Chopra A. *Structural Dynamics: Theory and applications to earthquake engineering*. 2nd ed: Prentice Hall; 2001. p. 455-8.
14. Wang J-N. *Seismic Design of Tunnels: A Simple State-of-the-art Design Approach*. Parsons Brinckerhoff; 1993.
15. Penzien J. Seismically induced racking of tunnel linings. *Earthquake Engineering*.29(5), 683-91 (2000).

# Damage simulation of reinforced concrete beams relating to corrosion of reinforcement in concrete

*Vu Ba Thanh<sup>1</sup>, Tran The Truyen<sup>1</sup>, Vo Van Nam<sup>2</sup>, Pham Duc Manh<sup>1</sup>*

<sup>1</sup>University of Transport & Communications

<sup>2</sup>University of Transport & Communications, Campus in Ho Chi Minh City

*Email: tranhetruyen@utc.edu.vn*

**Abstract.** The degree of reinforcement corrosion has a great influence on the load capacity and durability of reinforced concrete (RC) structures. This paper uses a simulation tool of finite element method (FEM) such as Abaqus combined with the concrete damage plasticity (CDP) model and steel - concrete deteriorated bond model to investigate the damage of corroded and non-corroded RC beams. Simulation results are compared with experimental ones to verify the influence of reinforcement corrosion degree on load-displacement behaviors and crack paths of the aforementioned RC beams.

**Keywords:** Reinforced Concrete Beam, Finite Element Method, Reinforcement Corrosion Resistance, Concrete Damage Plasticity.

## 1. Introduction

The durability of reinforced concrete structures is the most important issue for the construction industry. In particular, the problem of reinforcement corrosion in concrete structures has a great influence on the durability and service life of this structure. Vietnam is a country with a long coastline leading to coastal reinforced concrete structures that are heavily affected by the problem of sea vapor erosion into concrete structures, causing corrosion of reinforcement. Therefore, the issue of the influence of reinforcement corrosion on the behavior of RC beams needs to be researched seriously.

In the world, many reseachs on corrosion of reinforcement in RC structures have been deployed quite early, showing special interest in this problem, in which corrosion of reinforcement in concrete is the main cause which causes deterioration in the quality of RC structure has been demonstrated in studies [1-7].

In Vietnam, the researches on corrosion of concrete and corrosion of reinforcement have been interested and deployed by many scientists [8-13]. Calculations predicting service life according to the criteria of starting to corrode steel allow us to predict the service life or the time when the corrosion of reinforcement in concrete will begin to appear [11, 12]. Corrosion propagation calculations allow for the determination of how long the structure damaged due to corrosion [13]. The time of corrosion propagation usually does not last long (6-10 years) but it is the cause of the rapid decline in the resistance of the structure. The assessment of the corroded structure's bearing capacity corresponding to the degree of corrosion according to the life prediction levels has not been mentioned.

Recently, experimental research [14] determined the corrosion degree of reinforcement of reinforced concrete beams immersed in an electrolytic environment with 3-5% NaCl solution. After that, the test to determine the load capacity of the flexural beam was carried out to evaluate the influence of reinforcement corrosion on the behavior of reinforced concrete beams. In this study, the authors use a finite element method (FEM) simulation method like Abaqus with the use of a concrete damage plasticity model (CDP) [15, 16] to model the damage of RC beams considering the influence of reinforcement corrosion and compared with experimental results of [14].

## 2 Simulation method applied to corroded RC beams

### 2.1 Concrete damage plasticity (CDP)

The CDP model [16] built in the Abaqus finite element method simulation tool is applied to this study. This model combines the isotropic tensile and compressive plastic properties to represent the behavior in the non-elastic state of concrete. The CDP model can simulate the loading cases for concrete structures under uniform, cyclic or dynamic loads with small load increments [17]. In the case of uniaxial tension and compression, it is assumed that there are two main failure mechanisms: (i) tensile cracking and (ii) compression fracture of the concrete structure [18]. The indices  $t$  and  $c$  respectively represent the tension and compression states. Under uniaxial tensile loads, the stress-strain relationship of the concrete material is purely elastic until a state of destructive stress is reached  $\sigma_{t0}$ , at which cracks in the material begin to form.

Under uniaxial compression, the behavior is linear until the initial yield stress is reached  $\sigma_{c0}$ . During the plastic phase, the material behavior is characterized by the second part of the relationship curve (see Figure 1b) by the critical stress  $\sigma_{cu}$ . In both above loading states, the concrete material is simulated using the CDP model, with the use of two plastic strains respectively  $\bar{\varepsilon}_c^{pl}$  and  $\bar{\varepsilon}_t^{pl}$  to control the development of the yield and failure states of the concrete.

When the concrete is unloaded, this behavior is shown by the dashed line in Figure 1b showing the reduced elastic stiffness of the failed material. This failure elastic stiffness is characterized by two destructive variables in formula (1) as  $d_t$  and  $d_c$  below:

$$d_t = d_t(\bar{\varepsilon}_t^{pl}, f_i), 0 \leq d_t \leq 1; \quad d_c = d_c(\bar{\varepsilon}_c^{pl}, f_i), 0 \leq d_c \leq 1 \quad (1)$$

in which:  $d_t$ : Tension destructive variables  
 $d_c$ : Compression destructive variables  
 $f_i$  ( $i = 1, 2, \dots$ ): represent other relevant effects.

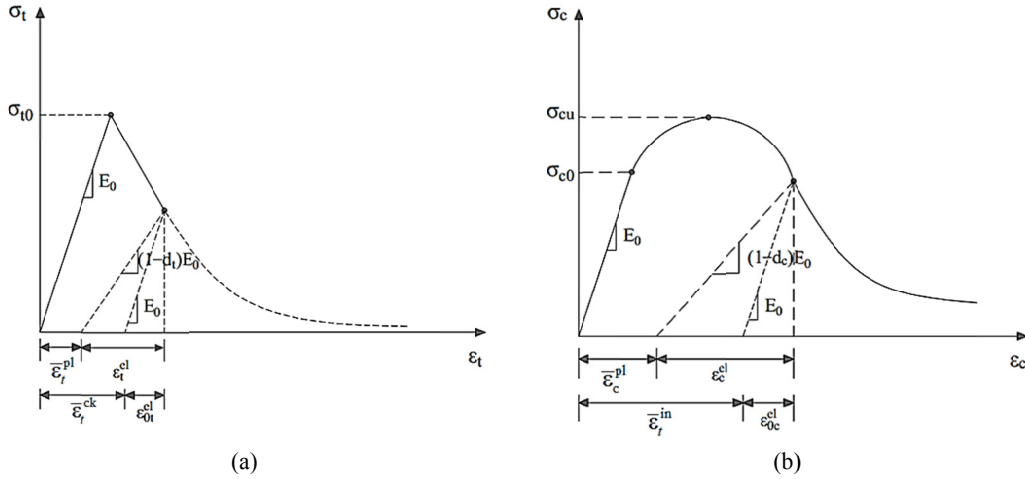


**Fig. 1.** The basic model of concrete under conditions: (a) Tensile; (b) Compressive

The stress-strain relationship under compression and tension when using two variables  $d_t$  and  $d_c$  is shown:

$$\sigma_t = (1 - d_t) E_0 (\varepsilon_t - \bar{\varepsilon}_t^{pl}); \quad \sigma_c = (1 - d_c) E_0 (\varepsilon_c - \bar{\varepsilon}_c^{pl}) \quad (2)$$

where  $E_0$  is the initial elastic modulus of concrete.

In the uniaxial tensile state, the post-failure behavior for cracked concrete is determined by the stress-strain relationship curve in Figure 1a. In reinforced concrete structures, post-failure stress is expressed through cracking strain  $\bar{\varepsilon}_t^{ck}$

$$\bar{\varepsilon}_t^{ck} = \varepsilon_t - \varepsilon_{0t}^{el} \quad (3)$$

in which  $\varepsilon_{0t}^{el} = \frac{\sigma_t}{E_0}$  following Figure 1.

According to Figure 1a,  $d_t - \bar{\varepsilon}_t^{ck}$  cracking deformation is converted to:

$$\bar{\varepsilon}_t^{pl} = \bar{\varepsilon}_t^{ck} - \frac{d_t}{(1-d_t)} \frac{\sigma_t}{E_0} \quad (4)$$

In the condition of uniaxial compression, the stress-strain behavior of concrete outside the elastic state is represented by the elastic external strain in compression,  $\bar{\varepsilon}_c^{in}$ . This strain was defined as the total strain  $\varepsilon_c$  minus the elastic strain corresponding to the undamaged material  $\varepsilon_{0c}^{el}$ .

$$\bar{\varepsilon}_c^{in} = \varepsilon_c - \varepsilon_{0c}^{el} \quad (5)$$

in which,  $\varepsilon_{0c}^{el} = \frac{\sigma_c}{E_0}$  following Figure 1b.

Using the behavior curve in Figure 1b,  $d_c - \bar{\varepsilon}_c^{in}$ , the elastic external strain in compression is transformed as

$$\bar{\varepsilon}_c^{pl} = \bar{\varepsilon}_c^{in} - \frac{d_c}{(1-d_c)} \frac{\sigma_c}{E_0} \quad (6)$$

## 2.2. Model of adhesion between concrete and corroded reinforcement

Two factors that affect the relationship between the adhesion-slip stress of concrete and reinforcement are the content of corroded reinforcement and the slip resistance of concrete at the position adjacent to the reinforcement. There is a phenomenon that the initial adhesion strength increases with the corrosion content in the pre-cracking stage at the boundary of concrete and reinforcement, but then this strength decreases significantly when the crack is caused by corrosion vertical steel developed [19]. However, damage due to adhesion in the corroded reinforcement is due to separation at the junction surface. Therefore, the stress-adhesion relationship parameters must be changed. In this research, the residual adhesion stress-slip curve of [20] was used for the degraded bond between reinforcement and concrete (see Figure 2). For non-corrosion reinforcement, the adhesion between reinforcement and concrete is illustrated by the stress-slip curve in CEB-FIB [21].

The relationship between adhesion force and slip is described by the following formulas:

$$U = U_1 \left( \frac{S}{S_1} \right)^{0.3} \quad (7)$$

$$S_\alpha = S_1 \left( \frac{\alpha' U_{\max,D}}{U_1} \right)^{\frac{1}{0.3}} \quad (8)$$

$$S_{\max} = S_1 \exp \left[ \left( \frac{1}{0.3} \right) L.n \left( \frac{U_{\max,D}}{U_1} \right) \right] + S_0 . L.n \left( \frac{U_1}{U_{\max,D}} \right) \quad (9)$$

in which,  $\alpha' = 0.7$ ,  $U_1 = 2.57 (f'_c)^{0.5}$  with  $f'_c$  is the compressive strength of uncorrosion concrete,  $S_1 = 0.15c_0$  with  $c_0 = 8.9\text{mm}$  is the interval between the adjacent tendon of the reinforcement,  $S_2 = 0.35c_0$  and  $S_0 = 0.15$  or  $0.4\text{mm}$  for unreinforced or reinforced concrete, respectively.

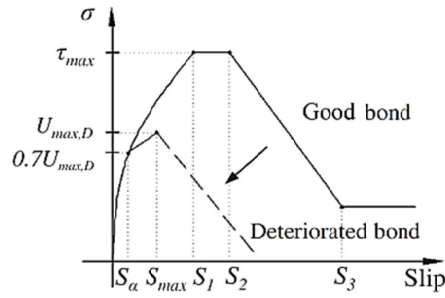


Fig. 2. Basic law of adhesion force when the reinforcement was corroded

$$U_{\max,D} = R \left[ 0.55 + 0.24 \left( \frac{c_c}{d_b} \right) \right] + 0.191 \left( \frac{A_{st} f_{yt}}{S_s d_b} \right) \quad (10)$$

$$R = A_1 + A_2 m_L \quad (11)$$

The residual adhesion strength  $U_{\max,D}$  is determined in formula (10), where  $c_c$  is the thickness of the protective concrete,  $d_b$  is the diameter of the reinforcement,  $A_{st}$  and  $f_{yt}$  are the cross-section area and yield strength of the stirrup,  $S_s$  is the spacing of the stirrup,  $R$  is the coefficient related to the residual adhesion strength of concrete and reinforcement with  $A_1 = 0.861$  and  $A_2 = -0.014$ ,  $m_L$  is the content of lost reinforcement (%). Eq. (11) includes two corresponding terms related to the influence of concrete and stirrup on adhesion strength.

### 2.3. Test beams of corroded reinforcement

In this paper, the results of reinforcement corrosion tests performed by [14] are used for concrete with design compressive strength  $f'_c = 30 \text{ MPa}$  (C30). The reinforcement used is a plain round bar of diameter D10 with yield strength  $f_y = 240 \text{ MPa}$ . The size of the test beam sample is  $500 \times 100 \times 100 \text{ mm}$  as shown in Figure 3.

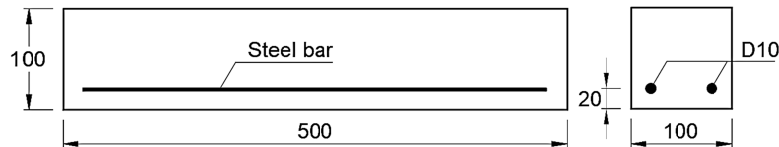


Fig. 3. Dimensions of the beam test

Boundary conditions and superimposed load diagrams are shown in Figure 4 with two symmetrical loading points 150 mm apart and two bearings 25 mm from the end of the beam. According to [14], the destructive bending force of the non-immersed beam sample has the value  $P_{\max} = 28$  kN and the sample immersed in the electrolyte solution has a content of corrosion of reinforcement up to 25.2%.

The obtained experimental results are compared with the simulation results by Abaqus on the load-displacement relationship and the crack path.

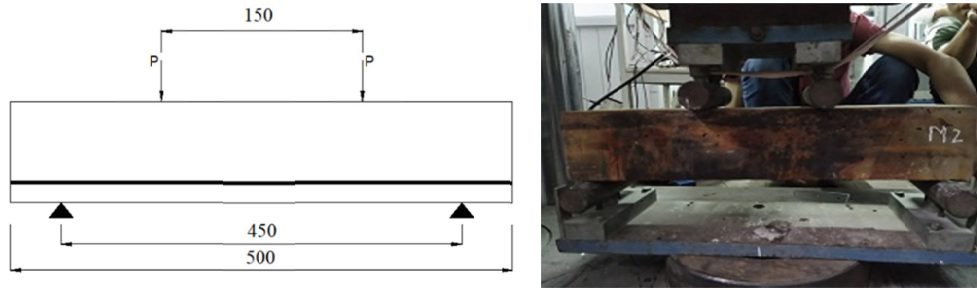


Fig. 4. Process of superimposed load

### 3. Analyze and compare results between experiment and simulation

In Abaqus software, reinforcement bars and concrete are modeled using the C3D8R 8-node element. The bond between reinforcement and concrete is described by the 8-node binding element COH3D8 as shown in Figure 5. Material properties for concrete according to CDP model for C30 concrete are shown in Table 1. Two the loading point is applied with a uniform load step of 1kN until the beam is completely damaged with the load diagram as shown in Figure 4.

Table 1. Material properties for the concrete damage plasticity (CDP) of C30 concrete

Material properties	C30	Plasticity factor	
		Expansion angle	31
Elastic properties of concrete		Eccentricity	0.1
E(GPa)	28.11	$f_{b0}/f_{c0}$	1.16
$\nu$	0.2	K	0.67
		Viscous factor	0
Compressive behavior of concrete		Compressive damage of concrete	
Yield stress $\sigma_{c0}$ (MPa)	Unelastic deformation $\bar{\epsilon}_c^{in}$	Sabotage parameter $d_c$	Unelastic deformation $\bar{\epsilon}_c^{in}$
15.3	0	0	0
19.2	0.000048249	0	0.000048249
22.5	0.000119844	0	0.000119844
25.2	0.000214786	0	0.000214786
27.3	0.000333074	0	0.000333074
28.8	0.000474708	0	0.000474708
29.7	0.000639689	0	0.000639689
30	0.000828016	0	0.000828016
29.7	0.001039689	0.01	0.001039689
28.8	0.001274708	0.04	0.001274708

27.3	0.001533074	0.09	0.001533074
25.2	0.001814786	0.16	0.001814786
22.5	0.002119844	0.25	0.002119844
19.2	0.002448249	0.36	0.002448249
15.3	0.0028	0.49	0.0028
10.8	0.003175097	0.64	0.003175097
5.7	0.003573541	0.81	0.003573541
Tensive behavior of concrete		Tensive damage of concrete	
Yield stress $\sigma_{10}$ (MPa)	Crack deformation $\bar{\varepsilon}_t^{ck}$	Sabotage parameter $d_t$	Crack deformation $\bar{\varepsilon}_t^{ck}$
4.01	0	0	0
0.03	0.001167315	0.99	0.001167315

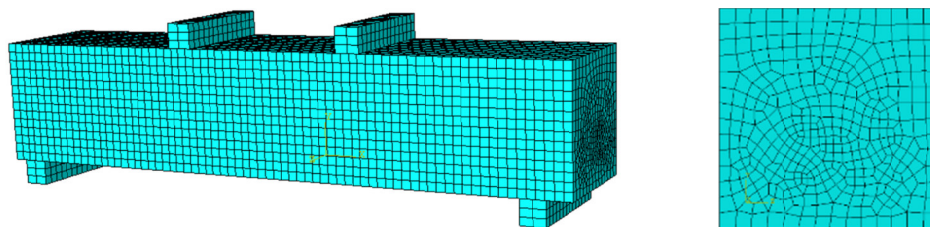


Fig. 5. Abaqus software: Mesh division for beam structures

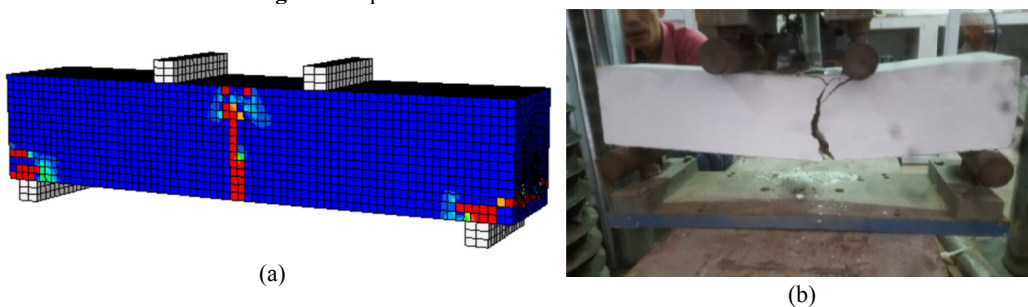


Fig. 6. Crack image of non-immersed beam: (a) Simulation with Abaqus; (b) Experimental test.

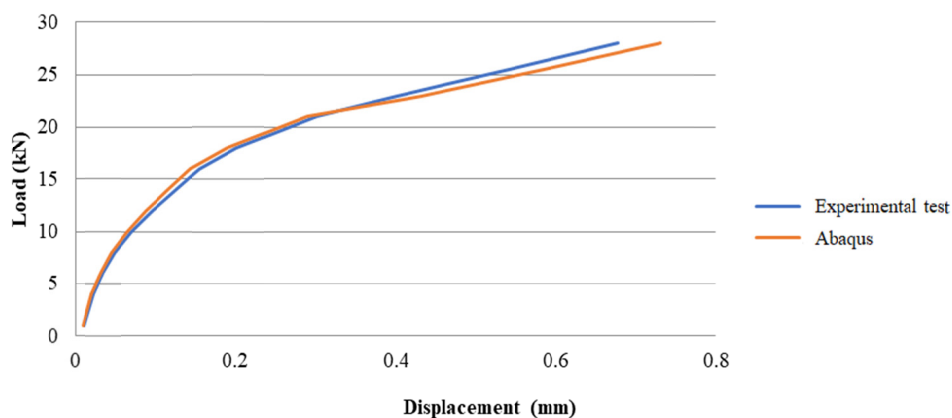
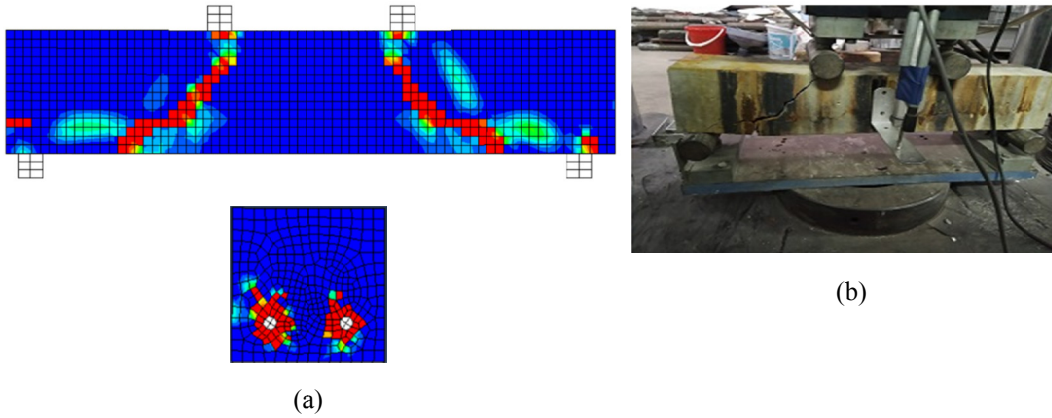
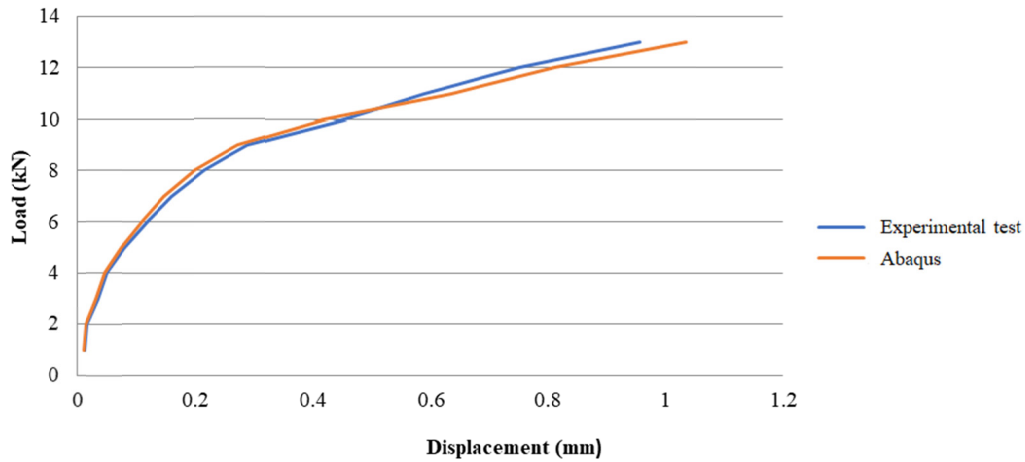


Fig. 7. Comparison of the behavior curve of non-immersed beams between simulation by Abaqus and experimental test.

The results obtained by experimental method [14] and simulated by Abaqus software for beams not immersed in NaCl solution are shown in Figure 6 and Figure 7. In which Figure 6 compares the beam's crack shape, The crack appears in the middle of the bottom of the beam and propagates almost vertically to the top of the beam. Figure 7 shows a comparison of displacement-load curves between the two methods with the maximum difference of values not more than 8%. From Figure 6 and Figure 7, we see that the results between the two methods are similar, which is the driving force to perform simulations for beams with 25.2% corroded reinforcement in the next example.



**Fig. 8.** Crack image of beam with 25.2% corroded reinforcement:  
(a) Simulation by Abaqus; (b) Experimental test.



**Fig. 9.** Comparison of the behavior curve of beam with 25.2% corroded reinforcement between simulation by Abaqus and experimental test.

The purpose of the second example is to simulate beams with corroded reinforcement because the beams are immersed in NaCl solution in combination to create electrodes that activate the galvanic corrosive environment as presented in [14]. The adhesion of reinforcement to concrete is weakened according to the adhesion model specified in section 2.2. The results obtained for this example are shown in Figure 8 and Figure 9. In which Figure 8 compares the crack between simulation [14] and experiment with two major cracks formed: the first crack appears from the bottom of the beam at an angle of  $45^\circ$  spreading to the point of application of the force on the top face of the beam and a second one appears at the junction between the concrete and the reinforcement propagates along the reinforcement bar. Figure 9 compares the load-

displacement curves between the two methods. We see that the simulation method by Abaqus software gives reliable results with the two examples aforementioned.

#### 4. Conclusions

The research used a FEM simulation tool such as Abaqus to simulate and compare the results with the experiment for two-beam samples: the beam sample was not soaked, and the beam was immersed in an electrolyte environment [14]. From this, a few conclusions can be drawn.

- The results between simulation and experiment are similar in the crack paths and load-displacement relationship curve when loading two aforementioned beam samples. This shows that the simulation method by Abaqus software is reliable.
- The load capacity of beams with corroded reinforcement is 25.2% lower than that of beams with non-corroded reinforcement. This shows that the degree of corrosion of reinforcement can affect the performance and life of the structure.
- Corrosion of the reinforcement beam appears diagonal crack at 45° angle from the bottom of the beam spreading to the point of application of force and cracks along the boundary between reinforcement and concrete due to a decrease in adhesion ability between reinforcement and concrete.

For the next research, in addition to the simulation by Abaqus, the authors can use another numerical method to model the damage of RC beams with different levels of corroded reinforcement and the influence of the parameters on the failure of the RC beams corroded.

#### Acknowledgments

This research is funded by the Vietnam Ministry of Education and Training under grant number B2022-GHA-05.

#### References

1. Berke N. S., Pfeifer D., Donal W., and Thomas G. W., Protection Against Chloride – Induced Corrosion, *Concrete International*, 10(12) (1988), 45 - 55
2. Soltani, M., Safiey, A., Brennan, A., A State-of-the-Art Review of Bending and Shear Behaviors of Corrosion-Damaged Reinforced Concrete Beams. *ACI Structural Journal*, 116(3) (2019), 53–64.
3. Almusallam, A. A., and Al-gahtani, A. S., Effect of Reinforcement Corrosion on Bond Strength. *Construction and Building Materials*, Vol. 10(2) (1996), 123–129. [https://doi.org/10.1016/0950-0618\(95\)00077-1](https://doi.org/10.1016/0950-0618(95)00077-1)
4. Wang L., Ma, Y., Zhang, J., Liu, Y., Probabilistic Analysis of Corrosion of Reinforcement in RC Bridges Considering Fuzziness and Randomness, *Journal of Structural Engineering*, Vol. 139(9) (2013).
5. Arslan, M. E., & Durmuş, A., Fuzzy logic approach for estimating bond behavior of lightweight concrete. *Computers and Concrete*, 14(3) (2014), 233–245. <https://doi.org/10.12989/cac.2014.14.3.233>
6. Petcherdchoo, A., Probability-based sensitivity of service life of chloride-attacked concrete structures with multiple cover concrete repairs. *Advances in Civil Engineering*, (2018). <https://doi.org/10.1155/2018/4525646>
7. Berra, M., Castellani, A., Coronelli, D., Zanni, S., and Zhang, G., Steel Concrete Bond Deterioration due to Corrosion: Finite-Element Analysis for Different Confinement Levels. *Magazine of Concrete Research*, 55(3) (2003), 237–247. <https://doi.org/10.1680/macr.2003.55.3.237>
8. Nguyen Viet Trung, Tran The Truyen, Ho Xuan Tu - Permeation and corrosion of reinforced concrete structures, *Construction publishing company (2014)*. *In Vietnamese*: Nguyễn Việt Trung, Trần Thế Truyền, Hồ Xuân Tú - Thẩm và ăn mòn kết cấu bê tông cốt thép, *NXB Xây dựng*, (2014).
9. Cao Duy Tien, Pham Van Khoan, Le Quang Hung, Final report on project of anti-corrosion and protection of concrete and reinforced concrete works in coastal areas, *Institute of Construction Science and Technology*, 11 (2003). *In Vietnamese*: Cao Duy Tiên, Phạm Văn Khoan, Lê Quang

- Hùng, Báo cáo tổng kết dự án chống ăn mòn và bảo vệ các công trình bê tông và BTCT vùng biển, *Viện KHCN Xây dựng*, 11 (2003).
10. Pham Duy Huu, Dao Van Dinh, Tran The Truyen, Thai Khắc Chien, Nguyen Thanh Sang: *Structural design according to durability*, Transport & Communications Publishing company, university textbook, 6 (2016). *In Vietnamese*: Phạm Duy Hữu, Đào Văn Đình, Trần Thế Truyền, Thái Khắc Chiển, Nguyễn Thanh Sang: *Thiết kế kết cấu theo độ bền*, NXB GTVT, giáo trình đại học, 6 (2016).
  11. Ho Van Quan, Nguyen Van Tuoi, Tran The Truyen, Pham Thai Uyet, Nguyen Trung, Forecasting the service life of reinforced concrete structures according to the criteria of reinforcement corrosion due to carbonation and chloride ion intrusion, *Journal of Transport and Communications*, 9 (2018). *In Vietnamese*: Hồ Văn Quân, Nguyễn Văn Tuổi, Trần Thế Truyền, Phạm Thái Uyết, Nguyễn Trung, Dự báo tuổi thọ của các kết cấu bê tông cốt thép theo tiêu chí ăn mòn cốt thép do cacbonat hóa và xâm nhập ion clo, *Tạp chí GTVT*, 9 (2018).
  12. Tran The Truyen , Ho Xuan Ba, Truong Van Quyet, Forecasting the service life of reinforced concrete bridge works according to the criterion of steel corrosion in concrete taking into account the effects of dead and live loads on the bridge, *Journal of Bridges and Roads*, 7 (2020). *In Vietnamese*: Trần Thế Truyền, Hồ Xuân Ba, Trương Văn Quyết, Dự báo tuổi thọ sử dụng của công trình cầu bê tông cốt thép theo tiêu chí ăn mòn thép trong bê tông có xét đến ảnh hưởng của tĩnh tải và hoạt tải trên cầu, *Tạp chí Cầu đường*, 7 (2020).
  13. Pham Duy Huu, Bui Trong Cau, Dao Van Dinh, Prediction of propagation time of reinforcement corrosion in reinforced concrete structures exposed to chlorine, *Vietnam Road and Bridge Journal*, April 2014 issue, 11-15 days. *In Vietnamese*: Phạm Duy Hữu, Bùi Trọng Cầu, Đào Văn Đình, Dự báo thời gian lan truyền ăn mòn cốt thép trong kết cấu bê tông cốt thép phơi nhiễm Clo, *Tạp chí Cầu đường Việt Nam* số tháng 4 (2014), 11-15.
  14. Vo Van Nam, Tran The Truyen, Analysis of the influence of the degree of corrosion of reinforcement in concrete on the behavior of reinforced concrete beams, *Journal of Construction*, October (2021), 62-65. *In Vietnamese*: Võ Văn Nam, Trần Thế Truyền, Phân tích ảnh hưởng của mức độ ăn mòn cốt thép trong bê tông đến ứng xử của dầm bê tông cốt thép, *Tạp chí Xây dựng*, số tháng 10 (2021), 62-65.
  15. Hafezolghorani, M. Hejazi, F., Vaghei, R., Jaafar, M., Karimzade, K., Simplified damage plasticity model for concrete, *Structural Engineering International*, 27(1) (2017), 68-78. <https://doi.org/10.2749/101686616X1081>.
  16. Shen, J., Gao, J., Li, L., Du, K., Jin, J., Chen, W., Xu, Y., Damage evolution of rc beams under simultaneous reinforcement corrosion and sustained load, *Materials*, 12(4) (2019), 627. <https://doi.org/10.3390/ma12040627>.
  17. Dong, Y., Xu, Z., Zeng, K., Cheng, Y., Xu, C., Seismic behavior, and cross-scale refinement model of damage evolution for RC shear walls. *Engineering structures*. 167 (2018), 13–25. <https://doi.org/10.1016/j.engstruct.2018.03.096>.
  18. Hibbitt, H.D., Karlsson, B.I.; Sorensen, E.P. ABAQUS User's Manual; Dassault Systemes Simulia Corp: Providence, RI, USA, (2011).
  19. Lim, S., Akiyama, M., Frangopol, D. M. Assessment of the structural performance of corrosionaffected RC members based on experimental study and probabilistic modeling. *Engineering Structures*, 127 (2016), 189–205. <https://doi.org/10.1016/j.engstruct.2016.08.040>.
  20. Kallias, A. N., Rafiq, M. I. Finite element investigation of the structural response of corroded RC beams. *Engineering Structures*, 32(9) (2010) 2984–2994. <https://doi.org/10.1016/j.engstruct.2010.05.017>.
  21. Thomas Telford, London, CEB-FIP Model Code. *Design code*. (1990). <https://doi.org/10.1680/ceb-fipmc1990.35430.0007>.

# Experimental study concrete shrinkage at high temperature due to climate changes

Ngoc-Long Tran<sup>1</sup>, Tien-Hong Nguyen<sup>1</sup>, Xuan-Hieu Nguyen<sup>1</sup>, Chung-Bao Nguyen<sup>2</sup>

<sup>1</sup> Department of Civil Engineering, Vinh university, Vietnam

<sup>2</sup> Master Student of Department of Civil Engineering, Vinh university, Vietnam

Email: longtn@vinhuni.edu.vn

**Abstract:** The report presents experimental results of concrete shrinkage strain measurement under high temperature conditions (above 40 degrees Celsius). High temperature is a reflection of climate change that has been taking place more and more seriously on earth. The experiment was carried out at Vinh University's laboratory, with a duration of 390 days, using a measuring device, the C363 KIT. The obtained data set reflects accurately and reliably. The obtained concrete shrinkage strain has a larger value, the growth rate is faster than that under normal conditions.

**Key word:** Experimental, shrinkage; concrete, temperature, climate change.

## 1. Introduction

The Asian Development Bank (ADB) commented that Viet Nam is extremely vulnerable to climate change impacts given its extensive coastline and river deltas, and highlands that have poor water retention capacity and are susceptible to severe erosion [5].

According to the Intergovernmental Panel on Climate Change, since the mid-1960s, the average sea level has risen 20 centimeters and the average temperature has increased 0.5 - 0.7 degrees in Viet Nam [5,6]. Sea level rise intensifies flood damage; during 2001 - 2010, natural disasters have resulted in damage equal to about 1.5% of annual gross domestic product (GDP). Sea level rise and potential changes in storm intensity are likely to increase the unpredictability of (and most likely exacerbate) natural disasters. As a result of climate change, Viet Nam's yearly mean temperature is expected to rise 2 - 3 degrees Celsius, with sea level 75 - 100 centimeters higher than 1980 - 1999 levels, at the end of this century. It is estimated that 10% - 12% of Viet Nam's population will be directly affected and the country will lose around 10% of GDP [6,7,8].

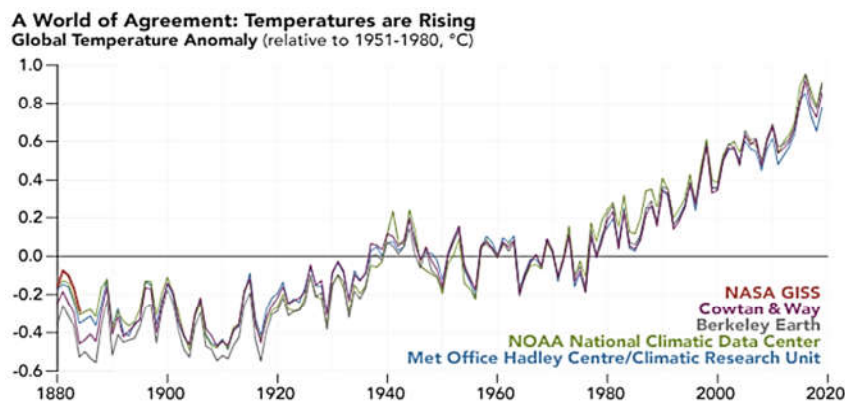


Fig. 1. Shows the gradual increase in temperature from 1880 to 2020, by NOAA's 2020 [1].

Though warming has not been uniform across the planet, the upward trend in the globally averaged temperature shows that more areas are warming than cooling. According to NOAA's 2020 Annual Climate Report the combined land and ocean temperature has increased at an average rate of 0.13 degrees Fahrenheit (0.08 degrees Celsius) per decade since 1880; however, the average rate of increase since 1981 (0.18°C / 0.32°F) has been more than twice that rate [7].

The increased temperature has had a significant effect on concrete, it makes the amount of water in the early concrete evaporate quickly. That causes concrete shrinkage to increase at a fast rate, with a large value, leading to cracks in the concrete structure.

Concrete shrinkage is of increasing concern when focusing on maintaining durable structures. Over time, the shrinkage induces cracking which can severely decrease concrete life expectancy. These volume changes are often attributed to drying of the concrete over a long time period, though recent observations have also focused on early age or plastic drying problems. At early ages the concrete is still moist and there are difficulties in measuring the fluid material. These difficulties have hindered comprehensive physical testing and understanding of the factors influencing plastic shrinkage. The most common solution to reduce early age volume changes is to avoid drying by proper handling of the concrete for the first few hours after placement. It is imperative that the concrete curing begins immediately and follows correct methods [9-14].

An experimental program was developed using fractional factorial principles to investigate the effects of high temperature and concrete mixture namely, water to cement ratio (w/c), water content (w), maximum aggregate size (size), silica fume replacement percent (SF), ground granulated furnace slag replacement percent (GGBFS), and volume of coarse aggregate (CA), on the magnitude of autogenous and drying shrinkage.

## 2. Testing concrete shrinkage at high temperature

High temperature causes water to evaporate quickly in concrete, leading to faster shrinkage. However, the time of high temperature only occurs during the period of about 4 - 5 hours during the day, then at night the temperature drops, and it is possible that the concrete will absorb moisture in the air [12].

An experimental program was developed to study the effects high temperature of on shrinkage of concrete. In this regard, six parameters were selected: water-to-cement ratio (w/c), water content (w), maximum aggregate size (size), silica fume (SF) as cement replacement, ground granulated blast furnace slag (GGBFS) as cement replacement, and bulk volume of coarse aggregate (CA). This chapter provides a description of the material properties, concrete mixture design method, curing regime, and testing methods [15,16].

The concrete shrinkage test was carried out in hot climate conditions, above 40 degrees Celsius. This high temperature is always present in the summer in Nghe An and Ha Tinh provinces. The process of carrying out the concrete shrinkage strain test has been based on [1], and referencing [2-4], and other experimental projects such as [11, 14-16].



Fig 2. Concrete example.

**Table 1.** Dataset on Shrinkage of concrete grade M150

Grades of concrete	C (kg)	S (kg)	a (kg)	W (Lit)
M150	243.8	674.9	1231.1	195.0
M200	292.5	648.3	1216.3	195.0

Shrinkage test with 2 grades of concrete M200 and M150, each of which consists of 3 samples, labeled with the name S. Besides, the purpose of this experiment also evaluates the influence of  $\text{Ca}(\text{OH})_2$  to concrete shrinkage, respectively named SC. Sample size is  $100 \times 100 \times 400$  mm. Measure concrete shrinkage at the laboratory of Vinh University, from March 2021 to April 2022 (390 days), test temperature 40 degrees Celsius, humidity 40 - 80%. This experiment took measurements a period of 390 days and obtained a set of data, see Tables 1 and 2 below. After analyzing the experimental data set, the time - dependent of concrete shrinkage graph of grade M150 and M200 is shown in Figs. 5 & 6.



**Fig. 3.** C363 KIT equipment.



**Fig. 4.** Temperature control cabinet.

**Tables 2.** Dataset on Shrinkage of concrete grade M150

Time (day)	Template (C)	H (%)	Number of days (t)	Dataset on Shrinkage of concrete grade M150					
				S1	S2	S3	SC1	SC2	SC3
	40	46		0.103	0.099	0.096	0.099	0.104	0.091
3/13/2021	28.5	74	1	0.055	0.054	0.051	0.051	0.052	0.048
	40	45		0.049	0.051	0.049	0.038	0.04	0.032
3/14/2021	29	72	2	0.045	0.051	0.047	0.053	0.064	0.051
	40	42		0.09	0.084	0.08	0.08	0.083	0.073
3/15/2021	30	68	3	0.04	0.048	0.035	0.031	0.036	0.031
	42	40		0.088	0.08	0.074	0.078	0.082	0.072
3/16/2021	28	74	4	0.027	0.028	0.023	0.024	0.033	0.024
	42	42		0.073	0.074	0.067	0.073	0.078	0.069
3/17/2021	31	70	5	0.024	0.026	0.019	0.021	0.027	0.018
	39	50		0.062	0.057	0.044	0.05	0.055	0.045
3/18/2021	31	77	6	0.016	0.018	0.01	0.021	0.028	0.02
	40	46		0.058	0.048	0.043	0.045	0.049	0.041
3/19/2021	35	70	7	0.02	0.022	0.015	0.016	0.025	0.018
	40	48		0.061	0.059	0.054	0.05	0.069	0.049
3/26/2021	23	78	14	0.01	0.01	0.013	0.02	0.01	0.01
	40	44		0.042	0.04	0.032	0.06	0.041	0.035

Time (day)	Template (C)	H (%)	Number of days (t)	Dataset on Shrinkage of concrete grade M150					
				S1	S2	S3	SC1	SC2	SC3
9/4/2021	28	78	21	0.02	0.02	0.029	0.02	0.01	0.02
	40	48		0.046	0.015	0.014	0.05	0.026	0.014
10/5/2021	30	75	30	0.05	0.05	0.052	0.02	0.04	0.05
	40	47		0.04	0.04	0.044	0.058	0.03	0.04
7/6/2021	40	75	90	0.09	0.09	0.096	0.03	0.08	0.09
	39	70		0.08	0.07	0.082	0.06	0.06	0.07
6/8/2021	38	70	150	0.11	0.11	0.119	0.02	0.1	0.11
	40	68		0.1	0.1	0.111	0.05	0.09	0.1
17/9/2021	33	75	180	0.09	0.09	0.097	0.03	0.07	0.08
6/12/2021	32	80	360	0.07	0.08	0.085	0.04	0.07	0.07
7/4/2022	33	75	390	0.06	0.07	0.078	0.03	0.05	0.06

Tables 3. Dataset on Shrinkage of concrete grade M200

Time (days)	Template (C)	H (%)	Number of days (t)	Dataset on Shrinkage of concrete grade M200					
				S1	S2	S3	SC1	SC2	SC3
3/7/2021	25	71	1	0.082	0.069	0	0	0.067	0.064
	30	60		0.068	0.081	0.071	0.071	0.075	0.065
3/8/2021	24.5	81	2	0.076	0.071	0.062	0.055	0.064	0.043
	30	58		0.064	0.061	0.058	0.047	0.057	0.045
3/9/2021	25	78	3	0.063	0.068	0.061	0.048	0.048	0.041
	40	44		0.091	0.073	0.08	0.076	0.082	0.068
3/10/2021	28	78	4	0.058	0.049	0.048	0.046	0.046	0.036
	40	44		0.095	0.079	0.094	0.068	0.078	0.068
3/11/2021	27	73	5	0.06	0.044	0.057	0.04	0.045	0.037
	42	42		0.086	0.074	0.085	0.07	0.07	0.071
3/12/2021	28	72	6	0.057	0.04	0.051	0.032	0.035	0.035
	40	46		0.083	0.067	0.085	0.066	0.066	0.078
3/13/2021	28.5	74	7	0.038	0.025	0.039	0.017	0.025	0.02
	40	45		0.069	0.043	0.065	0.05	0.048	0.049
3/22/2021	25	70	14	0.015	0.011	0.018	0.013	0.003	0.004
	40	40		0.035	0.004	0.042	0.008	0.012	0.019
5/4/2021	29	74	30	0.003	0.02	0.032	0.029	0.01	0.02
	40	48		0.042	0.016	0.04	0.006	0.026	0.02
4/5/2021	28	75	60	0.03	0.052	0.015	0.057	0.041	0.038
	40	45		0.008	0.035	0.025	0.037	0.016	0.022
5/6/2021	30	80	90	0	0.01	0.04	0.09	0.07	0.06
	40	45		0.05	0.08	0.02	0.07	0.06	0.05
5/7/2021	32	75	120	0	0.115	0.126	0.01	0.093	0.083
	42	50		0.058	0.094	0.104	0.09	0.072	0.062
6/8/2021	30	75	150	0.085	0.121	0.13	0.119	0.095	0.09
	41	55		0.075	0.117	0.123	0.107	0.09	0.078
17/9/2021	32	80	180	0.065	0.101	0.111	0.097	0.065	0.066
6/12/2021	31	70	240	0.052	0.094	0.098	0.081	0.063	0.077
7/4/2022	33	80	360	0.057	0.089	0.096	0.075	0.053	0.068

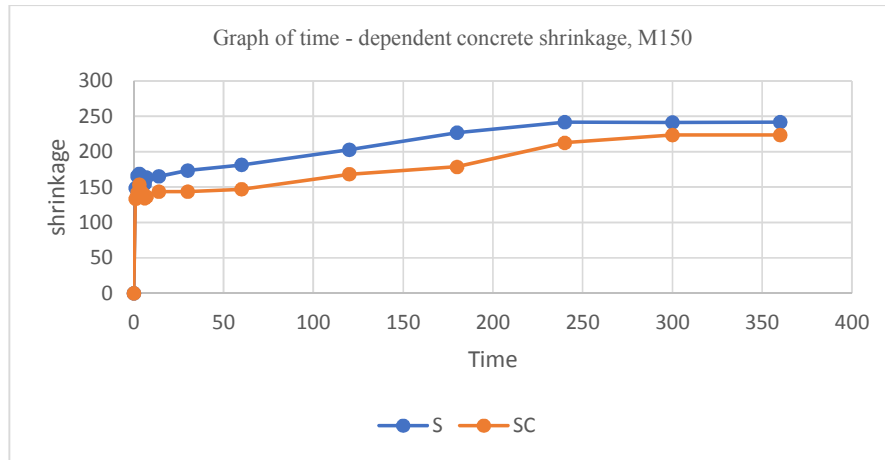


**Fig. 5.** Graph of time - dependent concrete shrinkage, M150.

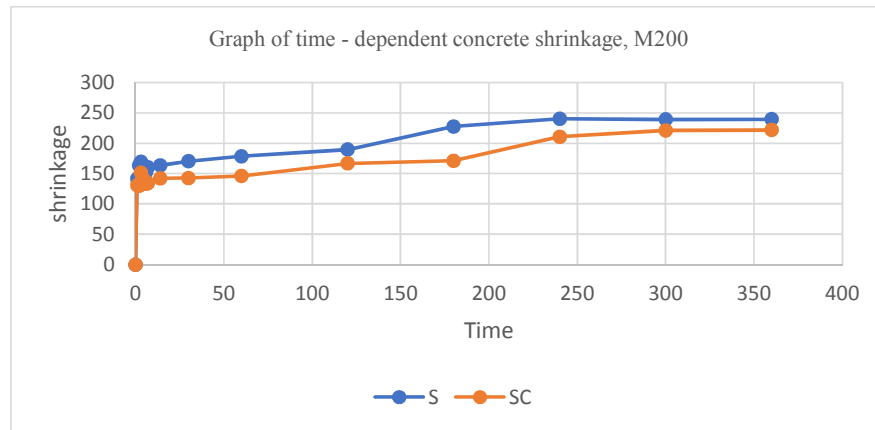


**Fig. 6.** Graph of time - dependent concrete shrinkage, M200.

In the first time, after 7 days of curing, the growth rate is fast, the graph is steep, but when entering the 7th day, the graph decreases gradually (Figures 5 & 6). The value of shrinkage strain obtained in the experiment is quite large compared to the value measured under standard conditions [1] (temperature  $27 \pm 20^\circ\text{C}$ , humidity  $80 \pm 5\%$ ).

### 3. Conclusion

Experimental data set of concrete shrinkage grade M150 and M200, with a duration of 390 days that includes ordinary concrete and the addition of  $\text{Ca}(\text{OH})_2$  admixtures. It has accurately reflected the properties and characteristics of concrete shrinkage.

- Early shrinkage of concrete with high temperature conditions and maintained at this temperature for 4 - 5 hours is faster than at normal temperature.
- Shrinkage of concrete with  $\text{Ca}(\text{OH})_2$  admixture is smaller than that of concrete without it.

## References

1. Bộ Xây dựng - TCVN 3117:1993, Bê tông nặng - Phương pháp xác định biến dạng co ngót, nhà xuất bản Xây dựng, Hà Nội.
2. Nguyễn Ngọc Bình (2016). Báo cáo về phân tích, đánh giá kết quả thực nghiệm biến dạng co ngót bê tông trong điều kiện tiêu chuẩn khí hậu Việt Nam, Hà Nội.
- [3] Phạm Bá Thạch (2019). Nghiên cứu thực nghiệm biến dạng co ngót của bê tông trong điều kiện khí hậu chuẩn tại Gia Lai.
- [4] Trần Ngọc Long (2016). Nghiên cứu thực nghiệm về biến dạng dài hạn của cột bê tông cốt thép chịu nén đứng tâm.
- [5] Smyle, J., and R. Cooke. "Comprehensive environment and climate change assessment in Viet Nam." The International Fund for Agricultural Development (IFAD) (2014). Comprehensive environment and climate change assessment in Viet Nam,
- [6] ADB. "Vietnam: Environment and climate change assessment." (2013): 1-69. Viet Nam Environment and Climate Change Assessment
- [7] Do, Hoang Nhat. "Viet Nam: Urban Environment and Climate Change Adaptation Project." (2015). Urban Environment\_43237-013-pam-en,
- [8] Garrett Kilroy, Senior Evaluation Specialist, IED ADB Support for Action on Climate Change, 2011 - 2020.
- [9] ACI 435R-95 (2003). Control of Deflection in Concrete Structures, American Concrete Institute, America.
- [10] American Concrete Institute Committee, ACI 209. 1R - 05. Factor Affecting Shrinkage and Creep of Hardened Concrete, American Concrete Institute, America.
- [11] Wahid Omar (2008). Creep, Shrinkage and elastic Modulus of Malaysian Concrete, Report of project No: LPIPM/CREAM/UPP 02-02-6-09-23, Mylasia.
- [12] Jón Guðni Guðmundsson (2013), Long-term creep and shrinkage in concrete using porous aggregate - the effects of elastic modulus, Master of Science in Civil Engineering with Specialization in Concrete Technology, Canada.
- [13] Missouri Department of Transportation Construction and Materials (2002). Creep, Shrinkage and Abrasion Resistance, Report D: Self-Consolidating Concrete (SCC) for Infrastructure Elements, Missouri University of Science and Technology, America.
- [14] Jón Guðni Guðmundsson (2013). Long-term creep and shrinkage in concrete using porous aggregate - the effects of elastic modulus, Master of Science in Civil Engineering with Specialization in Concrete Technology, Canada.
- [15] Khairallah, Rabih S. Analysis of autogenous and drying shrinkage of concrete. Diss. 2009. Analysis of Autogenous and Drying Shrinkage of Concrete
- [16] Holt, Erika Elaine. Early age autogenous shrinkage of concrete. University of Washington, 2001. Early age autogenous shrinkage of concrete
- [17] Lam, Jian-Ping. Evaluation of concrete shrinkage and creep prediction models. San Jose State University, 2002. Evaluation of concrete shrinkage and creep prediction models.

# Stress-strain state of a short reinforced concrete column cross-section subjected to biaxial compression

*Phan Van-Phuc<sup>1</sup>, Tran Van-Hoan<sup>2</sup>, Nguyen Van-Thanh<sup>3</sup>*

<sup>1,2,3</sup> Department of Civil Engineering, Vinh University, 182 Le Duan Street, Vinh, Vietnam

*E-mail: vanphuckxd@vinhuni.edu.vn*

**Abstract.** Introduction: reinforced concrete (RC) columns are one of the main bearing parts of the building, it is responsible for receiving loads from beams, floors, and transmitting to the foundation. During the working process, the column is subjected to centered or biaxial compression, and the calculation process for the column subjected to biaxial compression is quite complicated. The purpose of the study was to propose a simpler and more applicable method to calculate the stress-strain state of short RC columns with biaxial compression. provide post-design verification as well as support a simple analysis method for programming calculation of biaxial compressed columns. This study method has combined many theories to create balanced equations through mathematical matrices, the help of Mathcad software has also been mentioned. Instead of considering the balance equations through the nodes, this study considers the balance through the centroids of the concrete and reinforced elements. The bilinear stress-strain relationships of materials (concrete and reinforcement) are applied in this study. In addition, the finite element-based simulation method has been also studied to compare with the results of the analytical method. The problem has been conducted with 3 different load levels for both methods and gave the color spectrum of stress and strain on the cross-section of short RC column subjected to biaxial compression. The results have shown the stress and strain on the cross-section, showing the location of the tensile, compression, and dangerous stress values in the cross-section. The error of the analytical method with the numerical simulation method by ANSYS software is less than 5%. Thus, the analytical method with the bilinear model of the material gives quite accurate and acceptable results for application to the design process of reinforced concrete short columns.

**Keywords:** Analytical method, Stress-strain state, Biaxial compression, RC column.

## 1. Introduction

Columns are vertical or inclined compression members used for transferring superstructure load to the foundation. The structural design of reinforced concrete (RC) columns involves the provision of adequate compression reinforcement and member size to guaranty the stability of the structure. In typical cases, columns are usually rectangular, square, or circular in shape. Other sections such as elliptical, octagonal, etc. are also possible.

According to (BS EN 1992-1-1, 2004) column maybe classified as short or slender, braced or unbraced depending on various dimensional and structural factors. The problem of analysing of the stress-strain state of the axial compression load has been solved by many different methods. However, where the load is not at the along axial (biaxial compression), the stress-strain state is complex. Thus, few methods are available to analyse the stress-strain state of the cross-section of RC column with biaxial compression. To analyse this problem, it is possible to use the finite element method, particularly with the help of simulation software, such as SAP, ETABS, ABAQUS, or ANSYS. However, the finite element method has several shortcomings. For example, computational analysis is difficult and resource-intensive when dividing too many elements, and the element has many nodes.

Several studies have examined the biaxial compression problem of the short (RC) column. Tomoaki SATO (Sato, Shimada and Kobayashi, 2002) has proposed a simple numerical method for computing the bending moment-curvature relations for a reinforced concrete rectangular cross-section of bridge piers under biaxial bending action, which is essentially required at their seismic

design considering a horizontal force due to earthquake in an arbitrary direction. The cross-section is divided by several rectangular finite areas of concrete and reinforcing bar areas. And then numerical integration technique is developed to evaluate the stress-strain relation for each rectangular finite area divided. A general method for determining biaxial interaction diagrams for any direction of axial neutralization of a reinforced concrete (RC) short column of any cross-section under axial load and bending about two axes is specified. Presented by JA Rodriguez and J. Dario Aristizabal-Ochoa (Rodriguez and Aristizabal-Ochoa, 1999), to evaluate the final value of the strength theory of the short RC column, the authors used the Gauss integration method to balance; nonlinear stress-strain relationship for concrete; and polylinear elastic relationship for reinforcement. but the process of solving the problem of stress-strain states of short RC columns is quite complicated. D. G. Row and T. Paulay have developed interaction diagrams, in terms of suitable dimensionless parameters, with respect to a few distinct directions of loading. By utilizing a simple interpolation method the complete failure surface can effectively be created from particular interaction diagrams (Row and Paulay, 1973).

Biaxial bending of columns occurs when the loading causes bending simultaneously about both principal axes. The commonly encountered case of such loading occurs in corner columns. Corner and other columns exposed to known moments of each axis simultaneously should be designed for biaxial bending and axial load. A uniaxial interaction diagram defines the load-moment strength along a single plane of a section under an axial load  $P$  and a uniaxial moment  $M$ . The biaxial bending resistance of an axially loaded column can be represented schematically as a surface formed by a series of uniaxial interaction curves drawn radially from the  $P$  axis. Data for these intermediate curves are obtained by varying the angle of the neutral axis (for assumed strain configurations) with respect to the major axes (318, 2020). The difficulty associated with the determination of the strength of reinforced columns subjected to combined axial load and biaxial bending is primarily an arithmetic one. The bending resistance of an axially loaded column about a particular skewed axis is determined through iterations involving simple but lengthy calculations. F. N. Pannell has described a method of defining the curves relating ultimate load and moment for rectangular columns having an equal area of steel in each face, and subjected to any radial eccentricity of loading (Pannell, 1960). However, this method has used the lookup values from the interaction diagram of the longitudinal force, so the accuracy is not good.

In these studies, many approximations were used, as complex methods make application difficult and affect the reliability of the results. Most of the earlier proposals are used in design with approximate assumptions, but there is still difficulty with these methods in problem-solving. Thus, this study describes a method for calculating the stress-strain state of a section of short RC column under biaxial compression. The method has the advantages of accuracy, simple calculation, and ease of use. In addition, this analytical method has been applied by the author to calculate for other types of elements as in (Opbul et al., 2018; Ngoc-Long et al., 2021).

The analysis of short RC columns as well as other types of materials subjected to biaxial compression have been solved by various methods. However, for biaxial compression (the load is not on the longitudinal axis of the column), the problem becomes complex, and few methods are available, both numerical and analytical method. There are also some shortcomings such as time consuming and costly. On the other hand, the process also uses a lot of approximate assumptions.

This study has presented a method to determine the stress-strain state of a cross section of short RC columns subjected to biaxial compression. This method had easy to implement with simplicity and high accuracy. Accordingly, a short RC column with three input load values have been used in this study. The cross section of the short RC column is divided into several elements, and then the stress-strain states at the centers of these elements are analyzed. Material properties of concrete and rebar are both simulated using bilinear models. The results of this method are compared and verified with the finite element method (ANSYS software).

## 2. Methods

Two methods of analyzing the stress-strain state of RC columns with biaxial compression are performed and compared. The first method is the stress-strain analysis of the cross-section of the column (Fig. 1). The cross-section is divided into many elements and then the stress-strain of the element at its center is analyzed. With this method, it is assumed that in the microscopic elements, the positions around the center element work in the same way as other elements. The second method is to use a simulation with ANSYS software, which uses a finite element basis for analysis. The results of these two methods are analyzed and compared.

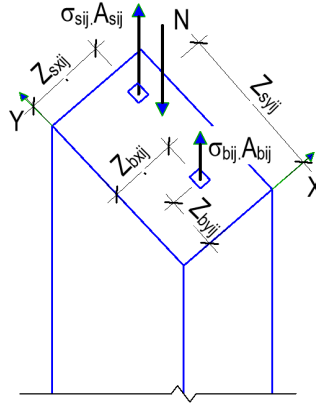


Fig. 1. The cross-section shows the parameters of concrete and reinforcement elements.

### 2.1. Proposed Analytical Method

The method of stress-strain analysis presented in this research divides a cross-section into many elements and then performs stress-strain analysis on the center of those elements. This is the main way in which the complexity of the computation is reduced.

To use the bilinear strain-stress relationship, we accept the following assumptions:

- Small elements of the cross-section are considered to work homogeneously, that is, the strain and stress in each element of the cross-section are the same.
- Flat cross-sections are used for the bending element (Chen and Yijun Liu, 2014).
- Under the impact of load, columns are bent in a certain direction with a certain radius of curvature.

With these concepts for the calculation, we divide the cross-section into many small parts as shown in Fig. 6,  $i$  and  $j$  are the indices of the elements for the  $x$  and  $y$ -axis respectively (for the selected coordinates  $Oxy$ ). The  $x$ -axis is divided into  $i$  parts, the  $y$ -axis into  $j$  parts.

$Z_{xij}; Z_{yij}$  are the distances from the centre of the concrete elements to the  $y$  and  $x$ -direction;

$Z_{xij}; Z_{yij}$  are the distances from the centre of the reinforcement elements to the  $y$  and  $x$ -direction;

$M_x, M_y$  are the moments of the short RC column about the  $y$  and  $x$ -axis from load  $N$ .

This analytical method is based on the stress-strain relationship of the concrete and the reinforcing material. The calculation process is made up of many steps; the first step takes the value of the elastic modulus. In the next step, the modulus value is taken from the stress and strain according to the following formulae:

$$E_{cij} = \frac{\sigma_{cij}}{\varepsilon_{bij}} \quad (1)$$

$$E_{sij} = \frac{\sigma_{sij}}{\varepsilon_{sij}} \quad (2)$$

where  $E_{cij}$  and  $E_{sij}$  are the element modulus of the  $i$  and  $j$  of the concrete and the reinforcement elements, respectively.

The formulae determine the internal force values according to (SP, 2019):

$$M_x = D_{11} \cdot \frac{1}{r_x} + D_{12} \cdot \frac{1}{r_y} + D_{13} \cdot \varepsilon_0 \quad (3)$$

$$M_y = D_{21} \cdot \frac{1}{r_x} + D_{22} \cdot \frac{1}{r_y} + D_{23} \cdot \varepsilon_0 \quad (4)$$

$$N = D_{31} \cdot \frac{1}{r_x} + D_{32} \cdot \frac{1}{r_y} + D_{33} \cdot \varepsilon_0 \quad (5)$$

where  $\varepsilon_0$  is the strain of the selected origin of the coordinate's axis Oxy, the coefficients  $D_{m,n}; (m, n = 1, 2, 3)$  Equations (3, 4, 5) can be rewritten as

$$D_{11} = \sum_i \sum_j A_{cij} \cdot Z_{cxij}^2 \cdot E_{cij} + \sum_i \sum_j A_{sij} \cdot Z_{sxij}^2 \cdot E_{sij} \quad (6)$$

$$D_{22} = \sum_i \sum_j A_{cij} \cdot Z_{cyij}^2 \cdot E_{cij} + \sum_i \sum_j A_{sij} \cdot Z_{syij}^2 \cdot E_{sij} \quad (7)$$

$$D_{12} = \sum_i \sum_j A_{cij} \cdot Z_{cxij} \cdot Z_{cyij} \cdot E_{cij} + \sum_i \sum_j A_{sij} \cdot Z_{sxij} \cdot Z_{syij} \cdot E_{sij} \quad (8)$$

$$D_{13} = \sum_i \sum_j A_{cij} \cdot Z_{cxij} \cdot E_{cij} + \sum_i \sum_j A_{sij} \cdot Z_{sxij} \cdot E_{sij} \quad (9)$$

$$D_{23} = \sum_i \sum_j A_{cij} \cdot Z_{cyij} \cdot E_{cij} + \sum_i \sum_j A_{sij} \cdot Z_{syij} \cdot E_{sij} \quad (10)$$

$$D_{33} = \sum_i \sum_j A_{cij} \cdot E_{cij} + \sum_i \sum_j A_{sij} \cdot E_{sij} \quad (11)$$

The strain of each concrete and reinforcement element is determined by the following formulae:

$$\varepsilon_{bij} = \frac{1}{r_x} \cdot Z_{cxij} + \frac{1}{r_y} \cdot Z_{cyij} + \varepsilon_0 \quad (12)$$

$$\varepsilon_{sij} = \frac{1}{r_x} \cdot Z_{sxij} + \frac{1}{r_y} \cdot Z_{syij} + \varepsilon_0 \quad (13)$$

In the first calculation, we used elastic modulus values  $E_{cij}; E_{sij}$  in equations (1) to (2) as follows:

For concrete:  $E_{cij} = E_{c,red}$ , (SP, 2019);

For reinforcement:  $E_{sij} = E_s$ .

In the next calculation steps, the calculation method is repeated but the module value is obtained according to formulae (1) and (2). The result of the problem is when there is no longer a deviation in the center curvature of the elements in the flex plane. Thus, the problem will have many calculations within the application; the results of the calculation process are accepted when the curvature is less than 1%. The stress-strain state of that step is accepted as the result and the

calculation of the stress-strain state of the structural section is completed. When calculating with the short RC column subjected to biaxial compression as above, the process of subdivision cross-section is as shown in Fig. 6. The selected coordinate system and the centre coordinate of the elements are shown in Fig. 7.

The origin O is selected at the left angle of the section, the x-axis is the downward vertical, and the y-axis is horizontal. With a rectangular cross-section, it is straightforward to determine the parameters for the size, area, and centre coordinates of the elements. The x-axis and y-axis are divided into 12 parts. For simplicity, we used matrix operations to process the requirements, programmed in MathCad 15. The element positions and their characteristics are made up of a matrix of 12 rows and 12 columns. From Equations (1) to (13) are performed on matrix calculations. The following presents the results of the above method with the support of MathCad 15 software.

A short RC column with biaxial compression was chosen to analyse the stress-strain state of the section (Fig. 1). The compressive force  $\mathbf{N}$  is applied at a point on the top of the column, which is placed with the x-direction by a segment  $e_y$ , with the y-direction by a segment  $e_x$ . The problem is to conduct the stress-strain state analysis of the rectangular cross-section of the short RC column that has the greatest stress with biaxial compression. Fig. 2 shows the detail of the section, layout of the reinforcing bar, and reinforcement distance.

Concrete materials C20/25 were selected according to the Eurocode standard (BS EN 1992-1-1, 2004), reinforced with Grade 250 cast iron (British Standard, 2001). Physical characteristics are according to the Eurocode standard, as follows:

Concrete C20/25 has calculated strength, compressive strength  $f_{cd} = 20MPa$ , tensile strength  $f_{ctd} = 1.5MPa$ ,  $\varepsilon_{c3} = 0.00175$ ;  $\varepsilon_{ct3} = 0.0035$ ; The values of the tensile concrete design strain can be ignored, but this study still considers the bilinear hypothesis for the compression zone, according to (SP, 2019), as follows:

$$\varepsilon_{cr3} = 8 \cdot 10^{-5}; \quad (14)$$

$$\varepsilon_{ctu3} = 15 \cdot 10^{-5}; \quad (15)$$

where:

$\varepsilon_{c3}, \varepsilon_{ct3}$ : the largest strain corresponds to the stage of elastic compression and tension (SP, 2019).

$\varepsilon_{cu3}, \varepsilon_{ctu3}$ : the largest strain of the compressive and tensile concrete (BS EN 1992-1-1, 2004);

$E_{c,red}, E_{ct,red}$ : converted modulus of compressive, tensile concrete.

The Grade 250 iron (British Standard, 2001) has the following parameters:

$$f_{yd} = 250MPa; \quad (16)$$

The elastic modulus of reinforcement is:

$$E_s = 2 \cdot 10^5 MPa; \quad (17)$$

$$\varepsilon_{s1} = \frac{f_{pd}}{E_s} = \frac{250}{2 \cdot 10^5} = 1.25 \cdot 10^{-3}; \quad (18)$$

$$\varepsilon_{ud} = 0.02 \cdot 0.9 = 0.018. \quad (19)$$

The bilinear deformation model of concrete is shown in Fig. 2 and the reinforcement is shown in Fig. 3.

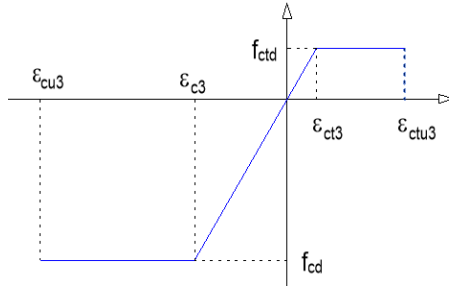


**Fig. 2.** The bilinear stress-strain relationship of the concrete

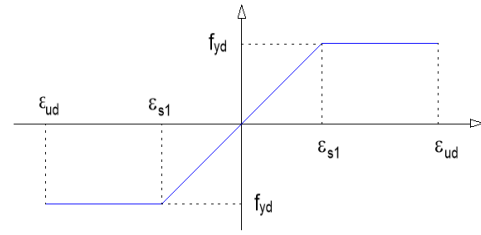


**Fig. 3.** The bilinear stress-strain relationship of the reinforcement

The stress-strain relationship of the bilinear model of concrete C20/25 are set out below. For the compression area:

For  $-\varepsilon_{cu3} < \varepsilon_{cij} < 0$ :

$$\sigma_{bij} = \varepsilon_{bij} \cdot E_{c,red} \text{ MPa}; \quad (20)$$

$$E'_{cij} = E_{c,red} = \frac{f_{cd}}{\varepsilon_{c3}} \text{ MPa}. \quad (21)$$

For  $-\varepsilon_{cu3} < \varepsilon_{cij} < -\varepsilon_{c3}$ :

$$\sigma_{cij} = f_{cd} = 20 \text{ MPa}; \quad (22)$$

$$E'_{cij} = \frac{f_{cd}}{\varepsilon_{cij}} = \frac{20}{\varepsilon_{cij}} \text{ MPa}. \quad (23)$$

For  $\varepsilon_{cij} < -\varepsilon_{cu3}$ :

$$\sigma_{ci} = 0; \quad (24)$$

$$E'_{ci} = 0. \quad (25)$$

For the tension area:

-  $0 < \varepsilon_{ctij} < \varepsilon_{ct3}$ :

$$\sigma_{ctij} = \varepsilon_{ctij} \cdot E_{ct,red} \text{ MPa}; \quad (26)$$

$$E'_{ctij} = E_{ct,red} = \frac{f_{ctd}}{\varepsilon_{ct3}} \text{ MPa}. \quad (27)$$

-  $\varepsilon_{ct3} < \varepsilon_{ctij} < \varepsilon_{ctu3}$ :

$$\sigma_{ctij} = f_{ctd} = 1.5 \text{ MPa}; \quad (28)$$

$$E'_{ctij} = \frac{0.73}{\varepsilon_{ctij}} \text{ MPa}. \quad (29)$$

-  $\varepsilon_{ctu3} < \varepsilon_{ctij}$ :

$$\sigma_{btij} = 0; \quad (30)$$

$$E'_{ctij} = 0. \quad (31)$$

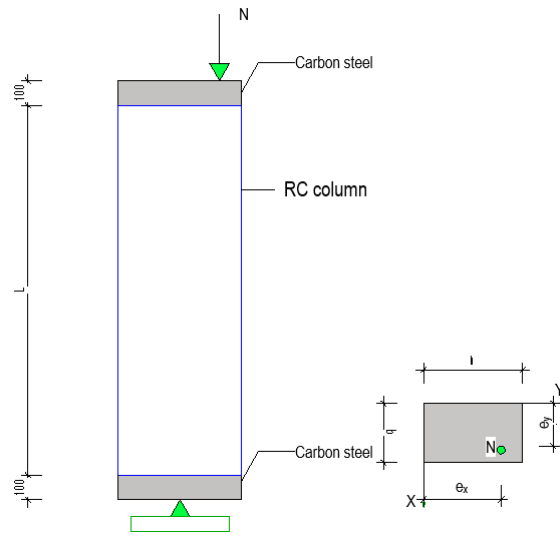


**Fig. 4.** Model of the short reinforced concrete column for biaxial compression

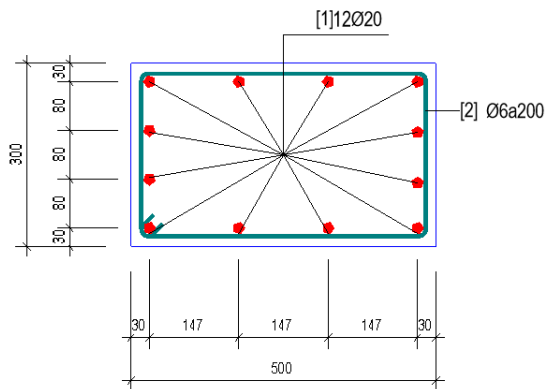


**Fig. 5.** Cross-section of the short reinforced concrete column

Fig. 4 and Fig. 5 describe the detail of short RC column subjected to biaxial compression. The cross-section is rectangular with 300 mm (width) and 500 mm (height). The cross-section consists of 12 bars with 20mm diameter as shown in Fig. 5.

The analysis was performed using two values of load N:

$N_1 = 100 \text{ KN}$ ;  $N_2 = 800 \text{ KN}$ ;  $N_3 = 2000 \text{ KN}$  The force N is placed  $e_y=300\text{mm}$  from x-axis,  $e_x=200$  from y-axis.

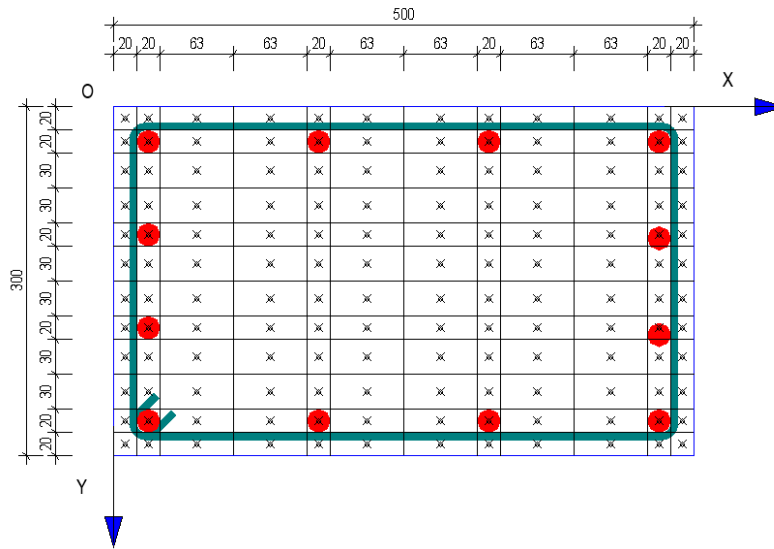


Fig. 6. Mesh cross-section

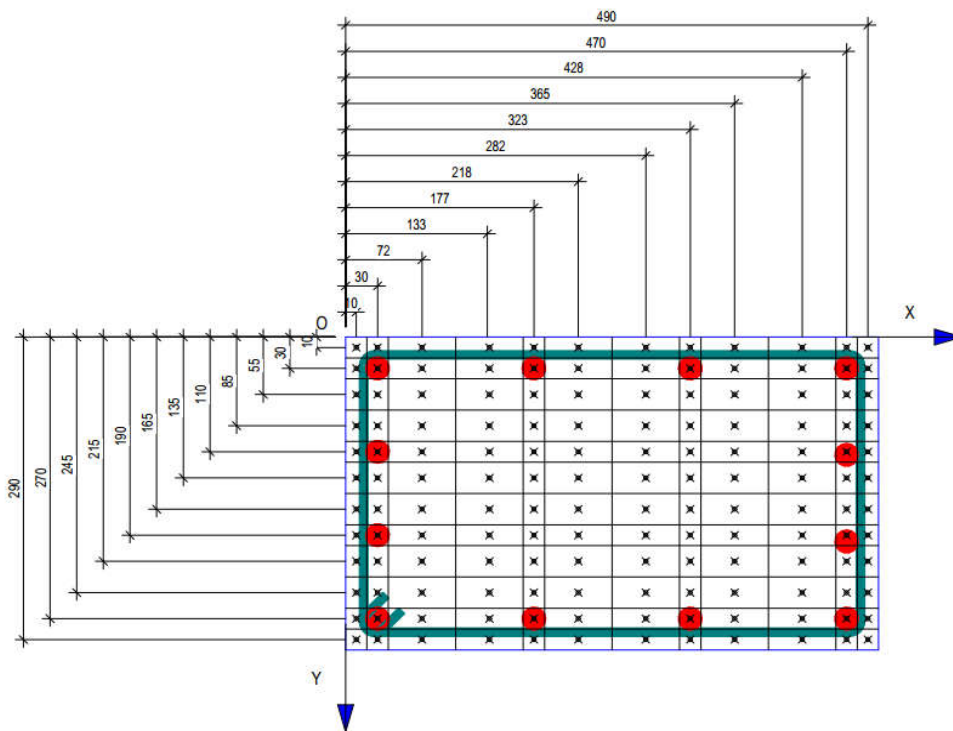


Fig. 7. The coordinates of the elements

## 2.2. Analysis by ANSYS

### a. The concrete material

The stress-strain relationship of the concrete was determined using the method from the study of Wight, James K (Wight, 2015). With concrete strength  $f = 20\text{MPa}$ , the stress-strain relationship curve is shown in Fig. 8. The maximum strain value of concrete  $\varepsilon_{\max} = 0.0035$  is taken according to the Eurocode (BS EN 1992-1-1, 2004), and the corresponding elastic modulus identified by Wight, James K (Wight, 2015) is  $E_c = 18200\text{ MPa}$ . The strain at the top of the stress-strain relation curve is  $\varepsilon_0 = 0.002$ . In this case, concrete is selected as the SOLID185 element (Jhung and Ryu, 2010; Chen and Y Liu, 2014; “Using ANSYS workbench for structural analysis,” 2018; Lee, 2021).

### b. The reinforcement material

We propose the stress-strain relationship of the reinforcement using the bilinear relation as shown in (James and Macgregor, 2009), the stress-strain relationship of the reinforcement with two necessary parameters, reinforcement elastic modulus ( $E_s$ ), and yield strength ( $f_y$ ) (Fig. 3).

The analytical model was established with the help of graphics software Design Modeler; the results of the analytical model are shown in Fig. 9. In which, the short RC column has a cross-sectional size of 300 mm (width) and 500 mm (height). The selected column length is  $L=1.5\text{m}$ . The two ends of the column are reinforced with two steel plates with a thickness of 100mm.

Due to the symmetrical structure of the beam, only half the structure is considered to reduce the analytical volume of the process. After modelling, analysis was carried out with Mechanical (ANSYS Static). The simulation results using ANSYS Workbench software are shown below.

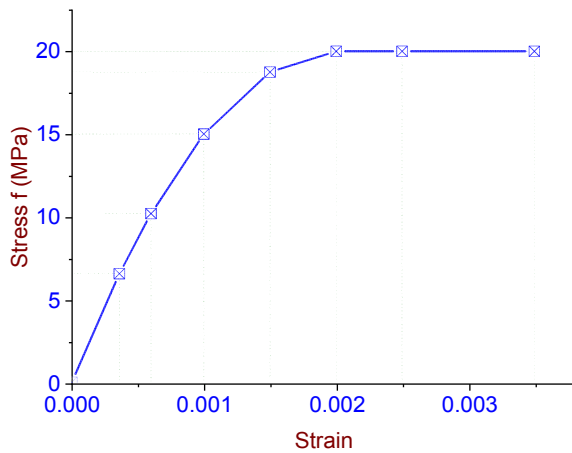


Fig. 8. The relationship of stress - deformation state of concrete

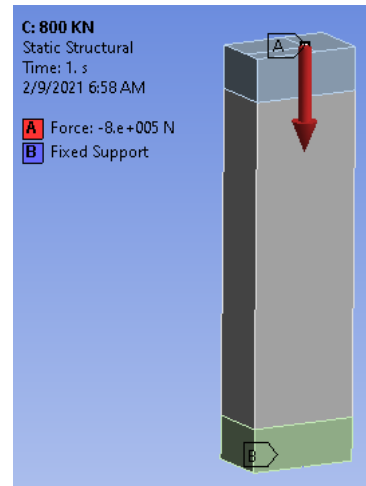


Fig. 9. The Model and boundary conditions of the short RC column

## 3. Results

The stress-strain state of the cross-section of the short RC column was analysed for two different load values. Results for the two analytical methods are shown below.

### 3.1. Recommended Analysis Method

The stress-strain state problems of short RC columns subjected to biaxial compression with the analytical method of this article are performed through some calculations. Calculations have been repeated with mathematical formulas, differing only in value in each calculation. In principle, the problem results converge when the error of two consecutive computations is zero. But within the technical scope, the problem can be accepted when the error is less than a certain value. The error value less than 1% has been chosen to consider the convergence problem in this study. On the table 1, 2, 3 is the error result between 2 consecutive calculation steps of curvature radius  $r_x$ ,  $r_y$ , and axial deformation of origin  $\epsilon_0$  for the case  $N_1=100\text{KN}$ ,  $N_2=800\text{KN}$ ,  $N_3=2000\text{KN}$ , respectively. So, for the case 1,2,3 the problem converges to the 4th, 5th, and 7th calculation step, respectively.

**Table 1.** The deviation between calculations steps for case 1

Step	Results			Declination (%)		
	$r_x$ (mm)	$r_y$ (mm)	$\epsilon_0$	$r_x$	$r_y$	$\epsilon_0$
1	-2834000	-11840000	0.0002975	-	-	-
2	-2730000	-11190000	0.0003364	-3.66972477	-5.48986486	13.07563
3	-2727000	-11180000	0.0003374	-0.10989011	-0.0893655	0.297265
4	-2727000	-11180000	0.0003374	0	0	0

**Table 2.** The deviation between calculations steps for case 2

Step	Results			Declination (%)		
	$r_x$ (mm)	$r_y$ (mm)	$\epsilon_0$	$r_x$	$r_y$	$\epsilon_0$
1	-354200	-1480000	0.000238	-	-	-
2	-346800	-1431000	0.0002558	-2.08921513	-3.31081081	7.478992
3	-346100	-1429000	0.0002572	-0.20184544	-0.1397624	0.547303
4	-346000	-1428000	0.0002573	-0.02889338	-0.06997901	0.03888
5	-346000	-1428000	0.0002573	0	0	0

**Table 3.** The deviation between calculations steps for case 3

Step	Results			Declination (%)		
	$r_x$ (mm)	$r_y$ (mm)	$\epsilon_0$	$r_x$ (mm)	$r_y$ (mm)	$\epsilon_0$
1	-141700	-591900	0.0005951	-	-	-
2	-130600	-530100	0.0007302	-7.83345095	-10.4409529	22.70207
3	-127600	-510100	0.0007705	-2.29709035	-3.77287304	5.519036
4	-126600	-506500	0.0007802	-0.78369906	-0.70574397	1.258923
5	-126500	-506700	0.0007786	-0.07898894	0.039486673	-0.205076
6	-126400	-506500	0.0007792	-0.07905138	-0.03947109	0.077061
7	-126400	-506300	0.0007795	0	-0.03948667	0.038501

• **Results of stress, deformation of cross-section for case 1.**

The results of stress and strain at the center of elements of the cross section of short RC columns subjected to biaxial compression have been shown in the form of a matrix. For easy observation, the article has presented them in the form of color spectrum corresponding to the values obtained as shown in Figs. 10, 11, 12, 13.

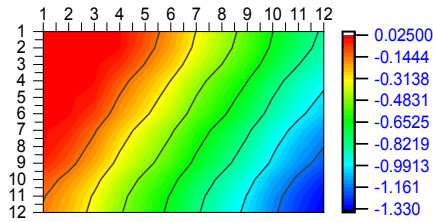


**Fig. 10.** Stress spectrum at the centre of concrete elements, (MPa)

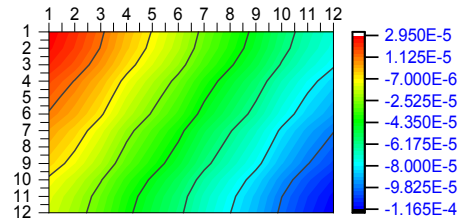


**Fig. 11.** Strain spectrum at the centre of concrete

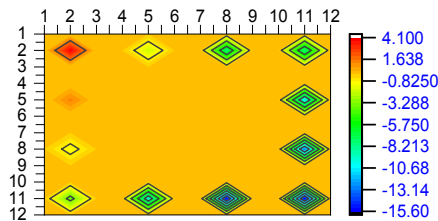


**Fig. 12.** Stress spectrum at the center of rebars, (MPa)

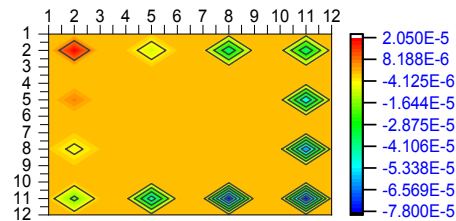


**Fig. 13.** Strain spectrum at the center of rebars

• **Results of stress, deformation of cross-section for case 2.**

Like case 1, the values of stress and strain at the center of concrete elements and reinforcement are also represented in color spectrum as shown in Figs. 14, 15, 16, 17.

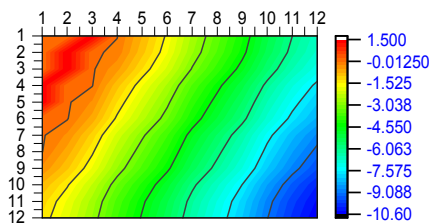


**Fig. 14.** Stress spectrum at the centre of concrete elements, (MPa)

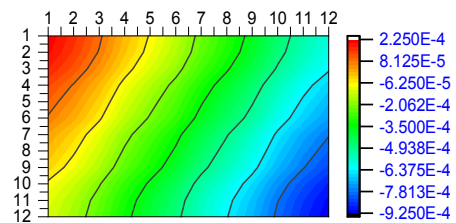


**Fig. 15.** Strain spectrum at the centre of concrete

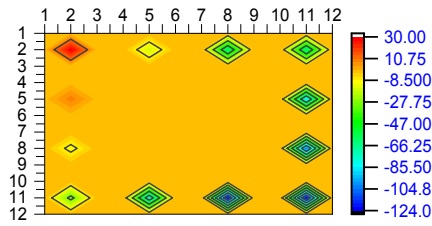


**Fig. 16.** Stress spectrum at the centre of rebars, (MPa)

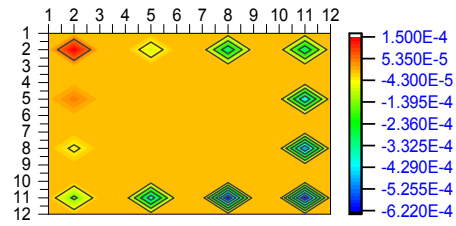


**Fig. 17.** Strain spectrum at the centre of rebars

• **Results of stress, deformation of cross-section for case 3.**

Like case 1 and case 2, the values of stress and strain at the center of concrete and reinforcement elements are also represented in the form of color spectrum as shown in Figs. 18, 19, 20, 21.

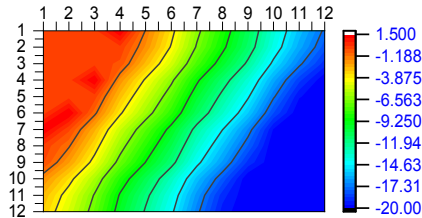


**Fig. 18.** Stress spectrum at the centre of concrete elements, (MPa)

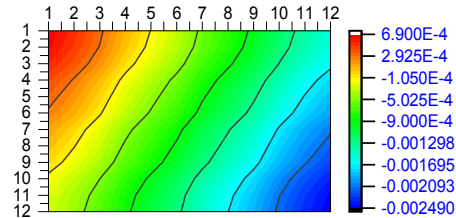


**Fig. 19.** Strain spectrum at the centre of concrete

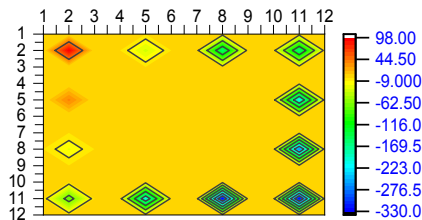


**Fig. 20.** Stress spectrum at the center of rebars, (MPa)

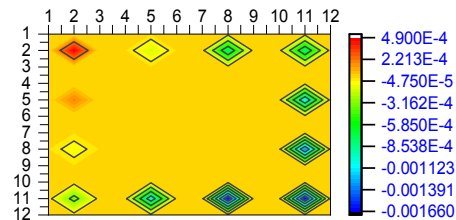


**Fig. 21.** Strain spectrum at the center of rebars

**3.2. Analysis results of ANSYS**

Analysis results for RC beams with ANSYS Workbench 2020 R1 are shown below. Figs. 22, 23 show the values of Equivalent elastic strain of the rebars and the z-direction elastic strain in the column. Simulation method by Ansys software is also conducted on the same model and boundary conditions, only for the biaxial compression force value is conducted with 3 cases in the Table 4. The distributions of stress on the cross-section of the short RC column are shown in the Fig. 24.



compressive stress for this case is  $\frac{1.4275-1.330}{1.4275} = 6.8\%$ . In this case, the small value of active load is considered small, so this error is acceptable.

Compare the stress results based on the stress spectrum for case 2 (N = 800 KN). Like case 1, the stress spectrum of cross section of the short RC column has the appearance of tensile and compression regions similar for the two methods above. The error of the maximum compressive stress values of the analysis method and the simulation method by Ansys software is:  $\frac{11.15-10.60}{11.15} = 4.9\%$  ( $(11.15-10.60)/11.15 = 4.9\%$ ). In this case, the difference value of the two methods is small, which proves that the analytical method gives quite accurate results.

Looking at Fig. 18 and Fig. 24, the results of the cross-sectional stress spectrum of the reinforced concrete short column are the same as the cases 1 and 2. The stress spectrum in the tensile and compressive regions appears almost the same. The error of the maximum compressive stress values in the cross-section is:  $\frac{20-18.951}{20} = 0.7\%$ . With this error value, it shows that the dangerous stress results of the two methods are nearly equal.

The results of the finite element method - ANSYS - also gave results like the proposed method. The error results are shown in Table 5.

**Table 5.** Table of summary and comparison of maximum compressive stress of concrete on the cross-section of short RC column.

Case	Stress (MPa)		difference
	Analysis method	ANSYS	
1	-1.330	-1.4275	6.8%
2	-11.15	-10.60	4.9%
3	-18.951	-20	0.7%

Table 5 summarizes the results of the three maximum compressive stresses of the three different load values and compares the results between the two methods; the difference is not significant. The deviations between the two methods for case 1, case 2, case 3 are 6.8%, 4.9%, and 0.7%, respectively. This confirms that the accuracy and reliability of the proposed method are acceptable.

## 5. Conclusions

The study proposed an analytical method for determining the stress-strain state of a short RC column cross-section subjected to biaxial compression. The results were compared and verified with the finite element method. From the results, the following conclusions are drawn:

- The method of stress-strain state analysis of the cross-section of short RC column proposed in this study is easy to implement. Furthermore, accurate and reliable results were obtained by integrating this method with simple programming language.
- The shape, the shape, area of the tensile zone and compressive zone from the proposed method results are in good agreement with reality.
- The results of the final analysis allow evaluation of the accuracy of the material selection and the initial layout of the rebars in the short RC column.

- The proposed analytical method can also be used for different cases, such as various values of load and cross-sectional shapes.

## Acknowledgements

The author would like to thank Valerii Morozov, D.Sc. in Engineering, Professor St. Petersburg State University of Architecture and Civil Engineering, 2-nd Krasnoarmeiskaya St. 4, 190005 St. Petersburg, Russia for helping me with my research.

## References

1. 318, A. C. I. C. (2020) “Building Code Requirements for Structural Concrete (ACI 318-19): An ACI Standard; Commentary on Building Code Requirements for Structural Concrete (ACI 318R-19),” in. American Concrete Institute.
2. British Standard (2001) “BS4449:1997 Carbon steel bars for the reinforcement of concrete,” p. 34.
3. BS EN 1992-1-1 (2004) “Eurocode 2: Design of concrete structures - Part 1-1 : General rules and rules for buildings,” *British Standards Institution*. doi: [Authority: The European Union Per Regulation 305/2011, Directive 98/34/EC, Directive 2004/18/EC].
4. Chen, X. and Liu, Yijun (2014) *Finite element modeling and simulation with ANSYS workbench, Finite Element Modeling and Simulation with ANSYS Workbench*. CRC Press. doi: 10.1201/b17284.
5. Chen, X. and Liu, Y (2014) *Finite Element Modeling and Simulation with ANSYS Workbench*. CRC Press. doi: 10.1201/b17284.
6. James, K. W. and Macgregor, J. G. (2009) *Reinforced concrete Mechanics and Design*. doi: 10.16309/j.cnki.issn.1007-1776.2003.03.004.
7. Jhung, M. J. and Ryu, Y. H. (2010) “Theory Reference for ANSYS and ANSYS Workbench Theory Reference for ANSYS and ANSYS Workbench, 2009,” *Journal of nuclear science and technology*, 47(11), pp. 1065–1074.
8. Lee, H.-H. (2021) *Finite Element Simulations with ANSYS Workbench 2021: Theory, Applications, Case Studies*. SDC publications.
9. Ngoc-Long, T. *et al.* (2021) “An analysis of the stress-strain state of reinforced concrete beam cross-sections subjected to biaxial bending,” *International Journal*, 21(84), pp. 9–23.
10. Opubl, E. K. *et al.* (2018) “Practical calculation of flexible members with the use of non-linear deformation model as exemplified by typical girder rcd 4.56-90,” *Architecture and Engineering*, 3(3), pp. 29–41. doi: 10.23968/2500-0055-2018-3-3-29-41.
11. Pannell, F. N. (1960) “The design of biaxially loaded columns by ultimate load methods,” *Magazine of Concrete Research*, 12(35), pp. 99–108.
12. Rodriguez, J. A. and Aristizabal-Ochoa, J. D. (1999) “Biaxial Interaction Diagrams for Short RC Columns of Any Cross Section,” *Journal of Structural Engineering*, pp. 672–683. doi: 10.1061/(asce)0733-9445(1999)125:6(672).
13. Row, D. G. and Paulay, T. (1973) “Biaxial flexure and axial load interaction in short rectangular reinforced concrete columns,” *Bulletin of the New Zealand Society for Earthquake Engineering*, 6(3), pp. 110–121.
14. Sato, T., Shimada, I. and Kobayashi, H. (2002) “A Simple Numerical Method for Biaxial Bending Moment-Curvature Relations of Reinforced Concrete Column Sections,” *Memoirs of the Faculty of Engineering Osaka City University*, pp. 59–67.
15. SP, R. B. C. (2019) “63.13330. 2018 Concrete and reinforced concrete structures,” *General provisions*.
16. “Using ANSYS workbench for structural analysis” (2018) in *Engineering Analysis with ANSYS Software*. Elsevier, pp. 511–540. doi: 10.1016/B978-0-08-102164-4.10000-7.
17. Wight, J. K. (2015) *Reinforced concrete: mechanics and design*. Prentice Hall.

# Exploring the shear strength characteristics and CBR value of an expansive soil by using brick dust and coir fiber

*Muhammad Umair Ashfaq<sup>1</sup>, Muhammad Irslan Khalid<sup>1</sup>,  
Muhammad Shahroz Khalid<sup>1</sup> and Van-Quang Nguyen<sup>2,3</sup>*

<sup>1</sup> Department of Civil Engineering, NFC Institute of Engineering and Fertilizer Research,  
Faisalabad, Punjab, Pakistan

<sup>2</sup> Department of Civil and Environmental Engineering, Hanyang University, Seoul, South Korea

<sup>3</sup> Department of Civil Engineering, Vinh University, Vietnam

*Email: engrarslan\_civil@outlook.com*

**Abstract.** Expansive soil is a term generally applied to any soil or rock material that has a potential for shrinking or swelling under changing moisture conditions. Expansive soils are widely found in many parts of Pakistan. This research aims to investigate the effect of brick dust and coir fiber on the stabilization of expansive soils. A sample of clayey soil was obtained from Nandipur Gujranwala, Punjab, Pakistan, which is expansive soil in nature. California Bearing Ratio (CBR) and direct shear tests were performed for the evaluation of shear strength and CBR value. Direct shear tests were performed at different percentages of brick dust to find an optimum percentage. Brick dust is used in intervals of 10%, 20%, 25%, 30% and coir fiber is used in interval of 0.3%, 0.6%, 0.9%, 1.2%, and 1.5%. The optimum value of brick dust (25%) was used, and the percentage of coir fiber was varied to find an optimum value of coir fiber. The results show that at the optimum value of brick dust, the cohesion value is lowest, and the friction angle is highest. Varying coir fiber percentage, cohesion, and friction angle both increases, and the CBR value also increases at an optimum value of 1.2% of coir fiber.

**Keywords:** Shear Strength, Brick Dust, Coir Fiber, CBR, Direct Shear.

## 1. Introduction

Nowadays, due to sustainable constructions, there has been a great consideration for soil reinforcement with various types of natural fibers. In highway and building construction, the layer of soil on which construction is being performed is most important. The success or failure of the foundation and pavement depends upon the underlying soil. A major challenge in geotechnical engineering is the improvement of expansive clays on which buildings are built. The soil stabilization technique is used to improve the performance and engineering properties of soil.

An important characteristic of clayey soil is that it swells when its moisture content is allowed to increase [1]. Therefore, the optimization of such clay soil is important for safety and to further prevent damage to the structure. Additives such as lime and cement have been added to soil with fibers [2-5]. Kumar et al. [6] used brick dust blended with varying percentages of lime as a stabilizing additive for the stabilization of black cotton soil. The results show that the combination of brick dust and lime produces maximum improvement in soil strength as compared to individual additive. Although, fiber-binder soil composites enhance the soil strength drastically, they may show an undesirable brittle behavior of fiber-soil mixtures.

Therefore, the concept of soil stabilization with different natural and synthetic fibers has gained widespread attention. Many researchers have reported different varieties of additive materials used on the subject of soil stabilization, the most common methods of soil stabilization of clay soils are plant saps, animal dung, and natural oils stabilization [7]. Li and Zornberg [8], [9] studied the shear strength behavior of soils reinforced with weak fibers and reported that the fiber increases the peak shear strength of the soil. Lakshmi et al. [10] performed soaked CBR and

unconfined compression (UCC) tests to increase the soil strength by adding non-woven coconut coir fiber. The experimental tests depicted that UCC strength and soaked CBR value increase with the addition of fibers in soil. Lone [11] studied the effect of natural fibers blended with fly ash for soil stabilization. The results of research depicted that the CBR value of soil increases with the addition of fibers and fly ash. Pokale et al. [12] studied the effect of admixture of 30% brick dust on the soil shear strength. Neha and Trivedi [13] performed experimental work for the stabilization of clayey soil with brick dust. It was reported that the soil properties improved with the addition of burnt brick dust. Khan and Sonthwal [14] performed the experimental study using fibers and brick dust. It was concluded that varying percentage of brick dust increases the soil strength.

It is evidential from earlier studies that, for the stabilization of soil different modifications procedures are used such as lime, fly ash, rice husk, cement, geogrids, geomembranes, etc. In this study, the effect of coir fiber in conjunction with brick dust on clay soil for enhancing the strength of the soil is investigated. The behavior of unreinforced and reinforced samples was observed.

## 2. Materials and methodology

### 2.1. Soil

Many areas of Pakistan such as Nandipur, Narowal, and Layyah contains expansive clayey soil. In this research, problematic expansive clayey soil was collected from Nandipur and used for further analysis. Nandipur is an industrial town located near Gujranwala, Punjab, Pakistan. The clayey soil in Nandipur is weak in shear strength and has swelling problems, which cause the failure of building and foundations. Table 1 shows the properties of soil used in the experimental work.

**Table 1.** Properties of Soil

Natural Moisture Content	21.9%
Specific Gravity	2.81
Liquid Limit	46.93 %
Plastic Limit	25.56 %
ASSTHO Classification	A-7-6(14)
USCS Classification.	CL (Sandy Lean Clay)

### 2.2. Brick dust

Brick dust is a local waste material generated through the burning of bricks with the soil. It is red in color and fine texture in nature. Due to the burning of soil bricks, it becomes hardened; when the set-up covering is removed, the powder in the form of brick dust is obtained. Brick dust is easily available at any brick kiln, provides additional strength to soil, makes it strong in shear strength, and increases the bearing capacity. It has a great ability to reduce the swelling potential for highly expansive clay soils.

### 2.3. Coir fiber

Coir fiber is a natural waste material of coconut husk, having the characteristics of a hard structural fiber. The use of these materials in soil reduces the pavement thickness, So the materials cost also decreases. Coir fiber increases the tensile strength of soil, so it reduced the cracking of soil which occurs due to long-term loading on the soil. Coir fiber twisting and curling without any breaking enhanced the plasticity of pavement. In this study, coir fibers were purchased from a local market. For experimentation purposes, its diameter varied from 0.2 to 0.3 mm. Further, the coir fiber was cut into pieces of 30 mm length and mixed with soil taking a percentage of 0.30%, 0.60%, 0.9%, and 1.2%.

## 2.4. Methodology

The current study was carried out in two stages. At the first stage, a series of laboratory direct shear strength tests were performed on clay soil samples with the addition of brick dust. Brick dust is replaced with the soil in proportions of 0%, 10%, 20%, 25%, and 30%. The optimum percentage of brick dust was selected through this testing.

In the second stage, the soil with the optimized brick dust was further mixed with coir fiber in proportions of 0%, 0.3%, 0.6%, 0.9%, and 1.2%. Modified proctor compaction tests were performed for the determination of optimum moisture content (OMC) and maximum dry density (MDD). direct shear strength test (DST) and California bearing ratio (CBR) tests were also performed on prescribed proportions of coir fiber. The CBR tests were performed on soaked samples which were immersed in water for 96 hours before testing.

## 3. Results and Discussion

### 3.1. Direct shear test

For evaluation of the shear strength behavior of soil, a series of direct shear tests was performed after treating the soil with brick dust. Soil samples were prepared by varying percentages of brick dust at 0%, 10%, 20%, 25%, and 30%. Fig. 1 and Fig. 2 show that as the percentage of brick dust increases in the soil the value of cohesion decreases but the angle of internal friction increases up to 25% brick dust addition. On further addition of brick dust after 25% the value of cohesion increases but angle of internal friction decreases which indicates that the optimum value of brick dust in the soil is 25%. The amount of brick dust was fixed 25% (optimum value) and varying percentages of coir fiber from 0%, 0.3%, 0.6%, 0.9% and 1.2 % with 0.3 % interval were added for further trails. Fig. 3 and Figure 4 show that as the percentage of coir fiber increases the value of cohesion and angle of internal friction increases up to the percentage of 1.2%, on further addition of coir fiber cohesion and angle of internal friction start to decrease.

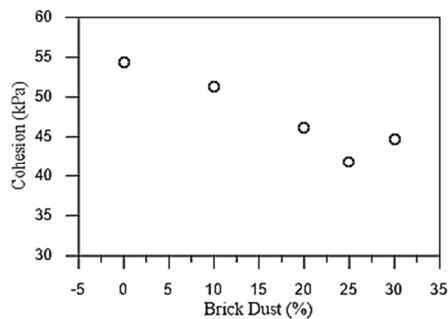


Fig. 1. Effect of brick dust on cohesion value

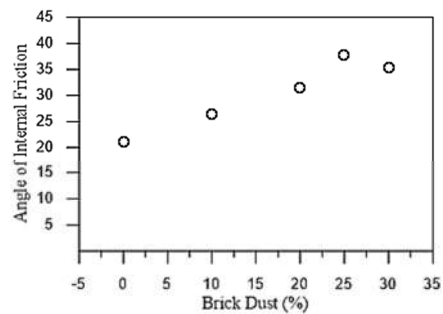


Fig. 2. Effect of brick dust on angle of internal friction

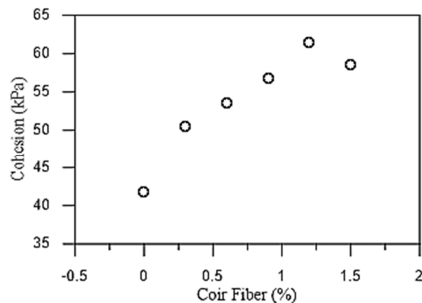


Fig. 3. Effect of coir fiber on cohesion value

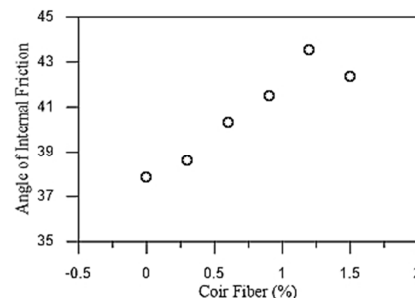


Figure 4. Effect of coir fiber on angle of internal friction

### 3.2. Modified proctor test

Modified proctors' tests were performed on clayey soil samples by taking the optimum value of brick dust and varying percentages of coir fiber from 0%, 0.3%, 0.6%, 0.9%, and 1.2 % with a 0.3% interval.

On 25% brick dust addition, the optimum moisture content decreases from 20.07% to 16.07% but maximum dry density increases from 1.87 g/m<sup>3</sup> to 2.18 g/m<sup>3</sup>. On the other hand, Fig. 5 showed that after the addition of varying percentages of coir fiber 0%, 0.3%, 0.6%, 0.9%, 1.2% and 1.5% with a 25% brick dust (optimum value) the value of optimum moisture content increases from 16.07% to 17.64% but maximum dry density decreases from 2.18 g/m<sup>3</sup> to 1.83 g/m<sup>3</sup>. So, with the addition of coir fiber maximum dry density increases significantly with less optimum moisture content.

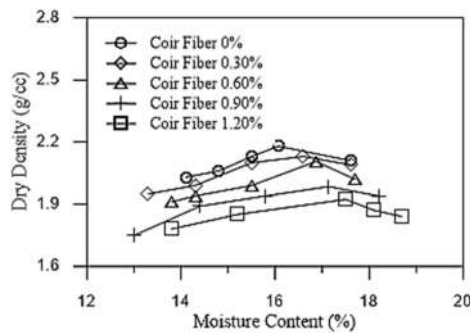


Fig. 5. Effect of coir fiber on moisture content and dry density

### 3.3. California bearing ratio test

Soaked California bearing ratio test was performed on clayey soil samples by taking the optimum value of brick dust and varying percentages of Coir fiber from 0%, 0.3%, 0.6%, 0.9%, and 1.2% with a 0.3% interval. From Fig. 6, it was observed that as the percentage of brick dust increases up to 25%, the CBR value increases from 35.7% to 44% and after taking 25% B.D constant and varying percentages of coir fiber i.e., 0.3%, 0.6%, 0.9%, 1.2%, and 1.5%, it was observed that CBR value increases from 44% to 59.9% up to 1.2% coir fiber. So optimum value of C.F is 1.2 % where 59.9 CBR is achieved. Therefore, an increase in the percentage of coir fiber increases the CBR value, higher the CBR means higher the bearing capacity and more the soil stable.

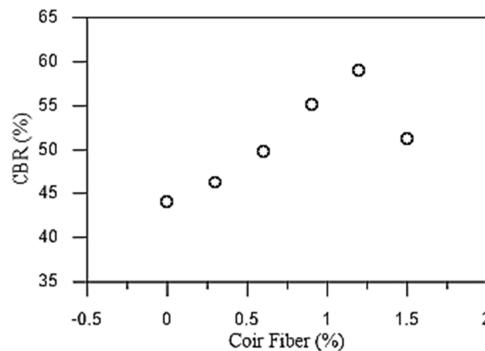


Fig. 6. Effect of coir fiber on CBR value

#### 4. Conclusions and recommendations

In this paper, the optimum value of brick dust and coir fiber was evaluated for the stabilization of locally expansive clayey soil. Following observations were made after performing a series of tests.

- Soil is classified as CL according to USCS and A-7- 6(14) according to the ASSTHO classification system, it is poor as a subgrade, as the G.I value is 14. Soil has 97% of silt and clay content.
- The addition of brick dust in soil decreases the cohesion of soil and increases the angle of internal friction. As the percentage of brick dust increases the angle of internal friction increases and the maximum increases up to 25% brick dust, which is the optimum value of brick dust. At 25% of brick dust, the maximum value of shear strength increases.
- After the addition of 1.2%, coir fiber with 25% brick dust the soil cohesion increases up to 46.7% and the angle of internal friction increases up to 15%.
- The CBR value increased by 23% with the addition of 25% brick dust. On further addition of 1.2% coir fiber with 25% brick dust, the CBR value increases by 65%.

#### References

1. Chan, R.H., *Foundation on Expansive Soil*, 2nd edition. 1975: Elsevier Scientific Publishing Company, New York.
2. Consoli, N.C., F. Zortea, M. de Souza, and L. Festugato, Studies on the dosage of fiber-reinforced cemented soils. *Journal of Materials in Civil Engineering*, 2011. **23**(12): p. 1624-1632.
3. Consoli, N., R. De Moraes, and L. Festugato, Split tensile strength of monofilament polypropylene fiber-reinforced cemented sandy soils. *Geosynthetics International*, 2011. **18**(2): p. 57-62.
4. Wei, L., S.X. Chai, H.Y. Zhang, and Q. Shi, Mechanical properties of soil reinforced with both lime and four kinds of fiber. *Construction and Building Materials*, 2018. **172**: p. 300-308.
5. Dang, L.C., B. Fatahi, and H. Khabbaz, Behaviour of expansive soils stabilized with hydrated lime and bagasse fibres. *Procedia engineering*, 2016. **143**: p. 658-665.
6. Kumar, D., S. Nigam, A. Nangia, and S. Tiwari, California bearing ratio variations in soil reinforced with natural fibres (a case study Bhopal Bypass Road). *International Journal on Emerging Technologies*, 2015. **6**(2): p. 95.
7. Anwar Hossain, K.M., Stabilized soils incorporating combinations of rice husk ash and cement kiln dust. *Journal of Materials in Civil Engineering*, 2011. **23**(9): p. 1320-1327.
8. Li, C. and J.G. Zornberg, Shear strength behavior of soils reinforced with weak fibers. *Journal of Geotechnical and Geoenvironmental Engineering*, 2019. **145**(9): p. 06019006.
9. Li, C. and J.G. Zornberg, Mobilization of reinforcement forces in fiber-reinforced soil. *Journal of geotechnical and geoenvironmental engineering*, 2013. **139**(1): p. 107-115.
10. Lakshmi, S.M., S. Sasikala, V. Padmavathi, S. Priya, and V. Saranya, Utilization of coconut coir fibre for improving subgrade strength characteristics of clayey sand. *International Research Journal of Engineering and Technology*, 2018. **5**(4): p. 2873-2878.
11. Lone, A.A., I & Bawa, "Utilization of fly-ash and coir fibre in soil reinforcement," *Int. J. Civ. Eng. Technol*, 2018. **9**(8): p. 341-346.
12. Pokale, K.R., Y.R. Borkar, and R.R. Jichkar, Experimental investigation for stabilization of black cotton soil by using waste material-brick dust. *International Research Journal of Engineering and Technology (IRJET)*, 2015. **2**(5): p. 726.
13. Neha, P. and M. Trivedi, Improvement of pavement soil subgrade by using Burnt Brick Dust. *International Journal for Research in Applied Science and Engineering Technology*, 2017. **5**(5): p. 218-221.
14. Khan, R. and V. Sonthwal, Soil stabilization using brick kiln dust and waste coir fibre. *Int. J. Recent Technol. Eng*, 2019. **8**(2): p. 2574-2578.

# Classification of concrete grade using machine learning methods

*Viet-Linh Tran<sup>1\*</sup>, Duc-Kien Thai<sup>1</sup>, Huy-Khanh Dang<sup>1</sup>, Trong-Cuong Vo<sup>1</sup>*

<sup>1</sup> Department of Civil Engineering, Vinh University, Vinh 461010, Vietnam

*Email: vietlinh.dhv@gmail.com*

**Abstract.** The concrete grade is designed based on the function of the concrete structure and its use conditions. However, accurate estimation of concrete grade is a challenging task because of the non-linear relationship between constituent materials. This paper investigates the performance of several machine learning (ML) methods, including Naïve Bayes, K-Nearest Neighbors, Decision Tree, Random Forest, and XGBoost, for classifying the concrete grades. A database of concrete available in the literature is used to develop ML models. The results of the ML models are evaluated and compared to choose the best ML model for classifying the concrete grades. The XGBoost model outperforms other models with 100% and 92% accuracy for the training and test set, respectively. As a result, the developed XGBoost model can save time and cost to classify the concrete grades without conducting any concrete samples.

**Keywords:** Classification, concrete grade, machine learning, reinforced concrete structure.

## 1. Introduction

Concrete is one of the most critical materials for high-rise structures, bridges, tunnels, and nuclear reactors. Concrete exhibits high compressive strength, excellent durability, sufficient workability, low permeability and diffusion, high abrasion resistance, high modulus of elasticity, and high resistance to chemical attack [1]. To plan and schedule construction projects, it is essential to predict the concrete strength or its grade as early as possible.

Civil engineering structures must meet different design criteria depending upon their operating function, their intended service lifespan, and possible environmental degradation problems throughout their service lives. The design of reinforced concrete structures relies on determining an appropriate concrete grade. Since the constituent materials of concrete do not behave linearly, estimating concrete grade can be challenging [2]. Usually, the concrete grade is determined by building several concrete samples for each material recipe and then curing and maintaining them for 28 days under standard conditions. The samples are tested destructively in the laboratory equipped with compression strength testing equipment after the required curing period has been completed. This process is expensive and time-consuming. Therefore, structural engineers must develop a robust method to predict the concrete grade to save time and money. Besides reducing time, material, and labor costs, developing non-destructive methods to predict and classify concrete grade would significantly enhance civil engineering practices [3]. A strong contender in classifying the concrete grade is the use of ML techniques to compensate for the drawbacks of conventional methods [4]. Using such prediction tools can reduce the number of trial batches required to achieve the desired concrete grade.

This study develops machine learning (ML) methods to classify the concrete grade with varying constituent materials. Firstly, a database is collected from the literature, comprising constituent materials associated with concrete strength. The concrete strength is encoded to the concrete grade for classification. Five ML models, including Naïve Bayes (NB), K-Nearest Neighbors (KNN), Decision Tree (DT), Random Forest (RF), and Extreme Gradient Boosting (XGBoost) are then developed to identify the concrete grade. The results show the XGBoost model is superior in identifying the concrete grade. As a result, the developed XGBoost model can save time and cost to classify the concrete grades without conducting any concrete samples.

## 2. Data description

The database of 1,030 samples is obtained from the University of California, Irvine (UCI) [5]. All tests were performed on 15 cm cylindrical concrete specimens. Table 1 presents the statistical attributes of the database. The predictor variables are cement (C), blast-furnace slag (BFS), fly ash (FA), water (W), super-plasticizer (S), coarse aggregate (CA), fine aggregate (FAG), and age of testing (AGE). The response is the concrete grade. As shown in the table, the C is in the range of 102.00 kg/m<sup>3</sup> to 540.00 kg/m<sup>3</sup>; the BFS is in the range of 0 to 359.40 kg/m<sup>3</sup>; the FA is in the range of 0 to 200.10 kg/m<sup>3</sup>; the W is in the range of 121.75 kg/m<sup>3</sup> to 247.00 kg/m<sup>3</sup>; the S is in the range of 0 to 32.20 kg/m<sup>3</sup>; the CA is in the range of 801.00 kg/m<sup>3</sup> to 1145.00 kg/m<sup>3</sup>; the FAG is in the range of 594.00 kg/m<sup>3</sup> to 992.60 kg/m<sup>3</sup>; the AGE is in the range of 1 Day to 365 Day. Fig. 1 shows the distribution of each variable in the database.

**Table 1.** Statistical properties of experimental data

Attribute	Unit	Category	Minimum	Mean	Maximum	StD	CoV
C	kg/m <sup>3</sup>	Input	102.00	281.17	540.00	104.51	2.69
BFS	kg/m <sup>3</sup>	Input	0.00	73.90	359.40	86.28	0.86
FA	kg/m <sup>3</sup>	Input	0.00	54.19	200.10	64.00	0.85
W	kg/m <sup>3</sup>	Input	121.75	181.57	247.00	21.36	8.50
S	kg/m <sup>3</sup>	Input	0.00	6.20	32.20	5.97	1.04
CA	kg/m <sup>3</sup>	Input	801.00	972.92	1145.00	77.75	12.51
FAG	kg/m <sup>3</sup>	Input	594.00	773.58	992.60	80.18	9.65
AGE	Day	Input	1.00	45.66	365.00	63.17	0.72

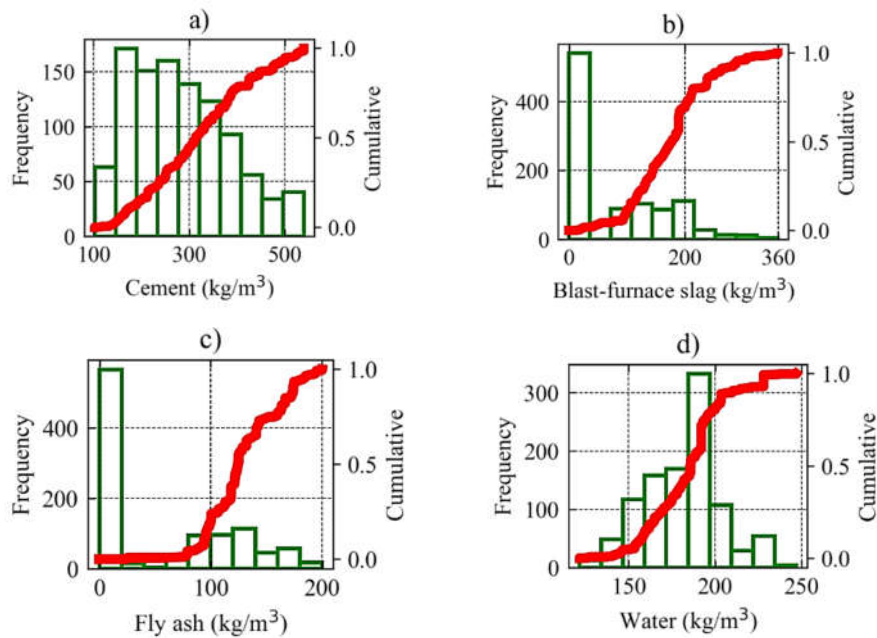


**Fig. 1.** Distribution of variables: a), b), c), d)

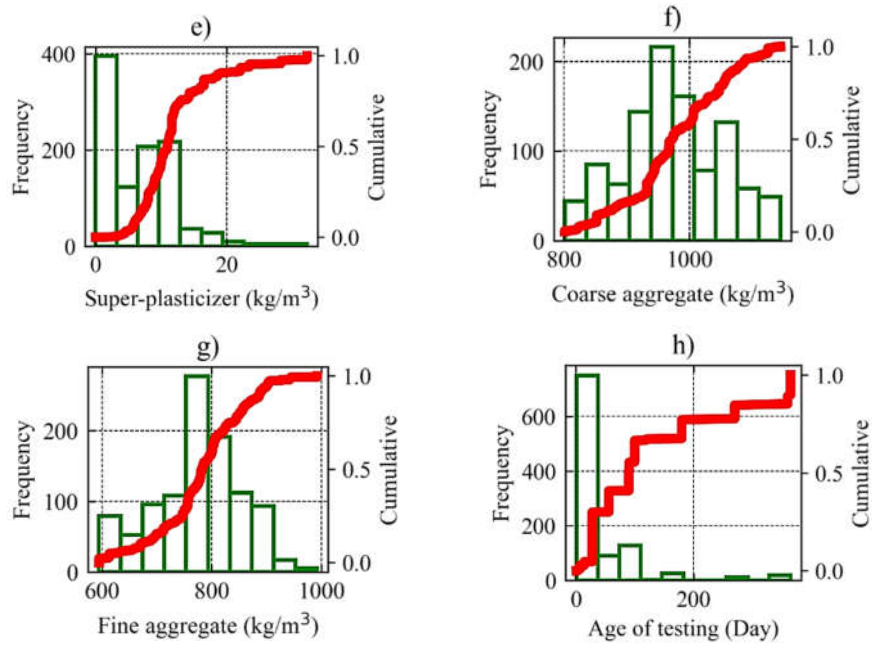


**Fig. 2.** Distribution of variables: e), f), g), h).

The concrete strength is in the range of 2.33 MPa to 82.60 MPa. This study aims to introduce ML models that focus on the classification problem. Concrete strength is thus encoded into three categories: low, normal, and high strengths, as shown in Fig. 2. The concrete strength values can be classified using the following rule [6]:

$$\text{Concrete strength} = \begin{cases} \text{Low} & \text{if } f'_c \leq 20 \text{ MPa} \\ \text{Normal} & \text{if } 20 < f'_c \leq 50 \text{ MPa} \\ \text{High} & \text{if } f'_c > 50 \text{ MPa} \end{cases}$$

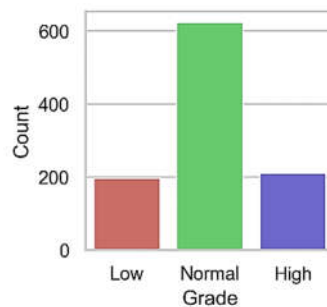


**Fig. 3.** Encode concrete strength to concrete grades.

### 3. Overview of machine learning techniques

#### 3.1. Naïve Bayes

In a Naïve Bayes classifier, an attribute value affects the class independently of other attributes [7]. It operates through the Bayes theorem as follows:

$$P_r(x) = P_r(Y = f|X = x) = \frac{\pi_f f_f(x)}{\sum_{i=1}^K \pi_i f_i(x)} \quad (1)$$

where  $\pi_f$  is the prior probability that a randomly chosen observation comes from the  $f^{\text{th}}$  class, and  $f_f(x)$  represents the density function that an observation comes from the  $f^{\text{th}}$  class.  $\pi_f$  is computed in the current study by computing the fraction of the training observations belonging to the  $f^{\text{th}}$  class, and a Gaussian distribution is assumed for  $f_f(x)$ .

### 3.2. K-Nearest Neighbors

The K-Nearest Neighbor algorithm is a non-parametric ML technique that does not assume any boundaries between classes for the decision-making process [7]. The method determines that a sample belongs to the specified class if  $K$  of its most similar samples is within the class. The conditional probability is then estimated for  $x$  in class  $f$  as:

$$P_r(x) = P_r(Y = f|X = x) = \frac{1}{K} \sum_{i \in N_K} I(y_i = f) \quad (2)$$

where  $N_K$  represents the  $K$  points in the training data that are closest to observation,  $f$ .

### 3.3. Decision Tree

Decision Tree is a non-parametric classification method that divides input data into decision levels based on a hierarchy of simple features [7]. There are two steps to modeling Decision Tree: (1) building the tree and (2) pruning it. The tree building process involves splitting up the training set space into non-overlapping regions, based on the Gini Index. A tree got in the previous step of the building is pruned in the next step to avoid over-fitting.

### 3.4. Random Forest

Random Forest classifiers are composed of several tree classifiers, in which each classifier is created by generating a random vector independent of the input vector [7]. Two methods are employed in Random Forest: the random feature subspace and out-of-bag estimation. The former allows for much faster construction of trees, while the latter allows for the evaluation of the relative importance of each input characteristic.

### 3.5. XGBoost

A boosting technique called XGBoost combines a series of weak classifiers to produce a strong one, thereby improving the performance of a model. It involves selecting weak classifiers in such a way that, when combined, their performance is significantly improved. XGBoost mitigates the misclassification error of the previous model to fit the new one. A more detailed description of the XGBoost algorithm can be found in the references [8].

## 4. Results and discussions

To use the ML models for classification of concrete grade, the cement (C), blast-furnace slag (BFS), fly ash (FA), water (W), super-plasticizer (S), coarse aggregate (CA), fine aggregate (FAG), and age of testing (AGE) are input parameters. 70% of the data (training set) is used to develop a prediction model, and 30% of the data (test set) is used to evaluate the model. The confusion matrix was used to evaluate the performance of each ML model. The confusion matrix is a table of the observed class versus the predicted class. Therefore, the diagonal elements in the confusion matrix represent the classes that were correctly classified by the ML algorithm, and the off-diagonal elements represent the classes that were not predicted correctly. For example, the

XGBoost model gets an extremely good result. For the training set, the concrete grade for all the columns is classified correctly. Specifically, 2 out of 721 columns are wrongly classified, in which none of the columns in normal grade, 1 of the columns in low grade, and 1 of the columns in high grade are mis-classified. For the testing set, only 24 out of 309 columns are mis-classified. Often, the identification of the high concrete grade is more difficult than others.

In this study, accuracy, recall, and precision are used to evaluate the model's performance. The accuracy of the model is expressed as:

$$\text{Accuracy} = \frac{\text{TP} + \text{TN}}{\text{TP} + \text{TN} + \text{FP} + \text{FN}} \quad (3)$$

Recall and precision are used to avoid misleading the prediction accuracy. Recall denotes the percentage of correct prediction for 'true positive' classes, expressed by:

$$\text{Recall} = \frac{\text{TP}}{\text{TP} + \text{FN}} \quad (4)$$

Precision denotes the percentage of correct prediction for 'true-negative' classes, expressed by:

$$\text{Precision} = \frac{\text{TN}}{\text{TN} + \text{FN}} \quad (5)$$

where the TP, TN, FP, and FN represent the True Positive, True Negative, False Positive, and False Negative, respectively.

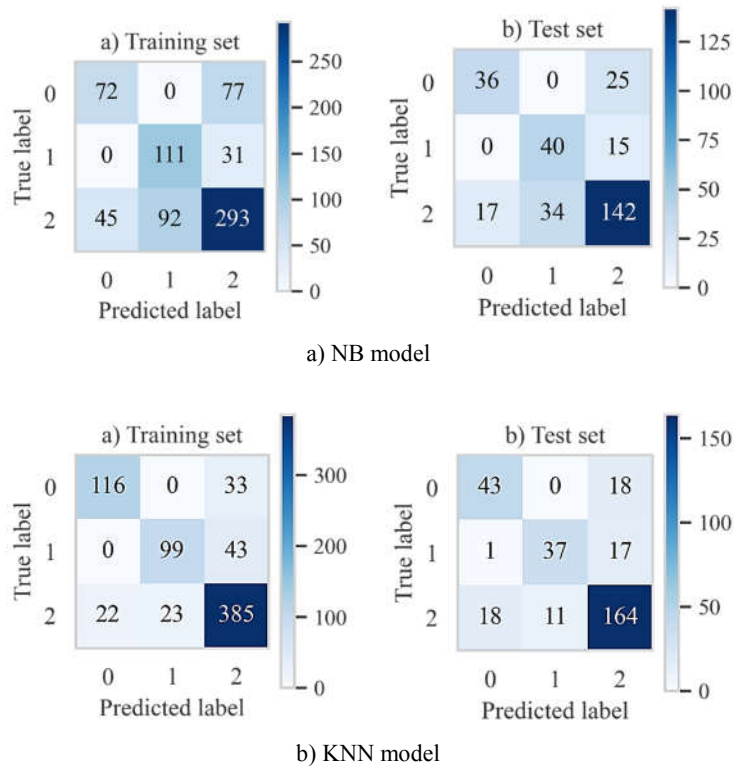


**Fig. 4.** Confusion matrices for different algorithms.

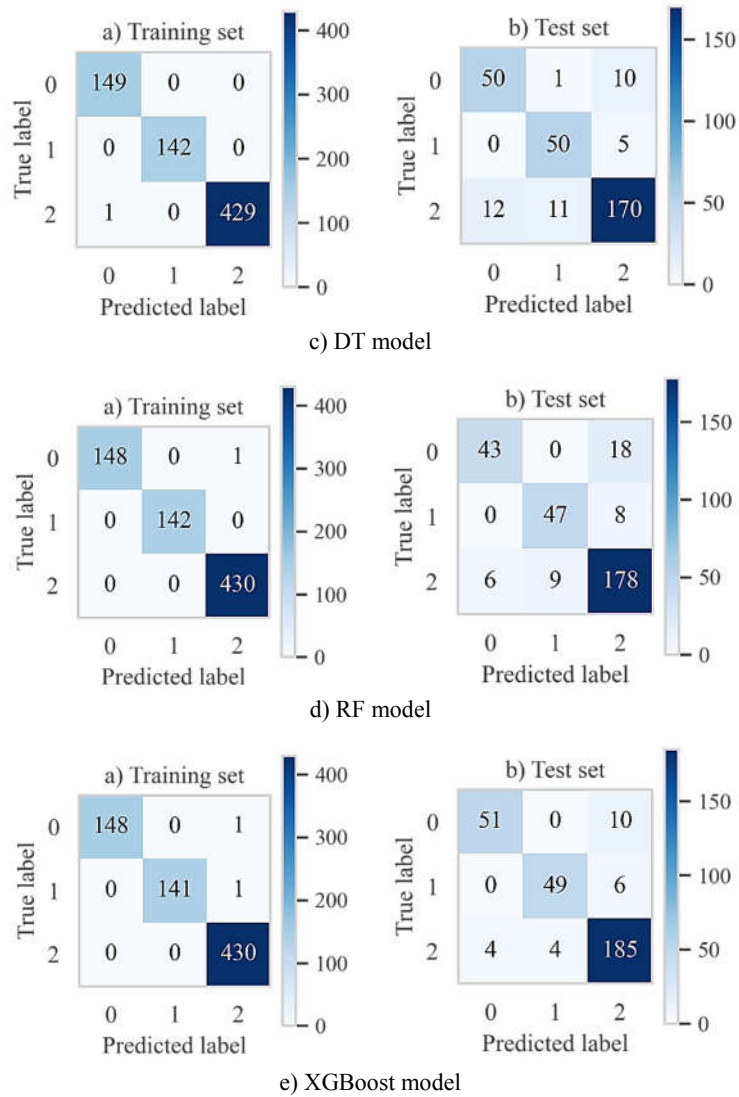


**Fig. 5.** Confusion matrices for different algorithms: d), e)

Fig. 3 shows the confusion matrix and Tables 2-6 give the performance metrics. The high accuracy, precision, and recall values in a model show it can accurately identify concrete grades. The following inferences can be drawn:

- XGBoost model had the highest accuracy, with 92% for the test set, followed by the RF model (87%) and the DT model (87%).
- For XGBoost model, the precision for high, low, and normal concrete grades are 1.0, 1.0, and 1.0 for training, respectively, while the precision for high, low, and normal concrete grades are 0.93, 0.92, and 0.92 for testing, respectively. The recall for high, low, and normal concrete grades are 0.99, 0.99, 1.0 for training, respectively, while the recall for high, low, and normal concrete grades are 0.84, 0.89, 0.96 for testing, respectively.

- The DT and RF algorithms achieved nearly the same results, whereas the KNN and NB models performed a little worse.
- Compared to parametric non-tree-based methods, such as Naïve Bayes, non-parametric tree-based methods performed better on average.

**Table 2.** Performance of NB model

Training			Testing	
	Precision	Recall	Precision	Recall
0 (High)	0.62	0.48	0.68	0.59
1 (Low)	0.55	0.78	0.54	0.73
2 (Normal)	0.73	0.68	0.78	0.74
Accuracy		0.66		0.71

**Table 3.** Performance of KNN model

Training			Testing	
	Precision	Recall	Precision	Recall
0 (High)	0.84	0.78	0.69	0.70
1 (Low)	0.81	0.70	0.77	0.67
2 (Normal)	0.84	0.90	0.82	0.85
Accuracy		0.83		0.79

**Table 4.** Performance of DT model

Training			Testing	
	Precision	Recall	Precision	Recall
0 (High)	0.99	1.0	0.81	0.82
1 (Low)	1.0	1.0	0.81	0.91
2 (Normal)	1.0	1.0	0.92	0.88
Accuracy		1.0		0.87

**Table 5.** Performance of RF model

Training			Testing	
	Precision	Recall	Precision	Recall
0 (High)	1.0	0.99	0.88	0.70
1 (Low)	1.0	1.0	0.84	0.85
2 (Normal)	1.0	1.0	0.87	0.92
Accuracy		1.0		0.87

**Table 6.** Performance of XGBoost model

Training			Testing	
	Precision	Recall	Precision	Recall
0 (High)	1.0	0.99	0.93	0.84
1 (Low)	1.0	0.99	0.92	0.89
2 (Normal)	1.0	1.0	0.92	0.96
Accuracy		1.0		0.92

## 5. Conclusions

This paper compares several ML methods for classifying the concrete grade into low, normal, and high strength. The results of the study showed that the XGBoost model had the highest accuracy for the training set and test set, followed by the DT model and RF model. The proposed XGBoost model had 100% and 92% accuracy for training and test sets in identifying the concrete grades. This study shows that machine learning-based classification can be applied to classify the concrete grade. To gain additional insights, the model can adapt to new experimental results.

## References

1. Y.H. Mugahed Amran, M.G. Soto, R. Alyousef, M. El-Zeadani, H. Alabduljabbar, V. Aune, Performance investigation of high-proportion Saudi-fly-ash-based concrete, *Results Eng.* 6 (2020) 100118. <https://doi.org/10.1016/j.rineng.2020.100118>.
2. Q. Han, C. Gui, J. Xu, G. Lacidogna, A generalized method to predict the compressive strength of high-performance concrete by improved random forest algorithm, *Constr. Build. Mater.* 226 (2019) 734–742. <https://doi.org/10.1016/j.conbuildmat.2019.07.315>.
3. H.I. Erdal, O. Karakurt, E. Namli, High performance concrete compressive strength forecasting using ensemble models based on discrete wavelet transform, *Eng. Appl. Artif. Intell.* 26 (2013) 1246–1254. <https://doi.org/10.1016/j.engappai.2012.10.014>.
4. J.-S. Chou, C.-K. Chiu, M. Farfoura, I. Al-Taharwa, Optimizing the Prediction Accuracy of Concrete Compressive Strength Based on a Comparison of Data-Mining Techniques, *J. Comput. Civ. Eng.* 25 (2011) 242–253. [https://doi.org/10.1061/\(asce\)cp.1943-5487.0000088](https://doi.org/10.1061/(asce)cp.1943-5487.0000088).
5. I.-C. Yeh, Modeling of strength of high-performance concrete using artificial neural networks, *Cem. Concr. Res.* 28 (1998) 1979–1808.
6. fib, fib Model Code for Concrete Structures 2010, Ernst Sohn, Ger. (2010) 420 pp.
7. S. Mangalathu, J.S. Jeon, Classification of failure mode and prediction of shear strength for reinforced concrete beam-column joints using machine learning techniques, *Eng. Struct.* 160 (2018) 85–94. <https://doi.org/10.1016/j.engstruct.2018.01.008>.
8. C.J.S. Leo Breiman, Jerome Friedman, Richard A. Olshen, *Classification and regression trees*, CRC, 1984.

# Research and application of Tuned mass dampers - type vibration absorber devices for buildings

*Nguyen Trong Kien<sup>1\*</sup>, Nguyen Duy Khanh<sup>1</sup>, Nguyen Thi Thu Hang<sup>1</sup>*

<sup>1</sup> Faculty of Civil Engineering, Vinh University, 182 Le Duan Str., Vinh City, Vietnam

*Email: nguyentrongkien82@gmail.com*

**Abstract.** Tuned mass dampers (TMD) is one of the most common devices for the passive control of structures subjected to wind, earthquakes, etc, the structure of these dampers consists of three main parameters: mass, damping, and spring. The article considers the use of TMD in building to reduce the acceleration and amplitude of vibrations on the upper floors. In this research, some current applications of TMD were proposed to study the response of 3-story height buildings with periodic load using time history analysis with and without the TMD. The study indicates that the response of structures such as displacements and acceleration of the upper floors can be dramatically reduced. The goal of the study is to identify an economically attractive solution that allows the fullest use of the potential of building structures in high-rise construction, abandoning the need to build massive frames leading to over-consumption of materials.

**Keywords:** Vibration absorber; TMD; Damped structure; High rise building.

## 1. Introduction

Urbanization, coupled with modern design and construction technologies, has resulted in taller and lighter structures. As an example, the world's tallest man-made structure the Burj Kalifa tower stands a remarkable 828 m from its base with an estimated weight of over 110,000 tonnes (Baker et al. 2007). One of the trade-offs of building to larger heights is the susceptibility to vibration due to the inherent flexibility of the structure. When excited by environmental dynamic loads, such as wind, this could result in large amplitude motion at the top of the structure.

There are two significant negative effects of structural vibrations on building structures (Sain et al. 2007). The first effect is the long-term fatigue of structures due to the periodic dynamic loading. It is well established that the leading cause of material failure in building structures is due to fatigue.

The second effect is the human perception of the induced motion. Humans are very perceptive to even minor vibrations. Sensitive people can perceive accelerations as low as 0.05g (Kareem et al. 2007). Between 0.1g and 0.25g, structural motions may affect an individual's ability to work, and over the long term, it may lead to motion sickness (Kareem et al. 2007).

The desire then is to mitigate structural vibrations in building structures. The control of structural vibrations can be achieved by various methods (Mendis et al. 2007). The amplitude and frequency of structural vibrations can be manipulated by modifying the structural mass, stiffness, shape, and damping. In the case of wind-induced vibrations, changing the geometry of the structure can reduce the aerodynamic forces; hence, lowering the amplitude of structural vibrations. Adding additional bracing will also stiffen the structure and reduce building sway (Mendis et al. 2007). Alternatively, the addition of passive or active stabilizing forces on the structure from an external dampening device can also be implemented to mitigate the effect of structural vibrations (Gerges and Vickery 2005). One such example is the tuned mass dampener (TMD). TMDs operate by providing additional dampening to the building structure. They are advantageous over conventional design methods-especially for taller lighter construction since they are economical and can be implemented as an add-on to existing or new structures. Real

structures may employ a combination of vibration suppression methods. An example of such a structure is Taipei 101, the second tallest man-made structure in the world. The skyscraper, which is shown in Figure 1, stands 508 m above ground level in a region which experiences strong winds, ground vibrations, and typhoons (Tamboli et al. 2008). Design elements of the structure include three TMDs, one of which is a pendulum TMD and the largest TMD in the world at 660 tonnes (Tamboli et al. 2008).

A TMD, or harmonic absorber, is a passive system (although variants include active elements) that can be modeled with a mass, a spring, and a damper. The TMD is tuned to a ratio of the structure's natural frequency (or another modal frequency). When the structure is excited at the tuned frequency, the damper resonates out-of-phase with the point of connection to the structure (Setareh et al. 2006). Vibration energy is dissipated from the structure via dissipative elements (dampers) that are a part of the TMD system. As a result, it reduces the vibration of the building. Although there are several different implementations of the TMD design, the two most common types of TMDs used are translational TMDs, and pendulum TMDs (PTMD). The concept of the TMD is not by any measure novel, and its performance is well documented (e.g., Gerges 2003, Chang 2010, and Mendis 2007). It was first developed by Herman Frahm in 1909 to reduce the vibration in the hull of ships (Conner 2003). Today it is commonly used in buildings, automobiles, and virtually any system where vibration suppression is desired.

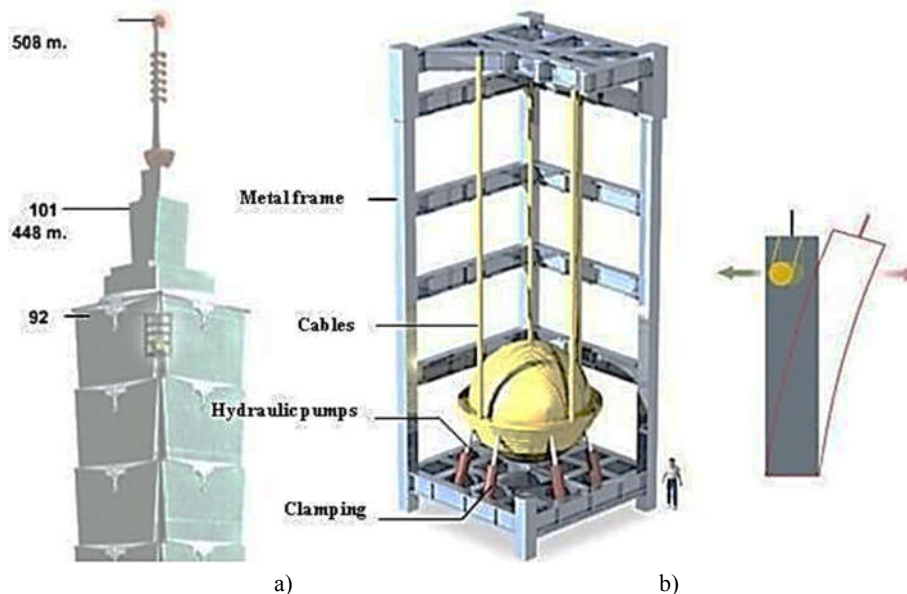


**Fig. 1.** (a) Taipei 101 (Powell 2007) (b) Taipei 101 PTMD.

The advantages of this system are external power is not needed, provides a large damping force, and can be installed on the existing structure. Some of its limitations are a narrow frequency, sensitivity to mistuning, and the need for a dedicated area to house the system.

The main purpose of this article is the following:

- Present a fundamental of tuned mass dampers (TMDs).
- Application of TMD on a simple frame.
- Comparison of the effectiveness of TMD with some other methods in reducing vibration of 2D frames 3- story.

## 2. Type of TMD

### 2.1. Translational TMD Systems

Translational TMD can be either unidirectional or bidirectional systems (Conner 2003). In unidirectional systems, the motion of the TMD mass is restricted to a single direction, often by placing the mass on a set of rails or roller bearings, as depicted in Figure 2. In bidirectional systems, the mass can move along both coordinate axes. In either topology, a set of springs and dampers are placed between the TMD mass and the supporting structure which is fixed to the structure.

Translational TMD systems have been implemented in large-scale structures for over 40 years (Kareem et al. 2007). Examples of structures containing translation TMD systems include the Washington National Airport Tower, the John Hancock Tower, and the Chiba Port Tower.

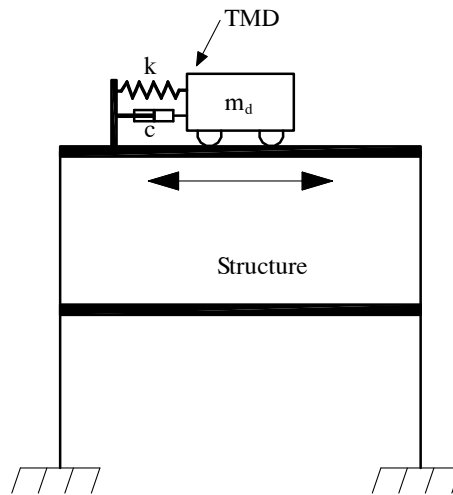


Fig. 2. Schematic of a unidirectional translational TMD.

### 2.2. PTMD Systems

PTMDs replace the translational spring and damper system with a pendulum, which consists of a mass supported by a cable that pivots about a point, as illustrated in Figure 3. They are commonly modeled as a simple pendulum. For small angular oscillations, they will behave similarly to a translational TMD and can be modeled identically with an equivalent stiffness and equivalent damping ratio. Hence, the design methodology for both the translational TMD system and PTMD systems are identical (Conner 2003).

A major motivating factor for using a PTMD system over an equivalent translational TMD system is the absence of any bearings to support the TMD mass (Conner et al. 2003). The bearing support structure used in the translational TMD assembly is expensive and susceptible to wear over the lifespan of the TMD system. As a result, PTMD designs can be less expensive to manufacture and last longer. Nearly 50% of structures in Japan that use TMD systems utilize PTMD systems (Kareem et al. 2007). Examples include Crystal Tower in Osaka, Higashiyama Sky Tower in Nagoya, and Taipei 101 in Taipei (Conner 2003). Studies on the use of PTMD systems generally focus on the optimization of PTMD design parameters to reduce excessive lateral deflections in structures. Gerges and Vickery (2003) utilized a non-linear wire rope spring PTMD system in an experimental case study, concluding that their performance approaches

optimal linear TMD designs while providing smaller relative displacements for lower mass ratios. Setareh et al. (2006) presented optimization algorithms for a PTMD system induced by pedestrian loading. With this pendulum system to increase the efficiency of reducing vibrations, it often installs an additional damper for the mass as shown in Figure 3b.

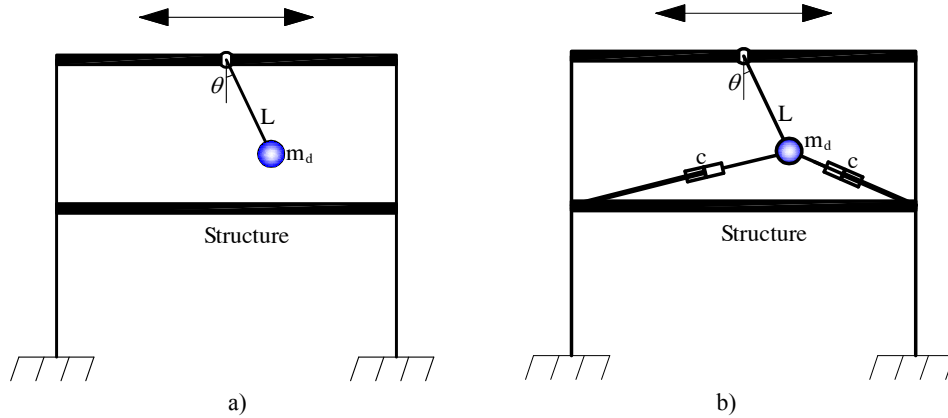


Fig. 3. Schematic of a PTMD.

### 3. Determining the parameters of TMD

The parameter of TMD will be based on Den Hartog optimization criteria assuming that the structure fits the condition for the optimization criteria.

#### 3.1. Den Hartog's Optimization Criteria

TMD efficiency in reducing structural response can be gained by following the basic development of Den Hartog for the simple case where the structural system is considered undamped ( $c=0$ ) and is subject to a sinusoidal excitation with frequency  $\omega$  ( $f(t) = P_0 \sin \omega t$ ) (Soong & Dargush, 1997). This procedure compares the dynamic effect of a TMD with the static deflection produced by the maximum force applied statically to the structure. The dynamic amplification factor for an undamped structural system,  $R$ , is

$$R = \frac{y_{\max}}{y_{st}} = \sqrt{\frac{(\alpha^2 - \beta^2)^2 + (2\zeta_d \alpha \beta)^2}{[(\alpha^2 - \beta^2)(1 - \beta^2) - \alpha^2 \beta^2 \mu]^2 + (2\zeta_d \alpha \beta)^2 (1 - \beta^2 - \beta^2 \mu)^2}} \quad (1)$$

Where:  $\beta = \omega_f / \omega$  External force excitation frequency ratio;

$\alpha = \omega_d / \omega$  TMD frequency ratio;

$\mu = m_d / m$  TMD mass ratio;

$\omega_d^2 = k_d / m_d$  Squared natural frequency of TMD;

$\omega^2 = k / m$  Squared natural frequency of structural system;

$\zeta_d = c / c_c = c / 2m \omega_d$  Damping ratio of TMD.

Figure 4, shows a plot of  $R$  as a function of the frequency ratio  $\beta$  for  $\alpha = 1$  (tuned case),  $\mu=0.05$ , and for various values of TMD damping ratio  $\zeta_d$ . Without structural damping, the response amplitude is infinite at two resonant frequencies of the combined structure/TMD system. When the TMD damping becomes infinite, the two masses are virtually fused and the result is an SDOF system with a mass of  $1.05m$  so that the amplitude at resonant frequency becomes infinite again. Therefore, somewhere between these extremes, there must be a value of  $\zeta_d$  for which the peak becomes a minimum.

There are two points (P and Q) in Figure 4 which is independent of damping ratio  $\zeta_d$  and the minimum peak amplitude can be obtained by first properly choosing  $\alpha$  to adjust these fixed points to reach equal heights. The optimum frequency ratio  $\alpha$  following this procedure is determined as

$$\alpha_{opt} = \frac{1}{1 + \mu} \quad (2)$$

Which gives the amplitude at P or Q:

$$R = \sqrt{1 + \frac{2}{\mu}} \quad (3)$$

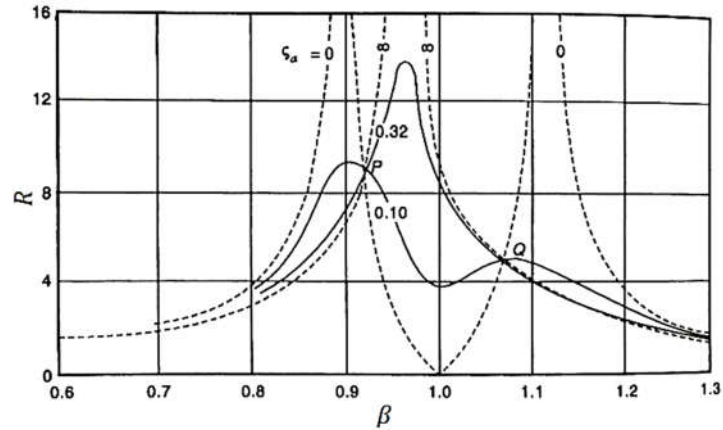


Fig. 4. Amplification Factor as a function of  $\beta$  (Soong & Dargush, 1997).

A good estimate for  $\zeta_{opt}$  can be determined as the average of two values which make the fixed points P and Q maxima in figure 4 gives

$$\zeta_{opt} = \sqrt{\frac{3\mu}{8(1 + \mu)}} \quad (4)$$

The maximum amplification factor and optimum absorber parameters are summarized in Table 1 for a variety of excitations and response quantities density is assumed.

**Table 1.** Optimum Absorber Parameters attached to undamped SDOF Structure (Warburton, 1982)

Case	Excitation		Optimized absorber parameter	
	Type	Applied to	$\alpha_{opt}$	$\zeta_{opt}$
1	Periodic Force	Structure	$\frac{1}{1 + \mu}$	$\sqrt{\frac{3\mu}{8(1 + \mu)}}$
2	Acceleration	Base	$\frac{\sqrt{1 - \mu/2}}{1 + \mu}$	$\sqrt{\frac{3\mu}{8(1 + \mu)(1 - \mu/2)}}$
3	Random Force	Structure	$\frac{\sqrt{1 + \mu/2}}{1 + \mu}$	$\sqrt{\frac{\mu(1 + 3\mu/4)}{4(1 + \mu)(1 + \mu/2)}}$
4	Random Acceleration	Base	$\frac{\sqrt{1 - \mu/2}}{1 + \mu}$	$\sqrt{\frac{\mu(1 - \mu/4)}{4(1 + \mu)(1 - \mu/2)}}$

### 3.2. Mass of TMD

The mass ratio  $\mu$  of the TMD mass to the kinetic equivalent structural mass has to be sufficient. For small ratios ( $\mu \leq 0.025$ ) big vibration amplitudes of the TMD mass relative to the structure are resulting. This can create a space problem for proper integration of the TMD in the available structural gap, but also the TMD gets usually much more expensive due to more and bigger springs.

In addition, a small mass ratio is decreasing the effective range of the TMD. The TMD mass movements are significantly smaller for bigger ratios ( $\mu \geq 0.025$ ) and the effective range for a 100% TMD efficiency around the resonance frequency is greater.

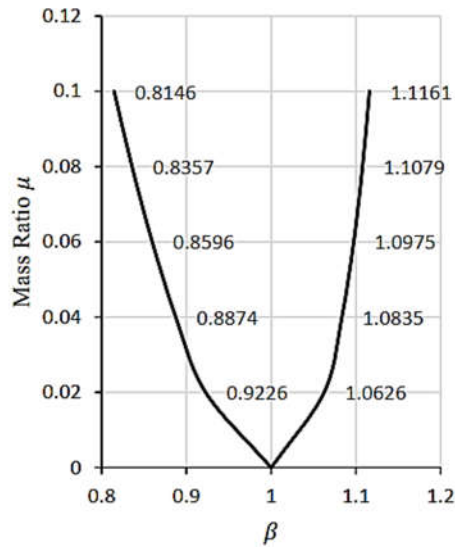


Fig. 5. Frequency range with respect to  $\mu$ .

### 4. Applied example

One example will be used in this paper. 2D frame three stories will be used for a preliminary TMD application study using FEA software as shown in Figure 6a.

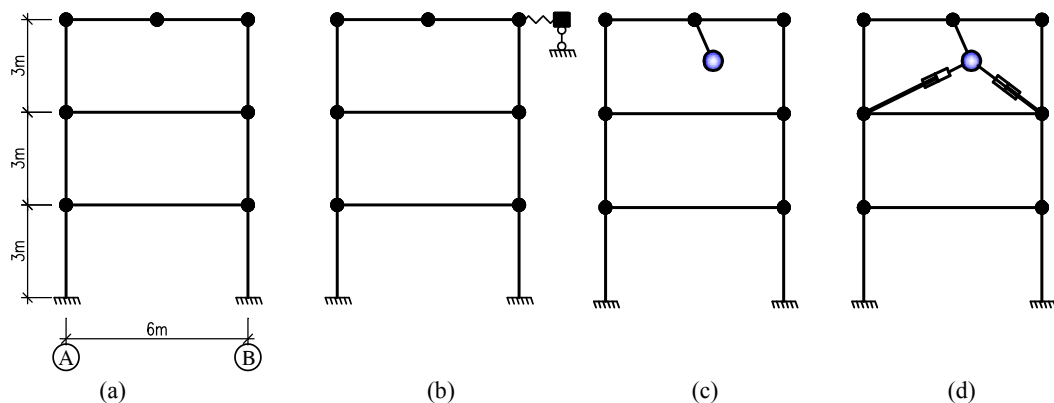


Fig. 6. (a) Frame model; (b) Frame with TMD; (c) Frame mounting a pendulum without damper; (d) Frame mounting a pendulum with damper.

**Table 2:** Model parameters

	Elastic modulus(MPa)	Section size	Mass
Beams	$27 \times 10^3$	20cm×60cm	0
Column	$27 \times 10^3$	20cm×30cm	0

A tuned mass damper is attached to the structure on the top floor, in three cases as shown in figure 6. Model parameters are shown in Table 2. The mass at each node is 25 tons. A sinusoidal force with amplitude 5000N was applied to the Frame with period  $T=1.13s$ .

The parameters of TMD will be based on Den Hartog optimization criteria. The mass ratio for the TMD will be 0.04 for this paper. Depending on the available space, a larger mass can be used where it will increase the efficiency range. Then optimum frequency ratio  $\alpha_{opt} = 1/(1+\mu)$  can be calculated. The frequency ratio gives up the frequency of the TMD which can be used to calculate the spring constant  $k$  of the system. The damping ratio of the TMD will be calculated by using the mass ratio  $\zeta_{opt}$  in(4). The damping coefficient can be found by using the damping ratio  $c = 2\zeta_{opt}m\omega$ .

The parameter of TMD will be calculated for 3 cases as shown in Figure 6.

- **Case Figure 6b**

Mass ratio chosen to be  $\mu=0.04$  so mass of TMD  $m_d=10.8$  tons.

Optimum frequency ratio  $\alpha_{opt}=0.962$ .

Frequency of damper  $f_d = 0.882$  Hz.  $\omega_d = 5.54$ rad/s.

Spring stiffness constant  $k_d = 33.15$  ton/m.

Optimum damping ratio  $\zeta_{opt} = 0.1155$ .

Damping coefficient  $c = 1.382$  ton.s/m.

- **Case Figure 6c**

Install a pendulum with a mass of 10.8 tons and a length of 0.3m. With these parameters, the natural frequency of the pendulum is also approximately the structure's natural frequency.

- **Case Figure 6d**

Install the pendulum similar to case 2 but with additional dampers. The damper is linear and has a damping coefficient of 1500 Ns/m.

- **Result**

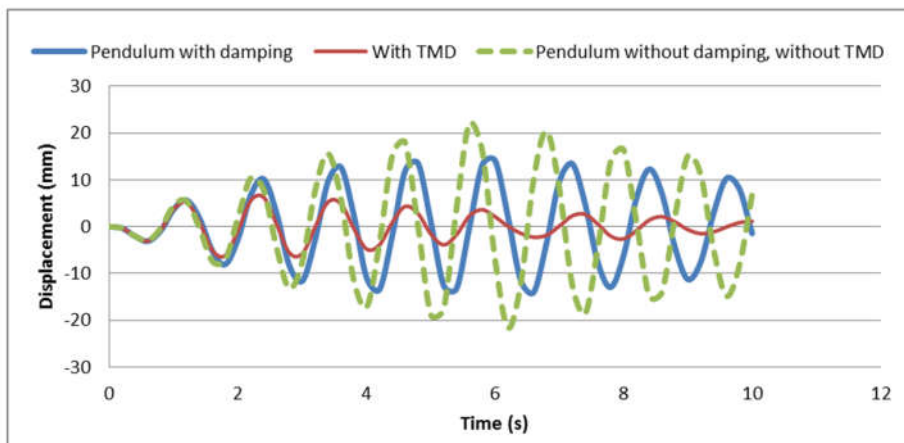


**Fig. 7.** Displacement over Time of Frame at the top floor.

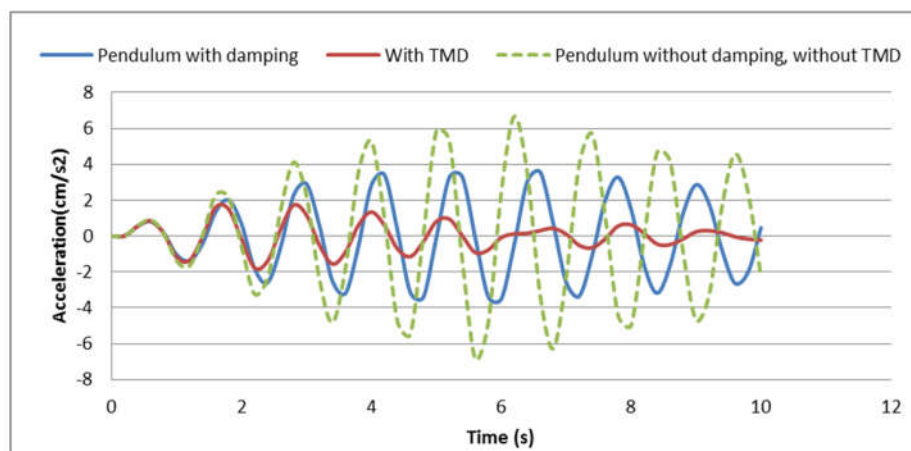


**Fig. 8.** Acceleration over Time of Frame on Top floor.

• **Remark**

In general, both TMD and PTMD can reduce the vibration of the structure. However, the TMD case still has a better effect on reducing vibration than the PTMD case. Theoretically, undamped devices (as in case 2) can only suppress oscillations in a very narrow frequency domain. In this example, given a sufficiently wide frequency domain of the load, the case pendulum without damping does not effectively reduce vibration.

**5. Conclusions**

This paper introduced the most popular device for passive control of structures, TMD. Practice calculating the optimal parameters of TMD by Den Hartog’s optimization criteria and applying TMD to the three-story frame structure for three cases. The results of numerical modeling using Sap2000 software have proved to be effective in reducing vibrations for the structure when TMD is installed. Of the three cases of TMD attachment, the TMD case gave the best vibration reduction results, the case of PTMD without damped did not have a significant effect. Therefore, to increase the effectiveness of PTMD in practice, it is necessary to add a damper to this device.

**References**

1. Biggs, J. M. (1964). Introduction to Structural Dynamics. New York: McGraw-Hill.
2. Brass, K., Wood, A., & Carver, M. (2013). Year in Review: Tall Trends of 2012. Council on Tall Buildings and Urban Habitat. Retrieved September 01, 2013.
3. Cheng, F. Y. (2008). Smart Structures: Innovative systems for seismic response control. Boca Raton: CRC Press.
4. Chopra, A. K. (1997). Dynamics of Structures. Singapore: Prentice Hall International.
5. Connor, J. J. (2003). Introduction to Structural Motion Control. New Jersey: Prentice Hall.
6. Hibbeler, R. C. (2006). Principles of Statics & Dynamics. New Jersey: Pearson Prentice Hall.
7. Kourakis, I. (2007). Structural Systems and Tuned Mass Dampers of Super Tall Buildings: Case Study of Taipei 101. Massachusetts Institute of Technology.
8. MAURER Tuned Mass and Viscous Dampers. (2011). Munchen: Maurer Sohne.
9. Mendis, P., Ngo, T., Haritos, N., & Hira, A. (2007). Wind Loading on Tall Buildings. EJSE Special Issue: Loading on Structures, 41–54.
10. Okhovat, M. R., Rahimian, M., & Ghorbani-tanha, A. K. (2006). Tuned Mass Damper for Seismic Response of Tehran Tower. In 4th International Conference on Earthquake Engineering. Taipei: 4ICEE

11. Sanhyun, L., Chung, L., Kim, Y., & Woo, S. (2012). Practical Application of Mass Type Damper for Wind-induced Vibration Control of Super-Tall Building. In IABSE (Ed.), 18th Congress of IABSE. Seoul.
12. Soong, T. T., & Dargush, G. F. (1997). Passive Energy Dissipation Systems in Structural Engineering. Buffalo: John Wiley & Sons.
13. Taranath, B. S. (2012). Structural Analysis and Design of Tall Buildings: Steel and Composite construction. London: CRC Press.
14. Warburton, G. B. (1982). Optimal Absorber Parameters for Various Combinations of Response and Excitation Parameters. Earthquake Engineering Structural Dynamic, 10, 381–401.

# Reality and difficulties in applying Building Information Modeling (BIM) in Vietnam

*Pham Ngoc Minh*

Department of Civil Engineering, Vinh University, 182 Le Duan, Vinh, Vietnam

**Abstract:** Building Information Modeling (BIM) is an advanced technology applied in the construction field and is a current global trend. BIM can be understood as "using technology to digitize the information of the building to support the process of design, construction, management and operation of the project". Compared with the traditional method that is heavy on human effort but difficult in terms of management and implementation, BIM has provided a solution by digitizing all information about construction projects. During operation, BIM is closely related to project participants, with the consolidation of information from all processes from design, construction, operation, monitoring, management, BIM will connect stakeholders to increase work efficiency for all many times. However, the application of BIM in the construction field in Vietnam is still new and still faces many difficulties. This article refers to the method of applying BIM in construction activities, construction management and operation in Vietnam and the remaining difficulties.

**Keywords:** Building Information Modeling-BIM, BIM application in Vietnam.

## 1. Introduction

The concept of BIM has been in development since the 1970s, but it only became an agreed term in the early 2000s. Development of standards and adoption of BIM has progressed at different speeds in different countries; standards developed in the United Kingdom from 2007 onwards have formed the basis of international standard ISO 19650, launched in January 2019.[1]

In May 2011 UK Government Chief Construction Adviser Paul Morrell called for BIM adoption on UK government construction projects [2]. Morrell also told construction professionals to adopt BIM or be "Betamax'd out".[3] In June 2011 the UK government published its BIM strategy,[4] announcing its intention to require collaborative 3D BIM (with all project and asset information, documentation and data being electronic) on its projects by 2016. In 2021, the National Institute of Building Sciences (NIBS) looked at applying UK BIM experiences to developing shared US BIM standards and processes.

In Vietnam, in 2017, the Institute of Construction Economics and the Ministry of Construction compiled and published a provisional guide to BIM application within the framework of a pilot project to apply building information modeling in construction and operation management activities according to Decision No. 2500/QĐ-TTg dated December 22, 2016, of the Prime Minister. In 2021, the Ministry of Construction published the Official Guide to apply Building Information Modeling (BIM) as an alternative to interim guidance.

## 2. Applying BIM in the construction investment process in Vietnam

In Vietnam today, grasping the trend of applying BIM technology, the concept of BIM has been relatively popular in the construction industry. From state management units to construction businesses, have initially realized the benefits of BIM application. Many design agencies and contractors have gradually put BIM software applications such as Autodesk Revit, Tekla Structure, etc. into application in actual works from the conceptual design stage to the construction management stage.

The investigation and survey of the status of BIM application in the construction industry in Vietnam is carried out on many different subjects, which are individuals, enterprises or state

management agencies in the construction industry. From survey data obtained through questionnaires, there are about 69% of respondents in Hanoi area, 21% in Ho Chi Minh City and 10% in some other provinces and cities (e.g., Hai Phong, Da Nang). In which, the survey respondents are mainly concentrated in the business sector, with 32% coming from private enterprises, 24% coming from foreign-invested enterprises and 19% coming from state-owned enterprises. State management agencies account for about 12% of the survey, the rest is from some other agencies [5] Current status of BIM application process in construction activities in Vietnam is carried out through the following basic stages:

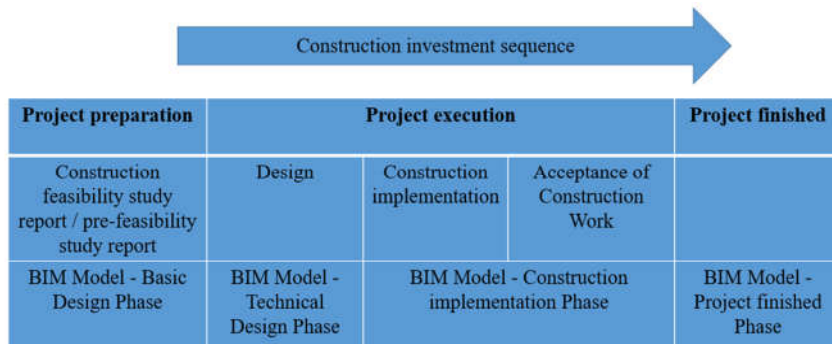


**Fig. 1.** Construction investment sequence.

Fig.1 shows the construction investment steps and the corresponding BIM model for each stage. When implementing a project in the traditional Design - Bid - Construction form, the BIM application process is divided into 2 phases: design and construction. Design consultancy deploying BIM in the design phase. Design consultancy or contractors deploy BIM for construction purposes [6].

*Design phase:*

- a. Establish BIM Execution Plan (BEP) before modeling.
- b. The design team builds BIM models for each discipline.
- c. Create federation models and detect clash, conflicts
- d. Clash and conflicts will be resolved in coordination meetings.
- e. Submit design documents after handling collisions and conflicts

*Construction phase:*

- a. BIM model and drawings will be released to the construction contractor for reference.
- b. Design consultancy create federation models or the main contractor will build the next models with detailed information to meet construction and manufacturing requirements.

## **2.1. Subjects participating in the process of applying BIM in the project**

### ***a. Employer***

The main tasks of Employer in the process of applying BIM in the project:

- The employer sets up a department or appoints an officer in charge of applying BIM to the project or assign this task to the Project Management Unit to perform
- Activities to prepare for selection of BIM Executor: Prepare information to develop Exchange Information Requirement (EIR).
- Develop bidding documents/requirements, including evaluation criteria, and contract content related to BIM contents; organize the assessment and select the implementing agencies.

- Approve the BIM Execution Plan (BEP) submitted by the implementing agencies.
- During BIM implementation, the Employer reviews and accepts the products handed over by the implementing organization according to the agreed timelines in the BEP. Consider adjusting the BIM implementation plan to suit the requirements and progress of the project.
- At the end of the BIM application process, the Employer shall assume the prime responsibility to coordinate with related parties to organize the storage of the model and evaluate the BIM application process.

**b. Implementing agency**

The implementing agency is responsible for coordinating information and coordination between the main Task Team and the Employer and other related parties.

Some of the main tasks of the Implementation agency include:

- Develop BIM Execution Plan (BEP) to submit to the Employer for consideration and approval.
- Acting in the role of coordinating and managing BIM model creation.
- Setting up plans, preparing resources, assigning tasks and powers among BIM implementations departments.
- Identify the risks that may occur in the process of applying BIM.

The implementing agency is proactive in managing the BIM implementation process of the Main Task Team.

**c. BIM Task Team**

The BIM Task Team is under the management and guidance of the Implement agency. The main task of the BIM Task Team is to coordinate with the implementing agency to finalize the BIM Execution Plan (BEP); direct modeling; propose necessary additions or modifications to the project's BIM modelling information standards, methods and procedures. The capacity of the BIM Task Team is evaluated based on 3 aspects:

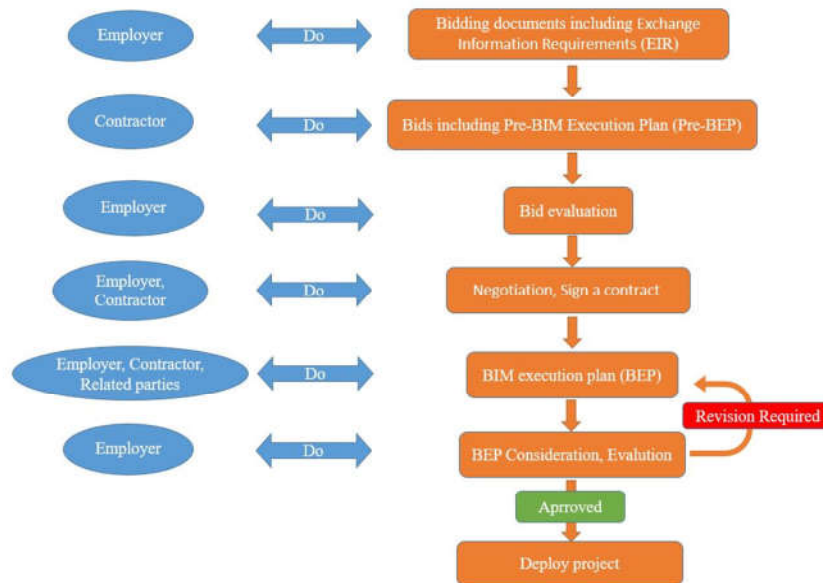


**Fig. 2.** Steps in the process of preparing to apply BIM.

- Information management capacity (Experience, human resources)
- Ability to create BIM models (Experience in building modeling methods and processes; quantity and level of human resources to perform modeling work)
- System hardware, software and appropriate support tools.

The BIM Task Team creates a BIM Model according to the standards, methods, and processes required in the BIM Execution Plan (BEP). The BIM Task Team checks the information areas on the Common Data Environment (CDE) to ensure that the information and data are consistent with the methods and processes that will be used to create the model information. Check the content of the information area on the CDE to ensure that it meets the information requirements and is appropriate for the scope of work and the level of information development. The process of preparing for the application of BIM in the project follows the steps shown in Figure 2.

### **3. Difficulties in applying BIM in Vietnam**

#### **3.1. Lack of expertise**

As mentioned above, BIM technology has not been introduced to Vietnam for a long time. Organizations and enterprises have to research and learn new software groups in the chain of many BIM software, each phase of the project has its own set of suitable software. The first difficulty is to master the software, then to identify the applicability to solve the actual work required. This is not a small challenge for organizations and enterprise starting to apply BIM for their construction activities.

For large projects, need to coordinate many disciplines that require a large number of BIM models working at the same time on the same project, which leads to difficulties in coordinating work. Enterprises need a BIM manager and qualified BIM coordinators to operate the project.

#### **3.2. Limitations in technical infrastructure**

When applying to other stages in the project and working with projects of higher scale and complexity, one thing is that the IT system infrastructure needs to be upgraded and changed. Difficulties arise when operating a high-performance BIM system that requires practical knowledge of the responsiveness of computer hardware and network infrastructure. In addition, to apply BIM, the core issue of enterprises is to have a common data environment (CDE), it can be said that CDE is the backbone of BIM operation. For many businesses in Vietnam, the concept of CDE may still be new.

#### **3.3. The lack of synchronization**

To apply BIM in the construction of large projects, it requires coordination between stakeholders (investor - design consultant - construction contractor - supervisor). It can be said that BIM coordination is an important factor for a BIM project to be completed from concept to operation. There should be regular coordinated BIM meetings according to the schedule with all members meeting to discuss and exchange design and construction issues, using the model as a shared data source.

In Vietnam, many large projects have been applied BIM with investors being corporations and private enterprises. Figure 3 is the Landmark 81 building applying the BIM technology that has Vingroup as the employer. However, for state budget projects, the application of BIM is still very limited. The fact is that there is no mandatory standard to apply BIM for public investment projects, so the application of BIM to these projects is only one-way, either as a design consultant,

or as a construction contractor. Therefore, the effectiveness of applying BIM to these projects is not high. Figure 3 is one of the few state budget projects applying BIM technology, the project has a total investment of 2,173 billion VND from the budget of Hai Phong People's Committee.

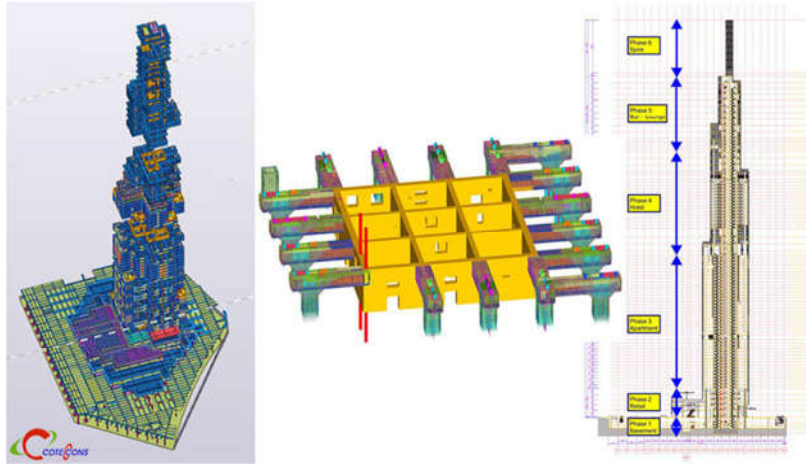


Fig. 3. Landmark 81 - Ho Chi Minh City - Viet Nam.



Fig. 4. Hoang Van Thu Bridge - Hai Phong - Viet Nam.

### 3.4. Legal issues

BIM is a great help for automating the calculation of the volume of elements, because today's BIM modeling software can automatically export the volume of elements from the built BIM model. On the other hand, when updating and changing the design into the model, the weight of the member can be exported very quickly according to the latest parameters of the elements, so the time required for the bill of quantity will be significantly reduced, the bill of quantity process takes place faster and more accurately than the current traditional methods that rely on design documents (2D drawings) to calculate [7].

However, with the actual conditions in Vietnam, the volume exported from BIM software has not been verified and there is no legal document to acknowledge this. Therefore, the bill of quantity results from BIM have almost no legal value.

### **3.5. Incurred expenses**

As stated above, in order to apply BIM, organizations or enterprises must invest in infrastructure, change the entire working system, need to pay to hire experts to train, and this transfer process cannot happen quickly. In the context that small enterprises in Vietnam do not have the financial capacity and strategic vision to invest in BIM technology.

## **4. Conclusions**

With the development of science and technology, BIM is an important solution to approach the Industrial Revolution 4.0 of the construction industry that Vietnam should not miss the opportunity to approach. With the reality of applying BIM and the difficulties mentioned in this article, I think the Government needs to develop a roadmap suitable to Vietnam's conditions and resources; complete relevant legal documents; supporting businesses in applying BIM in both finance and human resource training. For projects using state capital, state management agencies need to quickly issue guidelines on the formulation and cost management of BIM applications.

## **References**

1. [https://en.wikipedia.org/wiki/Building\\_information\\_modeling](https://en.wikipedia.org/wiki/Building_information_modeling)
2. "BIM Roundtable Discussion". Thenbs.com. Archived from the original on 22 October 2014. Retrieved 17 October 2014.
3. "Adopt bim or be 'Betamaxed out' says Morrell". Building Design. Archived from the original on 22 October 2014. Retrieved 17 October 2014.
4. "Modern Built Environment - innovateuk". Ktn.innovateuk.org. Retrieved 17 October 2014.
5. <https://onebimvn.com/tin-tuc/bim-tai-viet-nam>
6. Guideline for application of Building Information Model, Ministry of Construction, Vietnam, 2021.
7. Dang Thi Hong Duyen, Nguyen Van Tam, Ngo Van Yen, Le Thi Hoai An. Application of BIM for calculating volumetric measurement of buildings: Lesson learns from other countries. Journal of Science and Technology in Civil Engineering, 2(12), 46-52, 2018.

# Analysis of randomness and fuzziness of parameters related to corrosion of reinforcement in reinforced concrete structures

*Thu Minh Tran<sup>1</sup>, Duc Manh Tran<sup>1</sup>, The Truyen Tran<sup>1</sup>*

<sup>1</sup>University of Transports and Communication, Cau Giay Street, Hanoi, Vietnam

**Abstract.** Reinforced concrete structures are susceptible to damage in harsh environments. One of the main causes of deterioration of reinforced concrete structures in these environments is corroded. Many factors affect the corrosion of the reinforcement, such as chloride concentration on the structure surface, chloride diffusion coefficient, the thickness of the protective concrete layer, chloride ion concentration limit at the reinforcement surface, humidity, temperature... In preliminary calculations, these values are usually determined from laboratory and field test results. However, in reality, these parameters are unstable or fuzzy factors. Considering the randomness and fuzziness of these parameters, it is necessary to calculate and forecast the service life of reinforced concrete structures according to corrosion criteria more accurately and reliably. This paper analyzes the fuzziness and randomness of some input parameters in calculating and predicting the service life as a basis for analyzing the corrosion of reinforcement and predicting service life in reinforced concrete structures in reality.

**Keywords:** reinforced concrete, corrosion, randomness, fuzzy parameter, probability, service life, chloride.

## 1. Introduction

Over time, many old concrete structures show signs of deterioration due to harsh environmental conditions leading to the physical and chemical deterioration of concrete. Premature deterioration of concrete structures before expected life is a major cause of concern. There are many processes behind the premature deterioration of reinforced concrete structures. The condition of the cement reinforcement elements can be related to various parameters such as the rate and extent of corrosion, cracks, flaking, concentrations of harmful chemicals, etc. Many reinforced concrete structures may have to be repaired or replaced based on their service status, so it is necessary to evaluate and analyze the parameters affecting the service life of reinforced concrete structures with consideration of randomness and fuzziness in order to ensure accuracy when predicting the life of the building. Random theory and fuzzy sets are defined to analyze input data according to formal mathematical frameworks.

Several studies have determined that reinforcement corrosion is the most common cause affecting the service life of reinforced concrete structures. These oxide corrosion products cause tensile stress expansion on the surrounding concrete and thus lead to cracks in the concrete because of its poor bearing capacity. This is a matter of concern as the cracks can further lead to the access of oxygen or chloride ions which corrode the reinforcement. A reduction in the effective cross-sectional area of the reinforcement is also unavoidable because the iron is consumed in the oxidation process, and this can lead to a significant reduction in the load-carrying capacity. Therefore, reinforcement corrosion causes a significant threat to the usability and serviceability of the structure. Corrosion of reinforcement is an electrochemical process that induces the oxidation of iron and thus produces massive corrosion of the iron oxide product in the presence of water and oxygen [1]. The ACI Guidelines for Durable Concrete have recognized five general categories of concrete damage as a) Freezing and thawing, b) Exposure to aggressive chemicals, c) Abrasion, d) Corrosion to steel and other materials embedded in the concrete, and e) Chemical reaction with the aggregate [2]. On the other hand, the input parameters for predicting the service life of reinforced concrete structures according to the corrosion initiation stage are difficult to estimate. This

limitation makes it difficult to predict the life of the building, and therefore, finding or conventionalizing the parameters is extremely important to control the accuracy and reality of the results [4]. ... This limitation can be relatively overcome by applying the rules of normal distribution, fuzziness and randomness of mathematics to find the general rule. Using probability theory to transform a random distribution into a normal distribution provides a reasonable way to extend the precision processing framework for results. MB Anoop and K Balaji Rao presented the safety assessment process by investigating the state of stress corrosion cracking, considering the random evolution of stress corrosion cracking over time in tubular concrete samples [10-12].

The visual properties of damage appearing on the surface of the structure are used to assess the structural condition, together with the results obtained for the carbonation depth and chloride content. A methodology is developed using fuzzy concepts, which allows the assessment of reinforced concrete buildings subject to corrosion. Gopal Mitra, Kamal Kant Jain and Bishwajit Bhattachar-gee performed the BCI assessment based on a visual and experimental assessment of carbonate and chloride content. This index is used to make decisions about the need for building repair [3]. Sobhani and Ramezaninpour believe that the assessment of the corrosion level of reinforced concrete structures according to fuzzy theory is more reasonable and controllable than analyzing the parameters according to the random distribution [5]. The durability of reinforced concrete structures is affected by chloride penetration and the rebar's susceptibility to chloride-induced corrosion when exposed to environments with a lot of chloride or desalination salt.

Once the chloride content in the reinforcement reaches a threshold value and there is enough oxygen and moisture, the corrosion of the reinforcement will begin. Corrosion products then accumulate in the concrete-steel surface transition zone, exerting great stress on the surrounding concrete, and causing and spreading cracks [6]. The probability distribution functions for the corrosion initiation interval and the corrosion cracking time are converted to fuzzy sets. RC. J. Sobhani, A.A. Ramezaninpour has successfully built a module based on probability theory and fuzzy theory to develop a structural health monitoring system (SHMS) for reinforced concrete infrastructure [5,6]. The random evolution of reinforced concrete girder condition over time is modeled by a very complex model called the Markov series (MC). Various researchers have proposed the use of homogeneous MC models to model the progression of damage over time to bridge girders [7,8]. M B Anoop and K Balaji Rao used Markov chains built according to fuzzy theory to describe the performance of T-beams of Rocky Point viaduct [9]. Cheng and Hoang have proposed an artificial intelligence (AI) approach to infer risk scores for bridge maintenance projects [13]. Based on fuzzy least squares, the vector inference model evolves according to fuzzy theory. In the new algorithm called EFLSIM, the fuzzy theory is used to improve approximate inference. EFLSIM can operate automatically without human intervention. The magnetic test results convincingly demonstrate the ability of the new method to absorb and mimic human intelligence in assessing the degree of damage to a bridge structure. Many fuzzy theory applications have been applied to solve and simplify some reinforced concrete structural problems such as predicting concrete strength, optimizing the retrofit of fiber reinforced concrete for columns, predicting the shear strength of reinforced concrete beams reinforced with fiber reinforced polymers, finding the optimal concrete type for the grade design, and predicting the strength of concrete according to the concrete mix design [14-17]. This paper will provide definitions and analysis of important parameters of the corrosion process of reinforced concrete structures using Monte Carlo theory with consideration of randomness and fuzziness to assess the condition of the structure of the simple reinforced concrete beam. The obtained results are proposed as a scientific basis to evaluate the status of reinforced concrete structures, predict the service life of the constructions objectively and accurately, and help serve the maintenance and repair work in the life cycle of the structures.

## 2. Corrosion initiation time prediction

Corrosion initiation stage prediction will be based on chloride ion diffusion. Due to the concentration difference, chloride ions from the surface of the concrete structure will diffuse into the concrete to the reinforcement. The corrosion initiation phase will end when the chloride ion concentration at the reinforcement surface reaches the threshold of corrosive concentration.

From Fick's second law of diffusion:

$$\frac{\partial C(x,t)}{\partial t} = D \frac{\partial^2 C(x,t)}{\partial x^2} \quad (1)$$

where:

- C (x,t): chlorine concentration at depth x and time t;
- D: chlorine diffusion coefficient in concrete;
- x: thickness from the surface of the concrete;
- t: time.

In 1975, Crank [38] proposed a mathematical model for the diffusion process based on Fick's 2nd law. In case the diffusion coefficient is constant, surface chloride concentration in reinforcement from Equation 2.7 with boundary condition  $C_0 = C(0,t)$  (i.e. surface chloride content is constant) and initial condition the beginning  $C = 0$ ,  $x > 0$  and  $t = 0$ , is determined by:

$$C_x = C_s \left( 1 - \operatorname{erf} \left( \frac{x}{2\sqrt{K_c t}} \right) \right) \quad (2)$$

where:

- $C_x$ : chloride concentration at depth x;
- erf*: the error function;
- $C_s$ : is the chloride concentration at the concrete surface of the structure;
- $t$ : actual time;
- $x$ : is the depth from the concrete surface of the structure.
- $D$ : the chloride diffusion coefficient into the concrete.

The process of corrosion of reinforcement begins when  $C_x = C_{cr}$ , then  $x = h$  (thickness of the concrete cover) we have:

$$C_{cr} = C_s \left( 1 - \operatorname{erf} \left( \frac{h}{2\sqrt{K_c t}} \right) \right) \quad (3)$$

In 1996, A.Sara & E. Vesikari [37] proposed using a parabolic approximation for the error function ( $\operatorname{erfc}(z) = 1 - \operatorname{erf}(z) \approx$  when  $0 < z < 2$ ) to simplify the formula. (4.6) to :

The time of initiation of corrosion is rewritten as:

$$T_i = \frac{h^2}{4D} \left[ \operatorname{erf}^{-1} \left( \frac{C_s - C_{cr}}{C_s} \right) \right]^2 \quad (4)$$

where:

- $T_i$ : corrosion-initiation time (years);
- $h$ : thickness of concrete cover (cm);
- $D$ : chloride diffusion coefficient ( $\text{cm}^2/\text{year}$ );
- $C_{cr}$ : extreme chloride concentration at the time of corrosion initiation (% concrete weight);

$C_s$ : equilibrium chloride concentration at the concrete surface  
(% concrete weight).

In fact, the service life of constructions according to initiation of corrosion criteria is significantly higher than the results calculated by the above formula because chloride diffusion and surface chloride concentration are time-dependent factors.

### 3. Corrosion of reinforced concrete under the influence of fuzziness and randomness

The time when concrete begins to corrode depends on 4 factors: chloride diffusion coefficient, equilibrium chloride concentration at the concrete surface, limiting chloride concentration, and concrete cover [19]. In recent studies, critical chloride concentrations were considered to be normally distributed with mean and coefficient of variation (COV) of 0.027-0.045% and 0.05-0.296 (Enright and Frangopol 1998a; Stewart 2009; Stewart and Rosowsky 1998; Yanaka 2004). Surface chloride concentrations were modeled using a log-normal distribution with mean and COV ranges of 0.10-0.40% and 0.05-0.50, respectively (Vu and Stewart 2000). 2004) described the chloride diffusion coefficient as a normal distribution with mean and COV ranges of 0.32-2.58 cm<sup>2</sup>/year and 0.05-1.6, respectively. Concrete coating is affected by the build quality, are modeled according to a normal distribution or a lognormal probability distribution (Enright and Frangopol 1999a).

For reinforced concrete structures, typically bridge works, in reality, do not have a quality management system, so it is not possible to collect the exact statistical parameters of the four variables in the previous periods. These statistical parameters can be estimated based on design information and data for similar structures or as term variables from expert opinion. In these cases, the statistical parameters are considered to lie in a fuzzy range. The fuzzy random theory is used in this study to consider both types of the uncertainty of the four variables [19]. Therefore, four variables are assumed to be fuzzy random variables in the present study. The time of onset of corrosion for chloride ions is rewritten as:

$$\tilde{T}_l = \cup_{\alpha \in [0,1]} \alpha [T_{l\alpha}^-, T_{l\alpha}^+] = \frac{\tilde{h}^2}{4\tilde{D}} \left[ \text{erf}^{-1} \left( \frac{\tilde{C}_s - \tilde{C}_{cr}}{\tilde{C}_s} \right) \right]^2 \quad (5)$$

$$T_{l\alpha}^- = \frac{h_\alpha^{-2}}{4D_\alpha^+} \left[ \text{erf}^{-1} \left( 1 - \frac{C_{cr\alpha}^-}{C_{s\alpha}^+} \right) \right]^2 \quad (6)$$

$$T_{l\alpha}^+ = \frac{h_\alpha^{+2}}{4D_\alpha^-} \left[ \text{erf}^{-1} \left( 1 - \frac{C_{cr\alpha}^+}{C_{s\alpha}^-} \right) \right]^2 \quad (7)$$

where:

$[\ ]_\alpha^-$  and  $[\ ]_\alpha^+$ : infimum and supremum of variables;

$[\ ]$ : four variables (i.e., chloride diffusion coefficient, equilibrium chloride concentration at the concrete surface, critical chloride concentration, and concrete cover) affecting the corrosion initiation time.

Corrosion of reinforced concrete leads to a reduction in the diameter and cross-sectional area of the reinforcement. Based on Fick's law mentioned above on the diffusion of chloride ions, the time-varying region of the reinforcement steel is studied. The depth of corrosion is expressed as:

$$\tilde{p}(t) = \cup_{\alpha \in [0,1]} \alpha [p(t)_{I\alpha}^-, p(t)_{I\alpha}^+] = 0.3727R \left( 1 + \frac{27}{\tilde{f}_c - 13.5} \right)^{1.64} \frac{(t - \tilde{T}_I)^{0.71}}{\tilde{C}} \quad (8)$$

$$p(t)_{\alpha}^- = 0.3727R \left( 1 + \frac{27}{f_{c\alpha}^+ - 13.5} \right)^{1.64} \frac{(t - T_{I\alpha}^+)^{0.71}}{C_{\alpha}^+} \quad (9)$$

$$p(t)_{\alpha}^+ = 0.3727R \left( 1 + \frac{27}{f_{c\alpha}^+ - 13.5} \right)^{1.64} \frac{(t - T_{I\alpha}^+)^{0.71}}{C_{\alpha}^+} \quad (10)$$

where:

$\tilde{p}(t)$  : pit depth after t years (millimeters);

$\tilde{f}_c$  : concrete compressive strength (MPa);

$\tilde{h}$  : concrete cover (mm).

The upper and lower bounds of the reinforcement area are calculated as follows:

$$A_p(t) = \begin{cases} \frac{\pi D_0^2}{4} - A_1 - A_2, p(t) \leq \frac{\sqrt{2}}{2} D_0 \\ A_1 - A_2, \frac{\sqrt{2}}{2} D_0 \leq p(t) \leq D_0 \\ 0, p(t) > D_0 \end{cases} \quad (11)$$

where:

$D_0$ : initial diameter of the reinforcing bar:

$$A_1 = \frac{1}{2} \left[ \theta_1 \left( \frac{D_0}{2} \right)^2 - a \left| \frac{D_0 - p(t)^2}{D_0} \right| \right]$$

$$A_2 = \frac{1}{2} \{ \theta_2 p(t)^2 - a [p(t)^2 / D_0] \}$$

$$a = 2p(t) \sqrt{1 - \left| \frac{p(t)}{D_0} \right|}$$

$$\theta_1 = 2 \arcsin \left( \frac{a}{D_0} \right)$$

$$\theta_2 = 2 \arcsin \left( \frac{a}{2p(t)} \right)$$

Using the previously derived model and fuzzy random variable, the corrosion process according to the fuzzy variable and the random variable can be predicted. Experimental data are required to correct the input variables from which to calculate the life predictions of the structure.

#### 4. Experimental analysis of fuzziness and randomness affecting reinforcement corrosion and corrosion initiation time

In this study, the input parameters in the laboratory are used to calibrate the proposed fuzzy random corrosion model and validate its predictions. The input parameter is the typical type of

concrete commonly used in bridge works in Vietnam with expected strengths of 30 MPa (type C30) [36]. The initiate diameter of longitude reinforcing bars is 22 mm and the yield strength is 290 MPa.

**Table 1.** Statistical Parameters of Variables Affecting the Corrosion-Initiation Time

Parameters	Mean	Standard deviation	Coefficient of variation	Distribution
Concrete cover, $\tilde{h}$ (mm)	(1.028,1.078,1.128)	(0.0485,0.0505,0.0525)	-	Fuzzy normal
Equilibrium chloride concentration, $\tilde{C}_s$ (%)	(0.16,0.23,0.3)	-	(0.1,0.2,0.3)	Fuzzy lognormal
Critical chloride concentration, $\tilde{C}_{cr}$ (%)	(0.032,0.036,0.04)	-	(0.1,0.15,0.2)	Fuzzy lognormal
Chloride ion diffusion coefficient, $\tilde{D}$ (cm <sup>2</sup> /years)	(0.8,0.9,1.0)	-	(0.5,0.55,0.6)	Fuzzy lognormal
Initial diameter of reinforcement (mm), $\tilde{D}_0$	(0.95,1.00,1.05)	(0.0237,0.0247,0.0257)	-	Fuzzy normal
Concrete compressive strength on the 28 <sup>th</sup> day, $\tilde{f}_c$ (MPa)	(1.4262,1.5012,1.5762)	(0.2562,0.2662,0.2762)	-	Fuzzy normal

(Note: The three numbers in (...) are the infimum, the nonfuzzy value, and the supremum, respectively).

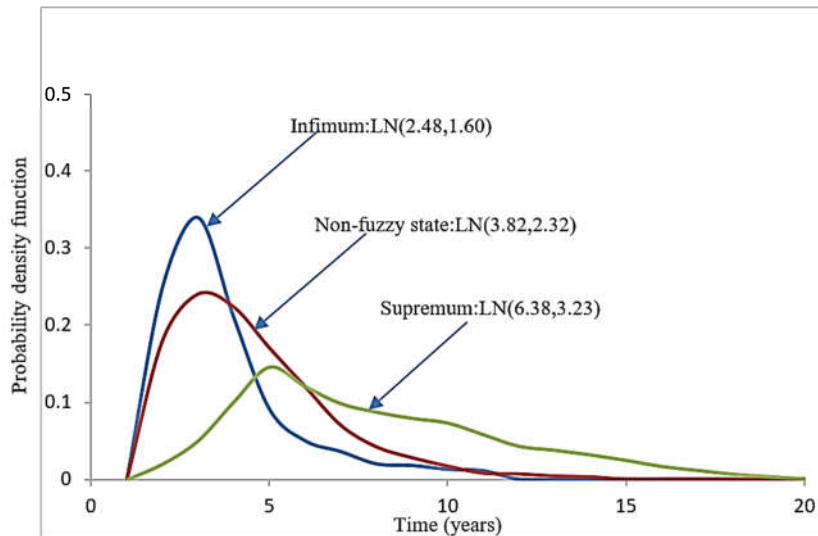


**Fig. 1.** The probability density function of corrosion-initiation.

Monte Carlo simulations were used to determine the mean, standard deviation and distribution function of the corrosion initiation time according to the statistical parameters in Table 1. In this study, ten thousand samples were used to ensure the accuracy of the simulation. Applying the formula (2) to determine the time of onset of corrosion combined with input parameters from the laboratory and in the field from which we can output a graph of the

probability density function of the time of corrosion. The average value of the time of initiation of corrosion in 3 states of maximum, non-opacity, and minimum is 2.48, 3.82, and 6.38 years, respectively. The coefficients of variation for the maximum, non-opaque and minimum states of the corrosion initiation time are respectively 1.60, 2.32 and 3.23.

And within the scope of this study, related to the long-term damage of the structure due to corrosion, the author only considers the assessment of the service life of a traffic structure made of reinforced concrete as the starting time. Corrosion of reinforcements in concrete due to chloride diffusion into concrete or more precisely time during which chloride concentration (C) at the surface of reinforcement reaches the critical value ( $C_{cr}$ ). The equation for calculating chloride concentration at the reinforcement surface is taken according to Fick's 2<sup>nd</sup> law (*RILEM 14 (2005) – A.Sara & E. Vesikari*).

## 5. Conclusions

Through this analytical paper, the use of random fuzzy modeling is proposed to simulate and predict the corrosion of reinforced concrete structures. The proposed method is a combination of randomness and opacity for the parameters related to the corrosion of reinforced concrete. From the normalization of the input parameters as fuzzy variables according to the law of random or normal distribution, we can infer the service life of the RC structures relatively accurately with a sufficiently large number of iterations. Several main conclusions can be drawn on the basis of the proposed study:

- The lack of information for a reinforced concrete structure is common, so it is difficult to get an accurate forecast of the life of the structure and assess the degree of corrosion of that structure.
- The fuzziness and randomness can be converted to a normal distribution or a logarithmic normal distribution, thereby giving the data to a mathematical framework to evaluate according to the mean and the variance.
- Simulation results show that all parameters can be approximated according to normal distribution or logarithmic distribution. For instance, the steel bar section area loss can be approximated using a lognormal distribution and the strength reduction can be approximated using the normal distribution.

The proposed study aims to model different uncertainties using fuzzy stochastic theory. This can be applied to health monitoring for bridge works, especially bridges that have been built for a long time, many test parameters have been lost. In addition, structural sustainability in terms of corrosion degradation is much more complex and needs to be investigated thoroughly. Future theoretical and experimental studies are needed to extend the proposed methodology to other complex failure types, such as fatigue, creep, and severe corrosion.

## References

1. Sarja and Vesikari, *Durability Design of Concrete Structures*, Architecture and Civil Engineering 7 (1996).
2. ACI Committee 201, "Proposed revision of: Guide to durable concrete", *ACI Material Journal* 1991, Vol. 88, No. 5, pp. 544-582, (1991).
3. Gopal Mitral<sup>1</sup>; Kamal Kant Jain<sup>2</sup>; and Bishwajit Bhattacharjee, *Condition Assessment of Corrosion Distressed Reinforced Concrete Buildings Using Fuzzy Logic*, *Journal of Performance of Constructed Facilities* (2010).
4. Saptarshi Sasmal, K. Ramanjaneyulu, S. Gopalakrishnan; and N. Lakshmana, *Fuzzy logic based condition rating of existing reinforced concrete bridges*, *Journal of Performance of Constructd Facilities* (2006).
5. J. Sobhani, A. A Ramezaninpour, *Modeling the corrosion of reinforced concrete structures based on the fuzzy systems*, CIVILCA (CD05-001),

6. Chen D., Mahadevan S., "Chloride-induced reinforcement corrosion and concrete cracking simulation", *Cement and Concrete Composites* 2008, Vol. 30, pp. 227-238.
7. Balaji Rao K, Anoop M B, Lakshmanan N, Gopalakrishnan S and Appa Rao, Risk-based remaining life assessment of corrosion affected reinforced concrete structural members. *J. Struct. Eng.* 31(1): 51–64 (2004).
8. Steven Chase, László Gáspár, Modeling the reduction in load capacity of highway bridges with age. *J. Bridge Eng. ASCE* 5(4): 331–336 (2000).
9. M B ANOOP\* and K BALAJI RAO, Performance evaluation of corrosion-affected reinforced concrete, Indian Academy of Sciences, (2016).
10. Anoop M B, Balaji Rao K and Lakshmanan, Safety assessment of austenitic steel nuclear power plant pipelines against stress corrosion cracking in the presence of hybrid uncertainties. *Int. J. Pressure Vessels Piping* 85(4): 238–247, (2008).
11. Corotision R B, Risk communication with generalized uncertainty and linguistics. *Structure Safety.* v.31: 113–117 (2009).
12. Shiraishi N and Furuta H, Reliability analysis based on fuzzy probability. *J. Eng. Mech. ASCE*, 109(6): 1445–1459 (2017).
13. Cheng M and Hoang N, Risk score inference for bridge maintenance project using evolutionary fuzzy least squares support vector machine. *J. Comput. Civ. Eng. ASCE* 28(3): 04014003(9) (2014).
14. Aktan A E, Ellingwood B R and Kehoe B, Performance-based engineering of constructed systems. *J. Struct. Engg. ASCE* 133(3): 311–323 (2007).
15. SOA Olawale1, OP Akintunde\*, MO Afolabi1 and OA Agbede, Fuzzy Logic Design Approach for A Singly Reinforced Concrete Beam; ISSN: 2754-4990; *Journal of Civil Engineering Research & Technology*, (10/1/2021).
16. Seyed Alireza Alavi, H. Naderpour, Application of Fuzzy Logic in Reinforced Concrete Structures, The Fourth International Conference On Soft Computing Technology In Civil, Structural And Environmental Engineering, (Sep/2015).
17. Cairns, J., Plizzari, G. A., Du, Y., Law, D. W., and Franzoni, C. "Mechanical properties of corrosion-damaged reinforcement." *ACI Mater. J.*, 102(4), 256–264 (2005).
18. Choe, D., Gardoni, P., Rosowsky, D., and Haukaas, T., "Probabilistic capacity models and seismic fragility estimates for RC columns subject to corrosion." *R liab. Eng. Syst. Saf.*, 93(3), 383–393 (2008).
19. Lei Wang; Yafei Ma; Jianren Zhang, and Yongming Liu, A.M.ASCE, Probabilistic Analysis of Corrosion of Reinforcement in RC Bridges Considering Fuzziness and Randomness, *Journal of Structural Engineering/ Volume 139 Issue 9 – (09/2013)*.
20. Choe, D., Gardoni, P., Rosowsky, D., and Haukaas, T., "Seismic fragility estimates for reinforced concrete bridges subject to corrosion." *Struct. Saf.*, 31(4), 275–283 (2009).
21. Dey, A., and Mahadevan, S., "Reliability estimation with time-variant loads and resistances." *J. Struct. Eng.*, 126(5), 612–620 (2000).
22. Du, Y. G., Clark, L. A., and Chan, A. H. C., "Residual capacity of corroded reinforcing bars." *Mag. Concr. Res.*, 57(3), 135–147 (2005).
23. Englund, S., and Sørensen, J. D., "A probabilistic model for chloride-ingress and initiation of corrosion in reinforced concrete structures." *Struct. Saf.*, 20(1), 69–89 (1998).
24. Enright, M. P., and Frangopol, D. M., "Probabilistic analysis of resistance degradation of reinforced concrete bridge beams under corrosion." *Eng. Struct.*, 20(11), 960–971 (1998a).
25. Enright, M. P., and Frangopol, D. M., "Service-life prediction of deteriorating concrete bridges." *J. Struct. Eng.*, 124(3), 309–317 (1998b).
26. Enright, M. P., and Frangopol, D. M., "Condition prediction of deteriorating concrete bridges using bayesian updating." *J. Struct. Eng.*, 125(10), 1118–1125 (1999a).
27. Enright, M. P., and Frangopol, D. M., "Reliability-based condition assessment of deteriorating concrete bridges considering load redistribution." *Struct. Saf.*, 21(2), 159–195 (1999b).
28. Ghosh, J., and Padgett, J. E., "Aging considerations in the development of time-dependent seismic fragility curves." *J. Struct. Eng.*, 136(12), 1497–1511, (2010).
29. Higgins, C., and Farrow, W. C., "Tests of reinforced concrete beams with corrosion-damaged stirrups." *ACI Struct. J.*, 103(1), 133–141, (2006).

30. Hong, H. P. "Assessment of reliability of ageing reinforced concrete structures." *J. Struct. Eng.*, 126(12), 1458–1465, (2000).
31. Jiang, Q., and Chen, C. H., "A numerical algorithm of fuzzy reliability." *Reliab. Eng. Syst. Saf.*, 80(3), 299–307, (2003).
32. Kwakernaak, H., "Fuzzy random variables. I. Definitions and theorems." *Inf. Sci.*, 15(1), 1–29, (1978).
33. Liu, Y., Qiao, Z., and Wang, G., "Fuzzy random reliability of structures based on fuzzy random variables." *Fuzzy Sets Syst.*, 86(3), 345–355, (1997).
34. Liu, Y., and Weyers, R. E., "Modeling the time-to-corrosion cracking in chloride contaminated reinforced concrete structures." *ACI Mater. J.*, 95(6), 675–680, (1998).
35. Malumbela, G., Alexander, M., and Moyo, P., "Variation of steel loss and its effect on the ultimate flexural capacity of RC beams corroded and repaired under load." *Construct. Build. Mater.*, 24(6), 1051–1059, (2010).
36. Tran The Truyen, Le Quang Vu, Ho Xuan Ba, Service life estimation of high performance reinforced concrete structures in considering the damage of concrete cover, Proceedings of the International Conference EASEC-14, HCM City, 1/2016.
37. Beeby A W Concrete in the Oceans – Cracking and Corrosion, Technical Report No. 1, CIRIA/UEG, Cement and Concrete Association, Dept of Energy, UK, 1978.
38. D. Whiting - American Concrete Institute SP-82-25, pp 501-524 (1981).

# Prediction of the cbl of the SDTC with tubular cross-section using Rayleigh-Ritz method

*Thi-Quynh Nguyen, and Thanh-Tung Nguyen Thi*

Department of Civil Engineering, Vinh University, Vinh, 461010, Vietnam

*Email: quynhntkxd@vinhuni.edu.vn*

**Abstract.** This paper proposes a procedure to determine the Critical Buckling Load (CBL) of the symmetry double tapered steel column (SDTC) with tubular cross-section using Rayleigh-Ritz methods. The computer program based on the Rayleigh-Ritz method and MATLAB has been presented. The computer program has been verified with previously published results and obtained reliably. An investigation of CBL of SDTS columns with changes in column length and outer diameters has been done. Finally, the regression formulas were proposed based on the tool Trendline options/Polynomial of Microsoft Excel 365 software can be helped the designer to predict the critical buckling load of the symmetry double tapered column with tubular cross-section.

**Keywords:** Rayleigh-Ritz Method; Prediction formula; Total potential energy; Euler's critical load; SDTS. columns.

## 1. Introduction

The tapered steel columns have been popularly used in civil engineering structures. Critical buckling load (CBL) is the most important parameter in designing this steel column. In 1961, Timoshenko and Gere proposed a solution for calculating the elastic buckling load of steel columns, in which this solution is similar to the Euler approach using a modified factor related to the maximum and minimum inertia moments of the cross-sections [1]. Lee et al. [2] developed a formula to calculate the critical load of tapered columns using the minimum cross-section with an equivalent factor. A similar approach was studied by Hirt and Crisinel [3] using an equivalent cross-section. Marques et al. [4] proposed a method for determining the critical buckling load of tapered steel columns. A study on the critical load of tapered steel columns using the differential equation approach combined with Newton Raphson iteration was conducted by Dang and Nguyen [5]. Recently, Nguyen and Nguyen [6] used artificial neural networks to predict the critical loading capacity of tapered I-section steel columns. The aforementioned studies focused on the critical load of tapered steel columns; however, the axial loading capacity of the double tapered steel column is different because of the shape. Moreover, the current design codes such as ASCE, Eurocode 3, BS and TCVN 5575 suggest considering the minimum cross-section with a multiplying coefficient when designing the tapered steel columns. However, this suggestion has caused a discrepancy in design practices [7].

So far, the determination of the CBL of the symmetric double tapered steel (SDTS) column with tubular cross-section (TC) was used approximate methods or the conversion method. This paper aims to apply Rayleigh-Ritz Method for predicting the CBL of the SDTS column with the tubular cross-section. The computer program based on the Rayleigh-Ritz method and MATLAB will be presented. The computer program will be verified with previously published results and obtained reliably. An investigation of CBL of SDTS columns with changes in column length and outer diameters will be done. Finally, the regression formulas have been proposed based on the tool Trendline options/Polynomial of Microsoft Excel 365 software can be helped the designer to predict the critical buckling load of the symmetry double tapered column with tubular cross-section.

## 2. Theoretical background

### 2.1. Euler's critical load

The Euler's critical load was proposed in 1757 by the Swiss mathematician Leonhard Euler. According to [8] the relationship between bending moment and the equation of elasticity  $v(x)$  was expressed the form differential equation as follows.

$$-Pv(x) = M(x) = EI \frac{d^2v(x)}{dx^2} \quad (1)$$

or

$$\frac{d^2v(x)}{dx^2} = \frac{P}{EI} v(x) \quad (2)$$

Where,  $E$  is elastic modulus;  $I$  is area moment of inertia of the cross section;  $M(x)$  is the variation of the bending moment along the column axis;  $x$  coordinates of the column axis.

### 2.2. Rayleigh-Ritz methods

The Rayleigh-Ritz method has been built based on elastic strain potential energy of the structure system is in the deflected state. The critical buckling load was determined by conditions of deflected state, the formula has the form as.

$$\delta U^* = \delta(U + U_p) = 0 \quad (3)$$

The selection solution of the numeric string. It has the form as

$$y = \sum_{i=1}^p a_i g_i(z) \quad (4)$$

Where,  $p$  are any integer;  $a_i$  are unknown coefficients;  $g_i(z)$  are the independent functions, which must satisfy the boundary condition

From deformation curve perform as as a numeric string. The elastic strain potential energy has the following.

$$U^* = U_0^* + \delta U - \delta T \quad (5)$$

Where,  $\delta U = \sum \int \frac{M^2}{2EI} ds$  is the variability of the elastic strain potential energy;  $\delta T = \sum_{k=1}^m P_k \delta_{P_k}$  is the variability of work done by an external force.

Formulate equations of total potential energy to determine  $a_i$ . It has the form as.

$$dU^* = \sum_{i=1}^p \frac{\partial U^*}{\partial a_i} da_i \quad (6)$$

Because  $a_i$  are independent parameters, conditions of the formula (3) must be  $da_i = 0$

$$\frac{\partial U^*}{\partial a_i} = 0 \quad (7)$$

Based on equation (7) we get a homogeneous system of algebraic equations with  $a_1, a_2 \dots$  are variables. The CBL of the SDTS column with the tubular cross-section will be determined by solving the determining coefficients of the homogeneous system of the algebraic equations.

### 3. Using Rayleigh-Ritz method for predicting CBL of SDTS columns with TC

This study considers SDTS columns with the tubular crosssection, as shown in Fig. 1. Considering SDTSC with the tubular cross-section as shown in Fig. 1. The area moment of inertia of the variable sections  $I = I_0 \frac{4x(H-x)}{H^2}$ , where  $I_0 = 0.05D^4 \left(1 - \frac{D}{d}\right)$  is the area moment of inertia of the maximum cross-section of variable sections. It should be noted that  $D$  and  $d$  are the outer and inner diameters of the column;  $H$  is the column length.

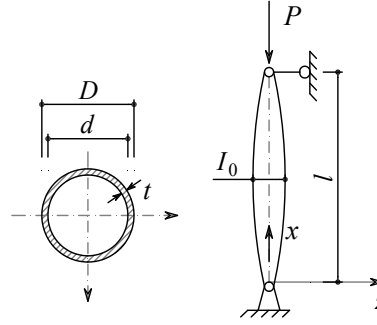


Fig. 1. Both ends pinned column and cross-section.

The solution of the numeric string is  $y(z) = az(l - z)$  with the solution conditions of existence. Application the Rayleigh-Ritz method for predict to the CBL of the SDTSC with the tubular cross-section.

The selection solution of the numeric string is  $y(z) = az(l - z)$ . From solution of the numeric string, we get:

$$\dot{y}(z) = a(l - 2z) \text{ và } \ddot{y}(z) = -2a \quad (8)$$

Elastic strain potential energy of the structure has the form as.

$$\delta U = \int \frac{M^2 ds}{2EI} = \frac{1}{2} \sum \int_0^H EI \dot{y}(z)^2 dz \quad (9)$$

$$\delta U = \frac{1}{2} EI_0 \left( 8a^2 H - \frac{16a^2 H}{3} \right) = \frac{4EI_0 a^2 H}{3} \quad (10)$$

Variability of work done by an external force, it has form

$$\delta T = \frac{P}{2} \int_0^H (\dot{y})^2 dz = \frac{P}{2} \int_0^H (a(l - 2z))^2 dz \quad (11)$$

$$\delta T = \frac{P}{2} a^2 \left( H^2 z - 2Hz^2 + \frac{4}{3} z^3 \right) \Big|_0^H = \frac{PH^3 a^2}{6} \quad (12)$$

Total potential energy has determined:  $U^* = U_0^* + \delta U - \delta T$ , therefore.

$$\delta U^* = U_0^* + \frac{4EI_0 a^2 H}{3} - \frac{PH^3 a^2}{6} \quad (13)$$

The extreme conditions of total potential energy:

$$\frac{\partial(\delta U^*)}{\partial a} = 0 \quad (14)$$

The equation (14) is extreme conditions of total potential energy. We apply the Rayleigh-Ritz method for calculating the CBL of the SDTS column with the tubular cross-section, which is presented in [8] for solving the critical buckling load of the symmetrically double tapered steel column, as shown in Fig. 1. The calculated results of the Rayleigh-Ritz and Bubnov - Galerkin methods are shown in Table 1. It can be found that the difference between two methods is very trivial error of 0.15%, implying the reliability of Rayleigh-Ritz method.

**Table 1.** Comparison of calculated critical buckling load between different solutions

Program computer		Ref. [8]	Error (%)
The solution of the numeric string	Pcr		
$y(z) = az(l - z)$	$8.00 \frac{EI_0}{H^2}$	$8.015 \frac{EI_0}{H^2}$	0.150

#### 4. Investigates of CBL of SDTS columns with changes of outer diameters

In this section, the study was investigating of CBL of SDTS columns with changes of outer diameters. Where changes of outer diameters intervals D-10 to D-30 and  $t = D - d = 15 \text{ mm}$ . The data of investigates of CBL of SDTS columns are shown in Table 2.

**Table 2.** Data of changes of the outer diameters

Sample	Outer diameters mm	Elastic modulus GPa	Column length m	Pcr kN
D-10	100	208.10	4.0	510.754
D-12	120	208.10	4.0	1059.100
D-14	140	208.10	4.0	1962.114
D-16	160	208.10	4.0	3347.279
D-18	180	208.10	4.0	5361.694
D-20	200	208.10	4.0	8172.068
D-22	220	208.10	4.0	11964.725
D-24	240	208.10	4.0	16945.600
D-26	260	208.10	4.0	23340.243
D-28	280	208.10	4.0	31393.816
D-30	300	208.10	4.0	41371.094

Table 2 shows that changes of outer diameters intervals from D-10 to D-30 and  $t = D - d = 15 \text{ mm}$ , The value received of CBL of SDTS columns was increased from 510.754 to 41371.094 kN (equivalent to 98.77%), respectively. The obtained results show that the outer diameters have a great influence on the CBL of SDTS columns.

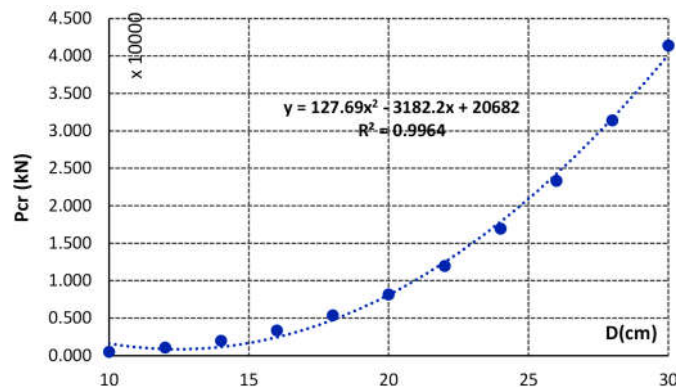


**Fig. 2.** The relationship between outer diameters and the CBL of SDTS columns.

Fig 2 shows the CBL of SDTS columns was increased. The relationship between changes of outer diameters and the CBL of SDTS columns has been regressed according to polynomial function 2 order, with  $R^2 = 0.9964$ . The regression formula and  $R^2$  were made based on the tool Trendline options/Polynomial of Microsoft Excel 365 software. The regression formula can be helped the designer to predict the critical buckling load of the symmetry double tapered column with tubular cross-section.

### 5. Investigates of CBL of SDTS columns with changes of columns length

The study investigates of CBL of SDTS columns with changes of columns length. Where changes of columns length intervals H-20 to H-40 and  $t = D - d = 15 \text{ mm}$ . The data of investigates of CBL of SDTS columns are shown in Table 3.

Table 3 shows that changes of columns length intervals from H-20 to H-40 and  $t = D - d = 15 \text{ mm}$ , The value received of CBL of SDTS columns was reduced from 32688.272 to 8172.068 kN (equivalent to 75.00%), respectively. The obtained results show that the column length increase has decreased the CBL of SDTS columns.

**Table 3.** Data of changes of the column length

Sample	Outer diameters mm	Elastic modulus Gpa	Column length m	Pcr kN
H-20	200	208.10	2.0	32688.272
H-22	200	208.10	2.2	27015.100
H-24	200	208.10	2.4	22700.189
H-26	200	208.10	2.6	19342.173
H-28	200	208.10	2.8	16677.690
H-30	200	208.10	3.0	14528.121
H-32	200	208.10	3.2	12768.856
H-34	200	208.10	3.4	11310.821
H-36	200	208.10	3.6	10088.973
H-38	200	208.10	3.8	9054.923
H-40	200	208.10	4.0	8172.068

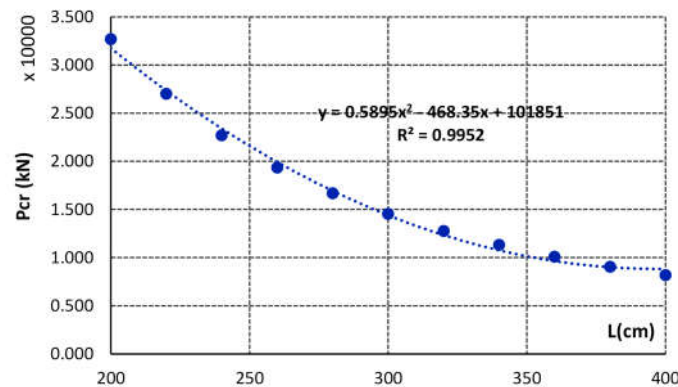


**Fig. 3.** The relationship between column length and the CBL of SDTS columns.

Fig. 3 shows the CBL of SDTS columns was decreased. The relationship between changes of column length and the CBL of SDTS columns has been regressed according to polynomial function 2 order, with  $R^2 = 0.9952$ . The regression formula and  $R^2$  were made based on the tool

Trendline options/Polynomial of Microsoft Excel 365 software. The regression formula can be helped the designer to predict the critical buckling load of the symmetry double tapered column with tubular cross-section.

## 6. Conclusions

This paper has presented the algorithm and built a computer program to predict the critical buckling load of the symmetry double tapered column with tubular cross-section based on the Rayleigh-Ritz method and MATLAB. The algorithm and computer program has been verified with previously published results and obtained reliably. Specifically, the paper has been done.

- A procedure based on the Rayleigh-Ritz method and MATLAB was proposed to calculate the critical buckling load of the symmetry double tapered column with tubular cross-section.
- Had investigated of CBL of SDTS columns with changes in columns length and outer diameters
- Had built the regression formula and  $R^2$  were made based on the tool Trendline options/Polynomial of Microsoft Excel 365 software. The regression formula can be helped the designer to predict the critical buckling load of the symmetry double tapered column with tubular cross-section.

## References

1. J. M. Gere and S. P. Timoshenko, 1961, *Theory of elastic stability*.
2. G. C. Lee, M. Morrell, and R. L. Ketter, "Design of Tapered Members," STATE UNIV OF NEW YORK BUFFALO DEPT OF CIVIL ENGINEERING1971, Accessed on.
3. M. A. Hirt and M. Crisinel, 2005, *Charpentes métalliques: conception et dimensionnement des halles et bâtiments*. PPUR presses polytechniques.
4. L. Marques, A. Taras, L. S. da Silva, R. Greiner, and C. Rebelo, 2012, "Development of a consistent buckling design procedure for tapered columns," *Journal of Constructional Steel Research*, vol. 72, pp. 61-74.
5. X.-H. Dang and T.-H. Nguyen, 2018, "Reliability assessment of buckling strength for tapered columns of steel portal frames with flexible joint of beam - column " (in en), *proceedings of the international conference on the 55th anniversary of establishment of Vietnam institute for building science and technology*.
6. T.-H. Nguyen, N.-L. Tran, and D.-D. Nguyen, 2021, "Prediction of Critical Buckling Load of Web Tapered I-Section Steel Columns Using Artificial Neural Networks," *International Journal of Steel Structures*, pp. 1-23.
7. N. Q. V, "Report on research results," Hanoi University of Civil Engineering2007, Accessed on.
8. L. T. Trinh and Đ. V. Binh, 2002, *Stability structures*. Science and Technics Publishing House.

# Causal Diagram of Project Management Knowledge Areas in Construction Projects

*Le Dinh Thuc<sup>1</sup>, Nguyen Quang Huy<sup>1</sup> and Nguyen Minh-Thu<sup>2</sup>*

<sup>1</sup> Campus in Ho Chi Minh City, University of Transport and Communications, Ho Chi Minh City, Vietnam

<sup>2</sup> Department of Civil Engineering, Vinh University, 182 Le Duan Vinh City, Vietnam

*Email: thucl\_d\_ph@utc.edu.vn*

**Abstract.** This paper aims to propose a causal relationship of project management in construction projects in Vietnam. A literature review process was conducted to identify fourteen project management knowledge areas. The questionnaire survey was sent to a group of five experts who had many experiences regarding construction projects in Vietnam. The collected data was applied to construct a cause-and-effect model for managing construction projects effectively by the fuzzy DEMATEL method. The finding indicated integration management, risk management, procurement management, stakeholder management, safety management, and claims management are effect factors that influence the affected group, namely, scope management, schedule management, cost management, quality management, human resource management, communication management, environmental management, and financial management. This evaluation model helps the practitioner insight understanding the causal relationship in project management. From which, he/she might propose strategies for improving the project management effectively.

**Keywords:** project management, Knowledge areas, Construction industry, Fuzzy DEMATEL.

## 1. Introduction

The construction industry maintains high risks and complexity [1]. They contain many challenges which need to be overcome for meeting the ultimate goals of a project [2]. Therefore, project management plays an important role to handle complicated issues in the construction industry in developing countries. Project management is carried out via the sufficient integration of the management knowledge areas for project management. A knowledge area is an aspect in project management defined by its knowledge requirements. The knowledge areas might impact one or many phases over the project life cycle [3]. Hence, considering the internal relationship of the knowledge areas is necessary for assuring success in construction project management [2]. Over two decades, assessment of the success in project management was exploited in the construction industry [4]. These studies mainly concentrated on key performance indicators (KPI) in project management, such as cost, time, quality, satisfaction, and safety [5,6,7,8,9,10]. Few studies interest the relationship of the project management knowledge areas (PMKAs). Therefore, this study aims to construct a causal diagram of PMKAs in construction projects in Vietnam.

This study is arranged as follows: Section 2 describes the literature review regarding project management knowledge areas. The fuzzy DEMATEL approach is presented in section 3. Section 4 shows the result of data analysis and discussion. Finally, section 5 is presented the conclusion and recommendations.

## 2. Literature review

Project management sets toward planning and control regarding on-time completion, within budget, and performance indicators [11,12]. Brown and Adam [13] considered time, cost, and quality as the empirical outputs for measuring the efficiency of building project management. However, ensuring an effective project performance not only relies on time, cost, and quality. A

project manager should comprehensively consider the impact of project management on project success via 14 knowledge areas which adopted by [2,3], including project integration management, scope management, schedule management, cost management, quality management, human resource management, communications management, risk management, procurement management, stakeholder management, safety management, environmental management, financial management, and claim management.

In the research of Demirkesen and Ozorhon [2], the authors used Structural Equation Modeling (SEM) technique for considering the impact of fourteen knowledge areas on project management performance in the construction industry. Unegbu et al. [14] constructed a relationship between project performance and nine project management knowledge areas in construction projects in Nigeria.

However, most of the previous studies mainly focused on one knowledge area for construction project management. There are few articles that interest the causal relationship between knowledge areas for managing projects effectively. Indeed, it is very difficult to organize and control the knowledge areas if the project managers do not carefully consider the mutual impact of factors in a construction project. Therefore, this research might bridge this gap by proposing a causal relationship in construction project management with the fuzzy DEMATEL application.

### 3. Research methodology

This study develops a causal diagram of PMKAs to assure the effectiveness of project performance in the Vietnamese construction industry. First, the pair-wise comparisons of 14 PMKAs are utilized to measure the mutual influence level rely on four scales from 0 to 4. Two main questions are raised to interviewees in the questionnaire survey: (1) Does the knowledge area (A) influence the knowledge area (B)? Which level? In contrast, (2) Does the knowledge area (B) influence the knowledge area (A)? Which level? Then, data will be obtained by interviewing experts who had many experiences involved in construction projects. Finally, the fuzzy DEMATEL application is used to develop the objective of this study (see Fig.1).

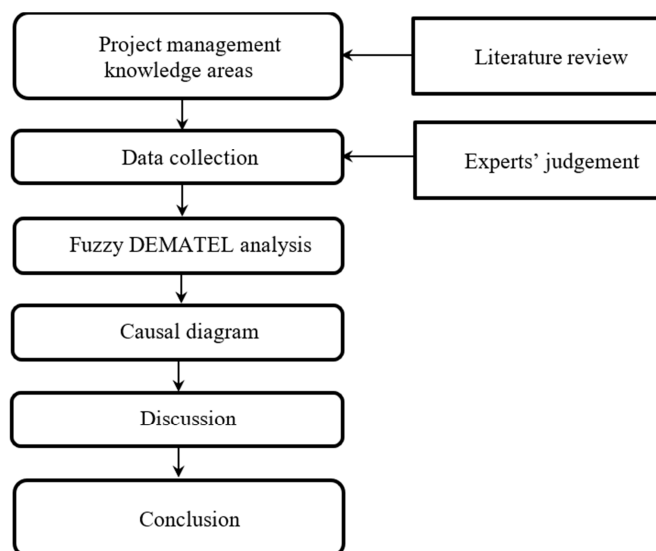


Fig. 1. Research methodology.

## 4. Data analysis

### 4.1. Questionnaire survey

In this study, fourteen evaluation factors are utilized and symbolized as follows: Integration management(A1), scope management (A2), schedule management (A3), cost management (A4), quality management (A5), human resource management (A6), communication management (A7), risk management (A8), procurement management (A9), stakeholder management (A10), safety management (A11), environmental management (A12), financial management (A13), claims management (A14). The fuzzy DEMATEL questionnaire was organized into three parts: Part 1 explained the definition of fourteen knowledge areas, which helped easier to understand for the respondents. Part 2 compared the mutual influence between each of pair factors via scores of 0, 1, 2, 3, 4 with 0="no influence", 1="very low influence", 2="low influence", 3="high influence", and 4="very high influence". The final part is the personal information of experts.

### 4.2. The fuzzy DEMATEL application

This study was interviewed a group of five experts who had many experiences regarding construction projects in Vietnam. The collected data was applied to construct a causal model for calculating project management performance by the fuzzy DEMATEL method. The results of analyzed data are presented in Table 1 and Figure 2.

Table 1 indicated the most five important knowledge areas for successful managing in construction projects, namely cost management (A4) (D+R=8.101), quality management (A5) (7.841), schedule management (A3) (7.815), financial management (A13) (7.570), and procurement management (A9) (6.757). Among them, cost, quality, schedule, and financial management are the affected group with (D-R) scores of -0.271, -0.097, -0.087, and -0.044, respectively, they are easily impacted by other factors. In fact, the owner and contractors face several difficulties from cost overrun and delay in a construction project in developing countries. Labours and project teams need to increase the production performance, which is easy to mistake and reworks. From which, the project quality can be affected. Therefore, cost, quality, and schedule management played a significant role in the failure or success of construction projects in these countries.

**Table 1.** The prominence and relation axis (D+R; D-R) for cause-and-effect group

Code	R	D	D+R	D-R
A1	2.209	2.264	4.473	0.055
A2	2.487	2.460	4.947	-0.027
A3	3.951	3.864	7.815	-0.087
A4	4.186	3.915	8.101	-0.271
A5	3.969	3.872	7.841	-0.097
A6	3.401	3.353	6.754	-0.048
A7	2.837	2.678	5.515	-0.159
A8	3.068	3.324	6.392	0.256
A9	3.356	3.401	6.757	0.045
A10	3.231	3.299	6.530	0.068
A11	2.984	3.022	6.006	0.038
A12	2.302	2.294	4.596	-0.008
A13	3.807	3.763	7.570	-0.044
A14	1.963	2.242	4.205	0.279

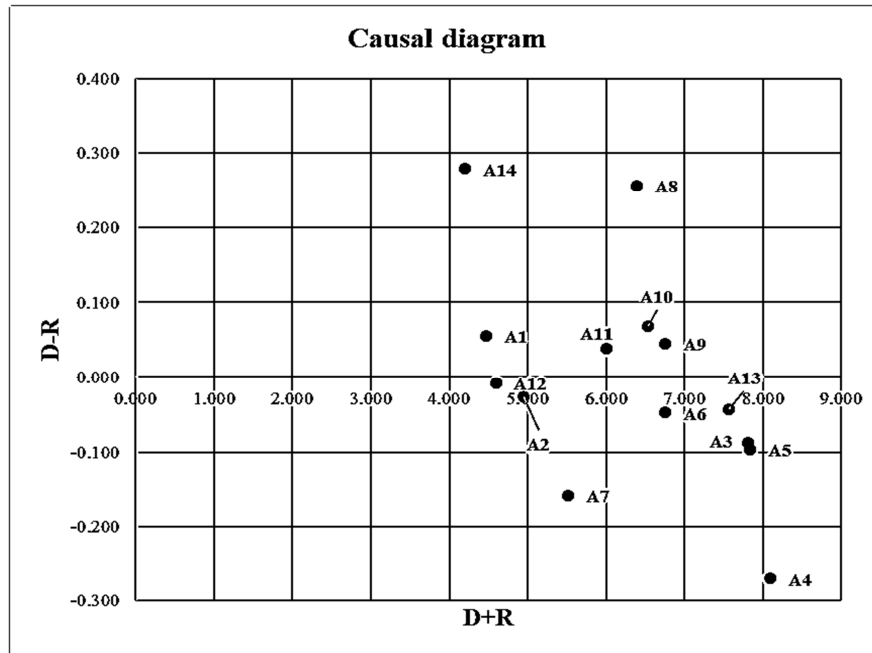


Fig. 2. Causal diagram of PMKAs.

Additionally, the experts noticed that stakeholder, integration, procurement, safety, claim, and risk management are considered as the cause factors with (D-R) scores of 0.068, 0.055, 0.045, 0.038, 0.279, and 0.256, respectively. These factors contribute to the success or failure of a construction project by their influence on the cost, time, and quality of that project. For instance, integration management plays an important role in the project management output, such as time, cost, and quality since effective project management begins from the integration of organized processes within a construction project. It ensures good coordination among project activities. Rowlinson and Cheung [15] asserted that the relationship management between the project's participants is essential for enhancing the project management performance and client satisfaction. Besides, an effective procurement process in the complex context of the construction environment impacts on meeting good outcomes and the overall objectives in any construction project [16]. On another aspect, a construction project is very complex at any phase of a project life-cycle due to containing various risks and hazards. If occurring, they can impact quality, time, cost, environment, scope, and financial management. Thus, risk management and safety management are necessary for construction projects. Finally, claim management might influence human resources management and communication management when construction claims consider as the result of various reasons as contract price, employee skill, lack of work, and sharing information between stakeholders [17]. Therefore, claims management is also a significant factor for successful project management.

## 5. Conclusion

The success of project management has been associated with the outcome of the project. Therefore, assuring effective project management performance is essential for a construction project. This paper aims to propose a causal relationship regarding fourteen knowledge areas in

project management. The result of the fuzzy DEMATEL method expressed that project integration, risk, procurement, stakeholder, safety, and claim management were the knowledge areas that impact scope, schedule, cost, quality, human resource, communication, environmental, and financial management belongs to the effect group. Besides, the most five important KAs in construction project management namely cost, quality management, schedule, financial, and procurement management. Based on the research results, the following recommendations are provided for improving project management performance as follows:

- Based on the impact of project integration, risk, procurement, stakeholder management, safety, and claim management, the project managers need to concentrate on these KAs for mitigating the negative influence to other areas.
- Based on the effect of scope management, schedule, cost, quality, human resource, communication, environmental, and financial management, the project managers try to control and improve the positive results for project management.

This study contains several limitations. First, a small group of experts has not ensured the validity of the research yet. Second, no case study has been conducted for illustrating this proposed framework. However, this evaluation model helps the practitioner insight understanding of the causal relationship of knowledge areas in construction project management in developing countries. From this, the project manager might apply this model to organize, manage, and control a specific project for improving the effectiveness of project management.

## References

1. Yiu, N.S.N., Chan, D.W.M., Shan, M., Sze, N.N. Implementation of safety management system in managing construction projects: Benefits and obstacles. *Safety Science* 117, 23–32 (2019).
2. Demirkesen, S., Ozorhon, B. Measuring project management performance: Case of construction industry. *Engineering Management Journal* 29(4), 258–277 (2017).
3. PMI: A guide to the project management body of knowledge. Sixth Edn. Project Management Institute, USA (2017).
4. Yang, H., Yeung, J.F.Y., Chan, A.P.C., Chiang, Y.H., Chan, D.W.M. A critical review of performance measurement in construction. *Journal of Facilities Management* 8(4), 269–284 (2010)
5. Cox, R.F., Issa, R.R.A., Ahrens, D. Management's perception of Key Performance Indicators for construction. *Journal of Construction Engineering and Management* 129 (2), 142-151 (2003).
6. Chan, A.P.C., Chan, A. P.L. Key Performance Indicators for measuring construction success. *Benchmarking: An International Journal* 11(2), 203-221 (2004).
7. Bassioni, H.A., Price, A.D.F., Hassan, T.M. Performance measurement in construction. *Journal of Management in Engineering* 20(2), 42-50 (2004).
8. Yeung, J.F.Y., Chan, A.P.C., Chan, D.W.M. Developing a Performance Index for relationship-based construction projects in Australia: Delphi study. *Journal of Management in Engineering* 25(2), 59-68 (2009).
9. Raisbeck, P., Duffield, C., Xu, M. Comparative performance of PPPs and traditional procurement in Australia. *Construction Management and Economics* 28 (4), 345-359 (2010).
10. Liu, J., Love, P.E.D., Sing, M.C.P., Smith, J., Matthews, J. PPP Social Infrastructure Procurement: Examining the Feasibility of a Lifecycle Performance Measurement Framework. *Journal of Infrastructure Systems* 23(3), 04016041 (2017).
11. Munns, A.K., Bjeirmi, B.F. The role of project management in achieving project success. *International Journal of Project Management* 14 (2), 81-87 (1996).
12. Alashwal, A.M., Fareed, N.F., Al-Obaidi, K.M. Determining Success Criteria and Success Factors for International Construction Projects for Malaysian Contractors. *Construction Economics and Building*, 17(2), 62-80 (2017).
13. Brown, A., Adams, J. 2000. Measuring the effect of project management on construction outputs: a new approach. *International Journal of Project Management*, 18(5), 327-335 (2000).

14. Unegbu, C.O., Yamas, D.S., Asabe, B.D. An investigation of the relationship between project performance measures and project management practices of construction projects for the construction industry in Nigeria. *Journal of King Saud University - Engineering Sciences*, (2020)
15. Rowlinson, S., Cheung, Y.K.F. Stakeholder management through empowerment: modelling project success. *Construction Management and Economics* 26(6), 611-623 (2008).
16. Araujo, M.C.B., Alencar, L.H. Mota, C.M.M. Project procurement management: A structured literature review. *International Journal of Project Management* 35(3), 353-377 (2017).
17. Seo, W., Kang, Y. Performance indicators for the claim management of general contractors. *Journal of Management in Engineering* 36(6), 04020070 (2020).

# Overview of causes of wheel rutting on some national highways in Viet Nam

*Trong Cuong Vo<sup>1</sup> and Thu Hien Nguyen Thi<sup>1</sup>*

<sup>1</sup> Department of Civil Engineering, Vinh University

*Email: cuongvqc@gmail.com*

**Abstract.** The cause of wheel rutting can come from a single cause, but sometimes it is a combination of many causes at the same time. With the aim of giving an overview of the phenomenon wheel rutting, this article is important on presenting in turn: the reality of wheel rutting on some national highways; classify the main groups of causes and go into some specific causes; Finally, a summary of the causes is listed.

**Keywords:** wheel ruts, asphalt concrete, road structures, highways.

## 1. Introduction

Recently, the phenomenon of premature deterioration of asphalt concrete pavement damage in the form of rutting is quite common. This problem is raising a concern of public opinion. Continuously, information about the subsidence of the wheel tracks on National Highway 5, the subsidence of the road surface of Thanh Tri Bridge, the subsidence on the East-West Highway, National Highway 18, National Highway 1 has appeared in many newspapers and online newspapers, creating interest attention not only of professionals, but also of social classes. There have been many conferences, seminars and articles analyzing the causes of wheel ruts, different opinions, and in-depth views on each area.

Due to the characteristics of traffic works being stretched and located in different geological and climatic regions, constructed by contractors with different qualifications, different exploitation and operation, the same streak phenomenon may occur rutting, but the cause is very different for each Km. With the goal of giving an overview of the causes of wheel ruts, the author wishes to put the possible causes of wheel ruts side by side to help engineers and experts not to miss out while driving. Analysis and treatment of wheel rutting.

## 2. Actual situation of wheel ruts

Recently, on some important national highways, the phenomenon of wheel rutting has occurred (referred to as wheel ruts for short), that is the phenomenon of subsidence at the wheel track and rise on the side, the cross section in this lane is wavy (Figure 1).



**Fig. 1.** The ruts of wheel tracks on National Highway 1, section Vinh - Ha Tinh [1].

The rut causes danger to vehicles and when it rains, the water will condense causing loss of control when the vehicle is traveling at high speed. According to Vietnamese regulations (According to TCN211-06): How to measure: Use a 1.22 m ruler to place the mark horizontally; Measure one place every 7.5 m and then take the average value for each segment. The average depth of the mark is 6-13 mm: light; 13-25 mm: medium and >25 mm: heavy. In fact, measured at National Highway 1, Vinh - Ha Tinh section, the subsidence in many sections is larger than 2.5 cm (Figure 2). According to the above classification, our ruts are all in the form of a high level of danger.



**Fig. 2.** Depth measurement of ruts at National Highway 1 section Vinh-Ha Tinh [1].

- The phenomenon of wheel tracks occurs over a wide geographical area from the South to the North, in many different climates and natural conditions: National Highway 1, National Highway 3, Highway 5, Highway 7.

- Along the National Highway 1 in the north, the Ha Noi - Lang Son section; Phu Ly - Ha Nam; The section through Ninh Binh (which has just been renovated and upgraded and has not yet handed over the warranty period), the road surface is also scattered with some ruts along the wheel tracks.

- The deeper into the central region, the more common the phenomenon of subsidence appears, many pieces of plastic surface drift, forming undulating "waves". On NH1 section Thanh Hoa - Thua Thien Hue, about 70 km (accounting for 13% of the length of the route) is "buffaloed", in which the heaviest damage is concentrated in the Vinh - Dong Ha area. The bypass of Vinh City (Nghe An), the asphalt concrete layer on the road surface is plasticized, creating scars along the wheels 5-7 cm deep running for nearly 20 km; section through Dien Chau (Nghe An), there is a subsidence of more than 10 cm deep. On the surface of Ben Thuy 2 bridge, which has only been exploited for less than a year, the bridge has printed wheel tracks about 10-12 cm deep.

- In the Da Nang - Khanh Hoa section, the rut is more than 90 km long (accounting for about 15%), in which, many subsidence sections are deeper than 7 cm, the settlement area is equivalent to 150,000 m<sup>2</sup>. Even, the section through Binh Dinh - Phu Yen, the area of Cu Mong and Ro Tuong passes, many places subsided 12 to 15 cm deep.

- The subsidence occurs in all three regions, not only projects that have been put into operation and used for 6 to 8 years, but also newly put into use, projects using government bonds and banks. State books, Build-Operate-Transfer or Official Development Assistance, on the road surface or on the bridge surface, all have rutted wheel tracks.

- Ninh Binh - Thanh Hoa, Vinh - Ha Tinh, from South to North, the subsidence is deeper and more frequent than the direction from North to South. Many sections on the route have the same driving conditions and ambient temperature but are still stable and undamaged (Figure 3).

- On the same section of the route, the construction contractors using asphalt concrete with different asphalt supply stations also differ in the phenomenon of damage. There are sections of the route that run mainly at night, but still have rutted wheels (Vinh - Ha Tinh section).

- Most of the road sections with rutting phenomenon of wheel tracks have many over-trucks in traffic. Through inspection, many sections of the route after cutting the asphalt layer, there are sections of the foundation layer that are not deformed, but the asphalt layer is still rutted with wheel tracks. Many samples when drilling appeared black residues (oil mineral) flowing from the drill bit, indicating that there is a foreign substance in the composition of asphalt (Figure 4). The pavement structure is generally quite similar in terms of thickness of the asphalt layer (usually the lower layer is about 7 cm of coarse-grained asphalt concrete, the upper layer is 5-6 cm of fine-grained asphalt concrete), or 7 cm of medium-grained asphalt concrete.



**Fig. 3.** In the same section of the route, there are still parts of the road that do not have rutted wheel tracks (National Highway 1 section of Vinh - Ha Tinh).



**Fig. 4.** Black streaks appear when drilling the National Highway 1 sample in the Vinh - Ha Tinh section [1].

### 3. Analyze the causes

Asphalt concrete road is a product formed over a long period of time, going through many stages and stages, subject to the interaction of many factors. Through the description of the current situation of wheel ruts, we can see that when the phenomenon of wheel rutting has occurred, there are many causes that can be the culprit. We can divide the causes into groups such as design causes, construction causes, and operational causes. But first, let get categorize wheel ruts according to the underlying cause.

#### 3.1. Classification of wheel ruts according to the underlying cause

Tire subsidence is the irreversible longitudinal deformation of the structure or the plastic deformation of the asphalt layer at the places where the wheel load coincides. Dripping ruts

reduces serviceability and causes structural damage to the pavement. Dripping is very dangerous for drivers, making it difficult to control the vehicle. When it rains, the water gets into the ruts, which is very dangerous. There are 3 common types of cake ruts that are: Structural cake rut; Plastic subsidence of the concrete layer; and Subsidence of the asphalt layer.

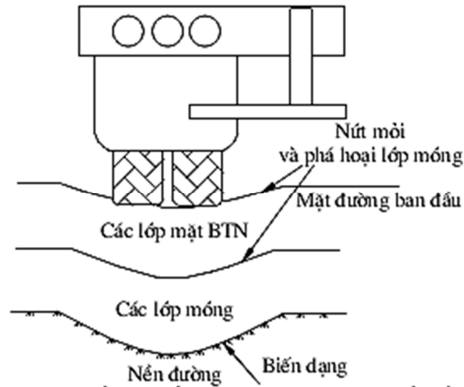


Fig. 5. Structural pie crust subsidence [3].

- Structural pie crust subsidence is the deformation of several structural layers below the asphalt layer. The deformation of the road surface depends on the failure characteristics of the foundation layers or the ground under the restoring effect of heavy loads. The foundation layers and the ground are not strong enough to resist the effects of heavy vehicle loads leading to irreversible deformation. Due to the deformation of the lower layers, the asphalt layers are deformed accordingly. Figure 5 depicts the rutting of a structural cake. Structural pie crust settlement can be easily recognized through two main features, which is settlement on a large scale and no obvious formation of tissue that accumulates plastic to the sides compared to the type of cake track settlement due to plastic melt of the concrete layer. The cause of the rutting of the structure cake is due to heavy loads, improper structural design, inappropriate selection of materials and design parameters, unsafe construction, roadbed and foundation layers weak, drainage in the structure is not good.

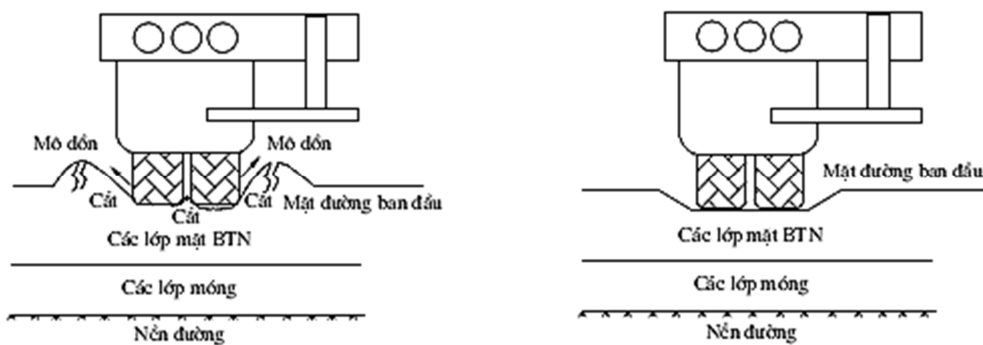


Fig. 6. Plastic subsidence of the concrete layer and subsidence of the concrete surface [3].

- Plastic subsidence in the asphalt layers formed agglomerated tissues along both sides of the wheel track (Figure 6). The cause of plastic melt settlement is because the shear strength of the concrete layer is smaller than the shear stress caused by the heavy vehicle load at the high temperature of the concrete surface. High stiffness of the foundation layers and roadbed is also the cause of plastic settlement. At this time, the foundation and foundation layers are not deformed, and cake streak settlement only appears in the upper layers of concrete. Subsidence occurs at

intersections, places where accelerating, decelerating, braking, stopping, parking, and slow-moving vehicles. Unsecured selection, design and construction of concrete layers is the cause of plastic settlement.

- Subsidence of the concrete surface layer occurs when the upper layers of asphalt are not compacted sufficiently (Figure 6). During the exploitation process, the asphalt layer is secondary compacted under the action of wheel load, leading to subsidence at the spot where the wheel track is restored. Subsidence is also caused by unreasonable aggregate distribution, high humidity and a lot of dust in the plastic. The asphalt layer cools quickly in the cold season, not ensuring the compaction temperature, leading to insufficient compaction. Subsidence of the surface layer does not generate accretion tissues.

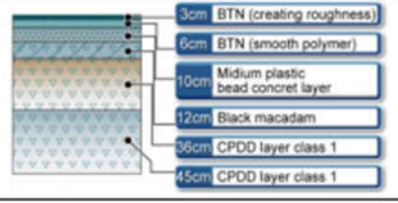
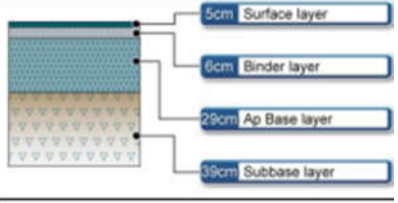
### 3.2. Group of causes by design

The most difficult and also the most dangerous thing for the project in general is that our engineers and consulting organizations have to propose and decide on issues they do not know well about. The result is a low-quality design that is both expensive and unsustainable. The following example might say a few things.

- Road surface structure, highway Ha Noi - Hai Phong in the basic design 2007 and comments of the Korea Expressway Corporation (KEC).

In 2007 the Government and the Ministry of Transport allowed the establishment of the Ha Noi - Hai Phong expressway project, the domestic consulting agency proposed a pavement structure with a total thickness of 112 cm. The Ministry of Transport introduced, and the investor hired KEC to verify the basic design, they proposed a pavement structure 79 cm thick with the comments below [2].

**Table 1.** Design of pavement section of main road in Basic design 2007 and evaluation by KEC

Category	Basic design 2007	KEC The proposed option KEC
Method design	Methods of Vietnam	The method of AASHTO
Section	 <p>T = 112cm</p>	 <p>T = 79cm</p>
Highlights	<ul style="list-style-type: none"> <li>+ Total thickness of face structure line is T=112cm</li> <li>+ Total thickness of material layers adhesion is T=31cm</li> <li>+ Total thickness of the layers T=81cm</li> <li>+ Construction cost is 744.220VND/m<sup>2</sup></li> </ul>	<ul style="list-style-type: none"> <li>+ Total thickness of face structure reduced line (T=79cm)</li> <li>+ Total dimension of material layers increased adhesion (T=40cm)</li> <li>+ Total thickness of feed material layer distribution decreased (T=39cm)</li> <li>+ Construction cost is 722.403VND/m<sup>2</sup> reduced by 3%</li> </ul>
Opinion of the consultant examine	<ul style="list-style-type: none"> <li>+ From the results of evaluating the pavement structure thickness, the method of AASHTO reduces total thickness by 30% but increases dimension thick layer of adhesive material.</li> <li>+ Applying the pavement structure design method according to AASHTO should be taken into account to get accurate coefficients including weather conditions, heavy truck traffic, analysis period, etc.</li> <li>+ It is recommended to use the AASHTO pavement design method because. This is a widely used method and in case the coefficients are applied correctly, the pavement structure thickness will be smaller than that proposed above (79 cm-65 cm).</li> </ul>	

- Current construction pavement structure :
  - Main road part: 71 cm thick pavement structure includes layers from top to bottom as follows:
    - + Layer of fine grained concrete: 5cm;
    - + Concrete asphalt 19 medium grain asphalt concrete: 14cm divided into two layers spread 7cm each;
    - + The base layer of crushed stone distribution reinforced with Alphant plastic is 12cm thick;
    - + The layer of crushed stone distribution type 1 is 40cm thick;
    - + After a few years, apply a roughening layer of 2-3cm.

The 71 cm pavement structure currently under construction compared to foreign countries has two disadvantages:

- + The first disadvantage is that the total thickness of the asphalt layers is 19cm, about 5 to 6cm more than the usual thickness of the countries, while the Asphalt Treated Base thickness of 12cm is less than 7 to 8cm. The price is more expensive, but the thermal stability is less;
- + The second, more serious disadvantage is the problem of fine-grained asphalt, which is the main risk of wheel ridge formation. This grade is very similar to pre-1980 road structures in Germany. Then, for the same reasons we see today, people have to change to using either a large porosity resin rock mixture, or Stone Mastic Asphalt. Both of these types when used must use plastic with polymer additives or rubber.

From the above example shows us:

- In order to have a high-quality pavement work like that of a foreign country, the design work must be very careful. The design needs to be done by consultants who are very knowledgeable about the product they make.
- But at any level, designers need professional help through design guidelines, formats, and normative processes.
- If all those documents are not clear, specifically at the key stages, the designers and approvers will often make mistakes, or have to compromise with harmful subjective judgments.

### 3.3. Group of causes due to construction

• Recent reports show a common result that the asphalt concrete composition is not correct, the asphalt is not enough, the stone powder is not enough, the particle size is not correct. These results are enough for us to conclude that the pavement is like that. broken. But it's not enough to say that, if you make the correct ingredients as required, you can ensure that the road is not damaged. But objectively speaking, we may be making the mistake of bringing the expected quality of a very advanced production to a very backward one. The following example may be somewhat telling.

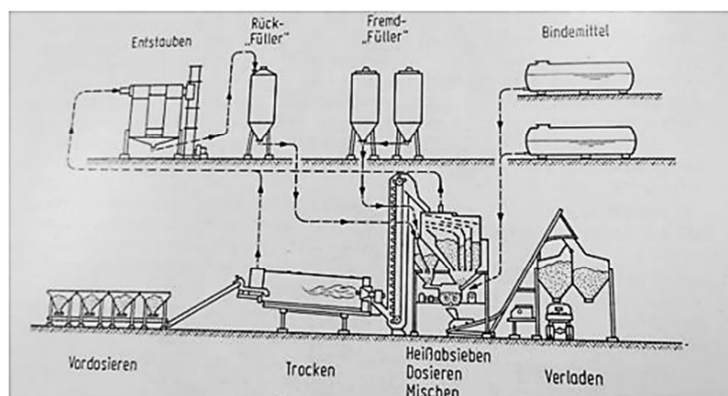
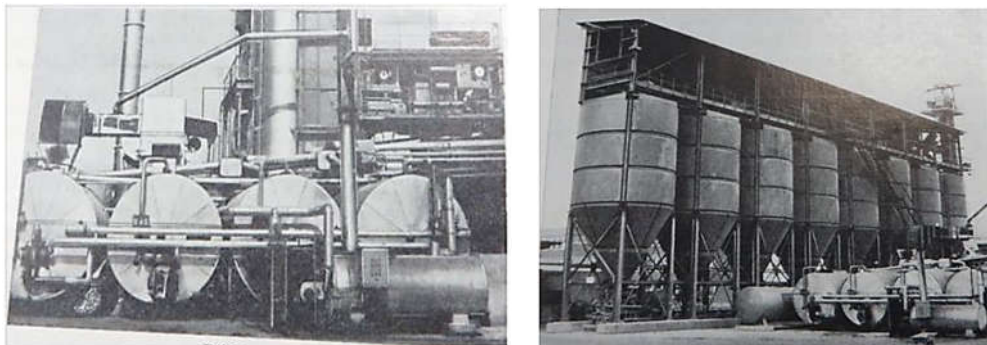


Fig. 7. Floor plan of asphalt batching plant [2].

The way to design the grain distribution for our asphalt is currently described as follows: Rocks and sand grains are classified according to each eye size, each size of sandstone is coordinated with each other according to a unique ratio determined. Then mixed with resin, stone powder and tested asphalt parameters. If these criteria are met, then we have a particle distribution. When there is a rock sample taken from a rock production site, the sand is taken from a certain source we size it according to the eye of the sieve. From there calculate it and tell the batching plant how much % of stone, how many % of sand mixed together will be finely distributed. If you do so, it will give very large errors. We take a look at the German way of managing grain distribution before 1975.



**Fig. 8.** Plastic storage and cooking area (left) and 8 tanks of each type of grain size each 250 m3 (right).

Brief description is as follows: Stone and sand according to each type of sieve are placed separately in each zone, transferred to each tank, preliminary mixed according to the design recipe, transferred by conveyor belt to the drying tank, and put into the mixing tank again over, re-weigh enough, then the excess is returned to the drying tank, the used part goes to the mixing tank (almost an experiment on how to do it right). If we do not see such devices, we can rest assured that the particle distribution is not correct and that there is no need to take a test sample. With such large error technology, the behavior of researchers and designers is to reduce the bearing capacity of the material. If not reduced enough, the design becomes the form.

- Weak surveillance

In order for the road surface subsidence to occur in the past time with the subjective responsibility of the subjects, we need to have a stricter and more professional management system. Traffic work is very professional, not everyone can do it, it is not necessary to have equipment to jump into the construction, every contractor will enter the carpet but requires the contractor to have a specialized technical team, management experience, including familiarity factor. In project quality control, the role of supervision consultant is especially important. However, with the current low cost, it is difficult for the consultant to fulfill the responsibility. Sometimes the cost is not enough for consulting to travel within a few tens of kilometers of the project. While the cost of foreign consultants is up to 7-8%, domestic consulting is less than 1% is not realistic.

### **3.4. Summary of causes coming from other declared sources**

Temperature, overloaded vehicles are big factors: The Institute of Science and Technology and the project investors to upgrade and expand National Highway 1 from Ha Nam to Thanh Hoa conduct quality checks. The vehicle counts results of both projects show that large trucks carrying construction materials, goods, containers, and passenger cars account for more than 50% of the vehicle lineup. Although the standard axle load is 10 tons, the rate of exceeding 12 tons axle load

is quite common, such as the section through Ninh Binh accounted for 23%, Thanh Hoa 15%. Even many trucks with axle loads up to more than 27 tons.

Through collecting data on temperature from 2010 to now, it shows that the hottest weather in these localities is around May, June, July and August, with the highest temperature around 38 - 41°C. At that time, the surface temperature of asphalt concrete will be up to about 54 - 68.5°C.

The test results of both projects show that the rutting phenomenon will develop faster in the summer, especially when the road has many heavy trucks. The large degree of overloading affects the road surface many times, causing rutting of wheel tracks, especially at disadvantageous locations such as: Poor construction quality, near toll stations, intersections, curve, etc.

#### 4. Overview of causes

Through the above analysis, we see that the same phenomenon of wheel rutting but the cause can be very different. Table 2 categorizes the causes according to a diagram to facilitate finding the true cause and then having the appropriate solutions.

**Table 2.** Causes of wheel rutting

Causes of wheel rutting	Cause by design	Geological, climatic and hydrological survey data is lacking and incomplete
		Processes, regulations and standards are not suitable for conditions of VietNam
		The pavement structure is not reasonable
		Choose a plastic with low thermal stability
		The design of the distribution curve is not reasonable
	Cause of construction	Engineer qualifications, weak contractor workers
		Machinery of contractor and equipment do not meet the requirements
		Main contractor for weak subcontractors to take on main items
		Weak supervision (supervisory responsibility, low cost norms for supervision)
	Cause of mining operation	Local temperature in some places is high
		Traffic is too big
		The axle load is much larger than the design

#### 5. Conclusion

The cause of wheel rutting can come from a single cause, but sometimes it is a combination of many causes at the same time. Causes can be classified into three large groups: causes from design, causes from construction, causes from operation and exploitation. Within each group there are many different causes. The presentation of a diagram of the causes of the rut formation helps to fully evaluate the causes, avoiding the omission of will-only deduction. From there, take preventive measures in advance, or handle arising problems in a timely manner.

#### References

1. Pham Huy Khang, Situation of rutted wheel tracks on some national highways, causes and remedial measures. Scientific Conference "Causes and solutions to overcome wheel ruts on asphalt pavement", (2014).
2. Nguyen Quang Toan, Tran Thi Thu Ha. Some suggestions to improve the quality of asphalt pavement.
3. Nguyen Quang Phuc. Irreversible deformation of asphalt concrete pavement structure under the effect of heavy load and high temperature. Scientific Conference "Causes and solutions to overcome wheel ruts on asphalt pavement", (2014).
4. Nguyen Manh Hung. Subsidence under wheel tracks on asphalt pavement. Causes and remedial measures. Scientific conference "Causes and solutions to overcome wheel marks on asphalt pavement", (2014).

5. Ho Anh Cuong, Vu Phuong Thao, Nguyen Huy Hung. Some solutions to enhance the resistance of wheel rutting for asphalt concrete. Scientific Conference "Causes and solutions to overcome wheel ruts on asphalt pavement", (2014).
6. Nguyen Quang Phuc. Choosing the right asphalt in asphalt concrete design. Scientific Conference "Causes and solutions to overcome wheel ruts on asphalt pavement", (2014).
7. Vo Trong Cuong, Research on building the correlation between softening point and penetration index of some asphalt types in Vietnam, Master's thesis in traffic construction engineering, Ha Noi, (2017).
8. Ministry of Transport, Socialist Republic of Vietnam (2005), Bitumen - Technical requirements TCVN: 7493-2005, Ha Noi.
9. Ministry of Transport, Socialist Republic of Vietnam (2005), Bitumen - Sampling method TCVN: 7494-2005, Ha Noi.
10. Ministry of Transport, Socialist Republic of Vietnam (2005), Bitumen - Method of determining penetration TCVN: 7495-2005, Ha Noi.
11. Ministry of Transport, Socialist Republic of Vietnam (2005), Bitumen - Determination of softening point TCVN: 7497-2005, Ha Noi.
12. Ministry of Transport of the Socialist Republic of Vietnam (July 28, 2014), Circular No. 27-2014/TT-BGTVT: Regulations on quality management of asphalt materials used in construction of traffic works , Ha Noi.
13. Nguyen Hoang Long (2017), Research and evaluation of bitumen quality by rheological dynamic cutters with experiments comparing with kinematic viscosity, Ministry level thesis 2017, code: DT 154014, Ha Noi.
14. Shell (1990), Asphalt Specification Shell 60/70, Singapore.
15. Vu Ngoc Tru (2013), Research on fiber reinforcement solutions to improve Marshall stability and plasticity of tight asphalt concrete, Key school-level science and technology project, code: 107-2013/KHXD-TD, Ha Noi.

# Study the procedure of compensation of differential shortening for super-high-rise buildings by the method of moving optimal compensation for construction projects in Vietnam

*Nguyen Duc Xuan<sup>1</sup>, Nguyen Sy Hung<sup>2</sup>, Ho Ngoc Khoa<sup>2</sup>, Nguyen Thi Thanh Tung<sup>2</sup>*

<sup>1</sup> Department of Civil Engineering, Vinh university, Vietnam

<sup>2</sup> Department of Civil Engineering, HCMC university of Technology and Education, 01 Vo Van Ngan, Linh Chieu, Thu Duc district, Ho Chi Minh city, Vietnam

Department of Civil Engineering, HaNoi university of Civil Engineering, 55 Giai Phong, Dong Tam, Hai Ba Trung district, Ha Noi city, Vietnam

*Email: ducxuandhv@gmail.com*

**Abstract.** In this paper, the authors present the procedure of compensation of differential shortening for super-tall buildings by the method of Moving Compensation Optimization (MCO). The MCO method has been studied as well as calculated by computers and clearly shows its superiority. This method has the minimum number of groups of compensation, the minimized compensation value of each group, and the compensated differential shortening values well controlled within the permissible limits of technical requirements, in comparison with methods of Uniform Compensation, Moving Averaging Correction method, and Optimal Compensation method. This differential shortening compensation procedure will be applied for Keangnam Landmark building with 70 floors. The results of the compensation procedure prove the advantages of the method, such as the effective flexibility to adjust the compensation plan in the actual construction phase, handling specific arising situations due to actual column shortening during construction sequences.

**Keywords:** column shortening; differential shortening; moving optimal compensation; super high-rise building; construction sequences.

## 1. Introduction

Column shortening is the phenomenon of vertically deformed reinforced concrete members, making columns and walls shorter under the effect of loads, shrinkage and creep. Among them, the deformation due to shrinkage and creep depends on the loading history, material properties, environmental humidity, construction progress, volume to surface area ratio of the member, and reinforcement content. Therefore, column shortening depends on time and is significant when the building has a high height, such as super high-rise buildings. The differential deformation between columns and walls and the core of the building in the same plan is called differential column shortening (DCS), which causes the floor-beams system to tilt, generating internal forces in the horizontal members, damage to partition walls, glass walls, and technical systems such as water pipes, elevators [1]. DCS can be minimized by optimizing the design for uniform compressive stress distribution in vertical members such as: using a cantilever or outrigger; using freely articulated connections for the structural system, and choosing a reasonable architectural shape [2]; increasing the axial stiffness for members that are expected to have large shrinkage by adding reinforcement [3]. However, these solutions generate relatively large construction costs, and it is not easy to ensure adequate control and remedy the DCS during actual construction [4].

A more straightforward but more effective solution is to compensate for the DCS value by providing the column in advance with a short amount of height loss due to shrinkage during construction. The height of the column at the time of construction is greater than the design height by a corresponding DCS value. In the world, super high-rise buildings Burj-Dubai Tower (United Arab Emirates, 828m, 164 floors); Petronas Twin Tower (Malaysia, 432m, 88 floors); Jin Mao Building (Shanghai - China, 421m, 88 floors); Texas Commerce Tower (USA, 305m, 75 floors);

Federasia Tower - Moscow City (Russia, 506m, 94 floors) has applied this method. In Vietnam, super high-rise buildings such as Bitexco Financial Tower (269m, 68 floors), Keangnam Landmark 72 Hanoi (350m, 72 floors); Lotte Center Hanoi (272m, 65 floors); Vincom Landmark 81 (461m, 81 floors) must also consider controlling and dealing with column shortening during construction. However, the entire construction process is a secret technology of construction contractors.

Based on the analysis of the advantages/disadvantages of some previous methods of compensating for contractions, such as lumped compensation method (LCM), optimal compensation approach (OC), and moving averaging correction approach (MAC), Xuan et al. [5, 6] proposed a new method of contraction compensation called Moving optimal compensation (MCO). The objective is to select the best shrink compensation plan with the smallest number of pooled groups and the optimal shrink compensation value for each group, and the shrinkage compensation error is controlled within the allowable limits. In addition, the proposed method is also easy to apply flexibly when the actual shrinkage value is much different from the predictive design shrinkage, which can be used by computers to calculate.

In this article, a construction process for DCS compensation of super high-rise buildings in Vietnam is established to solve the following problems: Establish a specific construction process; flexibly handle the situations that arise when the actual observed and forecast compensation values in the construction phases are different from the design offsets; Determine the most effective compensation plan to manage the accumulated DCS error after compensation at each floor level, meeting the technical criteria for the safety of use. That construction process is applied to Keangnam Landmark 72 Hanoi building.

## 2. Moving compensation optimization (MCO)

### 2.1. Formulation

The floors are divided into groups with an equal correction amount for every floor in a group as described in fig.1.  $x_j^i$  is the calculated shortening of a vertical element of the  $j$ th floor in  $i$ th group. To simplify the compensation or the construction process in practice, the number of lumped groups should be minimized. This can be achieved by maximizing the number of floors,  $N_i$ , in each group. On the other hand, there will be errors between the compensation amounts and the prediction amounts. The correction amount  $\delta_i$ , used for the  $i$ th group, therefore, should be chosen such that the cumulative error between the predicted differential shortening and the correction amounts is minimum. Thus, the objective function for the optimal compensation of the  $i$ th group is formulated in the following form:

$$\text{Min. } f(N_i, \delta_i) = -N_i + w \times \left| \sum_{k=1}^{i-1} \varepsilon_k + \sum_{j=1}^{N_i} (x_j^i - \delta_i) \right| \quad (1)$$

$$\varepsilon_k = \sum_{j=1}^{N_k} (x_j^k - \delta_k), k = 1, \dots, i-1 \quad (2)$$

where,  $w \geq 1$  is a weighted factor;  $\varepsilon_k$  is the cumulative error between the compensation amount and the predicted differential shortening in the  $k$ th group. The value of the weight factor  $w$  is chosen to ensure a numerical correlation between the two terms in the objective function. For example, if the unit of differential shortening is mm,  $w$  can be chosen to be 1; otherwise, if the unit is m, then the cumulative error will have a minimal value compared to  $N_i$  so we need to choose a large enough value of  $w$ .

To control the slab tilt caused by the axial shortenings, an allowable error value,  $\theta_i$  is introduced [6]. Moreover, the cumulative error is limited to a tolerance,  $d_j^i$ , which is limited by  $\xi_i$ . These constraints are written in the following forms [9]:

$$\left| x_j^i - \delta_i \right| \leq \theta_i \quad (3)$$

$$d_j^i = \left| \sum_{k=1}^{i-1} \varepsilon_k + \sum_{l=1}^i (x_l^i - \delta_l) \right| \leq \xi_i \quad (4)$$

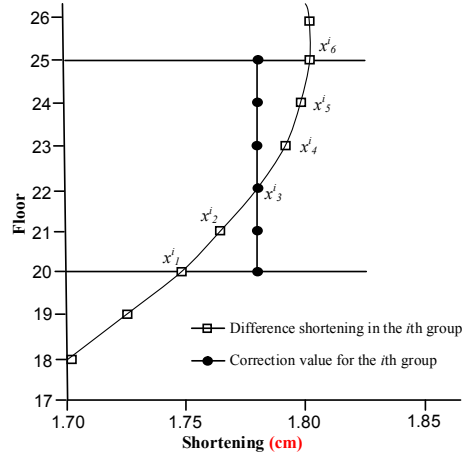


Fig. 1. Illustration of the lumped compensation approach.

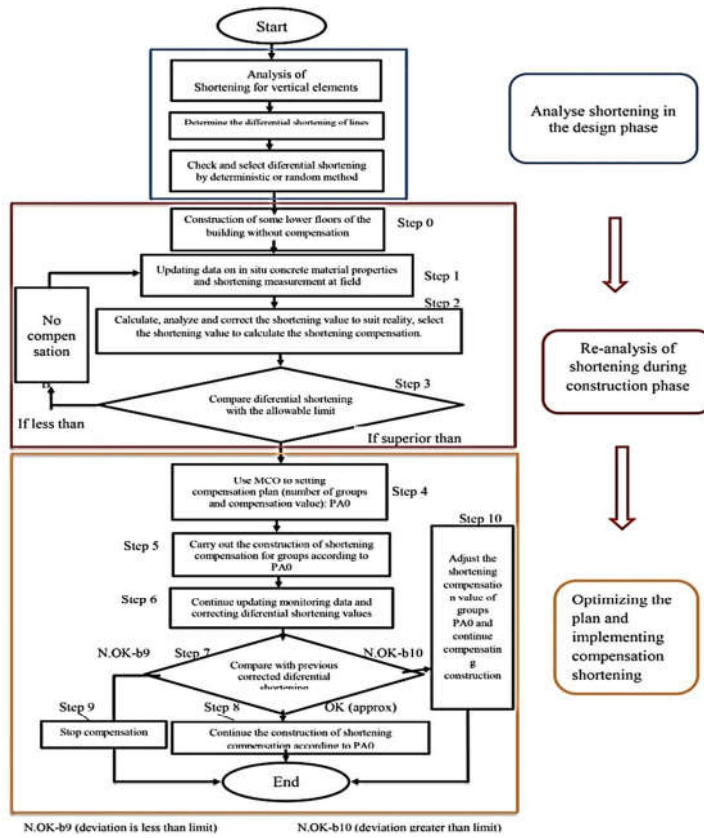


Fig. 2. Process of performing shortening compensation.

The optimal number of floors  $N_i$  together with the correction amount  $\delta_i$  for the  $i$ th group is determined by solving the above-constraint optimization problem (3) and (4).

### 3. Applications

#### a) Process of performing shortening compensation (Fig. 2)

Keangnam Hanoi Landmark Tower is a high-end complex project consisting of 3 high-rise buildings, including a 72-story hotel-office building and two 48-story apartment buildings, located on Pham Hung Street, Nam Tu Liem District, Hanoi. The buildings use a reinforced concrete floor-beam and column frame structure, a combination of a rigid core subjected to wind and earthquake loads, a hard outrigger floor, and a belt boundary wall, constructed by the method of pouring concrete in situ (full block) (Figure 3).

#### b) Realistic construction compensation application



Fig. 3. Landscape plan of Keangnam Hanoi Project.

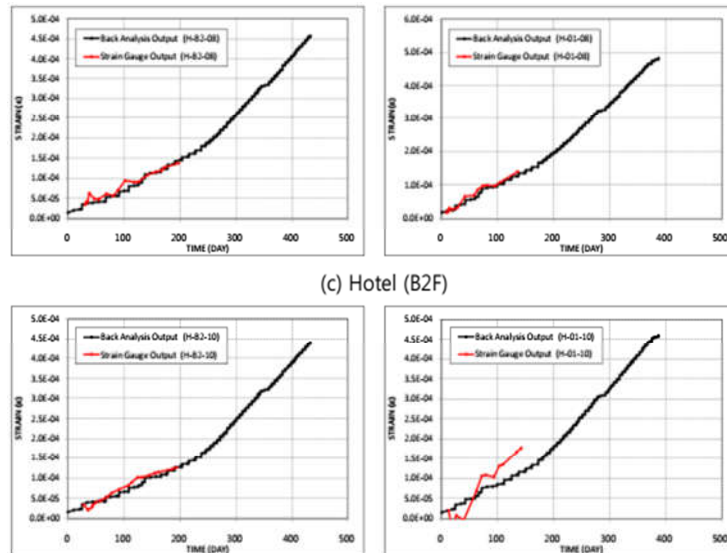
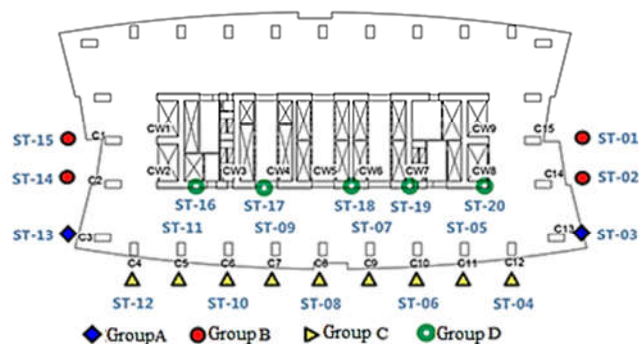


Fig. 4. Forecasted and monitoring shortening of columns C8 and C10 of basement B2 and first floor.

- **Analysing of forecast design data and monitoring data of shortening**

The field monitoring of shortening by strain gauge sensors was carried out for one year, from August 2008 to September 2009. The sensors are attached to the vertical members of basement B2, 1st floor, 3rd floor, and 7th floor, of which basement B2 and 1st floor are measured over three months. The results of the shortening comparison of the forecast design and the field measurement results are shown in Fig. 4.

In this analysis, the shortening of vertical elements divided into groups with similar structural characteristics on the basement structure plan B2 and first floor were updated within six months (from February 2009 to September 2009) to compare with shortened forecast design (Figure 4, Table 1). By comparing measured actual shortening with predicted design shortening, the design consultant evaluates, analyzes, and updates the characteristic parameters of concrete materials in situ and environmental conditions to apply for a shortening calculation more accurately the next time.



Group: A 104% (corner col); B 102% (short span); C 107% (typical col); D 98% (core wall)

Fig. 5. Location plan of measuring sensor for shortening by column /core-wall group.

- **Forecasted shortening and differential shortening in the long-term**

The forecasted long-term shortening and measured shortening of 15 columns and 9 core walls five years after the construction completion and use of the building are shown in Table 1.

**Table 1.** Forecasted maximum shortening and measured shortening five years after completion of construction [60]

Element	Maximum shortening/Floor				Difference
	Forecast at the design stage		Measure at construction stage		
	Max value	Floor	Max value	Floor	
C1	101.40	58F	85.9	44F	85%
C2	97.02	58F	83.2	44F	86%
C3	84.49	56F	76.1	46F	90%
C4	84.66	52F	78.8	44F	93%
C5	86.65	38F	80.8	43F	93%
C6	91.80	41F	87.0	43F	95%
C7	95.92	42F	91.9	44F	96%
C8	97.45	42F	94.1	44F	97%
C9	96.84	42F	93.3	44F	96%
C10	94.24	42F	90.2	43F	96%
C11	91.55	41F	86.1	43F	94%
C12	93.65	53F	87.0	43F	93%
C13	99.51	57F	83.5	46F	84%

Element	Maximum shortening/Floor				Difference
	Forecast at the design stage		Measure at construction stage		
	Max value	Floor	Max value	Floor	
C14	106.68	57F	87.6	43F	82%
C15	105.00	57F	86.1	44F	82%
CW1	50.29	52F	47.5	44F	94%
CW2	50.01	53F	47.2	46F	94%
CW3	36.28	55F	36.3	41F	100%
CW4	44.00	57F	43.3	43F	98%
CW5	47.38	57F	47.6	62F	100%
CW6	47.00	56F	42.1	43F	90%
CW7	44.95	54F	40.1	42F	89%
CW8	50.07	53F	49.07	46F	90%
CW9	49.01	53F	48.4	44F	99%

Differential shortening between adjacent vertical elements is established through lines (L), as shown in Figure 6.

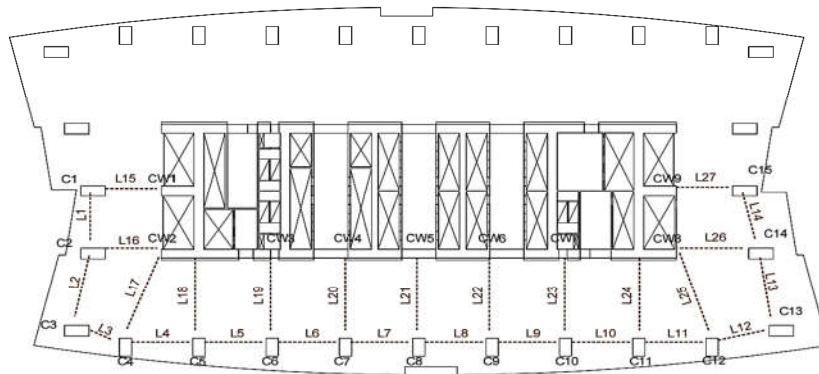


Fig. 6. Setting plan of differential shortening lines (L) to calculate the compensation.

Table 2. Maximum actual shortening after five years since completion of construction

Line	Elem. (i)	Elem. (j)	Distance between two elem. (L, mm)	Allowable limit of differential shortening ( $\Delta s$ ) = $L/240$ , mm)	Maximal differential shortening $\Delta s$ (mm)	Location of floor	$\Delta s/[\Delta s]$	Assessment	Check
L14	C14	C15	8986	37.4	3.6	61F	0.10	O.K	O.K
L15	C1	CW1	9050	37.7	41.2	58F	1.09	N.G	N.G
L16	C2	CW2	9050	37.7	39.7	61F	1.05	N.G	N.G
L17	C4	CW2	14038	58.5	37.7	57F	0.65	O.K	Check
L18	C5	CW2	13000	54.2	37.7	57F	0.70	O.K	Check
L19	C6	CW3	13000	54.2	50.8	44F	0.94	O.K	Check
L20	C7	CW4/C101	13000	54.2	63.5	46F	1.17	N.G	N.G
L21	C8	CW5/C102	13000	54.2	65.7	Out1	1.21	N.G	N.G
L22	C9	CW6/C103	13000	54.2	65.2	Out1	1.20	N.G	N.G
L23	C10	CW7	13000	54.2	50.2	44F	0.93	O.K	Check
L24	C11	CW8	13000	54.2	36.6	41F	0.67	O.K	Check
L25	C12	CW8	14038	58.5	37.4	43F	0.64	O.K	Check
L26	C14	CW8	11300	47.1	42.8	61F	0.91	O.K	Check
L27	C15	CW9	9050	37.7	40.7	58F	1.08	N.G	N.G

N.G: Exceeding the allowable limit of safe use; Check: Exceeding the control limit (taken 1/2 of the usage limit).

- **Establishing construction plans for adequate shortening compensation**

Run MCO to come up with a shortening compensation plan, in which the calculated shortening compensation value will be rounded to mm. The calculation results of the shortening compensation plan are presented in Table 3.

**Table 3.** MCO compensation plan for Kengnam Building

Group	Number of floors in group	Floor	Shortening compensation value (mm)
1	17	5 - 22	31
2	42	23 - 65	42
3	9	66 - PH2	26

The comparison of the proposed MOC compensation plan with that of the contractor MiDad applied to the Keangnam project is shown in Table 4. Midad's plan has four groups of shortening compensation with values of 10mm, 20 mm, 30 mm, and 40 mm, respectively. The proposed MCO plan has three groups with shortening compensation values of 17 mm, 42 mm, and 9 mm, respectively. Thus, the MCO compensation plan has a smaller number of compensation groups than the MiDad's plan.

**Table 4.** Comparison between MOC shortening compensation plan and MiDad's plan

PA Keangnam			PA-MCO		
<i>i</i> (group)	<i>N<sub>i</sub></i> (number of floors)	$\delta_i$ (mm) (compensation value)	<i>i</i> (group)	<i>N<sub>i</sub></i> (number of floors)	$\delta_i$ (mm) (compensation value)
0	5	No compensation	0	6	No compensation
1	4	10	1	17	31
2	7	20	2	42	42
3	10	30	3	9	26
4	48	40			

- **Checking the differential shortening after compensation**

Figure 7 shows the compensation curve (left image) and the post-compensation curve (right image) for the column-wall lines (Line 15-27). It can be seen that the shortening compensation plan according to the MCO's method controls the differential shortening of all lines, which is within the required limit of  $0.5 \cdot L/240$  (dotted line marked "check"). Meanwhile, according to MiDad's plan (PA-0), Line 21 still has differential shortening at the top 2 floors exceeding the test value (Figure 6).

In addition, the shortening compensation plan according to MCO has the value of differential shortening error after compensation asymptotically or equal to the allowable value (at Lines 27, 16, and 15), which is the preeminent feature of the proposed method. In contrast, the plan implemented by MIDAS is not optimal.

- **Compensating realization**

It is starting to perform shortening compensation from the 7th floor (the floor number is calculated starting from the basement) of the building with a shortening compensation value of 31mm by making column formwork with a length greater than the design length by 31mm. Alternatively, it is possible to make the formwork exactly according to the design length and adjust the compensation amount by applying the column head and column top compensation technique. From the 7th floor to the 22nd floor, maintain the value of shortening compensation of column of the 7th floor by constructing columns of 8th floors to 22nd floor according to the design length. Similarly, the construction of group 2 shall start from the 23rd floor with an offset value of 42mm by adjusting the length of the column formwork so that the actual height of the column head of the 23rd floor is 42mm higher than the design height of the column head, then maintain the amount of

shortening compensation for floors 24th to 65th by constructing the correct column length. Similarly, compensate for group 3 from the 66th floor to the PH2 floor with the compensation value of 26mm.

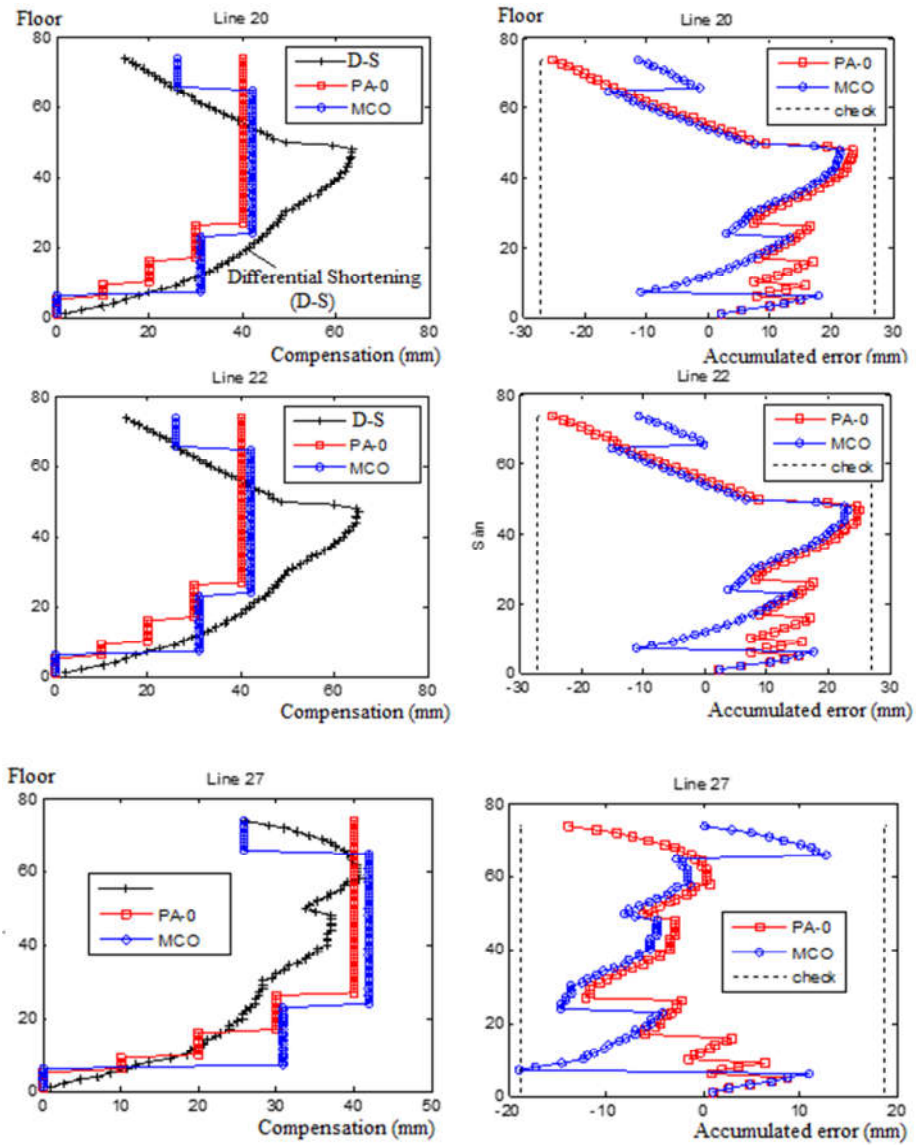


Fig. 7. Compensation curve (left) and differential shortening after compensation (right) of PA-0 (MiDad) and MCO.

- **Adjust the contract compensation plan when there is a big deviation**

If there is an actual fluctuation, the adjusted differential shortening value is much deviated compared to the forecast value. Accordingly, assuming this event occurs at the 49th floor, then

perform group shortening compensation from the 50th floor to the PH2 floor with an adjusted compensation value according to the fluctuating differential value and check the condition of the shortening compensation error for the group.

#### 4. Conclusions

This article has presented a construction process for shortening compensation of columns, walls in the construction of super high-rise buildings according to an effective method and its application in a practical project in Vietnam. This compensation method has been compared with other methods to test its effectiveness. Through the obtained results, the proposed process is effective and flexible when there is a change in the actual shortening value and the one of design forecast. In addition, the calculation program can be easily applied to ordinary computers. Specifically, the MCO method of shortening compensation has been applied to determine the column shortening compensation plan for a 72-story building in Vietnam. The research has investigated and applied to three cases occurring in reality: The actual shortening is much smaller than the design forecast; Actual shortening is roughly equal to design forecast; The actual Shortening is much larger than the design forecast.

#### References

1. Fintel M., Ghosh S., and Iyengar H. (1987). Column shortening in tall buildings-Prediction and compensation. Publ. EB108 D, Portland Cement Association, Skokie, 3: pp. 1-34.
2. Kim H.-S. (2017). Effect of outriggers on differential column shortening in tall buildings. *International Journal of High-Rise Buildings*, 6(1): pp. 91-99.
3. Kim H.S. (2015). Optimum distribution of additional reinforcement to reduce differential column shortening. *The Structural Design of Tall and Special Buildings*, 24(10): pp. 724-738.
4. Song, H. C., & Yoon, K. S. (2006). Probabilistic Prediction and Field Measurement of Column Shortening for Tall Building with Bearing Wall System. *Journal of the Korea Concrete Institute*, 18(1), 101-108.
5. Nguyễn Đ.X. (2015). Hiện tượng co ngấn cột và giải pháp xử lý trong thi công xây dựng nhà siêu cao tầng ở Việt Nam.
6. Xuân N.Đ., Anh P.H., and Khoa H.N. (2020). Bù vênh co ngấn trong thi công nhà cao tầng BTCT bằng phương pháp bù co hiệu quả. *Tạp chí Khoa học Công nghệ Xây dựng (KHCN XD)-ĐHXD*, 14(5V): pp. 66-76.
7. BS 8110: 1997: Structural use of concrete, Sheffield.
8. Mosley W.H., Hulse R., and Bungey J.H. (2012). Reinforced concrete design: to Eurocode 2. Macmillan International Higher Education.
9. ACI 318-19 Building Code Requirements for Structural Concrete  
Tiêu chuẩn Quốc gia TCVN 5574:2018 Thiết kế kết cấu bê tông và bê tông cốt thép
10. Pham H.-A., Nguyen D.-X., and Truong V.-H. (2021). An efficient differential-evolution-based moving compensation optimization approach for controlling differential column shortening in tall buildings. *Expert Systems with Applications*, 169: pp. 114531.
11. Choi S.W., Kim Y., Kim J.M., and Park H.S. (2013). Field monitoring of column shortenings in a high-rise building during construction. *Sensors*, 13(11): pp. 14321-14338.
12. IT M. (2011), Lotte Center Hanoi Project: Column Shortening - Report for Preliminary Analysis, Project Plan.
13. Gao F., Zhou H., Liang H., Weng S., and Zhu H. (2020). Structural deformation monitoring and numerical simulation of a supertall building during construction stage. *Engineering Structures*, 209: pp. 110033.
14. Khoa H.N. (2015). Organization of the construction of structural framing system of super high rise buildings in Vietnam. *Tạp chí Khoa học Công nghệ Xây dựng (KHCN XD)-ĐHXD*, 9(1): pp. 18-25.

# Characterizations of sugarcane bagasse ash and its use in blended mortar

*Duc-Hien Le<sup>1\*</sup> and Minh-Tung Tran<sup>1</sup>*

<sup>1</sup>PhD, Faculty of civil engineering, Ton Duc Thang University;

\*Corresponding author: Duc-Hien Le.

*Email: leduchien@tdtu.edu.vn*

**Abstract:** In present study, sugar cane bagasse ash (SBA) - an important by-product of sugar industries and mostly disposed in landfills, was employed to partially replace Ordinary Portland cement (OPC) in mortar. Utilization of blended cement leads to reduce the material cost and enhance the sustainability. To meet the demand, raw SBA after passing through the #100 sieve (opening 149  $\mu$ m, denoted as SBA-s) was pre-treated by re-burning in a furnace at 700°C for 1 hour (denoted as SBA-700). Two ash materials (SBA-s and SBA-700) were separately blended with OPC at various mass proportions (5-20%, increment 5%) to produce blended mortars. Properties of SBA samples were characterized; and performance SBA-blended mortar was evaluated and compared with that of OPC mortar. The results reveal that, silica-rich with amorphous form was detected for SBA samples. High loss on ignition (19.7%) was examined on the SBA-s sample and decreased to 14.3% for SBA-700 sample. Moreover, heating treatment of SBA-s significantly improves its pozzolanic activity. Both SBA-s and SBA-700 samples perform the pozzolanic characteristics as their SAI value above limitation of a pozzolan (75%). On the other hand, SBA-blended system requires greater amount of water demand in comparison with the cement system. Increasing level of SBA replacement is in conjunction with higher water-binder ratio to maintain workability. In addition, compressive strength of mortar containing up to 10% SBA (SBA-s and SBA-700) is slightly higher than that of cement mortar, determined at the same ages.

**Keywords:** sugarcane bagasse ash, mortar, pozzolanic activity, loss on ignition.

## 1. Introduction

Nowadays, Portland cement can be partially replaced by pozzolans, originated from solid wastes to reduce CO<sub>2</sub> emission to the atmosphere. Such implementation creates not only economic benefits but also friendly environment. In sugar production, the extraction of sugar juice from sugarcane will leave a huge amount of fibrous bagasse, which is mostly used as fuels in boilers for generating electricity. This process releases sugarcane bagasse ash (SBA) as final waste in sugar production chain. Approximately, combusting each ton of bagasse may generate 25 - 40 kg of bagasse ash [1]. As a result, a considerable amount of ash waste is dumped in free lands, causing negative impacts to the environment. In recent year, study on utilization of SBA in construction sector has been attracted to researchers due to pozzolanic characteristics of SBA. In fact, SBA can be used as a cement supplementary material, reported in the literature [2, 3]. Earlier authors concluded that incorporating a certain amount of SBA into concrete could enhance mechanical strength and long-life durability, reduce shrinkage of concrete as well. The chemical mechanism behind this application is the pozzolanic reaction of reactive silica present in bagasse ash and Ca(OH)<sub>2</sub> generating during cement hydration to further form additional hydrates [4]. However, raw SBA directly collected from landfills is basically unfitted to directly use as pozzolanic material because it contains unburnt fibrous particles, causing detrimental effects on cementitious systems. Besides, high loss on ignition (LOI) content in raw SBA (above limit of 6% for a pozzolan) could be obstacles for concrete implementation. Therefore, it is necessary to process SBA to enhance its pozzolanic activity prior use as SCM. Several processing approaches including grinding, burning, floating, sieving, or its combination have been suggested in earlier studies [5, 6].

The main objective of present study is to investigate mechanical strength of mortars containing SBA processed by sieving and re-burning at 700°C in a furnace for one hour. For that purpose, characterizations of SBA samples (unburnt and burnt) were determined. Moreover, a series of mortar modified with various SBA rate to replace OPC was prepared and their strength at 7 and 28 days were evaluated.

## 2. Materials and Methods

### 2.1. Sugarcane bagasse ash (SBA)

SBA material-collected from a disposal nearby a sugar company in South Vietnam was transported to the laboratory and dried at temperature of 105 - 110°C for 24 h in oven to completely remove the humidity content. The dried ash was first sieved through the #100 sieve (opening size of 149 µm) of a vibrating sieve machine to remove unburnt fibrous component and other impurities as much as possible. The sieved SBA was stored in plastic bags (denoted as SBA-s). The SBA-s was further burnt in a controlled-temperature furnace at 700°C for 60 min to improve pozzolanic activity, experienced from previous works [7]. Afterwards, the burnt material was rapidly cooled to room temperature and then stored in air-tight plastic bags until further tests (denoted as SBA-700).

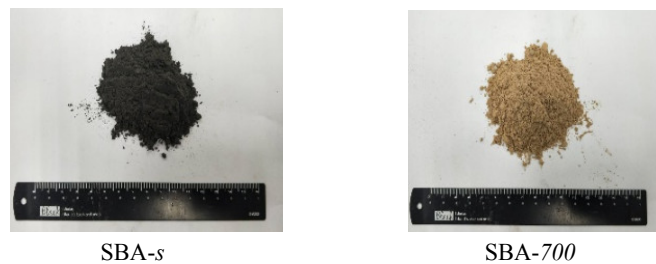


Fig. 1. Photos of the SBA-s and SBA-700 used in the investigation.

Moreover, Ordinary Portland cement (OPC) Type I was used. River sand with fineness modulus of 2.62 and water absorption of 1.45% was employed as fine aggregate. The tap water was used for mixing mortar.

### 2.2. Methods

#### *Characterization of SBA:*

The oxides compositions of OPC and bagasse ash (SBA-s) were determined using X-ray fluorescence spectrometry (XRF) analysis. Moreover, the X-ray diffraction (XRD) technique with Cu-K<sub>α</sub> radiation and a scanning angle from 10° to 80° step size of 0.02°/s was applied to identify mineral phases of the SBA samples. Morphology and texture of the two SBA samples were sequentially examined by scanning electron microscopy (SEM) technique and compared. In addition, loss on ignition (LOI) of the two ashes was determined by calculate the weight loss of samples before and after ignition for about 45 min in an electrical furnace at controlled-temperature (at 750 °C), specified in ASTM D7348 [8]. Moreover, density and specific surface area in Blaine's fineness of these materials were also determined.

#### *Mix proportions and compressive strength test for mortar:*

Mortars in this experiment were produced from natural river sand, OPC, and bagasse ashes. Each type of ashes (SBA-s and SBA-700) was used as partial replacement for cement at four rates (i.e., 5%, 10%, 15%, and 20% by mass), symbolized as 5SBA, 10SBA, 15SBA, and 20SBA, accordingly, where the SBA represents for the SBA-s and SBA-700. In addition, the control

mixture (with pure OPC) was also provided for comparison. The binder: river sand mass ratio was fixed at 1:2.75 for all mixes, as specified in ASTM C109 [9]. The water: binder mass ratio (w/b) for each rate of ash replacement were found after several trials until reaching a standard flow value of  $110 \pm 5\%$  with flow table test. Totally, nine mortar mixtures were systematically generated, as summarized in Table 1.

**Table 1.** Mix proportion of mortar mixtures used in this investigation

Mix ID.	% SBA	% OPC	Water: binder ratio	Sand: binder: ratio	Flow (%)	Compressive strength (MPa)		Strength activity index, SAI (%)	
						7 days	28 days	7 days	28 days
Control	0	100	0.57	2.57	115	36.15	42.04	100	100
5SBA-s	5	95	0.60		111	34.02	39.78	94.1	94.6
10SBA-s	10	90	0.63		98	31.26	38.69	86.5	92.0
15SBA-s	15	85	0.67		90	31.03	37.60	85.8	89.4
20SBA-s	20	80	0.71		83	28.79	31.52	79.6	75.0
5SBA-700	5	95	0.60		115	37.94	42.86	105.0	102.0
10SBA-700	10	90	0.63		111	36.76	42.71	101.7	101.6
15SBA-700	15	85	0.67		106	32.96	38.62	91.2	91.9
20SBA-700	20	80	0.71		96	29.84	34.89	82.5	83.0

### 3. Results and Discussion

#### 3.1. Characterizations of SBA-s and SBA-700 samples

Table 2 shows the oxide composition of OPC and sieved bagasse ash (SBA-s). In different with cement, the ash sample is highlighted with high content of  $\text{SiO}_2$  (75%) - an important oxide for a pozzolanic material, followed by  $\text{Al}_2\text{O}_3$  (6.48%) and low content of  $\text{CaO}$  (1.4%). Summation of these oxides is about 83%, well over the minimum requirement of a natural pozzolan (75%), as specified in ASTM C618 [10]. The result of oxide composition were observed similar to that in previous studies [5]. Normally, in cogeneration boilers at around 500 - 550°C, bagasse is incompletely burnt. Hence, rather high LOI (19.7%) was examined for the SBA-s sample, possibly attributed to presence of unburnt carbon particles, even though the sieving operation was carried out. This comment is supported by the fact that dark-black color was visually observed on the SBA-s sample [see Fig.1 (a)]. In addition, SEM images in Fig. 2 shows that SBA has a rough surface with highly microporous structures. Based on this characteristic, SBA would absorb more water.

**Table 2.** Chemical composition (%) of sieved SBA and OPC type I

$\text{SiO}_2$	$\text{Al}_2\text{O}_3$	$\text{Fe}_2\text{O}_3$	$\text{CaO}$	$\text{MgO}$	$\text{TiO}_2$	$\text{P}_2\text{O}_5$	$\text{SrO}$	$\text{BaO}$	$\text{MnO}_2$	$\text{Na}_2\text{O}$	$\text{K}_2\text{O}$
74.94	6.48	2.14	1.42	1.13	0.40	0.78	0.02	0.04	0.06	0.79	2.75

**Table 3.** Physical properties of different SBA samples

Physical properties	OPC	SBA-s	SBA-700
Specific gravity	3.15	2.17	2.44
Blaine fineness, $\text{cm}^2/\text{g}$	3480	4449	2260
Loss on ignition (LOI), %	-	19.7	14.3

\*LOI denotes as loss on ignition, determined at 750°C.

Changes in physical properties of ashes due to burning at controlled temperature are presented in Table 3. Particularly, the density of the ashes was 2.17 and 2.44 for SBA-s and SBA-700, respectively and lighter than that of cement. In line with this, the LOI value was found severely high on the unburnt sample (19.7%) and substantially reduced 14.3% (for SBA-700). That is, when the material was ignited at high temperature, trends of increase in specific gravity and

decrease in the LOI value were performed, expressing effectiveness of the heat treatment. Moreover, change in color from dark black for SBA-s to reddish for burnt samples was also clearly seen [Fig. 1 (b)]. Reduction of lightweight fibrous particles during re-burning may be responsible for these changes [5].

Furthermore, a marked decrease in specific surface area was observed on the burnt samples in comparing to the unburnt one. For instance, Blaine fineness in surface area of the SBA-s was 4449 cm<sup>2</sup>/g, which decreased to 2260 cm<sup>2</sup>/g for SBA-700. This result indicates that, coarser particles were seen on the burnt samples at elevated temperature, supported by the SEM images in Fig. 2. A similar result could be found in a study of Bahurudeen and Santhanam [11], who stated that specific surface area of burnt SBA samples at 800 °C and 900 °C was decreased to 118 and 110 m<sup>2</sup>/kg from 145 m<sup>2</sup>/kg for raw ash material. Thermal decomposition and phase transition of SBA particles from amorphous silica to crystalline form at high temperature would be justified for the observation.

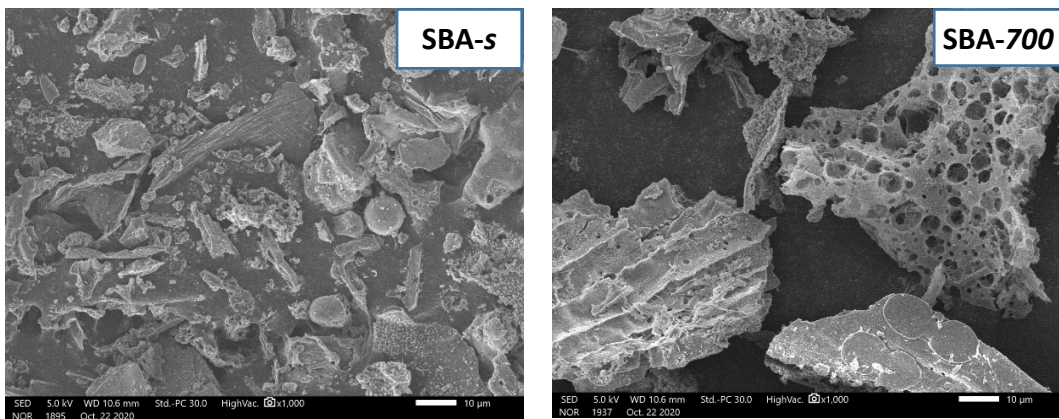


**Fig. 2.** Typical SEM images ( $\times 1000$ ) of the SBA-s and SBA-700 samples.

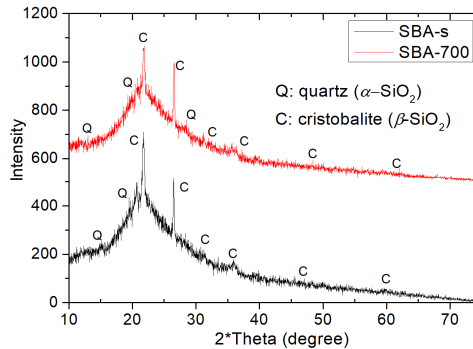


**Fig. 3.** XRD patterns for SBA-s and SBA-700.

Additionally, Fig. 3 shows the XRD patterns of SBA-s and SBA-700 samples. It is seen that these spectra were quite similar with the predominance of silica as cristobalite and quartz (SiO<sub>2</sub>). The amorphous humps are located at between 20° and 27° (2θ angle), evidenced to the presence of reactive silica, which suggested pozzolanic activity for the SBA [11].

### 3.2. Effect of SBA on water demand of mortar mixtures

All mortar mixtures (with and without SBA) were prepared to satisfy an equivalent flow value (110 with tolerance of 5%); and the suitable w/b values for mixes are reported in Table 1. The w/b

ratios for the control, 5SBA, 10SBA, 15SBA, and 20SBA mix series are 0.57, 0.60, 0.63, 0.67, and 0.71, respectively. It is clearly that SBA-blended system required a greater amount of mixing water in comparison with the control. Increasing percentage of SBA replacement for OPC was in conjunction with higher  $w/b$  to maintain workability. Higher water demand for mixtures containing bagasse ash has been published elsewhere [2, 5]. Several reasons could be explained for the result: (1) the irregular sharp with spongy surface of ash particles tends to increase friction between particles and reduce the workability [2]; (2) fibrous structure of SBA and presence of voids would absorb water significantly, hence, higher mixing water was required; (3) lower density of SBA than that of OPC, when replacing OPC by mass resulted in higher volume of SBA in blended system would be additional cause for increasing water requirement.

### 3.3. Mortar compressive strength at 7 and 28 days

Table 1 presents the results of 7 and 28-day compressive strength for all mortars. The SBA-blended-mortar has the strength value of 28.79 - 34.02 MPa (at 7 days) and 31.52 - 39.78 MPa (at 28 days). Whereas the mortar modified with the burnt ash has the corresponding strength of 29.84 - 37.94 MPa and 34.89 - 42.86 MPa. The control specimen has the compressive strength of 36.15 MPa and 42.04 MPa tested at 7- and 28 days, respectively.

It is observed that strength of specimens containing up to 10% SBA-700 was slightly higher than that of control, determined at the same ages. Moreover, the greater amount of ash replacing OPC in mixture led to a gradual decrease of the strength. Two reasons may be justified for the strength reduction. First, higher water demand (also high  $w/b$ ) were required for mixture with increasing SBA percentage as shown in Table 1. Consequently, strength was reduced due to growing porosities after evaporation of free water. Abbas et al. [12] studied the properties of mortar made with 10 - 40% bagasse ash with cement and reported that the required water/cement ratio increased from 0.51 to 0.64, respectively; the 28-day compressive strength of mortars incorporating 40% of SBA reduced 55% compared to that of the control mixture. Second, less amount of OPC available, leading to unavailability of the required amount of calcium hydroxide (CH) to react with silica in bagasse ash (pozzolanic reaction) would be another reason. The nucleation sites may have located at the areas where formation of CH is insufficient to form secondary CSH gels because of pozzolanic reaction [6, 13]. This means that more unreacted SBA particles is available, resulted in formation of more weak areas [2]. However, it would be noted that presence of SBA was not solely responsible for the compressive strength loss. In fact, increase in bagasse ash content and higher  $w/b$  both resulted in strength reduction [13].

In addition, presence of SBA-700 enhanced strength mortar by 4 - 18% and 3 - 11% after 7 and 28 days, respectively as compared with the SBA-s. Lesser LOI content observed on the burnt SBA (14.3%) than that of the unburnt sample (19.7%) could be main reason for the strength improvement. Cordeiro et al. [14] revealed that for bagasse ash, calcination temperature of 600°C or greater was sufficient to remove carbon component resulted in LOI values decreased. They found that bagasse ash burnt at 700°C was sufficient to improve the compressive strength.

### 3.4. Evaluation of Strength activity index (SAI)

Strength activity index (SAI) of the two ashes (SBA-s and SBA-700) and replacement ratios (5%, 10%, 15%, and 20%) was determined at 7- and 28 days. The SAI is calculated as the relative compressive strength (in percent) of the SBA-blended mortar to the corresponding control. The results of SAI for the two ashes are tabulated in Table 1. It is seen that all SBA-based samples have the SAI value to be approximate or greater than the minimum requirement for a pozzolan (75%), as specified in ASTM C618. The lowest SAI was observed on mixture with 20% OPC replacing with SBA-s, approximately 80% (at 7 days) and 75% (at 28 days). Clearly, SBA processed by re-burning leads to enhance the SAI value at testing ages. Previous studies also expressed similar observations [11]. The result discussed above implies the effectiveness of enhancing pozzolanic activity through re-burning of SBA-s.

## 4. Concluding Remarks

Based on experimental results, following points can be remarked:

1. Silica-rich with amorphous form was detected for SBA samples. Moreover, high LOI content (19.7%) was examined on the SBA-s sample. Treatment of the SBA by re-burning at 700 °C for one hour reduced the LOI value to 14.3% and improve the pozzolanic activity. Both SBA-s and SBA-700 performed the pozzolanic characteristics as their SAI value above limitation for a pozzolan (75%).
2. SBA-blended mixtures required a greater amount of mixing water in comparison with the cement mortar. Increasing percentage of SBA replacement for OPC was in conjunction with higher *w/b* to maintain workability.
3. Mortar specimens containing up to 10% SBA (SBA-s and SBA-700) had compressive strength to be slightly higher than the control, determined at the same ages. Moreover, the greater amount of ash replacing OPC in mixture led to a gradual decrease of strength.

## 5. Acknowledgment

This research is funded by Vietnam National Foundation for Science and Technology Development (NAFOSTED) under grant number 107.01-2020.01.

## References

1. Q. Xu, T. Ji, S.-J. Gao, Z. Yang, N. Wu, Characteristics and Applications of Sugar Cane Bagasse Ash Waste in Cementitious Materials, 12(1) (2019) 39.
2. P. Jagadesh, A. Ramachandra Murthy, R. Murugesan, Effect of processed sugar cane bagasse ash on mechanical and fracture properties of blended mortar, Construction and Building Materials 262 (2020) 120846.
3. D.-H. Le, Y.-N. Sheen, M.N.-T. Lam, Fresh and hardened properties of self-compacting concrete with sugarcane bagasse ash–slag blended cement, Construction and Building Materials 185 (2018) 138-147.
4. F. Martirena, J. Monzó, Vegetable ashes as Supplementary Cementitious Materials, Cement and Concrete Research 114 (2018) 57-64.
5. A. Akkarapongtrakul, P. Julphunthong, T. Nochaiya, Setting time and microstructure of Portland cement-bottom ash–sugarcane bagasse ash pastes, Monatshefte für Chemie - Chemical Monthly 148(7) (2017) 1355-1362.
6. A. Bahurudeen, D. Kanraj, V. Gokul Dev, M. Santhanam, Performance evaluation of sugarcane bagasse ash blended cement in concrete, Cement and Concrete Composites 59 (2015) 77-88.
7. S.A. Zareei, F. Ameri, N. Bahrami, Microstructure, strength, and durability of eco-friendly concretes containing sugarcane bagasse ash, Construction and Building Materials 184 (2018) 258-268.
8. ASTM:D7348, Standard Test Methods for Loss on Ignition (LOI) of Solid Combustion Residues, (2013).
9. ASTM:C109, Standard Test Method for Compressive Strength of Hydraulic Cement Mortars (Using 2-in. or [50-mm] Cube Specimens), 2008.
10. ASTM:C618, Standard Specification for Coal Fly Ash and Raw or Calcined Natural Pozzolan for Use in Concrete, 2008.
11. A. Bahurudeen, M. Santhanam, Influence of different processing methods on the pozzolanic performance of sugarcane bagasse ash, Cement and Concrete Composites 56 (2015) 32-45.
12. S. Abbas, A. Sharif, A. Ahmed, W. Abbass, S. Shaukat, Prospective of sugarcane bagasse ash for controlling the alkali-silica reaction in concrete incorporating reactive aggregates, Structural Concrete 21(2) (2020) 781-793.
13. S.M.S. Kazmi, M.J. Munir, I. Patnaikuni, Y.-F. Wu, Pozzolanic reaction of sugarcane bagasse ash and its role in controlling alkali silica reaction, Construction and Building Materials 148 (2017) 231-240.
14. G.C. Cordeiro, R.D. Toledo Filho, E.M.R. Fairbairn, Effect of calcination temperature on the pozzolanic activity of sugar cane bagasse ash, Construction and Building Materials 23(10) (2009) 3301-3303.

# Nonlinear static analysis of functionally graded porous thin plates resting on elastic foundations

Thanh-Hai Le<sup>1\*</sup>, Van-Long Nguyen<sup>2</sup>, Minh-Tu Tran<sup>2</sup>, Tuan-Anh Nguyen<sup>1</sup>

<sup>1</sup> Vinh University, 182 Le Duan Road, Vinh, Nghe An, Viet Nam

<sup>2</sup> Ha Noi University of Civil Engineering, 55 Giai Phong Road, Hanoi, Viet Nam

\*Email: haidhvinh@gmail.com

**Abstract.** This paper presents an analytical approach to study the nonlinear bending behaviour of functionally graded porous (FGP) plates resting on the Pasternak elastic foundation. The porous materials with three different distribution patterns namely uniform, non-uniform symmetric and non-uniform asymmetric are considered. Governing equations are derived based on the classical plates theory (CPT) taking into account von Kármán nonlinearity and neutral surface position. Using the displacement approach in conjunction with the Galerkin method, the analytical solution is obtained for various boundary conditions (moveable and immovable simply-supported). The effect of porosity coefficient, porosity distribution types, and various boundary conditions on nonlinear bending behavior are investigated.

**Keywords:** nonlinear bending analysis; functionally graded porous plate; neutral surface position; classical plate theory.

## 1. Introduction

Functionally graded porous materials (FGPMs) are a new class of functionally graded materials. Porous materials are characterized by the internal pores in the microstructure with size and local density varying according to certain rules, such as material properties can be considered as continuously and smoothly changes in the space of structures. It is a type of lightweight material with excellent energy-absorbing capability, and thermal conductivity, thereby making them the perfect candidate for structures that can withstand dynamic or impact loading, for thermal and sound isolators. Profound understanding of mechanical behaviors of FGP structures is therefore essential in design.

There have been many published works on the static and dynamic response of FGP structures. Using the analytical solution based on nonlinear displacement functions taking into account shearing deformations and finite element (FE) model with ANSYS software, Magnucki et al. [1] investigated bending and buckling behaviors of FGP plates. Arani et al. [2] predicted the natural frequencies of the FGP plates rested on the Winkler elastic foundation by utilizing higher-order shear deformation theory (HSDT) with DQM (differential quadrature method). Rad et al. [3] presented an analytical approach in the framework of Reddy's higher-order and Mindlin's first-order plate theories to explore the buckling response of rectangular FGP plates under various types of mechanical loading. Dong and Li [4] analyzed static, buckling and vibration characteristics of porous plates by employing the unified nonlinear analytical solution, the effect of temperature, material heterogeneity and geometrical parameters are studied in detail. Kumar et al. [5] used smoothed finite element technique to present linear and nonlinear analyses of Mindlin quadrilateral composite plates. Hung et al. [6] studied the non-linear buckling and post-buckling behavior of FGP toroidal shell segments with variable thickness FGP surrounded by an elastic foundation subjected to axial compressive loads. Ansari et al. [7] investigated the geometrically nonlinear static bending of arbitrarily shaped graphene FG-reinforced composite porous plates.

Using the stress-based and displacement-based approach in the framework of first-order shear deformation theory, Long and his colleagues investigated the nonlinear static bending

behavior of FGP plates resting on Pasternak elastic foundation under different boundary conditions [8-10], the effect of porosity coefficient, porosity distribution patterns, and various boundary conditions on nonlinear bending are investigated. With the same approach, these authors [11, 12] analyzed the buckling and post-buckling response of the imperfect porous plate based on the classical plate theory and the first-order shear deformation theory.

From the above-mentioned review, it can be seen that studies on the nonlinear static response of FGP plate are quite few, therefore this paper aims to enrich this gap. By introducing the physical neutral surface concept, nonlinear governing equations are established based on classical plate theory considering von Kármán nonlinearity. The Airy's stress function and Galerkin method are employed to obtain the analytical solution with several boundary conditions. The accuracy of the proposed approach is confirmed by comparing the numerical results with those of published ones available in the open literature. The effect of material parameters, elastic foundation stiffness, and boundary conditions on deflection, and bending moments will be investigated in detail.

## 2. The functionally graded porous plate

Consider a rectangular FGP plate of thickness  $h$ , length  $a$ , and width  $b$ , as shown in Fig. 1-a. The plate is referred to a Cartesian coordinate system  $x, y, z$ , where  $xy$  is the mid-plane of the plate and  $z$  is the thickness coordinator. The plate is rested on the Pasternak's elastic foundation with stiffness coefficients:  $K_w$  - Winkler foundation stiffness,  $K_{si}$  ( $i = x, y$ ) - shear layer stiffness of Pasternak foundation.

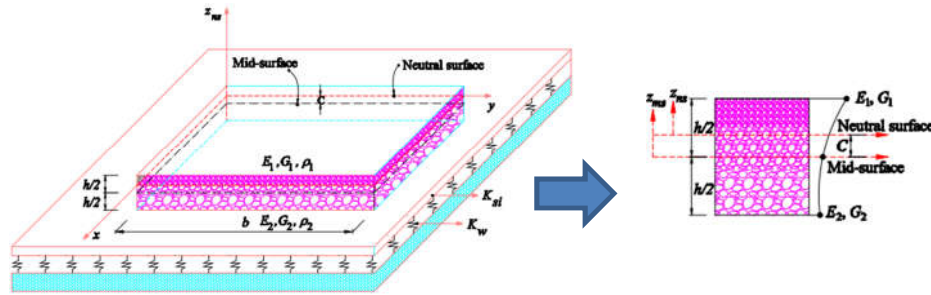


Fig. 1. The geometry and coordinate system of rectangular FGP plate resting on Pasternak elastic foundation.

The plate is made of open-cell porous materials (metal foam) with elasticity moduli varying through the thickness of the plate according to three different distribution patterns [11, 12]:

For uniform distribution (Type 1 - Fig. 2-a):

$$\{E, G\} = \{E_1, G_1\}(1 - e_0 \chi); \quad \chi = \frac{1}{e_0} - \frac{1}{e_0} \left( \frac{2}{\pi} \sqrt{1 - e_0} - \frac{2}{\pi} + 1 \right)^2 \quad (1)$$

For non-uniform symmetric distribution (Type 2- Fig. 2-b):

$$\{E(z), G(z)\} = \{E_1, G_1\} \left[ 1 - e_0 \cos \left( \frac{\pi z}{h} \right) \right] \quad (2)$$

For non-uniform asymmetric distribution (Type 3- Fig.2-c):

$$\{E(z), G(z)\} = \{E_1, G_1\} \left[ 1 - e_0 \cos \left( \frac{\pi z}{2h} + \frac{\pi}{4} \right) \right] \quad (3)$$

in which  $E_1, G_1$ , are maximum values of Young's modulus and shear modulus and similarly,  $E_2, G_2$ , are minimum values, respectively. Assume that Poisson coefficient  $\nu$  is constant along with the plate thickness. The porosity coefficient for moduli of elasticity is expressed by:

$$e_0 = 1 - \frac{E_2}{E_1} = 1 - \frac{G_2}{G_1} \quad (0 < e_0 < 1) \quad (4)$$

For the FGP plate with an asymmetric distribution pattern, the neutral surface location has not coincided with the middle surface, and is indicated by the following condition [13]:

$$\int_{-h/2}^{h/2} (z - C) E(z) dz = 0 \Rightarrow C = \left[ \int_{-h/2}^{h/2} z E(z) dz \right] / \left[ \int_{-h/2}^{h/2} E(z) dz \right] \quad (5)$$

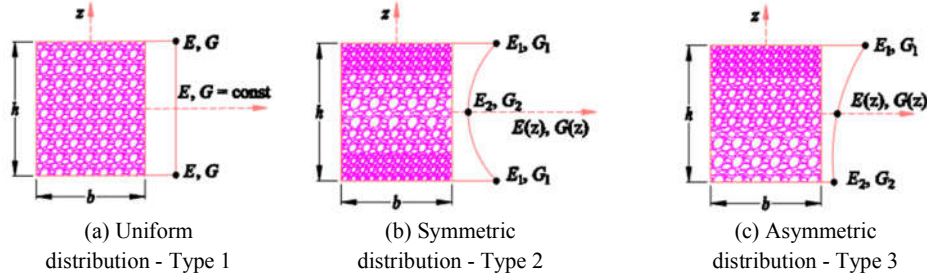


Fig. 2. The FGP plate with different porosity density distribution patterns.

### 3. Classical plate theory - CPT

Based on CPT, applying the neutral surface position concept as shown in Fig. 1-b, the displacement components ( $u, v, w$ ) at an arbitrary point ( $x, y, z_{ns}$ ) along  $x, y$  and  $z$  axes of the FGP plate are expressed as follows [14]:

$$\begin{aligned} u(x, y, z_{ns}) &= u_0(x, y) - z_{ns} w_{0,x}; & v(x, y, z_{ns}) &= v_0(x, y) - z_{ns} w_{0,y}; \\ w(x, y, z_{ns}) &= w_0(x, y). \end{aligned} \quad (6)$$

where ( $u_0, v_0, w_0$ ) are the displacements of the neutral-plane point along  $x, y$  and  $z_{ns}$  axes, respectively.

The commas subscript denote the partial differentiation with respect to the spatial variables.

The nonzero strains at the neutral surface of the FGP plate, including von Kármán nonlinearity are defined as [14]:

$$\begin{Bmatrix} \varepsilon_x \\ \varepsilon_y \\ \gamma_{xy} \end{Bmatrix} = \begin{Bmatrix} \varepsilon_x^0 \\ \varepsilon_y^0 \\ \gamma_{xy}^0 \end{Bmatrix} + z_{ns} \begin{Bmatrix} \kappa_x \\ \kappa_y \\ \kappa_{xy} \end{Bmatrix}; \quad (7)$$

in which:  $\varepsilon_x^0 = u_{0,x} + \frac{w_{0,x}^2}{2}$ ;  $\varepsilon_y^0 = v_{0,y} + \frac{w_{0,y}^2}{2}$ ;  $\gamma_{xy}^0 = u_{0,y} + v_{0,x} + w_{0,x}w_{0,y}$ ;  $\kappa_x = -w_{0,xx}$ ;  $\kappa_y = w_{0,yy}$ ;  $\kappa_{xy} = -2w_{0,xy}$ .

Stresses are determined from Hooke's law and written as:

$$\begin{Bmatrix} \sigma_x \\ \sigma_y \\ \sigma_{xy} \end{Bmatrix} = \begin{bmatrix} Q_{11} & Q_{12} & 0 \\ Q_{21} & Q_{22} & 0 \\ 0 & 0 & Q_{66} \end{bmatrix} \begin{Bmatrix} \varepsilon_x \\ \varepsilon_y \\ \gamma_{xy} \end{Bmatrix}; \quad (8)$$

where:  $Q_{11} = Q_{22} = \frac{E(z_{ns})}{1-\nu^2}$ ,  $Q_{12} = Q_{21} = \frac{\nu E(z_{ns})}{1-\nu^2}$ ,  $Q_{66} = \frac{E(z_{ns})}{2(1+\nu)}$ .

The force and moment resultants per unit length of the plate are defined as:

$$\begin{Bmatrix} N_x \\ N_y \\ N_{xy} \end{Bmatrix} = \begin{bmatrix} A_{11} & A_{12} & 0 \\ A_{12} & A_{11} & 0 \\ 0 & 0 & A_{66} \end{bmatrix} \begin{Bmatrix} \varepsilon_x^0 \\ \varepsilon_y^0 \\ \gamma_{xy}^0 \end{Bmatrix}; \quad \begin{Bmatrix} M_x \\ M_y \\ M_{xy} \end{Bmatrix} = \begin{bmatrix} C_{11} & C_{12} & 0 \\ C_{12} & C_{11} & 0 \\ 0 & 0 & C_{66} \end{bmatrix} \begin{Bmatrix} \kappa_x \\ \kappa_y \\ \kappa_{xy} \end{Bmatrix}; \quad (9)$$

$$\text{where: } (A_{ij}, C_{ij}) = \int_{-h/2-C}^{h/2-C} Q_{ij}(1, z_{ns}^2) dz_{ns}; \quad ij = 11, 12, 66.$$

The equilibrium equations of the FGP plate resting on the elastic foundation are derived from the principle of minimum total energy [15], its mathematical formulation has the form:

$$0 = \delta U_P + \delta U_F + \delta V \quad (10)$$

where  $\delta U_P$ ,  $\delta U_F$ ,  $\delta V$  are the variation of plate strain energy, of Pasternak's foundation strain energy, and work done by external loads, respectively.

The nonlinear equilibrium equations of plate based on the classical plate theory are given by [15]:

$$\begin{aligned} N_{x,x} + N_{xy,y} &= 0; \quad N_{xy,x} + N_{y,y} = 0; \\ M_{x,xx} + 2M_{xy,xy} + M_{y,yy} + N_x w_{0,xx} + 2N_{xy} w_{0,xy} + N_y w_{0,yy} \\ &\quad - K_w w_0 + K_{sx} w_{0,xx} + K_{sy} w_{0,yy} + q = 0 \end{aligned} \quad (11)$$

Using Airy stress function  $\varphi(x, y)$  defined by:

$$N_x = \varphi_{,yy}, \quad N_y = \varphi_{,xx}, \quad N_{xy} = -\varphi_{,xy} \quad (12)$$

It is seen that the first two equations in Eqs. (11) are automatically satisfied. Applying the relationship of Eqs. (9), (7) and (12), the one rest Eqs. (11) are re-written in terms of the displacements and stress function as follows:

$$\begin{aligned} -C_{11} \nabla^4 w_0 + \varphi_{,yy} w_{0,xx} - 2\varphi_{,xy} w_{0,xy} + \varphi_{,xx} w_{0,yy} \\ - K_w w_0 + K_{sx} w_{0,xx} + K_{sy} w_{0,yy} + q = 0 \end{aligned} \quad (13)$$

The geometrical compatibility equation for the rectangular plate is expressed [16]:

$$\varepsilon_{x,yy}^0 + \varepsilon_{y,xx}^0 - \gamma_{xy,xy}^0 = w_{0,xy}^2 - w_{0,xx} w_{0,yy} \quad (14)$$

Based on the Eqs. (9) and (12), the strains can be expressed as:

$$\begin{aligned} \varepsilon_x^0 &= \frac{A_{11}}{A_{11}^2 - A_{12}^2} N_x - \frac{A_{12}}{A_{11}^2 - A_{12}^2} N_y = \frac{A_{11}}{A_{11}^2 - A_{12}^2} \varphi_{,yy} - \frac{A_{12}}{A_{11}^2 - A_{12}^2} \varphi_{,xx}; \\ \varepsilon_y^0 &= \frac{A_{11}}{A_{11}^2 - A_{12}^2} N_y - \frac{A_{12}}{A_{11}^2 - A_{12}^2} N_x = \frac{A_{11}}{A_{11}^2 - A_{12}^2} \varphi_{,xx} - \frac{A_{12}}{A_{11}^2 - A_{12}^2} \varphi_{,yy}; \\ \gamma_{xy}^0 &= \frac{1}{A_{66}} N_{xy} = -\frac{1}{A_{66}} \varphi_{,xy} \end{aligned} \quad (15)$$

Substituting Eq. (15) into geometrical compatibility Eq. (14), we obtain:

$$\nabla^4 \varphi = D \left[ \left( \frac{\partial^2 w_0}{\partial x \partial y} \right)^2 - \frac{\partial^2 w_0}{\partial x^2} \frac{\partial^2 w_0}{\partial y^2} \right] \quad (16)$$

$$\text{in witch: } \nabla^4 = \frac{\partial^4}{\partial x^4} + \frac{\partial^4}{\partial y^4} + 2 \frac{\partial^4}{\partial x^2 \partial y^2}; \quad \nabla^2 = \frac{\partial^2}{\partial x^2} + \frac{\partial^2}{\partial y^2}; \quad D = A_{11} (1 - \nu^2).$$

The system consisting of two equations in Eq. (13) and Eq. (16) are the governing equations used to investigate the nonlinear bending behavior of FGP plates. This is a system of four nonlinear equations with 2 independent unknowns:  $w_0, \varphi$

#### 4. Nonlinear bending analysis

Based on the Galerkin method, analytical solutions for nonlinear bending analysis of FGP rectangular plate under two cases of boundary conditions (BCs) are proposed.

**Case 1:** All four edges of plates are simply supported and freely movable in both the  $x$  and  $y$  directions and referred to as SSSS-FM. The associated BCs are:

$$w_0 = 0, N_{ns} = 0, M_n = 0, N_n = N_{n0} = 0 \quad (17)$$

**Case 2:** All four edges of plates are simply supported and immovable and referred to as SSSS-IM. The associated BCs are:

$$w_0 = 0, N_{ns} = 0, M_n = 0, N_n = N_{n0} = 0 \quad (18)$$

in which  $N_{x0}, N_{y0}$  are in-plane compressive loads at movable edges of the rectangular plate and are fictitious compressive edge loads at immovable edges.

The in-plane immovable boundary conditions, such as  $u_0 = 0$  (at  $x = 0, a$ ) and  $v_0 = 0$  (at  $y = 0, b$ ) are satisfied on the average sense [17, 18]:

$$\int_0^b \int_0^a u_{0,x} dx dy = 0; \quad \int_0^b \int_0^a v_{0,y} dx dy = 0 \quad (19)$$

The stress function is chosen as:

$$\varphi = \bar{\varphi}(x, y) + N_{x0} \frac{y^2}{2} + N_{y0} \frac{x^2}{2} \quad (20)$$

in which, for moveable in-plane BCs:

$$N_{x0} = \frac{1}{b} \int_0^b \hat{N}_x dy = 0; \quad N_{y0} = \frac{1}{a} \int_0^a \hat{N}_y dx = 0 \quad (21)$$

For immovable in-plane, from Eq. (19) we obtain in-plane support reactions as follows:

$$N_{x0} = \frac{1}{ab} \int_0^b \int_0^a \left( -\bar{\varphi}_{,yy} + \frac{A_{11}}{2} w_{0,x}^2 + \frac{A_{12}}{2} w_{0,y}^2 \right) dx dy; \quad (22)$$

$$N_{y0} = \frac{1}{ab} \int_0^b \int_0^a \left( -\bar{\varphi}_{,xx} + \frac{A_{12}}{2} w_{0,x}^2 + \frac{A_{11}}{2} w_{0,y}^2 \right) dx dy$$

With the SSSS, the displacement solutions are assumed as follows:

$$w_0 = \sum_m \sum_n w_{0mn} X_m(x) Y_n(y) = \sum_m \sum_n w_{0mn} \sin \alpha_m x \sin \beta_n y; \quad (23)$$

$$\alpha_m = \frac{m\pi}{a}, \beta_n = \frac{n\pi}{b}; \quad m, n = 1, 3, 5 \dots$$

where:  $w_{0mn}$  are unknown coefficients to be determined.

Substituting Eq. (23) into Eq. (16), we obtain:

$$\bar{\varphi} = \sum_p \sum_q \sum_r \sum_s w_{0pq} w_{0rs} \left\{ \begin{array}{l} K_1 \cos(\alpha_p - \alpha_r) x \cos(\beta_q - \beta_s) y \\ + K_2 \cos(\alpha_p + \alpha_r) x \cos(\beta_q + \beta_s) y \\ + K_3 \cos(\alpha_p - \alpha_r) x \cos(\beta_q + \beta_s) y \\ + K_4 \cos(\alpha_p + \alpha_r) x \cos(\beta_q - \beta_s) y \end{array} \right\} \quad (24)$$

where, coefficients  $K_1, K_2, K_3, K_4$  are presented in **Appendix 1**.

Substituting expressions of  $\bar{\varphi}$  in Eq. (24) into Eq. (22) in-plane support reactions can be written in the form:

$$N_{x0} = \sum_p \sum_q \sum_r \sum_s w_{0pq} w_{0rs} K_{pqrs}^{(1)}; \quad N_{y0} = \sum_p \sum_q \sum_r \sum_s w_{0pq} w_{0rs} K_{pqrs}^{(2)} \quad (25)$$

Substituting  $\bar{\varphi}$  and  $N_{x0}, N_{y0}$  into Eq. (20) to get the stress function  $\varphi(x, y)$ ; then substituting into Eq. (13);

$$\sum_m \sum_n w_{0mn} l_{mn}^{(33)} + \sum_m \sum_n \sum_p \sum_q \sum_r \sum_s w_{0mn} w_{0pq} w_{0rs} g_{mnpqrs}^{(33)} + q = 0 \quad (26)$$

In wich:  $l_{mn}^{(33)}(x, y) = -C_{11} \left( X_m''' Y_n + 2 X_m'' Y_n'' + X_m Y_n''' \right) - K_w X_m Y_n + K_{sx} X_m'' Y_n + K_{sy} X_m Y_n''$ ;

$g_{mnpqrs}^{(33)}(x, y)$  are presented in **Appendix 2**.

Multiplying each equation of Eqs. (26) with the corresponding eigenfunction and integrating over the domain of solution, the following equations are gotten:

$$\sum_m \sum_n w_{0mn} L_{mnij}^{(33)} + \sum_m \sum_n \sum_p \sum_q \sum_r \sum_s w_{0mn} w_{0pq} w_{0rs} G_{mnpqrsij}^{(33)} + F_{ij} = 0 \quad (27)$$

where:  $\left\{ L_{mnij}^{(33)}, G_{mnpqrsij}^{(33)} \right\} = \int_0^a \int_0^b \left\{ l_{mn}^{(33)}, g_{mnpqrs}^{(33)} \right\} X_i Y_j dx dy$ ;  $F_{ij} = \int_0^a \int_0^b q X_i Y_j dx dy$ .

Approximate roots of nonlinear algebraical equations (27) obtained by using the minteractive Newton-Raphson method are coefficients  $\{w_{0mn}\}$ , from which we can determine displacements, strains, stresses and stress resultants for nonlinear bending analysis of FGP plate.

For linear analysis, the set of algebraic linear equations is obtained by neglecting nonlinear strains  $G_{mnpqrsij}^{(33)}$  in Eqs. (27).

$$\sum_m \sum_n w_{0mn} L_{mnij}^{(33)} + F_{ij} = 0 \quad (28)$$

## 5. Numerical results and discussion

Based on the above mentioned analytical solution, Matlab's code is built to implement numerical examples. Numerical results are presented for nonlinear analysis unless previously stated. For convenience, the non-dimensional results are used in the form [19, 20]:

$$\bar{w} = \frac{1}{h} w_0 \left( \frac{a}{2}, \frac{b}{2} \right); \quad K_0 = \frac{K_w a^4}{E_0 h^3}; \quad J_0 = \frac{K_{sx} a^2}{E_0 h^3 \nu} = \frac{K_{sy} b^2}{E_0 h^3 \nu}; \quad (29)$$

$$E_0 = 1.0 \text{ GPa}; \quad P = \frac{q_0 a^4}{E_1 h^4}$$

### 5.1. Validation Examples

In this section, the accuracy of self-written Matlab's code and analytical solutions using stress-based approaches is validated. Because there are not any published works on nonlinear analysis of

rectangular FGP plates, thus validation examples are performed with a particular type of FGP: isotropic material.

**Example 1:**

Consider a simply supported isotropic square plate ( $E = 7.8 \cdot 10^6$  psi,  $\nu = 0.3$ ) with  $h = 1$  in.,  $a = b = 10h$ , under uniformly distributed load. The non-dimensional central deflection  $\bar{w}$  is calculated as shown in Table 1. The results are compared with those of Putcha and Reddy [21], which used the finite element method based on the five-variable higher-order shear deformation theory, Kapoor and Kapania [22] using the isogeometric analysis in the framework of first-order shear deformation theory, and abaqus software.

**Table 1.** The non-dimensional central deflection  $\bar{w}$  of the simply supported isotropic square plate (SSSS) under uniformly distributed load.

$P$	Putcha and Reddy [21]	Kapoor and Kapania [22]	Abaqus	Present
SSSS-FM				
6.25	0.2812	0.2840	0.2846	<b>0.2702</b>
12.5	0.5185	0.5244	0.5350	<b>0.5070</b>
25	0.8672	0.8790	0.9168	<b>0.8680</b>
50	1.3147	1.3341	1.3900	<b>1.3313</b>
100	1.8679	1.8918	1.9120	<b>1.8792</b>
SSSS-IM				
6.25	0.2790	0.2784	0.2667	<b>0.2541</b>
12.5	0.4630	0.4626	0.4572	<b>0.4361</b>
25	0.6911	0.6910	0.7042	<b>0.6700</b>
50	0.9575	0.9579	1.0030	<b>0.9456</b>
100	1.2688	1.2696	1.3650	<b>1.2660</b>

This example shows slight discrepancies between present results and published ones, thus the reliability of proposed approaches as well as self-written Matlab's codes are confirmed.

**5.2. Nonlinear analysis**

Considering the FGP (metal foam) rectangular plate ( $h = 0,1$  m,  $G_1 = 26.923$  GPa,  $\nu = 0.3$ ,  $a/h = 50$ ,  $b/a = 1$ ) rested on the elastic foundation, under the uniformly distributed load  $P$ .

The influence of the porosity coefficient on the nonlinear bending response of SSSS-IM square FGP plates ( $K_0 = 300$ ,  $J_0 = 100$ ) is illustrated in Figure 3. It can be seen that under the given applied load, the central nondimensional deflection increases as the porosity coefficient increases. This is because the increasing porosity coefficient increases the size and amount of internal pores which results in a decrease in the FGP plate stiffness. In addition, porosity distribution patterns affect significantly deflection: non-uniform symmetric porosity distribution (Type 2) produces the lowest deflection, two remaining uniform porosity distributions (Type 1) and non-uniform asymmetric porosity distribution (Type 3) produce almost similar deflections (Type 1 produces larger deflection than Type 3). Furthermore, the larger the porosity coefficient, the bigger gap between porosity coefficient-deflection curves of different porosity distribution patterns.

Load-deflection curves ( $P - \bar{w}$ ) corresponding to various pairs of elastic foundation stiffness are illustrated graphically in Fig. 4. It can be seen that the presence of elastic foundation increases plate stiffness, resulting in a decrease in deflection. In addition, the influence of foundation parameter  $J_0$  is more significant than  $K_0$ .

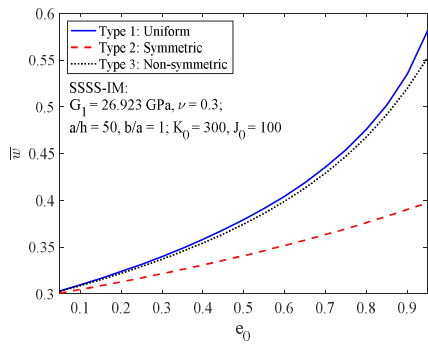


**Fig. 3.** Variation of nondimensional deflection  $\bar{w}$  of FGP plate versus porosity coefficients  $\epsilon_0$  with various porosity distribution patterns

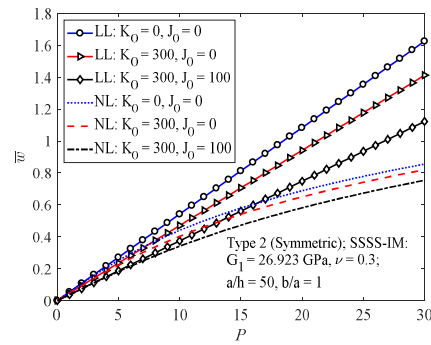


**Fig. 4.** Variation of deflection  $\bar{w}$  of FGP plate versus uniform load parameter  $P$  resting on different types of elastic foundations

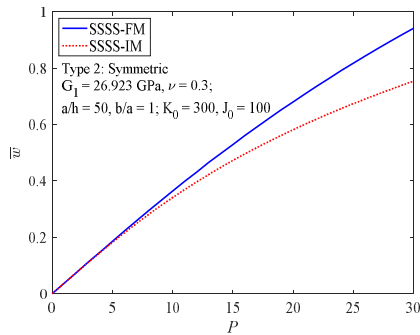


**Fig. 5.** The variation of nondimensional deflection  $\bar{w}$  of FGP plate versus uniform load parameters  $P$

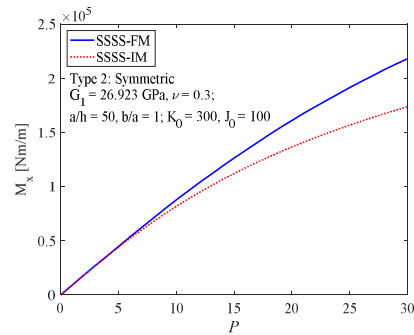


**Fig. 6.** The variation of bending moments  $M_x$  of FGP plate versus uniform load parameters  $P$

Figs. 5 and 6 show the influence of moveable and immovable simply-supported boundary conditions on load-deflection curves ( $P - \bar{w}$ ) and load-bending moment curves ( $P - M_x$ ). It can be noticed that the variation of deflection and bending moment versus applied load has a similar trend. As expected, the boundary conditions with in-plane constrain (immovable-IM) have smaller deflection and bending moment than the boundary conditions with in-plane un-constrains (moveable-FM). When the load is small, the effect of the boundary condition is slight, while with larger loads this effect becomes more significant.

## 6. Conclusion

This paper developed basic relations and governing equations to analyze the nonlinear buckling of FGP plates resting on the elastic foundation, including the physical neutral surface position, and geometrical von Kármán nonlinearity, in the framework of the classical plate theory. Based on the stress approach in conjunction with the Bubnov-Galerkin method, analytical solutions are derived to investigate the nonlinear bending response of the FGP plate. The numerical investigations show a significant effect of material and elastic foundations parameters as well as boundary conditions on the static response of the FGP plate. The obtained data together with technical notes are useful benchmarks for the design, construction and maintenance process of FGP structures in practice.

## References

1. Magnucki, K., M. Malinowski, and J. Kasprzak, *Bending and buckling of a rectangular porous plate*. Steel and Composite Structures, 2006. **6**(4): p. 319-333.
2. Arani, A.G., et al., *Free vibration of embedded porous plate using third-order shear deformation and poroelasticity theories*. Journal of Engineering, 2017. **2017**.
3. Rad, E.S., et al., *Shear deformation theories for elastic buckling of fluid-infiltrated porous plates: an analytical approach*. Composite Structures, 2020. **254**: p. 112829.
4. Dong, Y. and Y. Li, *A unified nonlinear analytical solution of bending, buckling and vibration for the temperature-dependent FG rectangular plates subjected to thermal load*. Composite Structures, 2017. **159**: p. 689-701.
5. Kumar, A., M. Singha, and V. Tiwari, *Nonlinear bending and vibration analyses of quadrilateral composite plates*. Thin-Walled Structures, 2017. **113**: p. 170-180.
6. Hung, D.X., et al., *Nonlinear buckling and postbuckling of FG porous variable thickness toroidal shell segments surrounded by elastic foundation subjected to compressive loads*. Aerospace Science and Technology, 2020. **107**: p. 106253.
7. Ansari, R., et al., *Nonlinear bending analysis of arbitrary-shaped porous nanocomposite plates using a novel numerical approach*. International Journal of Non-Linear Mechanics, 2020. **126**: p. 103556.
8. Tung, P.T., et al. *Nonlinear bending analysis of fgp plates under various boundary conditions using an analytical approach*. in *Structures*. 2021. Elsevier.
9. Long, N.V., T.M. Tú, and V.T.T. Trang, *Phân tích phi tuyến ứng xử uốn của tấm bằng vật liệu FGM xốp đặt trên nền đàn hồi Pasternak với các điều kiện biên khác nhau có xét đến vị trí thực của mặt trung hòa*. Tạp chí Khoa học Công nghệ Xây dựng (KHCN XD)-ĐHXDHN, 2020. **14**(4V): p. 1-15.
10. Long, N.V., T.M. Tú, and C.T. Binh, *Phân tích tĩnh tấm bằng vật liệu fgm xốp trên nền đàn hồi Pasternak theo phương pháp chuyển vị có kể đến tính phi tuyến hình học và vị trí mặt trung hòa*. Tạp chí Khoa học Công nghệ Xây dựng (KHCN XD)-ĐHXDHN, 2020. **14**(5V): p. 166-179.
11. Chen, D., J. Yang, and S. Kitipornchai, *Free and forced vibrations of shear deformable functionally graded porous beams*. International Journal of Mechanical Sciences, 2016. **108**: p. 14-22.
12. Barati, M.R. and A.M. Zenkour, *Investigating post-buckling of geometrically imperfect metal foam nanobeams with symmetric and asymmetric porosity distributions*. Composite Structures, 2017. **182**: p. 91-98.
13. Larbi, L.O., et al., *An efficient shear deformation beam theory based on neutral surface position for bending and free vibration of functionally graded beams*. Mechanics Based Design of Structures and Machines, 2013. **41**(4): p. 421-433.
14. Reddy, J.N., *Theory and analysis of elastic plates and shells*. 2006: CRC press.
15. Reddy, J.N., *Energy principles and variational methods in applied mechanics*. 2017: John Wiley & Sons.
16. Brush, D.O. and B.O. Almroth, *Buckling of bars, plates, and shells*. Vol. 6. 1975: McGraw-Hill New York.
17. Librescu, L. and M. Stein, *A geometrically nonlinear theory of transversely isotropic laminated composite plates and its use in the post-buckling analysis*. Thin-Walled Structures, 1991. **11**(1-2): p. 177-201.
18. Shen, H.-S., *Thermal postbuckling behavior of shear deformable FGM plates with temperature-dependent properties*. International Journal of Mechanical Sciences, 2007. **49**(4): p. 466-478.
19. Thai, H.-T. and D.-H. Choi, *A refined plate theory for functionally graded plates resting on elastic foundation*. Composites Science and Technology, 2011. **71**(16): p. 1850-1858.
20. Zenkour, A.M., *The refined sinusoidal theory for FGM plates on elastic foundations*. International journal of mechanical sciences, 2009. **51**(11-12): p. 869-880.
21. Putcha, N. and J. Reddy, *A refined mixed shear flexible finite element for the nonlinear analysis of laminated plates*. 1986.
22. Kapoor, H. and R. Kapania, *Geometrically nonlinear NURBS isogeometric finite element analysis of laminated composite plates*. Composite Structures, 2012. **94**(12): p. 3434-3447.

**Appendix 1:** The coefficients in Eq. (24) for SSSS boundary condition:

$$K_1 = \frac{\frac{D}{4}(\alpha_p \alpha_r \beta_q \beta_s - \alpha_p^2 \beta_s^2)}{\left[ (\alpha_p - \alpha_r)^2 + (\beta_q - \beta_s)^2 \right]^2}; \text{ (when } p=r \text{ and } q=s: K_1 = 0);$$

$$K_2 = \frac{\frac{D}{4}(\alpha_p \alpha_r \beta_q \beta_s - \alpha_p^2 \beta_s^2)}{\left[ (\alpha_p + \alpha_r)^2 + (\beta_q + \beta_s)^2 \right]^2};$$

$$K_3 = \frac{\frac{D}{4}(\alpha_p \alpha_r \beta_q \beta_s + \alpha_p^2 \beta_s^2)}{\left[ (\alpha_p - \alpha_r)^2 + (\beta_q + \beta_s)^2 \right]^2};$$

$$K_4 = \frac{\frac{D}{4}(\alpha_p \alpha_r \beta_q \beta_s + \alpha_p^2 \beta_s^2)}{\left[ (\alpha_p + \alpha_r)^2 + (\beta_q - \beta_s)^2 \right]^2};$$

**Appendix 2:** The coefficients  $g_{mpqrs}^{(3)}$  in Eq. (26)

$$g_{mpqrs}^{(3)} = g_{mpqrs}^{(3a)} + g_{mpqrs}^{(3b)} + g_{mpqrs}^{(3c)};$$

$$g_{mpqrs}^{(3a)} =$$

$$H_{1a} \cos \frac{(p-r)\pi x}{a} \sin \frac{m\pi x}{a} \cos \frac{(q-s)\pi y}{b} \sin \frac{n\pi y}{b}$$

$$+ H_{2a} \cos \frac{(p+r)\pi x}{a} \sin \frac{m\pi x}{a} \cos \frac{(q+s)\pi y}{b} \sin \frac{n\pi y}{b}$$

$$+ H_{3a} \cos \frac{(p-r)\pi x}{a} \sin \frac{m\pi x}{a} \cos \frac{(q+s)\pi y}{b} \sin \frac{n\pi y}{b}$$

$$+ H_{4a} \cos \frac{(p+r)\pi x}{a} \sin \frac{m\pi x}{a} \cos \frac{(q-s)\pi y}{b} \sin \frac{n\pi y}{b};$$

$$g_{mpqrs}^{(3b)} =$$

$$-2H_{1b} \sin \frac{(p-r)\pi x}{a} \cos \frac{m\pi x}{a} \sin \frac{(q-s)\pi y}{b} \cos \frac{n\pi y}{b}$$

$$-2H_{2b} \sin \frac{(p+r)\pi x}{a} \cos \frac{m\pi x}{a} \sin \frac{(q+s)\pi y}{b} \cos \frac{n\pi y}{b}$$

$$-2H_{3b} \sin \frac{(p-r)\pi x}{a} \cos \frac{m\pi x}{a} \sin \frac{(q+s)\pi y}{b} \cos \frac{n\pi y}{b}$$

$$-2H_{4b} \sin \frac{(p+r)\pi x}{a} \cos \frac{m\pi x}{a} \sin \frac{(q-s)\pi y}{b} \cos \frac{n\pi y}{b};$$

$$g_{mpqrs}^{(3c)} = -\left( K_{pqrs}^{(1)} \alpha_m^2 + K_{pqrs}^{(2)} \beta_n^2 \right) \sin \frac{m\pi x}{a} \sin \frac{n\pi y}{b};$$

in which:

$$H_{1a} = K_1 \left[ (\beta_q - \beta_s)^2 \alpha_m^2 + (\alpha_p - \alpha_r)^2 \beta_n^2 \right];$$

$$H_{2a} = K_2 \left[ (\beta_q + \beta_s)^2 \alpha_m^2 + (\alpha_p + \alpha_r)^2 \beta_n^2 \right];$$

$$H_{3a} = K_3 \left[ (\beta_q + \beta_s)^2 \alpha_m^2 + (\alpha_p - \alpha_r)^2 \beta_n^2 \right];$$

$$H_{4a} = K_4 \left[ (\beta_q - \beta_s)^2 \alpha_m^2 + (\alpha_p + \alpha_r)^2 \beta_n^2 \right];$$

$$H_{1b} = K_1 (\alpha_p - \alpha_r) (\beta_q - \beta_s) \alpha_m \beta_n; \quad H_{2b} = K_2 (\alpha_p + \alpha_r) (\beta_q + \beta_s) \alpha_m \beta_n;$$

$$H_{3b} = K_3 (\alpha_p - \alpha_r) (\beta_q + \beta_s) \alpha_m \beta_n; \quad H_{4b} = K_4 (\alpha_p + \alpha_r) (\beta_q - \beta_s) \alpha_m \beta_n;$$

# Experimental Study on Engineered Cementitious Composites Reinforced with Polypropylene Fiber

*Xuan-Vinh Tran<sup>1\*</sup>, Manh-Hung Nguyen<sup>1</sup>, Tien-Hong Nguyen<sup>1</sup>, Van-Thuc Luu<sup>2</sup>*

<sup>1</sup> Vinh University, Nghe An, Vietnam

<sup>2</sup> National University of Civil Engineering, Hanoi, Vietnam

*Email: vinhxd1989@gmail.com*

**Abstract.** This paper presents the results of experimental investigation on the influence of polypropylene (PP) fibers content on the compressive and flexural strengths of Engineered Cementitious Composites (ECC). Five ECC cube specimen groups under compression and five ECC thin beam groups under a four-point bending procedure with the PP fiber content ranging from 0% to 2.0% with an increment of 0.5% (by volume) were tested to determine the compression strength and flexural strength, respectively. For compressive specimens, the results showed that a higher content of fiber results in a significant decrease in the compressive strength. The PP fiber content of 0.5% achieves the highest compressive strength. For flexural specimens, the results revealed that with a higher content of PP fiber, the flexural strength of the mix decreases, and the deflection capacity increases. The PP fiber content of 1.5% achieves the highest flexural strength. In addition, the deflection capacity of specimens remarkably increases from 0.74mm for the specimen without PP fiber to about 14.89mm for the specimen with a 2.0% volume of PP fiber. It means that PP fibers help significantly enhance the ductility of flexural specimens. Finally, the addition of PP fiber changes the failure mode. The specimen without PP fiber fails suddenly without any warning, while specimens added with PP fiber have larger deformation.

**Keywords:** Bendable concrete, Composites concrete, Engineered Cementitious, Polypropylene fiber

## 1. Introduction

Traditional concrete has brittle and rigid behaviors, so it is almost unbendable. While subjected to tensile loading, conventional concrete produces cracks which leads to undesirably sudden failure of the concrete specimen without warning with the ultimate strain of 0.01% [1]. One solution to overcome this challenge is applying bendable concrete, known as Engineered Cementitious Composites (ECC). This is a unique type of high-performance fiber reinforced cementitious composites [2,3], characterized by high ductility and tight crack control capacity even at large deformation. The fibers added in the concrete mix act as bridges across the cracks to delay their propagation. This allows the mix to attain a higher ultimate strain and a more ductile failure mode. The tensile strain capacity of typical ECC is often above 2% which is 200 times greater than that of normal concrete, even up to 3-5% in some studies as reported by [4,5]. In addition, ECC has excellent energy absorption capabilities [6]. The unique properties of ECC make it a good choice for high-rise buildings and critical elements in seismic zones

ECC is made from the same basic ingredients as conventional concrete without coarse aggregates. It is because coarse aggregates in the mix will increase crack width. These composites are composed of binder, sand, water, a small number of admixtures, and an optimal number of fibers. Besides, comparing to traditional concrete, the power content of ECC is significantly higher, and it also is often supplemented with other cementitious materials such as fly ash, silica fume or blast furnace slag [6]. As a result, the cost of ECC is often higher than that of traditional concrete. Therefore, to achieve higher cost/performance ratio, ECC should be strategically applied in some parts of a structure where their advantages can be fully exploited. In detail, the flexural and fatigue behavior of ECC play an important role in many construction

applications such as coupling beams in multi-buildings, highway and airfield pavements, bridge decks and pavement overlays. In addition, ECC has the high resistance to crack growth, so the cooperation of an ECC layer in the tensile side of concrete components where cracks will initiate may enhance the flexural and fatigue performance of these components [7]. Moreover, because of brittle nature of traditional concrete, it cracks under tensile loading. This allows water and corrosive agents to intrude through the concrete material, hence destructing the structures. The high ductility and tight crack width control of ECC may help deal with these serious problems [8].

In early studies, many types of fiber including steel, glass, carbon, and polymer fibers were used to improve the bendability of concrete [7]. Unlike the fiber reinforced concrete, the ECC does not include large volume of fiber, and it normally uses short and discontinuous fibers with the low content, typically 2% by volume. Currently, there are many studies focusing on PP fiber and polyvinyl alcohol (PVA) fiber. An important advantage of ECC using these two fibers is its insulator which allows it not to carry current. This resistant is applied for many specific construction applications such as concrete rail ties, electrical power plant slabs, and hospital operating room floors [9]. Both PVA fiber and PP fiber are suitable for being reinforcing materials for cementitious composites. On the one hand, PVA fiber has higher modulus of elasticity, bonding, and tensile strength than PP fiber, so it seems to be investigated by many studies [4,5,7,10,11,12,13,14,15]. On the other hand, PP fiber's elongation is about four times higher than that of PVA fiber [1]. Nematollahi [16] investigated the effect of PP fibers on hardened properties of 3D-printed fiber-reinforced geopolymer mortars, a type of ECC, but this study only investigated with different percentages of PP fibers ranging from 0,25% to 1,00% by volume. Even though there has been some research regarding the effect of PP fibers on the engineering properties of ECC, a comprehensive study is needed to understand the influence of PP fiber with varying content on properties of ECC.

The present study aims at investigating the effect of PP fibers on compressive and flexural behavior of ECC with larger content, from 0% to 2%. A series of experiments were conducted to determine the mechanical properties as well as optimal content of PP fiber. Four-point bending tests on ECC thin beams were carried out to determine the flexural strength and establish the load-deflection behavior of ECC. The results were also compared to the values of ECC specimen without PP fibers to estimate the effective level of using PP fiber.

## 2. Materials and experiment setup

### 2.1. Materials

- **Binder (cement, fly ash, silica fume):** Portland cement PC40 of Vincem But Son with a density, fineness and the average particle size of  $3.07 \text{ g/cm}^3$ ,  $3550 \text{ cm}^2/\text{g}$  and  $22.13 \text{ }\mu\text{m}$ , respectively, and conforms with TCVN 2682:2009 standard. Fly ash (FA) was a class F type, following TCVN 10302:2014 standard. FA was obtained from Pha Lai heat power plant, Quang Ninh province. The average particle size of the FA was about  $19.42 \text{ }\mu\text{m}$ . The density and fineness of the FA were about  $2.23 \text{ g/cm}^3$  and  $3.65 \text{ cm}^2/\text{g}$ , respectively. Silica fume had a density of  $2.40 \text{ g/cm}^3$  and conforms with TCVN 8827:2011 standard.
- **Fine aggregate:** The nature sand from Red River with the modulus size of 2.76 had a density of  $2.63 \text{ g/cm}^3$ , conforming with TCVN 7570:2006 standard. The maximum particle size of the silica sand was 0.2 mm. As mentioned before, coarse aggregates were not used in the mix because the property of ECC is formation of micro cracks with large deflection. Meanwhile, coarse aggregates in the mix will increase crack width, which is not suitable with the property of ECC.
- **Polypropylene (PP) fiber:** PP fiber conforms with ASTM C1116 standard. The properties of PP fiber are listed in Table 1.

- **Chemical Admixtures:** BiFi-HV298 superplasticizer based on modified polymer with the specific gravity of 1,05 equivalent to the G type following ASTM C-494 standard. Superplasticizer was used to improve the matrix fluid properties resulting in an enhancement in the dispersion of PP fibers in the mix. Water used was clear water and suitable with TCVN 4506:2012 standard.

**Table 1.** Material properties of PP fiber

Type	Diameter (mm)	Length (mm)	Specific Gravity (kg/m <sup>3</sup> )	Tensile Strength (MPa)	Elastic Modulus (GPa)	Elongation (%)
PP	0.03	15	910	500	3.5	25

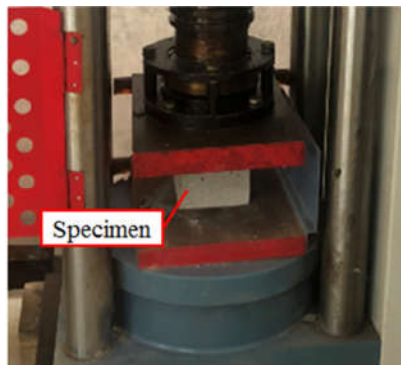
## 2.2. Mix proportions

Table 2 presents the ingredients and their mix relative proportions in ECC used in this investigation. The volumetric fraction of PP fiber was varied as 0%, 0.5%, 1.0%, 1.5%, 2.0%, added in total volume of concrete mix. Fly ash and silica fume make up 20% and 10%, respectively, of the total amount of binder. To enhance the workability of ECC, polycarboxylate based superplasticizer was added. The mix ratios of cement, sand, fly ash, silica fume, the percentage of fibers, water cement ratio and the amount of superplasticizer were chosen from trail mix and previous work so that the mix achieved the workability. The most suitable mix proportion is represented in Table 2.

**Table 2.** Mixture proportions of all ECC mixtures (by weight)

Mix ID	Sand	Cement	Fly Ash	Silica fume	Water	Superplasticizer	PP Fiber (by volume)
PP-0.0%	2.15	1	0.285	0.15	0.4	0.01	0.0%
PP-0.5%	2.15	1	0.285	0.15	0.4	0.01	0.5%
PP-1.0%	2.15	1	0.285	0.15	0.4	0.01	1.0%
PP-1.5%	2.15	1	0.285	0.15	0.4	0.01	1.5%
PP-2.0%	2.15	1	0.285	0.15	0.4	0.01	2.0%

## 2.3. Mixing, casting, curing



**Fig 1.** The setup for compressive test.

Table 3 shows the steps of mixing ECC used in this study. After mixing, the workability of ECC concrete was tested. Then the fresh ECC was casted into moulds to make specimens for hardened property tests. The compressive specimen size was 150×150×150 mm, and three specimens were made for each mix as required by the TCVN 3015:1993 standard, refer to Fig 1. The flexural specimen size was 600×150×20 mm, with three specimens for each mix. To determine the flexural strength of ECC, the thickness of specimen changed to 20mm, compared to 150mm as mentioned in TCVN 3119:1993 standard. This size helps to clearly observe flexural behavior of ECC specimens, as confirmed by other studies [11,12]. The specimens were covered with a plastic sheet in order to avoid moisture lost and cured at room temperature of  $27 \pm 2^\circ\text{C}$  for 24 hours, afterward they were demoulded and cured by water for 28 days. The linear variable differential transformer (LVDT) displacement sensors were employed to measure displacement. This device was placed at the mid-span of the bottom surface of the flexural specimen. The LVDT related to a data acquisition system via a computer and the readings were recorded and stored, as shown in Fig 2.

**Table 3.** ECC mixing process

Step	Description
1	Adding 100% of the total quantity of cement, sand, fly ash and silica fume
2	Adding gradually PP fiber, and mixing the dry materials evenly
3	Adding 50% of water and superplasticizer, and mixing evenly
4	Adding gradually remaining quantity of water and superplasticizer
5	Mixing till the homogenous mixture is formed
6	Discharging the mixture

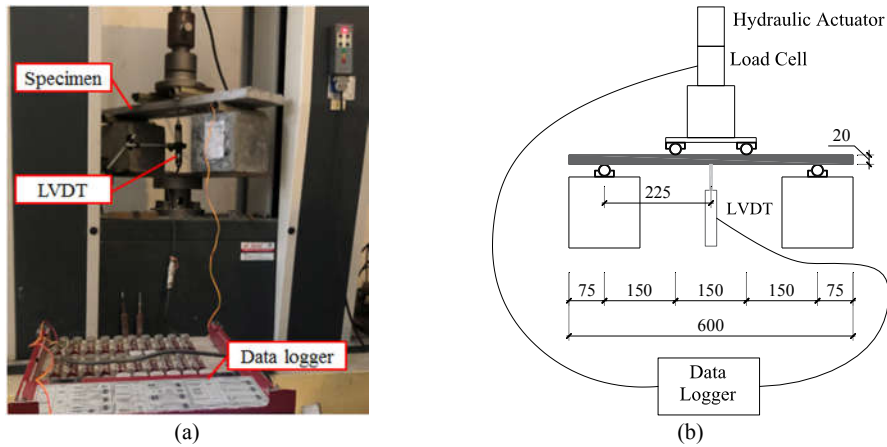


**Fig 2.** Test setup and arrangement of instrument of the bending test.

#### 2.4. Experiment setup

- **Compression test:** Apparatus and test procedure were applied according to TCVN 3118:1993 standard. The cubes of 150×150×150 mm were placed in the machine. The load direction was

perpendicular to the casting direction. Align carefully and load is applied till the specimen is broken.

- **Flexure Test:** Apparatus and test procedure were applied according to TCVN 3119:1993 standard. Four-point bending test was carried out to evaluate the flexural properties of ECC. The experimental load span was 150 mm (one third of the 450 mm support span). Flexural deformation was imposed on the surface of the specimen by the LVDT system. The experimental setup is shown in Fig 2. The tests were also conducted on the cube specimens at the age of 28th day.

### 3. Experimental results and discussion

#### 3.1. Compressive strength

Fig. 3 represents the 28-day compressive strength corresponding to every mixture with different percentages of PP fibers. The compressive strength of the PP-0% mix is about 30.1 Mpa. The value of compressive strength increases to about 34.9 Mpa (an increase of 16%) for the PP-0.5% mix because of the addition of 0.5 % PP fiber. However, with a further increasing amount of PP fiber, the value of compressive strength significantly reduces. The compressive strength of PP-1.0%, PP-1.5% and PP-2.0% declines to 29.5 Mpa, 26.7 Mpa and 24.3 Mpa, respectively. Compared to the PP-0% mix, the compressive strength of these mix decreases by 2%, 11.3% and 19.3%, respectively. This is because a higher content of fiber can result in an increase of the entrapped air, hence making the mixture become more porous. Thus, in terms of compressive strength, the mixture in which 0.5 % volume is PP fiber was the optimal mixture.

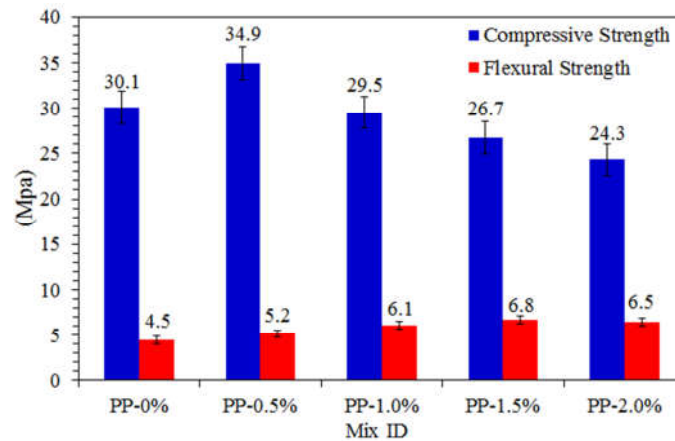


Fig 3. Compressive and flexural strength of the ECC with different content of PP fiber.

#### 3.2. Flexural strength

As shown in the Fig. 3, the flexural tensile strength of specimens increases along with the increase in volume fraction of PP in the mix until PP occupies 1.5% of volume. In detail, the flexural strength of the PP-0% mix, in which no PP fiber was used, is about 4.5Mpa. Meanwhile, the figure for the PP-1,5% mix is about 6.8 Mpa, a growth of above 40%. This increase is more pronounced in comparison to that observed for the compressive strength in section 3.1. This proves the effectiveness of PP fiber in enhancing the flexural behavior of the ECC. However, in the case of PP-2.0% mix, with higher content of PP fiber, the flexural strength of the mix tends to decrease.

Therefore, it can be concluded that the optimum PP fiber content is 1.5% of volume if considering the flexural strength of ECC.

The load-deflection behavior of all ECC specimens with different content of PP fiber is presented in Fig. 4. The flexural deflection capacity of the ECC thin beam reflects the ductile behavior of that ECC mixture. It is observed that an increase in the content of PP fiber increases deflection capacity of specimens which means that the addition of PP fibers significantly enhances the deflection hardening behavior. In detail, the specimen without PP fiber (PP-0.0%) fails when its deflection is just 0.74 mm. Meanwhile, the addition of 0.5% (PP-0.5%), 1.0% (PP-1.0%), 1.5% (PP-1.5%) and 2.0% (PP-2.0%) volume of PP fibers increase their deflection capacity to 5.25 mm, 10.12 mm, 11.32 mm and 14.89 mm, respectively. Furthermore, the addition of PP fiber changes mode of failure of specimens. With bristle nature of concrete, specimens without PP fiber rupture suddenly (Fig. 4a) without any warning while specimens with PP fiber have large deformation before failing (Fig. 4b).

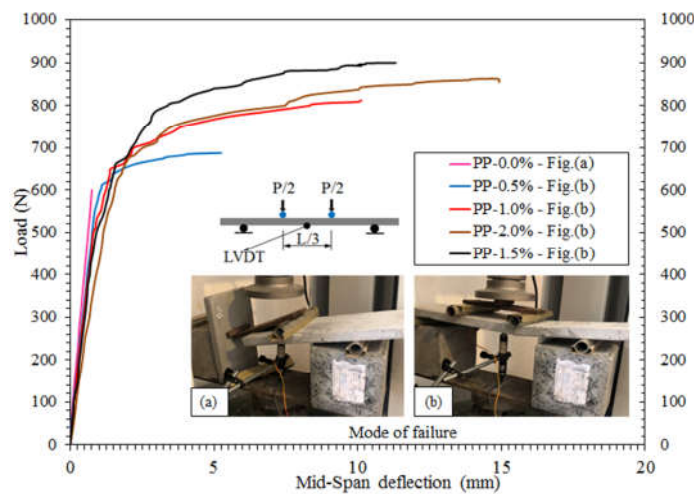


Fig. 4. Load-deflection relationship of the ECC flexural samples with different content of PP fiber.

#### 4. Conclusion

This study experimentally investigated the compressive and flexural behaviour of ECC with different scenarios of PP fiber content. Based on the test results obtained from the five different ECC mixtures, the following conclusions can be drawn:

- With a suitable content, the PP fiber can enhance compressive strength of ECC. The optimum value of the fiber content is about 0.5% by volume. Thereby, specimen whose 0.5% volume is PP fiber has compressive strength which is 16% higher than that of specimen without PP fiber. However, when the content of PP fiber is greater than 0.5%, the compressive strength significantly decreases.
- An increase in the content of the PP fiber leads to a rise in flexural strength. It can be concluded that the optimum PP fiber content is 1.5% of volume when considering the flexural strength. Compared to specimen without PP fiber, the flexural strength of the specimen with PP-1.5% mix is 40% higher. However, with higher content of PP fiber, the flexural strength of the specimen tends to decrease.

- It is observed that an increase in the content of PP fiber increases the deflection capacity of specimens which means that the addition of PP fibers significantly enhanced the ductility of ECC. Deflection capacity of specimens remarkably increases from 0.74mm (specimens without PP fiber) to about 14.89mm (specimens with 2.0% PP fiber).
- The addition of PP fiber change mode of failure of specimens. Specimen without PP fiber failed suddenly without any warning while specimens added with PP fiber have large deformation before failing.

## References

1. Sharbatdar Mohammad Kazem, Karami Mohammad (2008). Improving the mechanical properties of concrete elements by bendable concretes. *The 3rd ACF International Conference-ACF/VCA*, 2008: 571-577.
2. Victor C Li (2003). On engineered cementitious composites (ECC). *Journal of advanced concrete technology*, 1 (3): 215-230.
3. Victor C Li (2012). Tailoring ECC for special attributes: A review. *International Journal of Concrete Structures and Materials*, 6 (3): 135-144.
4. Kallepalli Bindu Madhavi, Mandala Venugopal, V Rajesh, Kunchepu Suresh (2016). Experimental study on bendable concrete. *Int. J. Eng. Res. Tech*, 5 (10): 501-504.
5. Yadavalli Sandeep, Bandaru Ambika (2019). Experimental Investigation on Bendable Concrete.
6. Sagar Gadhya, TN Patel, Dinesh Shah (2015). Bendable concrete: a review. *international journal of structural and civil engineering research*, 4.
7. Tushar R Patil, B. V. Birajdar (2017). Flexible Behaviour of Concrete Using Engineered Cementitious Composites. *International Journal of Advance Engineering and Research Development*, 4 (5): 5.
8. Michael Lepech, Victor C Li (2005). Design and field demonstration of ECC link slabs for jointless bridge decks. *Proceedings of the 3rd International Conference on Construction Materials: Performance, Innovations and Structural Implications*, Citeseer: 22-24.
9. Michael Lepech, Victor C Li (2005). Durability and long term performance of engineered cementitious composites. *Proceedings of the International Workshop on HPFRCC in Structural Applications*: 23-26.
10. Ganesh S Ghodke, Nilesh S Daphal, Yogesh S Bandgar, Dattatraya S Gadekar, Sagar A Chavan, Ashwini Waghule (2017). Experimental study of bendable concrete by using admixture and fiber. *Int J Tech Res Eng*, 4 (9).
11. IR Mithanthaya, M Shriram, VS Sandeep (2017). "Flexural behaviour of fiber reinforced concrete using PVA-ECC", Ed. Editors, IJCRT.
12. Yen-Fang Su, Romika Roshan Kotian, Na Lu (2018). Energy harvesting potential of bendable concrete using polymer based piezoelectric generator. *Composites Part B: Engineering*, 153: 124-129.
13. S Uttamraj, K Ashwanth, Md Rafeeq (2016). A comparative study on conventional concrete and engineered cementitious composites(ecc-pva)-review. *Iosr Journal of Mechanical and Civil Engineering (IOSR-JMCE) E-ISSN: 2278-1684*.
14. Shuxin Wang, Victor C Li (2006). High-early-strength engineered cementitious composites. *ACI Materials journal*, 103 (2): 97.
15. UL Deshpande, Pranesh B Murnal (2016). Ductile Concrete Using Engineered Cementitious Composites. *Inter. J. Eng. Res*, 5013 (5).
16. Behzad Nematollahi, Praful Vijay, Jay Sanjayan, Ali Nazari, Ming Xia, Venkatesh Naidu Nerella, Viktor Mechtcherine (2018). Effect of polypropylene fiber addition on properties of geopolymers made by 3D printing for digital construction. *Materials*, 11 (12): 2352.

# A Study on Elastic Critical Buckling Strength of Continuous Steel Beams Subjected to Uniformly Distributed Load

Xuan-Tung Nguyen<sup>1(✉)</sup>, Minh-Thu Nguyen<sup>2</sup> and Xuan-Ba Ho<sup>1</sup>

<sup>1</sup>Campus in Ho Chi Minh City, University of Transport and Communications, Ho Chi Minh City, Vietnam

<sup>2</sup>Department of Civil Engineering, Vinh University, Vinh City, Vietnam

Emails: tungnx\_ph@utc.edu.vn, thunm@vinhuni.edu.vn, bahx\_ph@utc.edu.vn

**Abstract.** This paper presents a numerical study on elastic critical buckling strength of continuous steel beams subjected to uniformly distributed load at the top flange. Numerical analysis was employed by using a finite element analysis program, ABAQUS. The effect of the length-to-height ratio on elastic critical buckling strength of continuous steel beams was considered. The equations from existing design codes and literature were also used to determine the elastic critical buckling and compared to finite element results. The results show that the elastic critical buckling strengths of continuous steel beams using existing equations from design codes and literature give conservative for most cases and tend to be over-conservative as the length-to-height ratio rises.

**Keywords:** Steel Beam; Finite Element Analysis; Elastic Critical Buckling; Length-to-Height Ratio.

## 1. Introduction

Continuous beam is the common structure in high-rise buildings and bridges. When they are subjected to uniformly distributed load, the negative moment occurs at interior supports, as shown in Fig. 1. The elastic critical buckling of steel beams has been widely studied. Kitipornchai and Wang [1], Kitipornchai et al. [2], Wang and Kitipornchai [3] proposed design graphs to determine the elastic buckling strength of the simple beam with the monosymmetric cross-section. Lim et al. [4] performed a numerical study to investigate the elastic buckling of steel I-beams under linear moment gradient. Elastic buckling of the steel beam subjected to simultaneous transverse loadings and end moments was also studied [5-7]. In addition, studies on the influence of load height on the elastic buckling of the beam were also performed [8-10]. Park et al. [11] and Park [12] conducted numerical studies on the lateral buckling of stepped beams with continuously laterally braced top flange. Nonetheless, the elastic critical buckling of continuous steel beams subjected to uniformly distributed load at the top flange has not been studied.

To investigate the elastic buckling of continuous beams subjected to uniformly distributed load at the top flange, the simple beam subjected to simultaneous uniformly distributed load at the top flange and negative end moments was employed. The effect of the length-to-height ratio on elastic critical buckling strength of continuous steel beams was also considered. Numerical analysis was employed by using a finite element analysis program, ABAQUS.

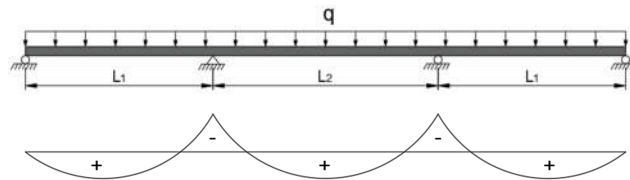


Fig. 1. Continuous beam.

## 2. Specifications and Previous Study

Timoshenko and Gere [13] presented the elastic buckling for doubly symmetric I-beam subjected to pure bending as follow

$$M_{ocr} = \frac{\pi}{L} \sqrt{EI_y GJ + \left(\frac{\pi E}{L}\right)^2 I_y C_w} \quad (1)$$

where  $L$  is the unbraced length;  $E$  and  $G$  are Young's modulus and the shear modulus, respectively;  $I_y$  is the inertia moment of the cross-section about the minor axis;  $J$  is the torsional constant;  $C_w$  is the warping constant.

Existing design codes provided guidelines to determine the elastic critical buckling of steel beams subjected to general loading conditions by multiplying  $M_{ocr}$  by a moment correction factor ( $C_b$ ). The moment correction factor ( $C_b$ ) was proposed by Kirby and Nethercot [14] and used in ANSI/AISC Specifications [15] as presented in Eq. (2).

$$C_b = \frac{12.5M_{max}}{2.5M_{max} + 3M_A + 4M_B + 3M_C} \quad (2)$$

where  $M_{max}$  is the absolute value of maximum moment;  $M_A$ ,  $M_B$ , and  $M_C$  are the absolute value of moments at the quarter point, the center point, and three-quarter point, respectively.

The equation of  $C_b$  used in the BS 5950 [16] is given as

$$C_b = \frac{M_{max}}{0.2M_{max} + 0.15M_A + 0.5M_B + 0.15M_C} \leq 2.273 \quad (3)$$

AS 4100 [17] provides the moment correction factor with Eq. (4)

$$C_b = \frac{1.7M_{max}}{\sqrt{M_A^2 + M_B^2 + M_C^2}} \leq 2.5 \quad (4)$$

Helwig et al. [18] proposed a formula for the moment gradient factor of simple beams considering the effect of load height as presented in Eq. (5) and also mentioned in Ziemian [19].

$$C_b^* = (1.4^{2y/h}) C_b \quad (5)$$

where  $C_b$  is calculated using Eq. (2);  $h$  is the beam depth;  $y$  is the distance from the midheight of the cross-section to the position of loading.

## 3. Finite Element Modeling

The numerical investigation on the elastic critical buckling of continuous steel beams subjected to uniformly distributed load was conducted utilizing the finite element analysis (FEA) software, ABAQUS [20]. The cross-section of the steel beam used was H700x300x13x24. The length-to-height ratios ( $L/h$ ) of the steel beam used were from 10 to 40. The steel beam had an elastic modulus ( $E_a$ ) of 210 GPa and a yield strength ( $f_y$ ) of 275 MPa. In order to investigate the elastic buckling of continuous beams subjected to uniformly distributed load at the top flange, the simple beam subjected to simultaneous uniformly distributed load at the top flange and negative end moments was employed. A four-node reduced integration shell element S4R was chosen for the beam model. Fig. 2 shows the boundary condition of the simple steel beam in this study. Both ends of the beam were restricted against vertical, lateral displacements. The axial displacement of one end was prevented for the hinge support and the other one was free for the roller support.

The simple steel beams were subjected to uniformly distributed load on the top flange with negative end moments, as shown in Fig. 3.  $M_1$  and  $M_2$  are the larger and smaller end moments.  $\alpha$  is the ratio between  $M_1$  and  $M_2$  to consider the end moments variation. The  $\alpha$  values are 0, 0.5, 0.75, and 1.  $M_q$  is the moment at midspan of the simple beam caused by the uniformly distributed load with respect to unbraced length  $L$ . To consider the influence of the variation in the negative end moments and uniformly distributed load, the  $M_q/M_1$  ratios ranging from 0.5 to 3 with an

interval of 0.5 were used in this study. The negative end moments were expressed as the compression at the bottom flange and tension forces at the top flange, as shown in Fig. 4.

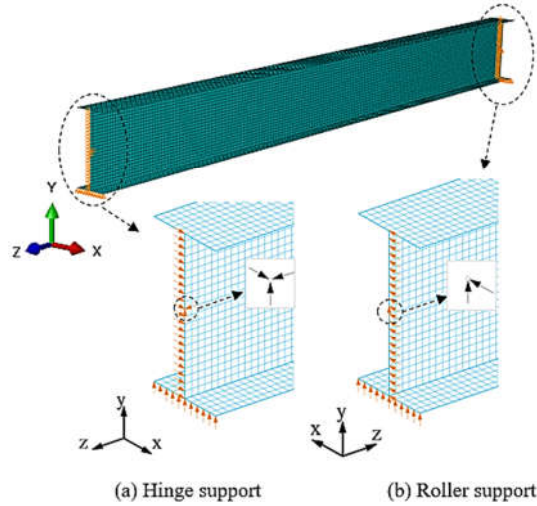


Fig. 2. Beam model and boundary conditions.

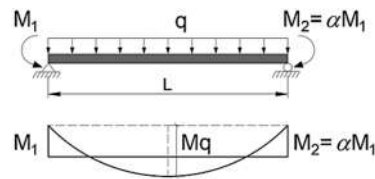


Fig. 3. Loading conditions.

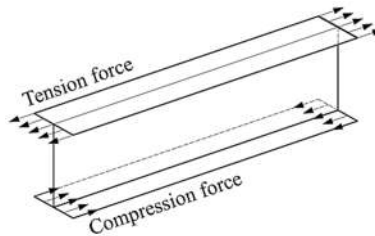


Fig. 4. End moment simulation.

#### 4. Finite Element Results

Figs. 5(a) and (b) present FEA results for steel beams for representative cases with  $\alpha$  of 0 and 1 corresponding to the cases of one negative end moment and negative end equal moments, respectively. The results are presented as the ratio of the elastic critical buckling of beams,  $M_{cr}$ , to the elastic critical buckling of beams subjected to end equal moments,  $M_{ocr}$ , with respect to  $M_q/M_1$ . The results show that the ratio  $M_{cr} / M_{ocr}$  increases as the ratio  $L/h$  increases. These figures also indicate that the  $M_{cr} / M_{ocr}$  values are larger than 1 and change with the shape of bending moment diagrams.

The equations to calculate the  $C_b$  factor were obtained from Eqs. (2), (3), (4), and (5) corresponding to AISC [15], BS 5950 [16], AS 4100 [17], and study of Hewlig et al. [18]. Fig. 6 shows comparisons between the FEA results and the existing equations. The results show that the predicted values utilizing AISC, BS 5950, and AS 4100 are conservative for most cases and tend to be over-conservative as the  $L/h$  ratio increases, as shown in Figs. 6(a), (b), and (c), respectively. There are a few cases for unconservative results with small  $L/h$  values. Helwig's study gives over-conservative values for all models which increase as the  $L/h$  ratio increases, as shown in Fig. 6(d). AISC, BS 5950, AS 4100, and Helwig's study give maximum differences for conservative values of 50.7%, 59.3%, 55.3%, and 64.8%, respectively. The maximum differences for unconservative values are -35.4%, -4.6%, and -27.4% for AISC, BS 5950, and AS 4100, respectively.

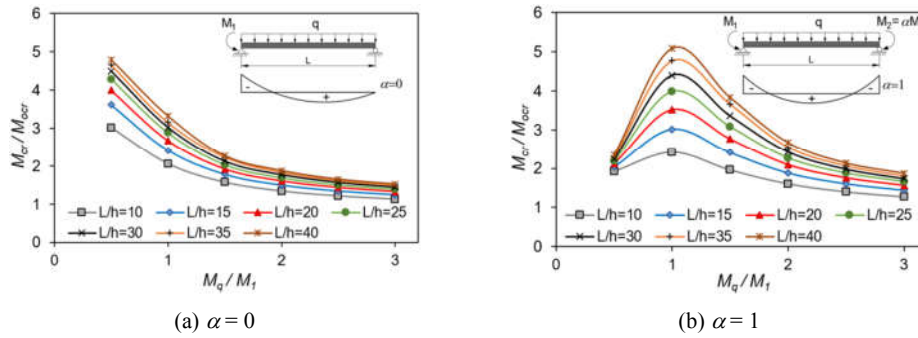


Fig. 5. Finite element analysis results.

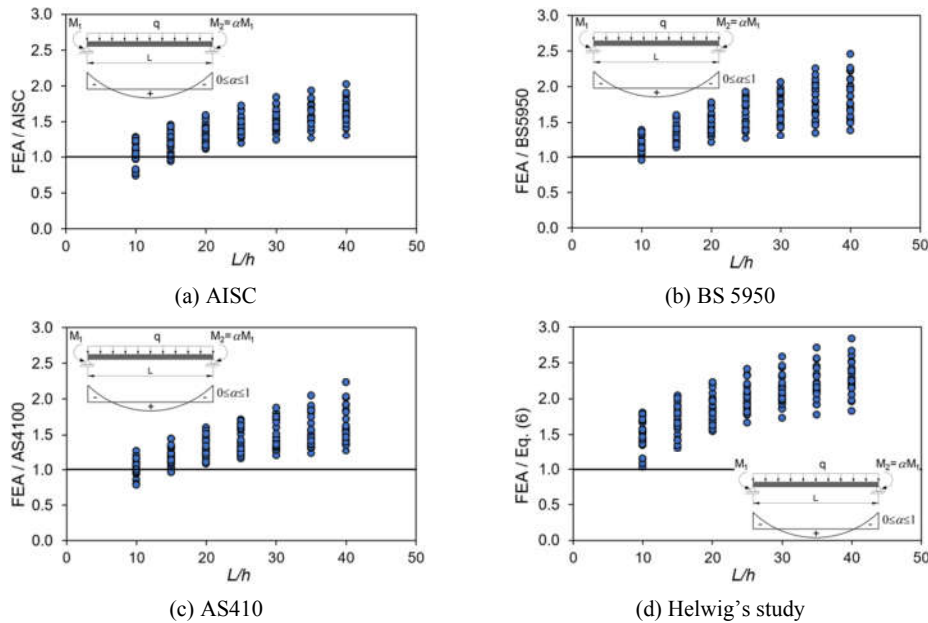


Fig. 6. Comparison of elastic critical buckling between FEA results and existing equations.

In Eqs. 2, 3, and 4, the loads are placed at the cross-sectional center. The effect of the length to height ratio of the beam is not considered in these equations. Therefore, the predicted values are

conservative and tend to be over-conservative as the  $L/h$  ratio increases. Helwig et al. [18] proposed the formula for the moment gradient factor of simple beams considering the effect of load height. Thus, the results for the continuous beam subjected to uniformly distributed load at the top flange are more conservative than those from AISC, BS 5950, and AS 4100.

## 5. Conclusions

This paper presents a numerical study on elastic critical buckling strength of continuous steel beams subjected to uniformly distributed load at the top flange. In order to investigate the elastic buckling of continuous beams, the simple beam subjected to simultaneous uniformly distributed load at the top flange and negative end moments was employed. Numerical analysis was employed by using a finite element analysis program, ABAQUS. The effect of the length-to-height ratio on elastic critical buckling strength of continuous steel beams was considered. The equations from existing design codes and literature were also used to determine the elastic critical buckling and compared to finite element results. The results show that the elastic critical buckling strengths of continuous steel beams using existing equations from design codes and literature give conservative for most cases and tend to be over-conservative as the length-to-height ratio rises.

## References

1. Kitipornchai, S., Wang, C.M.: Lateral buckling of tee beams under moment gradient. *Computers & Structures* 23, 69-76 (1986).
2. Kitipornchai, S., Wang, C.M., Trahair, N.S.: Buckling of monosymmetric I-beams under moment gradient. *Journal of Structural Engineering* 112, 781-799 (1986).
3. Wang, C.M., Kitipornchai, S.: Buckling capacities of monosymmetric I-beams. *Journal of Structural Engineering* 112, 2373-2391 (1986).
4. Lim, N.H., Park, N.H., Kang, Y.J., Sung, I.H.: Elastic buckling of I-beams under linear moment gradient. *International Journal of Solids and Structures* 40, 5635-5647 (2003).
5. Suryatmono, B., Ho, D.: The moment-gradient factor in lateral-torsional buckling on wide flange steel sections. *Journal of Constructional Steel Research* 25, 1247-1264 (2002).
6. Serna, M.A., López, A., Puente, I., Yong, D.J.: Equivalent uniform moment factors for lateral-torsional buckling of steel members. *Journal of Constructional Steel Research* 62, 566-580 (2006).
7. Wong, E., Driver, R.G.: Critical evaluation of equivalent moment factor procedures for laterally unsupported beams. *Engineering Journal, American Institute of Steel Construction* 47, 1-20 (2010).
8. Park, N.H., Kang, Y.J., Jo, Y.M., Lim, N.H.: Modification of C-equation in the SSRC Guide for buckling of monosymmetric I-beams under transverse loads. *Engineering Structures* 29, 3293-3300 (2007).
9. Bijak, R.: The lateral buckling of simply supported unrestrained bisymmetric I-shape beams. *Archives of Civil Engineering* 61, 127-140 (2015).
10. Lamb, A.W., Eamon, C.D.: Load height and moment factors for doubly symmetric wide flange beams. *Journal of Structural Engineering* 141 (2015).
11. Park, J.S., Stallings, J.M.: Lateral-torsional buckling of stepped beams with continuous bracing. *Journal of Bridge Engineering* 10, 87-95 (2005).
12. Park, J.S.: Lateral buckling formula of stepped beams with length-to-height ratio factor. *Structural Engineering and Mechanics* 18, 745-757 (2004).
13. Timoshenko, S., Gere, J.M.: *Theory of elastic stability*. McGraw-Hill International Book Company, New York (1961).
14. Kirby, P.A., Nethercot, D.A.: *Design for structural stability*. John Wiley and Sons, New York, USA, (1979).
15. ANS/AISC 360-16: *Specification for structural steel buildings*. American Institute of Steel Construction, Chicago, IL, USA (2016).
16. BS 5950: *Structural use of steelwork in building - Part 1: Code of practice for design - Rolled and welded sections*. British Standards Institution (2000).
17. AS4100: *Steel structures*. Standard Australia, NSW, Australia (2020).

18. Helwig, T.A., Frank, K.H., Yura, J.A.: Lateral-torsional buckling of singly symmetric I-beams. *Journal of Structural Engineering* 123, 1172-1179 (1997).
19. Ziemian, R.D.: *Guide to Stability Design Criteria for Metal Structures*. 6th edn. John Wiley & Son, Inc., New Jersey, USA, (2010).
20. ABAQUS/CAE: Version 6.20. Dassault Systèmes: RI, USA. (2020).

# Analyzing the causes and proposed some solutions to minimize water inflation during the rainy season in Vinh City, Nghe An

*Thu-Hang Nguyen Thi*

Department of Civil Engineering, Vinh university, Vietnam

*Email: thuhang@vinhuni.edu.vn*

**Abstract:** Flooding is a typical phenomenon in urban areas in Central Vietnam during the rainy season that lasts from June to October every year. Vinh city of Nghe An province is greatly affected by this phenomenon. In recent times, the rapid urbanization has caused rivers to be filled a lot, flood storage space is narrowed, the drainage system is overloaded causing widespread flooding in the rainy seasons, leading to economic activities such as fisheries, Industry, agriculture will emit a large source of wastewater containing many toxic chemicals. This article aims to analyze the causes and proposed some measures to overcome the prolonged flooding in the flood season in Vinh city of Nghe An province.

**Keywords:** Vinh city, Flooding, technical infrastructure, drainage, flooding.

## 1. Introduction

In recent years, the appearance of the city has changed significantly. The city's economic structure start turning positively, economic growth is on rise, urban infrastructure is focused on investment, architecture, urban landscape is interested in renovating and building new. However, along with the fear of socio-economic development, the rapid pace of urbanization, the urban space is constantly expanding, which means that the rate of concretization increases rapidly the area of ponds and low-lying areas decreases leading to the drainage completely dependent on new construction ditches. In addition, the drainage system has been around for a long time, many ditches are settled and degraded, while the construction of new, repaired and repaired is not synchronized, causing many drainages to not be fully promoted effectively.

Urban flooding suffers great economic and even life-threatening damage, so fighting urban flooding is a measure to help grow the economy. In order to effectively prevent flooding in Vinh city, it is necessary to have a synchronous solution, strategic planning and especially need the input of experts and community consciousness in flood prevention.

This article outlines the causes and solutions to limit flooding in the city with non-construction solutions and works combined harmoniously, supporting each other. In parallel with the construction measures such as: Expanding drainage canals, adding valve doors at the sewer site, building flood reservoirs and slowing floods, it is necessary to take non-construction measures such as: land management of flood zones, flood forecasting, restoration and flood insurance, share the losses caused by the flood.

## 2. Natural characteristics - society of Vinh city affect the flood situation

### 2.1. Geographic location

Vinh City is a Class I municipality, the political and economic and cultural center of Nghe An province, located in the south of the province, downstream of the Nam - Hung - Nghi region, surrounded by 4 main rivers: Dao River, Cua Tien River in the South, Ke Gai River in the West, Rao Dung River in the Northeast, The Lam River in the east and south of the city. The city centre is 17km west of the East Ocean, the nearest point about 3km from the East Ocean.

## 2.2. Climate

Average annual rainfall from 1.800 ÷ 2.043 mm (Nghị Loc: 1.800 mm, Vinh: 2.043 mm). Concentrated mainly on the rainy season, rainfall in 3 months 8, 9, 10 (accounting for 61% of the rainfall for the whole year). The largest 1-day rainfall reached 596,7 mm (11<sup>th</sup> October 1989), the largest 3-days rainfall can reach 950 mm (14<sup>th</sup> ÷ 16<sup>th</sup> October 2019), the heaviest 5-day rain can reach over 1.000 mm (14<sup>th</sup> ÷ 18<sup>th</sup> October 2010). The highest hourly rainfall was 142 mm (8<sup>th</sup> October 1965 in Vinh). Largest water level on Lam River: In Ben Thuy: 5,64 m; at Rao Dung: 3,15 m (28<sup>th</sup> September 1978) [2].

According to the climate change scenario of the Ministry of Natural Resources and Environment published in 2011: The average rainfall forecast will increase by 1,2% (in 2020) by 1,7% (in 2030) 3,1% (in 2050) 5,9% (in 2100). Sea level rise forecast increase 7 ÷ 8 cm (2020) 11 ÷ 13 cm (2030) 20 ÷ 24 cm (2050), 49 ÷ 65 cm (2100) [3]

## 2.3. Social

In recent years, the speed of urbanization in Vinh has been rapid: the administrative boundaries have been opened further to the west, from 13 wards now increased to 16 wards, 5 communes increased to 9 communes, the natural area of the whole city increased from 67.53 km<sup>2</sup> to 104.96 km<sup>2</sup>, of which the area of the central area reached nearly 36 km<sup>2</sup>. By 2020, the area of the whole city is up to 250 km<sup>2</sup>. Regarding the future, Vinh city urban area includes: Vinh urban area, Cua Lo town, Quan Hanh town and new urban areas according to the plan. Vinh was recognized as a class 1 municipality in decision No. 1210 dated 5<sup>th</sup> September 2008 of the Prime Minister.

## 2.4. Drainage system

According to the natural terrain, the main escape direction of the city is to the South and Southeast flowing into the main rivers such as the Lam River, Vinh River, Ke Gai River, and Dao Rung River. Vinh City's drainage system includes:

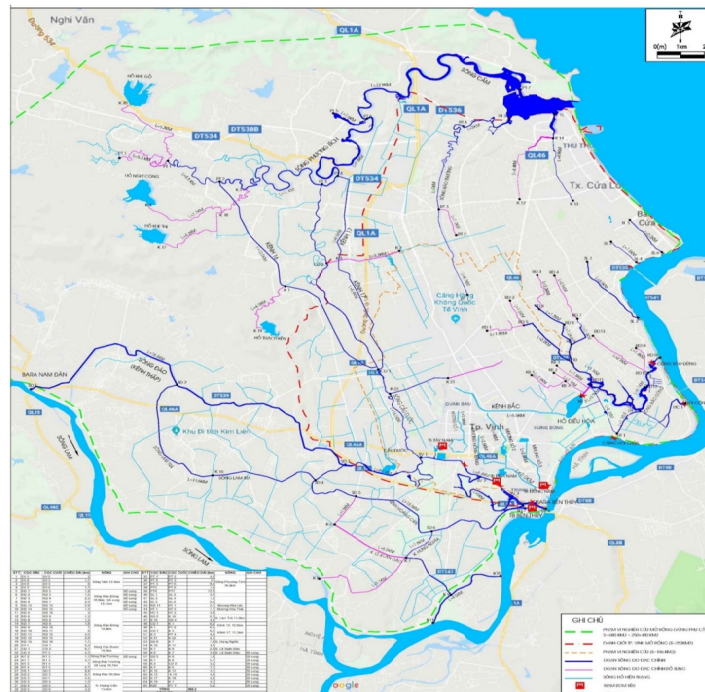


Fig. 1. Map of Vinh city river basin (source of Nghe An irrigation department).

- Vinh – Ke Gai River system and Rao Dung River serve the drainage of the Lam River and The East Ocean.

- The main ditch system consists of North Canal, head canal, secondary canal, tertiary canal, Hong Bang Ditch and Dong Vinh Ditch with a total length of about 15km. The main ditch system drains the water itself or pumps forcibly into the river when the flood rise.

- Secondary and tertiary canal system of the basin with a total length of about 400 km.

The system operates according to the principle: Rainwater of each basin is collected to the system of ditches, secondary and tertiary sewers, and flow to the system of head ditches, then flow to the Ke Gai River in the west, Vinh river in the south and Rao Dung River in the east flowing to the Lam River. The city is divided into 4 main drainage basins.

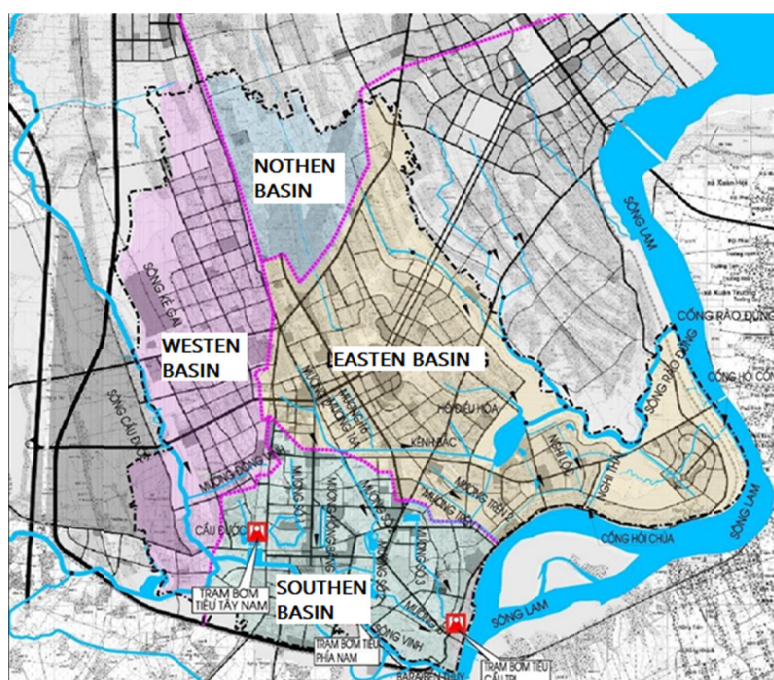


Fig. 2. Drainage basins of the city (source: Nghe An Irrigation Department).

## 2.5. Status of drainage works system

Sedimentation and congestion on the ditch routes are common. The main reason is that the funding allocated to maintain, dredge, connect the drainage system is located too little compared to the scale of the system. People's awareness in protecting the drainage system is not high, the situation of dumping waste into drainage ditches causes local congestion at many points on the system while it is difficult to check for treatment.

Some focal works (pump, water saving installation, full tide cofferdam) no longer meet the real needs. The reason is that the application of calculation parameters at the time of planning in 2004 is no longer suitable for the current period due to the negative impact of climate change (unseasonal rain, heavy rainfall, rising sea and river levels). According to calculations for rainfall exceeding 120 mm/hour, the works in the city's drainage system will not meet. However, the reality is that the system only works about 70% of the capacity (equivalent to about 84 mm/hour of rainfall).



**Table 2.** Assessment of the situation of flooding of Vinh city in recent years

Year	Flooded area, flooded route	Flooding depth	Damages
2016	Quang Trung, Phan Boi Chau, Ly Thuong Kiet, Dinh Cong Trang, Hong Bang, Nguyen Thai Hoc, Nguyen Van Cu, Le Hong Phong, Nguyen Thi Minh Khai, Le Loi, Le Nin, Mai Hac De	0,5m-1,0m	
2017	- Yen Giang area, Vinh Tan, Cua Tien, Ben Thuy - Dinh Cong Trang, Hong Bang, Dan Thai Than, Quang Trung - Vinh Market	>1,0m 0,5m-1,0m 1,5m	
2018	-Nguyen Van Cu, Dang Thai Than, Quang Trung, Nguyen Thi Minh Khai, Dinh Cong Trang, Le Hong Phong, Ly Thuong Kiet, Le Nin -Truong Thi	0,5m-0,7m 0,4m	
2019	- Nguyen Thi Minh Khai, Dang Thai Than, Phan Boi Chau, Dinh Cong Trang, Le Ninh, Phong Dinh Cang, Quang Trung, Ly Thuong Kiet, Le Hong Phong, Le Nin, Nguyen Van Cu - Vinh Market	0,5m-1,0m 1,2m	-Evacuate 250 households -20,000 birds died -370ha of ponds and lakes for farming -54ha of rice, 195ha of vegetables
2020	- Trung Do, Ben Thuy - Vinh Market	0,8m-1,5m 1,5m	

## 2.6. General assessment of the cause of flooding in Vinh City

Rapid urbanization: The settlement with a high population density leads to the rapid concrete of the urban surface, which makes the area of water permeability less, preventing the possibility of on-site drainage in the event of heavy rain. The technical infrastructure is not synchronized, incomplete, the size of the sewer is too small, the quality of materials is low. Inadequate operation and maintenance, lack of cooperation from the community leading to reduced capacity of flow, clogged pipes and manholes due to indiscriminate waste. In recent years, unusual climatic conditions have caused extreme rainfall events of intensity, frequency and morphology, along with sea level rise leading to high flood risks for Vinh city. Heavy rain lasted for many days, and the rain drainage system was not guaranteed, again encountered when the water level on the Lam River was high, leading to drainage for Vinh city area very slowly causing flooding in the urban and surrounding areas.

## 3. Flood protection solution for Vinh city

### 3.1. Rainwater storage solution

#### 3.1.1. Solutions for planning and development of Equalizing basin system

Vinh city has 22 lakes with a total area of about 400 ha scattered in the city. Lakes play a very important role in storing buffer water to drain water for residential areas.

However, urban development along with the increase in population leads to the exploitation of unplanned premises, occupied open surfaces, obstructed flow. Meanwhile, the drainage system is built in a patchwork style, exists in the planning of design, construction, management, so every rainy season, many parts of the city are flooded. Taking advantage of the water storage capacity of the air-conditioned lakes to minimize flooding for Vinh city in the current urbanization context is very necessary.





**Fig. 5.** Pervious concrete.

Vinh city is building 4 pedestrian streets including: Ho Tung Mau Street; Nguyen Van Cu Street; Nguyen Trung Ngan Street connects to Lane 2, Nguyen Trung Ngan Street, the end point intersects Nguyen Van Cu Street and Nguyen Tai Street. Expected parking space for cars includes Parking space No. 1 at Ho Chi Minh Square, Parking space for Giao Te Hotel and Provincial Labor Culture department. Reticulated molding can be applied in these parking lots.



**Fig. 6.** Reticulated molding of Car park tile.



**Fig. 7.** Expected parking space on pedestrian street.

### **3.1.3. Water flood by reservoir**

Rainwater reservoir solutions have been applied over the years and are still being used in cities around the world today. Rainwater is stored on the roof or channeled into ground water tanks. It is possible to use regulations or encourage people to use this method.

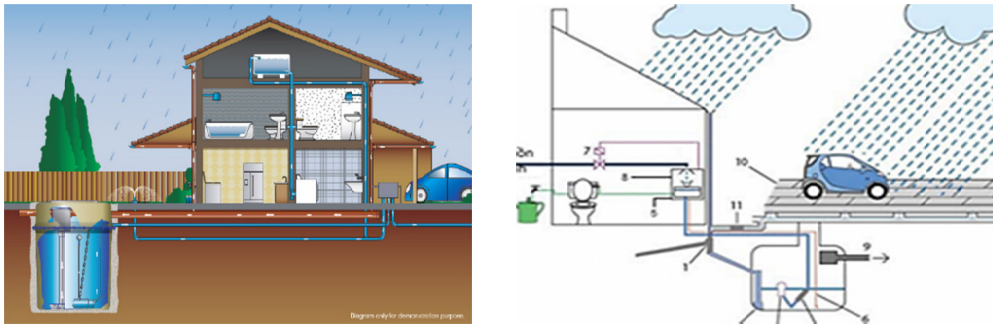


**Fig. 8.** Typical rainwater collection system of houses.

Build underground water tanks with tanks higher than the road surface to store rainwater. Flood computation Calculate the tank capacity and the reasonable amount to accommodate the above amount of water. Use large capacity pumping stations to pump the amount of flooded water into the tank. Using this water for watering plants, washing roads, fighting fires will not be wasted water resources. Locations can be built bus station, green park, stadium, amusement park, square, school campus.

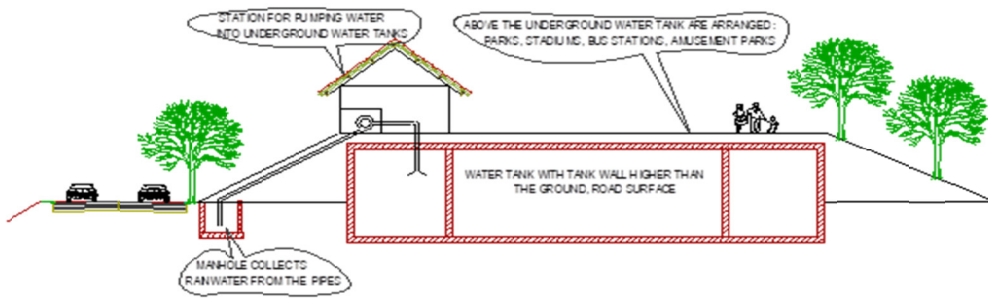


**Fig. 9.** Rainwater storage under the parks.

### 3.2. Methods of Improvement

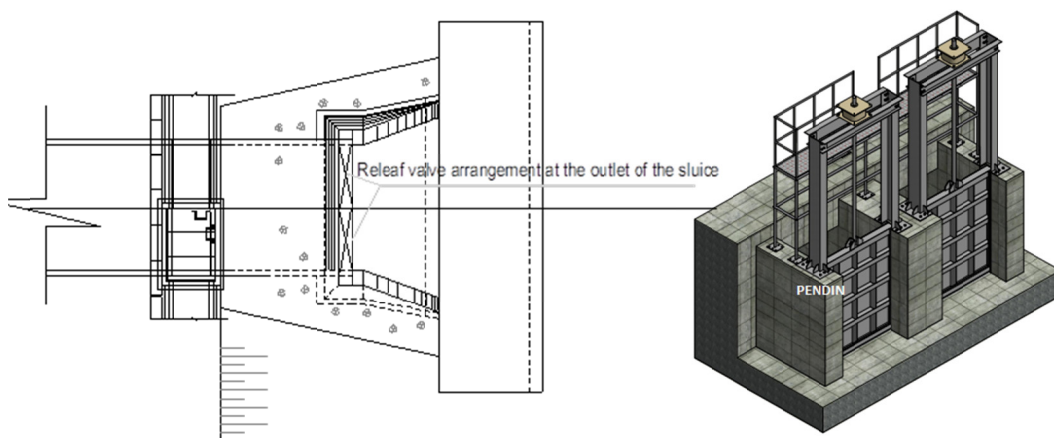


**Fig. 10.** Arrange the valve door at the drain site.

Reduce the level of flooding by adding a relief damper structure and in combination with a portable pumping station. When the rain is heavy, the water level in the urban area will be lower than the water level in the canal or river, the valve door will close. The pumping station operates to draw water from the water collection pit to the river or canal while increasing the speed at which the water flows to the drain until the internal water pressure is greater than outside the river, then the valve door will open to drain the water to the river. If localized flooding occurs due to the flow velocity in the small drain, we can use the pump at the outlet to increase the flow velocity in the drain, then the level of flooding and the time of flooding in the area will be reduced and shortened.

Proposing the list of works in the order of priority of construction in phases based on the current status quo, the general planning of Vinh city and the zoning plan of approved communes is also an effective method of improvement.

**Table 3.** Expected immediate investment in projects that need improvement

No.	Project	Technical solutions	Investment objectives
1	Expand the water collector and increase the capacity of the Black Bridge pumping station	Construction and expansion of the water collector of the Black Bridge pumping station as planned; increase the total pumping station capacity from 54,000m <sup>3</sup> /h to 71,000m <sup>3</sup> /h	Addressing flooding in Hung Binh, Hung Phu, Truong Thi, Trung Do and Vinh Tan wards
2	Raising the capacity of The Tri Bridge Pumping Station (Ben Thuy)	Increase the total pumping station capacity from 20,000m <sup>3</sup> /h to 40,000m <sup>3</sup> /h	Flood settlement for Truong Thi wards, Ben Thuy
3	Construction of pepper pumping station in Vinh market area	Investment in building a reservoir Vinh market water and building a pumping station with a capacity of 25,000 m <sup>3</sup> /h	Flood settlement for Le Mao, Quang Trung and Hong Son
4	Construction of Can Linh Pagoda pumping station to replace Tay Nam pumping station	Construction of new pumping station at Can Linh Pagoda with capacity of 30,000 m <sup>3</sup> /h	Flood settlement for Cua Nam, Đoi Cung, Hung Chinh
5	Construction of Cua Tien bridge pumping station (Pham Hong Thai)	Construction of Cua Tien bridge pumping station for water consumption and water supply with a capacity of 5000 m <sup>3</sup> /h	Flood settlement for Quang Trung and Cua Nam
6	Construction of Bald Pagoda pumping station	Construction of new pumping station capacity of 130,000m <sup>3</sup> /h, in Hung Hoa	Flood settlement for North channel, Hung Dung, Hung Loc, Hung Hoa wards.
7	Construction of Hung Hoa equalizing basin 2	New construction of Hung Hoa equalizing basin 2, water surface area from 40-45ha	Flood settlement for North channel, Hung Dung, Hung Loc, Hung Hoa wards
8	Renovation of Vinh river	Dredging and renovating embankments on both sides of the Vinh River	Renovating the landscape, solving flooding in Vinh Tan ward
9	Channel system connecting Hung Hoa 1 equalizing basin and Hung Hoa 2 equalizing basin	New construction of canal system connecting 2 equalizing basin and bald pumping station	Flood settlement for North channel, Hung Dung, Hung Loc, Hung Hoa wards.

**Table 4.** Expected long-term improvement of facilities

No	Project	Technical solutions	Investment objectives
1	Channel 80m section from The Thorny River to The Barrier River	New construction of 80m canal according to general planning and zoning plan of Vinh city	Building the main channel for Bac Vinh area, renovating the landscape and solving flooding for Hung Dong commune, Quan Bau ward, Ha Huy Tap and Nghi Phu commune, Nghi Duc completed the main target system of the city
2	Construction of Nghi Duc air-conditioned lake	New construction of air-conditioned lakes according to the general planning and zoning planning of Vinh City	Renovating the landscape, establishing buffer water consumption zones for Nghi Duc and Nghi Phu communes
3	Construction of canal from Nghi Duc Air-conditioned Lake to Hung Hoa 1 Air Conditioning Lake	New construction of canal according to general planning and zoning plan of Vinh city	To build the main drainage canal for the North Vinh area, improve the landscape and deal with flooding for the area of Hung Dong commune, Quan Bau ward, Ha Huy Tap and Nghi Phu commune, Nghi Duc to complete the city's main drainage system.
4	Construction of canal and air-condition Nghi Kim - Nghi Lien - Ke Gai	New construction of canal and air-condition according to general planning and zoning plan of Vinh city	Shaping the main drainage system for the Northwest region to serve urban development and complete the City's technical infrastructure
5	Dredging, renovating and embankment of Ke Gai river, section through Vinh city	Rehabilitation of rivers and works on the route according to general planning and zoning plan of Vinh city	Landscape improvement, urban space expansion, drainage for the area of Cua Nam, Dong Vinh, Hung Chinh, Nghi Kim, Nghi Lien wards

#### 4. Conclusions

This study proposed some solutions to minimize water inflation during the rainy season in Vinh urban area, Vietnam. The level of flooding can be reduced by adding a relief damper structure and in combination with a portable pumping station. When the rain is heavy, the water level in the urban area will be lower than the water level in the canal or river, the valve door will close. The pumping station operates to draw water from the water collection pit to the river or canal while increasing the speed at which the water flows to the drain until the internal water pressure is greater than outside the river, then the valve door will open to drain the water to the river. If localized flooding occurs due to the flow velocity in the small drain, we can use the pump at the outlet to increase the flow velocity in the drain, then the level of flooding and the time of flooding in the area will be reduced and shortened. Those proposals can be useful for management departments in Nghe An province and other areas in Vietnam.

#### References

1. Resolution No. 26-NQ/TW dated 30<sup>th</sup> July 2013 of the Politburo.
2. Statistics on climate situation in Nghe An of Nghe An Irrigation Department.
3. Japan International Cooperation Agency JICA (1999). Research on municipal drainage and wastewater treatment systems.
4. Tran Hieu Nhue, Tran Duc Ha, Do Hai, Ung Quoc Dung, Nguyen Van Tin (1996) Water supply and drainage, Hanoi Science and Technology Publishing House.
5. Le Sam et al. (2014). Flood protection solutions for big cities. Agriculture Publishing House.

# Prediction of ground surface settlements of deep excavations in Vietnam

Nguyen Van-Hoa and Nguyen Tien-Hong, Phan Dinh-Quoc

Department of Civil Engineering, Vinh university, Vietnam

Email: vanhoakxd@vinhuni.edu.vn

**Abstract.** In major cities of Vietnam, such as Hanoi and Ho Chi Minh city, there are many facilities for the construction of underground spaces, such as the basement of high-rise buildings, underground parking, and subway ... Vietnamese geological characteristics of weak water-saturated soils are represented by clay soils and loose Sands are often organic, in some places including layers of silt and peat, as well as high groundwater levels, therefore, when the construction of underground structures leading to precipitation of the soil surface affecting adjacent buildings. The article presents the content of the method of constructing a model of the sediment of the soil surface around the deep pits when the load of the neighbors of the building and the distance from the pit to the building program Plaxis 2D. Consider the case of a deep pit with a depth of  $H_k = 8$  m using the top-down method, the ground load varies  $q = (10-50)$  kN / m and the distance to the pit is  $L = (0.5-1.5)H_k$ . Based on the results obtained, using Matlab software, simulate the subsidence of the soil surface around a deep pit.

**Keywords:** settlements, deep excavation, soft ground, diaphragm wall, numerical modeling.

## 1. Introduction

During the construction of deep excavations, the deforming effect on neighboring buildings. In addition, during construction, a common problem during the settlement monitoring process is that the observation mark is affected, and the deformation of the observation point or the lost observation point leads to incorrect results. The study of the influence of deep excavation of the soil on the subsidence of the soil was also studied by the authors [1-14]. Therefore, the establishment of a settlement model of the soil surface around the deep pit during the construction of underground works will allow determining the settlement at different locations of the structure.

## 2. Principles of building settlement model of the ground around the deep excavation

Factors affecting soil displacement around deep excavations can be mentioned [15]:

- Factors related to the group of leading causes of subsidence  $(x_1, x_2, \dots, x_n)$  such as the size of the excavation, the stiffness of the wall in the ground and protection systems, and the depth of the excavation, soil characteristics.
- Change in external conditions as a result of human impact  $(y_1, y_2, \dots, y_n)$  such as environmental conditions, and level of construction.
- Immediate factors do not determine the degree of their influence on the project  $(z_1, z_2, \dots, z_n)$  such as wind, storm, seismic.

In principle, the soil deformation model is expressed by the function.

$$S = F[f_1(x) + f_2(y) + f_3(z)] \quad (1)$$

where

- $f_1(x)$  - Influence of a group of leading causes;
- $f_2(y)$  - Impact of changing external conditions;
- $f_3(z)$  - Components are influenced by direct factors.

In this section, if we ignore the influence of changes in external conditions, with the same type of excavation and the same geological conditions, we will consider only the factors that cause the deformation of the soil around the excavation. As distance and load, the calculation model can be expressed as (2)

$$S = f\left(\frac{x+L}{H_k}, q\right) \quad (2)$$

where

$x$  - point coordinate along the length of the building (m);

$L$  - distance from the pit to the building (m);

$H_k$  - pit depth, (m);

$q$  - foundation pressure (kN/m).

### 3. Types of geological conditions and model calculations

#### 3.1. Typical geological conditions in Vietnam

The studies were carried out for the following types of engineering-geological conditions characteristic of Hanoi and Ho Chi Minh City, proposed [9, 16-18].

**Table 1.** Type soils in Ha Noi and Ho Chi Minh City

Soil type	Main characteristics of soils	City
Type I: (0-20m) clays and loams, soft plastic (более 20m) clay with a consistency from semi-solid to refractory	( $\varphi = 4 - 6^\circ, c = 5 - 6 \text{ kN/m}^2, E = 1.1 \times 10^3 \text{ kN/m}^2$ ); ( $\varphi = 12 - 16^\circ, c = 24 - 28 \text{ kN/m}^2, E = 4 \times 10^3 \text{ kN/m}^2, \text{SPT} = 12 - 30$ )	Ho Chi Minh city
Type II: (0 - 20m) clays and loams, soft plastic более 20m sandy loam (sometimes with gravel)	( $\varphi = 4 - 6^\circ, c = 5 - 6 \text{ kN/m}^2, E = 1.1 \times 10^3 \text{ kN/m}^2$ ); ( $\varphi = 25 - 26^\circ, c = 5.4 - 8.0 \text{ kN/m}^2, E = 5 \times 10^3 \text{ kN/m}^2$ )	Ho Chi Minh city
Type III: sandy loam (sometimes with gravel)	( $\varphi = 23 - 26^\circ, c = 5.4 - 7.5 \text{ kN/m}^2, E = (7 - 9) \times 10^3 \text{ kN/m}^2, \text{SPT} = 12 - 30$ )	Ho Chi Minh city
Type IV: (0 - 10m) sandy loam plastic and soft plastic loam (10 - 20m) Sands of medium density, silty and medium size more than 20m soft plastic loam	- ( $\varphi = 7 - 14^\circ, c = 14 - 21 \text{ kN/m}^2, E = (7 - 12) \times 10^3 \text{ kN/m}^2$ ); - ( $\varphi = 32 - 34^\circ, E = 15 - 28 \times 10^3 \text{ kN/m}^2, \text{SPT} = 14 - 22$ ); - ( $\varphi = 7 - 11^\circ, c = 14 - 18 \text{ kN/m}^2, E = (15 - 28) \times 10^3 \text{ kN/m}^2, \text{SPT} = 7 - 11$ )	Ha Noi
Type V: (0 - 10m) sandy loam plastic and soft plastic loam (10 - 40m) silty Sands from medium density to dense gravelly	- ( $\varphi = 7 - 14^\circ, c = 14 - 21 \text{ kN/m}^2, E = (7 - 12) \times 10^3 \text{ kN/m}^2$ ); - ( $\varphi = 32 - 34^\circ, E = (15 - 50) \times 10^3 \text{ kN/m}^2, \text{SPT} = 14 - 50$ )	Ha Noi

#### 3.2. Calculation model

To establish a model of soil subsidence around the pit, the author used the Plaxis 2D software to simulate the operation of deep pits during construction and the impact of neighboring workloads on them. To analyze the applicability of soil models for the excavation of deep pits in Viet Nam

conducted numerical geotechnical modeling for the building with two basements. The selected structural solution is the use of diaphragm walls for resisting the deep excavations  $H_k = 8\text{m}$  ( $H_k$  – depth of pit). The thickness of the diaphragm wall was equal to 0.8 m, the parameters of the model:  $EA = 2.304 \times 10^7 \text{ kN}$ ;  $EI = 1.23 \times 10^6 \text{ kNm}^2/\text{m}$ , Poisson's ratio  $\nu = 0,18$ . Concrete B40 has  $EA = 6.5 \times 10^6 \text{ kN}$ . The loadings of surrounding buildings are calculated as a pressure  $q = 10 - 50 \text{ kN/m}$  on the ground surface. This load is located at distances from excavation  $0.5H_k$ ,  $1.0H_k$ , and  $1.5H_k$ . The ground – water level is at a depth of - 6m from the ground surface.

The finite element code Plaxis 2D is used for all analyses. The following computational steps have been performed [6]:

- Stage 1: activation of diaphragm walls
- Stage 2: excavation step 1 (to level - 2.9m)
- Stage 3: Construct slab 1 (0.0m)
- Stage 4: excavation step 2 (to level - 4.5m)
- Stage 5: Construct slab 2 (- 4.3m)
- Stage 6: groundwater lowering and excavation step 3 (to level - 8.0m)

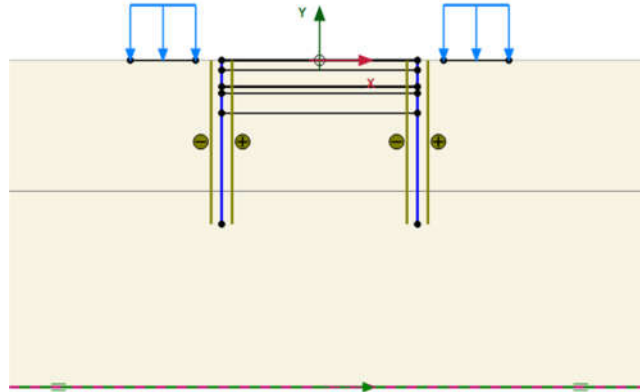


Fig. 1. Calculation model in the PLAXIS program.

### 3.3. Calculation result

Carrying out calculations with loads  $q = (10 \text{ kN/m}; 50 \text{ kN/m})$ , pit depth  $H_k = 8\text{m}$ ; This equation can be used in the range of values  $(x + L) = (1 \text{ m}; 70 \text{ m})$  where  $L$  is the distance from the pit to the building;  $q$  - pressure under the foundation.

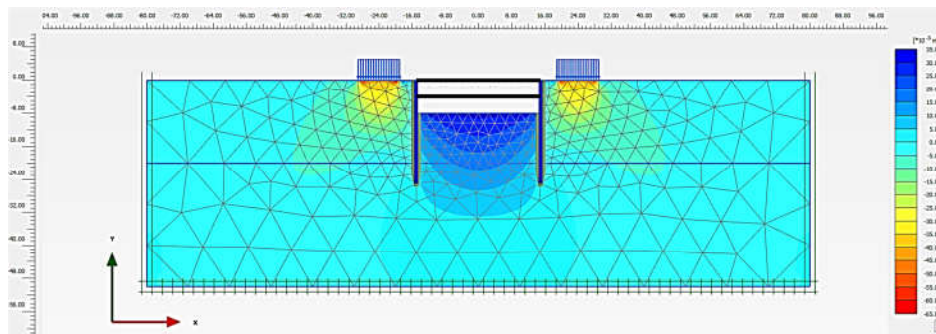


Fig. 2. Deformation of ground surface settlements of deep excavations in the case  $L/H_k = 1,0$ ;  $q = 50 \text{ kN/m}$ .

By proceeding to use the MATLAB calculation software, obtain a formula for predicting the settlement of neighboring buildings in the zone of influence of deep pits:

$$S\left(\frac{x+L}{H_k}, q\right) = K1 + K2 \cdot \left(\frac{x+L}{H_k}\right) + K3 \cdot q + K4 \cdot \left(\frac{x+L}{H_k}\right)^2 + K5 \cdot \left(\frac{x+L}{H_k}\right) \cdot q + K6 \cdot \left(\frac{x+L}{H_k}\right)^3 + K7 \cdot \left(\frac{x+L}{H_k}\right)^2 \cdot q + K8 \cdot \left(\frac{x+L}{H_k}\right)^4 + K9 \cdot \left(\frac{x+L}{H_k}\right)^3 \cdot q$$

The coefficients K1 - K9 of equation (3) are given in Table 2.

**Table 2.** The coefficients of equation (2) settlement of the building.

Calculation case	Coefficients of equation								
	K1	K2	K3	K4	K5	K6	K7	K8	K9
III - II - 8 - 4	1.194	- 4.304	- 0.4981	2.696	- 0.1945	- 0.4652	0.0218	0.02337	- 0.0001473
III - II - 8 - 8	- 0.9555	- 5.19	- 0.5088	3.167	- 0.1617	- 0.5329	0.01523	0.02657	0.000129
III - II - 8 - 12	- 4.28	- 4.192	- 0.3573	3.014	- 0.2061	- 0.5202	0.0205	0.02605	- 1.947e - 05

Notation calculation option: Type of soil - Method of protection of pits - Depth of the pit ( $H_k$  - (m)) - Distance from the pit to the building ( $L$  - (m)), with III - II - 8 - 4: Soil type III, II - method top - down,  $H_k = 8$  m,  $L = 4$  m.

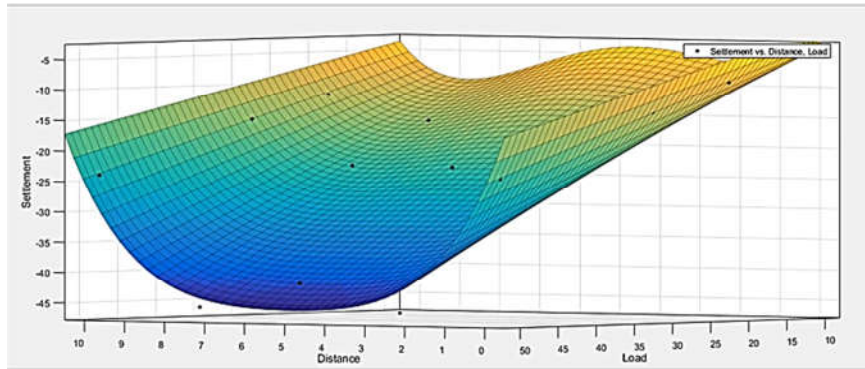


**Fig. 3.** Modeling of soil surface settlement in the case III - II - 8 - 8.

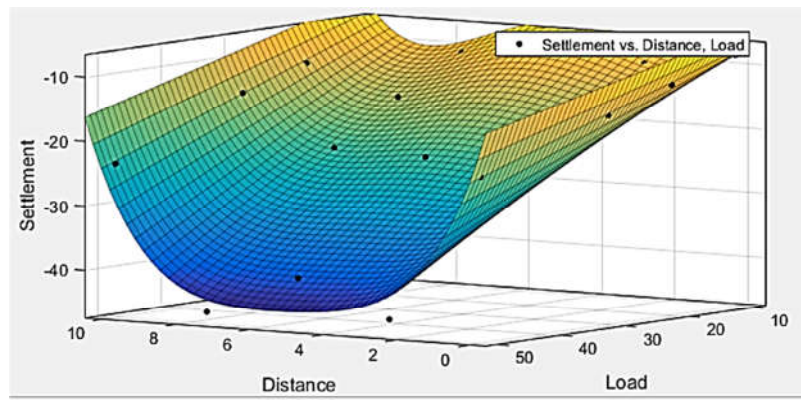


**Fig. 4.** Modeling of soil surface settlement in the case III - II - 8 - 12.

## 4. Conclusion

This paper has been building formulas for predicting settlement of the ground surface around a deep excavation with two factors: distance and load, which can be used to predict settlement at different locations in the project. It is possible to predict the greatest soil settlement in the zone of influence of underground structures to the excavation, thereby predicting the deformation of neighboring buildings.

## References

1. Nikiforova N S., Deformation of the buildings near deep excavations and underground construction and protection measures (Moscow: Doctor Diss) 324 p (2008).
2. Ilyichev V.A et al., Computing the evaluation of deformations of the buildings located near deep foundation tranches., in Proc. of the XVIth European conf. on soil mechanics and geotechnical engineering, Madrid, Spain 24 - 27th September 2007 "Geotechnical Engineering in Urban Environments", 2007.
3. Nguyen Ba Ke., Construction of urban underground works by open excavation method., Hanoi, 2006, p. 336.
4. Nguyen Trong Ky., Study the effect of construction methods of deep excavation to the settlement of neighboring buildings in Hai Phong: Thesis master, Hai Phong private university, 2017.
5. S. S. Y. Lam., Ground movements due to excavation in clay: Physical and analytical models, 2010, p. 305.
6. Nguyen Van - Hoa et al., Semic displacement prediction of retaining walls upon deep excavations in Ha Noi., Journal of Transportation Science and Technology, ISSN 1859 - 4263, Vol 27+28, pp. May, c192 - 197, 2018.
7. Nguyen Hong Nam, Do Van Thieu, Tran Van Bao, Proceedings of 50th anniversary conference of Thuy Loi University, pp. 290 - 299 (2009).
8. Nikiforova N.S et al., Weak soils deformations during excavation of deep pits in seismic regions and adjacent buildings protection., Construction Machinery Bulletin (BCT), vol. 6/2018, pp. c62 - 64, 2018.
9. Nguyen Van Tuan, Stress - strain state of Foundation soils and sides of the pit taking into account the spatial factor, 197 (2006).
10. Phi Hong Thinh, L.A. Strokova., Dangerous geological processes on the territory of Hanoi (Vietnam), Bulletin of Tomsk State University Publisher: National Research Tomsk State University. Vol. No. 349, 2011, pp200 - 203.
11. Trinh Tuan Viet., The interaction of long bored piles of finite stiffness with the surrounding and underlying soils and Foundation, 22 (2015).
12. Nguyen Xuan Bac, Forecast of displacements and deformations of rock mass and earth surface during construction of tunnels in Ho Chi Minh city, 21(2012).
13. Vu Khac Diep., Research on the effects of deep excavation construction on neighboring works, Hai Phong: Master of Engineering Thesis, Vietnam Maritime University, 2016.
14. Nguyen Van Tuan, Stress - strain state analysis around the excavation taking into account spatial factors., Journal of Science - technology construction, 06 (2008).
15. Tran Ngoc Dong, Nguyen Chi Cong., Establishment of construction foundation settlement model based on settlement monitoring data., Journal of Science - technology construction, vol. 1, pp. 54 - 62, 2017.
16. Nguyen Van Hoa, Nikiforova N.S., Engineering - geological surveys, design and construction of foundations and underground structures. Sat. Tr.All - Russian scientific. - techne. Conf. 1 - 3 February 2017., pp. 277 - 281(2017).
17. Nguyen Quang Hung, Method of selection of optimal foundations of high - rise buildings in the conditions of Ho Chi Minh city, dissertations, 204(2008).
18. Nguyen Duc Manh., Engineering - geological support of underground space development in Hanoi (Viet Nam), Abstract. thesis phd. Saint - pt. (2010).

# Vibration analysis of functionally graded porous plates resting on Kerr elastic foundations

*Van-Long Nguyen<sup>1\*</sup>, Minh-Tu Tran<sup>1</sup>, Thanh-Hai Le<sup>2</sup>, Xuan-Thuc Phan<sup>2</sup>*

<sup>1</sup> Ha Noi University of Civil Engineering, 55 Giai Phong Road, Hanoi, Viet Nam

<sup>2</sup> Vinh University, 182 Le Duan Road, Vinh, Nghe An, Viet Nam

*\*Email: longnv@huce.edu.vn*

**Abstract.** This paper presents the free vibration analysis of functionally graded porous materials (FGPMs) plates, in the framework of classical plate theory (CPT). The plate is rested on Keer's elastic foundation with the three-parameter elastic model. Functional graded porous material, in particular, open-cell metal foam with porosities that vary smoothly along thickness direction according to three porosity distribution patterns: uniform, nonuniform symmetric and nonuniform asymmetric are considered. Based on Hamilton's principle, the equations of motion are derived. The numerical examples are performed and compared with those available in the literature to show the accuracy of the present results. The effect of porosity coefficient, porosity distribution patterns, geometrical and Kerr elastic foundation parameters on natural frequencies are investigated.

**Keywords:** Vibration analysis, functionally graded porous plate, classical plate theory, Kerr elastic foundations.

## 1. Introduction

Functionally graded porous materials (FGPMs) are a new class of functionally graded materials that in the microstructure there are internal pores with local density and size distributed according to certain rules, so the material properties can be considered as smoothly and continuously changing in the space of structures. Metal foam is one of the highly porous materials with cellular structures possessing many outstanding properties, such as excellent energy-absorbing capability, electrical conductivity, and thermal management, thus they are widely used in aerospace engineering, automotive industry, and civil constructions. An in-depth understanding of the mechanical behaviors of FGP structures is pivotal in the design, construction and maintenance process.

Vibration is one of the important problems in the design of structural elements, thus a study of their vibrational characteristics attracted the local and international scientific community. Chen et al. [1] investigated the effect of porosity distribution patterns and porosity coefficient on free and forced vibration characteristics of FGP beams. Employing the differential transformation method, Wattanasakulpong et al [2] presented the linear and nonlinear analysis of FG beams under different types of elastic supports. Leclaire [3] analyzed the free vibrations of a rectangular thin FGP plate with liquid. Using three-dimensional elastic theory, Zhao et al. [4] studied the free vibration of thick rectangular FGP plates with various boundary conditions. Zhao et al. used an improved Fourier series method to analyze the free vibration of the Mindlin porous plate [5]. Using the state space approach and a four-variable plate theory, Demirhan et al. [6] investigated the free vibration and bending behavior of FGP plate with two opposite simply-supported edges. Tran et al. [7] analyzed the static and free vibration of FGP variable-thickness plates by employing an edge-based smoothed finite element method (ES-FEM).

The interaction action between structures and elastic foundations is an important topic and always attracted the attention of designers. Arani et al [8] studied the free vibration of an FGP rectangular plate resting on a Winkler foundation using Reddy's third-order shear deformation theory and differential quadrature method. Hashemi et al. [9] non-linear free vibration analysis of a bidirectional functional hierarchical rectangular plate in a plane with voids located on a Winkler-Pasternak elastic

foundation. Based on the sinusoidal shear deformation theory and analytical approach, Benferhat et al. [10] investigated the effect of porosity on bending and free vibration behavior of simply supported FGP plate resting on the Winkler-Pasternak foundation. Zaoui et al. presented a closed-form solution to predict the fundamental natural frequency of FG plate substrates on Pasternak elastic foundation by using two dimensional (2D) and quasi three dimensional (quasi-3D) shear deformation theories. Huang et al. [11] nonlinear free and forced vibrations of FGP plates on nonlinear elastic foundations. Shahsavari et al. [12] used a novel quasi-3D hyperbolic theory is presented for the free vibration analysis of functionally graded (FGP) porous plates resting on elastic foundations with a Winkler/Pasternak/Kerr foundation (three-parameter elastic model). Utilizing the Navier solution technique, Kim et al. [13] investigated the bending, free vibration, and buckling response of FGP micro-plates resting on Winkler/Pasternak/Kerr elastic foundation using the classical and first-order shear deformation plate theories. Kerr's elastic foundation model was also used in the study on free vibration of simply supported FG sandwich plates of Daikh [14].

In this paper, the basic relationships and governing equations are established to analyze the free vibration of the FGP plates resting on Kerr's elastic foundation in the framework of the classical plate theory. Uniform, nonuniform symmetric and nonuniform asymmetric porosity distribution patterns of FGPM are considered. Navier's technique is used to determine the natural frequency of the simply supported rectangular FGP plate. Verification examples are performed through comparison with some existing results. The effect of porosity coefficient, porosity distribution patterns, Kerr elastic foundation parameters and geometrical parameters on natural frequencies is investigated in detail.

## 2. Theoretical formulation

### 2.1. The functionally graded porous plate

Consider a thin rectangular FGP plate of length  $a$ , width  $b$  and thickness  $h$ , respectively as shown in Fig. 1, referring to the rectangular Cartesian coordinates  $(x, y, z)$ , where  $(x, y)$  plane coincides with the middle surface of the plate and  $z$  is the thickness coordinate  $(-h/2 \leq z \leq h/2)$ . The plate is rested on Keer's elastic foundation with a three-parameter elastic model including an independent upper (with stiffness  $K_u$ ), shear (with stiffness  $K_s$ ) and lower (with stiffness  $K_l$ ) elastic layers.

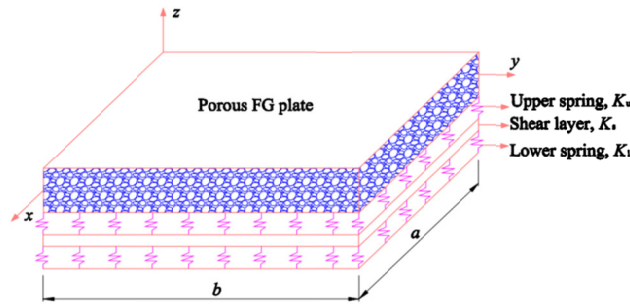


Fig. 1. The configuration of rectangular FGP plates resting on the Kerr foundation.

Three different porosity distribution patterns are considered as follows [1, 15, 16]:

- Uniform porosity distribution (Type 1- Fig. 2-a):

$$\begin{aligned} \{E, G\} &= \{E_{\max}, G_{\max}\} (1 - e_0 \lambda); \\ \rho &= \rho_{\max} \sqrt{1 - e_0 \lambda}; \\ \lambda &= \frac{1}{e_0} - \frac{1}{e_0} \left( \frac{2}{\pi} \sqrt{1 - e_0} - \frac{2}{\pi} + 1 \right)^2. \end{aligned} \quad (1)$$

- Non-uniform symmetric distribution (Type 2- Fig. 2-b):

$$\begin{aligned} \{E(z), G(z)\} &= \{E_{\max}, G_{\max}\} \left[ 1 - e_0 \cos\left(\frac{\pi z}{h}\right) \right]; \\ \rho(z) &= \rho_{\max} \left[ 1 - e_m \cos\left(\frac{\pi z}{h}\right) \right]. \end{aligned} \quad (2)$$

- Non-uniform asymmetric distribution (Type 3- Fig. 2-c):

$$\begin{aligned} \{E(z), G(z)\} &= \{E_{\max}, G_{\max}\} \left[ 1 - e_0 \cos\left(\frac{\pi z}{2h} + \frac{\pi}{4}\right) \right]; \\ \rho(z) &= \rho_{\max} \left[ 1 - e_m \cos\left(\frac{\pi z}{2h} + \frac{\pi}{4}\right) \right]. \end{aligned} \quad (3)$$

where  $E_{\max}$ ,  $G_{\max}$ , and  $\rho_{\max}$  are the maximum values of elasticity moduli, shear moduli and mass density;  $E_{\min}$ ,  $G_{\min}$ , and  $\rho_{\min}$  denote the minimum values, respectively. The porosity coefficients are defined by:

$$\begin{aligned} e_0 &= 1 - \frac{E_{\min}}{E_{\max}} = 1 - \frac{G_{\min}}{G_{\max}} \quad (0 < e_0 < 1); \\ e_m &= 1 - \frac{\rho_{\min}}{\rho_{\max}} = 1 - \sqrt{1 - e_0} \quad (0 < e_m < 1). \end{aligned} \quad (4)$$

Poisson's coefficient  $\nu$  is assumed to be constant along with the plate thickness.

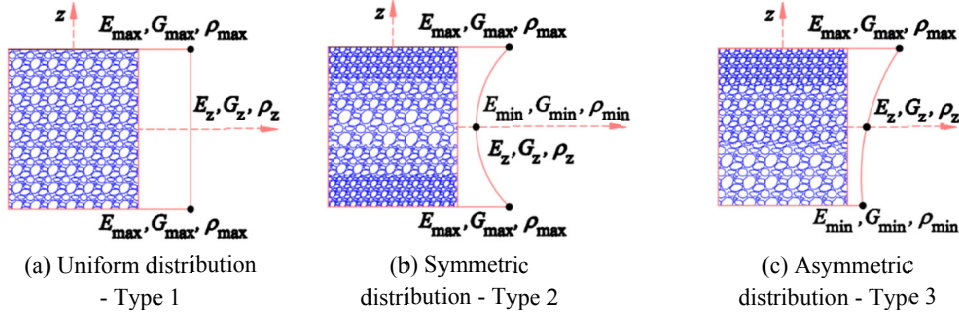


Fig. 2. The FGP plate with different porosity density distribution patterns.

## 2.2. Classical plate theory (CPT) - Equations of motion

Based on CPT, the displacement components ( $u$ ,  $v$ ,  $w$ ) along  $x$ ,  $y$  and  $z$  axes of an arbitrary point ( $x$ ,  $y$ ,  $z$ ) of the FGP plate are expressed as follows [17]:

$$\begin{aligned} u(x, y, z, t) &= u_0(x, y, t) - zw_{0,x}; \quad v(x, y, z, t) = v_0(x, y, t) - zw_{0,y}; \\ w(x, y, z, t) &= w_0(x, y, t). \end{aligned} \quad (5)$$

in which:  $t$  is a time variable;  $u_0$ ,  $v_0$ ,  $w_0$  are the displacement components in the mid-plane.

The strain components based on the CPT can be written as follows [17]:

$$\begin{Bmatrix} \varepsilon_x \\ \varepsilon_y \\ \gamma_{xy} \end{Bmatrix} = \begin{Bmatrix} \varepsilon_x^0 \\ \varepsilon_y^0 \\ \gamma_{xy}^0 \end{Bmatrix} + z_{ns} \begin{Bmatrix} \kappa_x \\ \kappa_y \\ \kappa_{xy} \end{Bmatrix} \quad (6)$$

where:  $\varepsilon_x^0 = u_{0,x}$ ;  $\varepsilon_y^0 = v_{0,y}$ ;  $\gamma_{xy}^0 = u_{0,y} + v_{0,x}$ ;  $\kappa_x = -w_{0,xx}$ ;  $\kappa_y = w_{0,yy}$ ;  $\kappa_{xy} = -2w_{0,xy}$ .

The commas subscripts denote the partial differentiation with respect to the spatial variables  
Stresses are determined from Hooke's law and written as:

$$\begin{Bmatrix} \sigma_x \\ \sigma_y \\ \sigma_{xy} \end{Bmatrix} = \begin{bmatrix} Q_{11} & Q_{12} & 0 \\ Q_{21} & Q_{22} & 0 \\ 0 & 0 & Q_{66} \end{bmatrix} \begin{Bmatrix} \varepsilon_x \\ \varepsilon_y \\ \gamma_{xy} \end{Bmatrix} \quad (7)$$

$$\text{in which: } Q_{11} = Q_{22} = \frac{E(z)}{1-\nu^2}; \quad Q_{12} = Q_{21} = \frac{\nu E(z)}{1-\nu^2}; \quad Q_{66} = \frac{E(z)}{2(1+\nu)}.$$

The force and moment resultants per unit length of the plate are defined as:

$$\begin{Bmatrix} N_x \\ N_y \\ N_{xy} \end{Bmatrix} = \begin{bmatrix} A_{11} & A_{12} & 0 \\ A_{12} & A_{11} & 0 \\ 0 & 0 & A_{66} \end{bmatrix} \begin{Bmatrix} \varepsilon_x^0 \\ \varepsilon_y^0 \\ \gamma_{xy}^0 \end{Bmatrix}; \quad \begin{Bmatrix} M_x \\ M_y \\ M_{xy} \end{Bmatrix} = \begin{bmatrix} D_{11} & D_{12} & 0 \\ D_{12} & D_{11} & 0 \\ 0 & 0 & D_{66} \end{bmatrix} \begin{Bmatrix} \kappa_x \\ \kappa_y \\ \kappa_{xy} \end{Bmatrix} \quad (8)$$

$$\text{where: } A_{11} = \frac{E_1}{1-\nu^2}; \quad A_{12} = \nu A_{11}; \quad A_{66} = \frac{E_1}{2(1+\nu)}; \quad D_{11} = \frac{E_3}{1-\nu^2}; \quad D_{12} = \nu D_{11}; \quad D_{66} = \frac{E_3}{2(1+\nu)};$$

$$(E_1, E_3) = \int_{-h/2-C}^{h/2-C} E(z) (1, z^2) dz.$$

Based on classical plate theory (CPT), equations of motion of FGP plates resting on Kerr elastic foundations can be expressed as [17, 18]:

$$\begin{aligned} N_{x,x} + N_{xy,y} &= I_0 \ddot{u}_0 - I_1 \ddot{w}_{0,x}; \quad N_{xy,x} + N_{y,y} = I_0 \ddot{v}_0 - I_1 \ddot{w}_{0,y}; \\ M_{x,xx} + 2M_{xy,xy} + M_{y,yy} + q - \frac{k_l k_u}{k_l + k_u} w_0 + \frac{k_s k_u}{k_l + k_u} \nabla^2 w_0 & \\ = I_0 \ddot{w}_0 + I_1 \ddot{u}_{0,x} + I_1 \ddot{v}_{0,y} - I_2 \nabla^2 \ddot{w}_0. & \end{aligned} \quad (9)$$

$$\text{where: } I_i \text{ are the mass moment of inertia } I_i = \int_{-h/2-C}^{h/2-C} \rho(z_{ns}) z^i dz; \quad (i = 0, 1, 2);$$

Substituting Eq. (7) and (9) into Eq. (10) we obtain the system of equations in terms of displacements:

$$\begin{aligned} A_{11} \frac{\partial^2 u_0}{\partial x^2} + A_{66} \frac{\partial^2 u_0}{\partial y^2} + (A_{12} + A_{66}) \frac{\partial^2 v_0}{\partial x \partial y} &= I_0 \ddot{u}_0 - I_1 \ddot{w}_{0,x}; \\ (A_{12} + A_{66}) \frac{\partial^2 u_0}{\partial x \partial y} + A_{66} \frac{\partial^2 v_0}{\partial x^2} + A_{11} \frac{\partial^2 v_0}{\partial y^2} &= I_0 \ddot{v}_0 - I_1 \ddot{w}_{0,y}; \\ -C_{11} \frac{\partial^4 w_0}{\partial x^4} - 2(C_{12} + 2C_{66}) \frac{\partial^4 w_0}{\partial x^2 \partial y^2} - C_{11} \frac{\partial^4 w_0}{\partial y^4} + q - \frac{k_l k_u}{k_l + k_u} w_0 & \\ + \frac{k_s k_u}{k_l + k_u} \nabla^2 w_0 &= I_0 \ddot{w}_0 + I_1 \ddot{u}_{0,x} + I_1 \ddot{v}_{0,y} - I_2 \nabla^2 \ddot{w}_0. \end{aligned} \quad (10)$$

### 3. Navier's solution for free vibration analysis

In the case of free vibration analysis, by setting the mechanical load to zero ( $q = 0$ ). The simply supported boundary conditions based on CPT are as follows:

$$\begin{aligned}
\text{at } x=0 \text{ and } x=a: v_0 = 0, w_0 = 0, N_x = 0, M_x = 0; \\
\text{at } y=0 \text{ and } y=b: u_0 = 0, w_0 = 0, N_y = 0, M_y = 0
\end{aligned} \tag{11}$$

The displacement solutions satisfying the boundary conditions (12) are chosen in the following form:

$$\begin{aligned}
u_0(x, y, t) &= \sum_{m=1}^{\infty} \sum_{n=1}^{\infty} u_{0mn} e^{i\omega_{mn}t} \cos \alpha x \sin \beta y; \\
v_0(x, y, t) &= \sum_{m=1}^{\infty} \sum_{n=1}^{\infty} v_{0mn} e^{i\omega_{mn}t} \sin \alpha x \cos \beta y; \\
w_0(x, y, t) &= \sum_{m=1}^{\infty} \sum_{n=1}^{\infty} w_{0mn} e^{i\omega_{mn}t} \sin \alpha x \sin \beta y.
\end{aligned} \tag{12}$$

in which:

$$i = \sqrt{-1}; \alpha = \frac{m\pi}{a}, \beta = \frac{n\pi}{b}; m, n \text{ are the number of sine half-wavelength in the } x, y \text{ axes}$$

(reflect the vibration form);

$u_{0mn}, v_{0mn}, w_{0mn}$  are unknown coefficients need to be determined;

$\omega_{mn}$  is the angular natural frequency with mode  $(m, n)$ , respectively.

Substituting Eq. (13) into Eq. (11), we obtain:

$$\left( \begin{bmatrix} s_{11} & s_{12} & 0 \\ s_{12} & s_{22} & 0 \\ 0 & 0 & s_{33} \end{bmatrix} - \omega_{mn}^2 \begin{bmatrix} m_{11} & 0 & m_{13} \\ 0 & m_{11} & m_{23} \\ m_{13} & m_{23} & m_{33} \end{bmatrix} \right) \begin{Bmatrix} u_{0mn} \\ v_{0mn} \\ w_{0mn} \end{Bmatrix} = \begin{Bmatrix} 0 \\ 0 \\ 0 \end{Bmatrix} \tag{13}$$

or in the form of a simple matrix form:

$$\left( \left[ K_{mn}^{kc} \right] - \omega_{mn}^2 \left[ M_{mn} \right] \right) \{ Q_{mn} \} = \{ 0 \} \tag{14}$$

where:  $s_{11} = A_{11}\alpha^2 + A_{66}\beta^2$ ;  $s_{12} = (A_{12} + A_{66})\alpha\beta$ ;  $s_{22} = A_{66}\alpha^2 + A_{11}\beta^2$ ;

$$s_{33} = C_{11}(\alpha^2 + \beta^2)^2 + \frac{k_l k_u}{k_l + k_u} + \frac{k_s k_u}{k_l + k_u}(\alpha^2 + \beta^2)$$

$$m_{11} = I_0; m_{13} = -I_1\alpha; m_{23} = -I_1\beta; m_{33} = I_0 + I_2(\alpha^2 + \beta^2).$$

For each pair of values  $(m, n)$ , we can determine the respective natural frequency by the criterion of non-trivial displacement solution of Eq. (15).

#### 4. Numerical results and discussion

Based on the above mentioned presented analytical solution, Matlab's code is built to implement numerical examples. The rectangular FGP plate is resting on the Keer elastic foundation, all four edges of the plates are simply supported. The porous materials made of aluminium with the physical properties are as follows:  $\nu = 0.3$ ;  $\rho_1 = 2707 \text{ kg/m}^3$ ;  $G_1 = 26,923 \text{ GPa}$ ;  $E_1 = 2G_1(1+\nu)$  [19]. For convenience, the non-dimensional results are used in the form [12]:

$$\bar{\omega} = \omega h \sqrt{\frac{\rho_{\max}}{E_{\max}}}; K_l = \frac{k_l a^4}{D_m}; K_u = \frac{k_u a^4}{D_m}; K_s = \frac{k_s a^2}{D_m}; D_m = \frac{E_{\max} h^3}{12(1-\nu^2)} \tag{15}$$

#### 4.1. Validation examples

In this section, the natural frequency of simply supported square isotropic plates made of aluminum ( $E_m = 380$  Gpa,  $\rho_m = 3800$  kg/m<sup>3</sup>) and alumina ( $E_m = 70$  Gpa,  $\rho_m = 2702$  kg/m<sup>3</sup>);  $\nu = 0,3$  resting on Kerr's elastic foundation are validated with existing results of Shahsavari et al. [12]. The obtained results are presented in Table 1 with non-dimensional parameters computed in the form  $\bar{\omega} = \omega_0 h \sqrt{\rho_m / E_m}$ ;  $K_l = 100$ ;  $K_u = k_u a^4 / D_m$  and four types of elastic foundation ( $K_u, K_s$ ). Shahsavari and his co-workers used quasi-3D solution and first-order shear deformation theory.

**Table 1.** Non-dimensional fundamental frequency  $\bar{\omega}$  of isotropic square plate  
( $K_l = 100, a/h = 20$ )

$K_u$	$K_s$	Source	Isotropic plate	
			Ceramic - Al <sub>2</sub> O <sub>3</sub>	Metal - Al
100	0	Shahsavari et al. [12]	0.0294	0.0157
		<b>Present</b>	<b>0.0296</b>	<b>0.0158</b>
100	100	Shahsavari et al. [12]	0.0356	0.0285
		<b>Present</b>	<b>0.0357</b>	<b>0.0285</b>
200	100	Shahsavari et al. [12]	0.0375	0.0317
		<b>Present</b>	<b>0.0377</b>	<b>0.0318</b>
200	200	Shahsavari et al. [12]	0.0440	0.0419
		<b>Present</b>	<b>0.0442</b>	<b>0.0420</b>

Table 2 tabulated non-dimensional natural frequencies  $\bar{\omega}$  of simply supported square FGP plate ( $a/h = 10$ ) with various porosity coefficients. The present results are compared with those of Rezaei and Saidi [19] using the state space method, and of Thang et al. [20] using the Navier solution. As illustrated in Table 1- 2, very good agreements between proposed model and reported studies can be clearly observed.

**Table 2.** Non-dimensional fundamental frequency  $\bar{\omega} = \omega h \sqrt{\rho_1 / E_1}$   
of porous square plate - nonuniform asymmetric ( $a/h = 10$ )

Source	$e_0 = 0.1$	$e_0 = 0.3$	$e_0 = 0.5$	$e_0 = 0.7$
Rezaei and Saidi [19]	0.0570	0.0551	0.0526	0.0491
Thang et al. [20]	0.0574	0.0555	0.0531	0.0495
<b>Present</b>	<b>0.0584</b>	<b>0.0565</b>	<b>0.0540</b>	<b>0.0503</b>

#### 4.2. Parametric studies

The fundamental natural frequencies of simply supported rectangular FGP plates are predicted with following input data:  $G_1 = 26,923$  GPa;  $\rho_1 = 2702$  kg/m<sup>3</sup>;  $h = 0.01$  m;  $a/h = 50$ ;  $b/a = 1$ ;  $m = n = 1$ . The effect of porosity coefficient and porosity distribution patterns on fundamental natural frequencies is shown in Figure 2. It can be seen that for the FGP plate without an elastic foundation (Fig. 2a): the non-dimensional natural frequency decreases as the porosity coefficient increases for uniform porosity distribution and non-uniform asymmetric porosity distribution with the same quantitative and qualitative trend, while symmetric porosity distribution gives the opposite result. This can be explained by the correlation between the mass effect and flexural stiffness effect of FGP plates with individual porosity distribution patterns when the porosity coefficient varies. For the FGP plate resting on the elastic foundation (Fig. 2b), the non-dimensional natural frequency increases as the porosity coefficient increases for all three porosity distribution patterns.

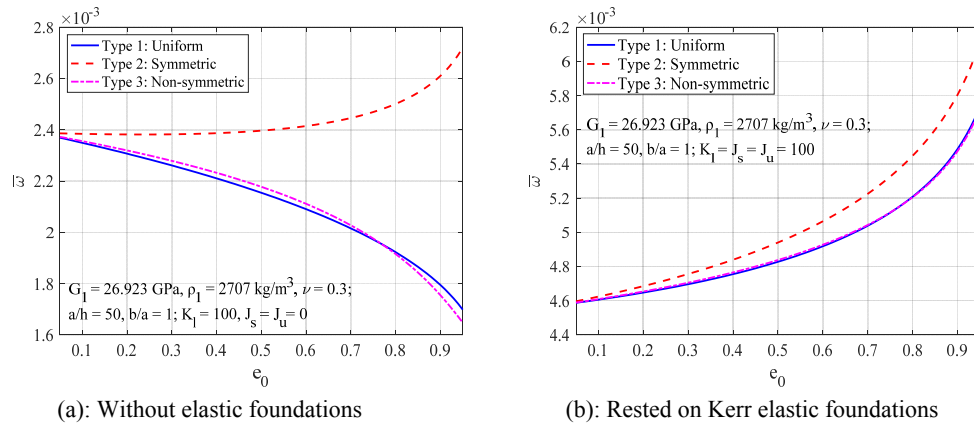


**Fig. 2.** Variation of the non-dimensional natural frequency of FGP plate with porosity coefficients  $e_0$  and various porosity distribution patterns.

Fig. 3 illustrates the effect of aspect ratio ( $b/a$ ) and side-to-thickness ratio ( $a/h$ ) on non-dimensional natural frequency. It is observed from the results that by increasing  $b/a$  and  $a/h$  ratios, the non-dimensional natural frequency decreases, significantly decreases in a small range of  $b/a$  and  $a/h$  ratios, and then slows down.

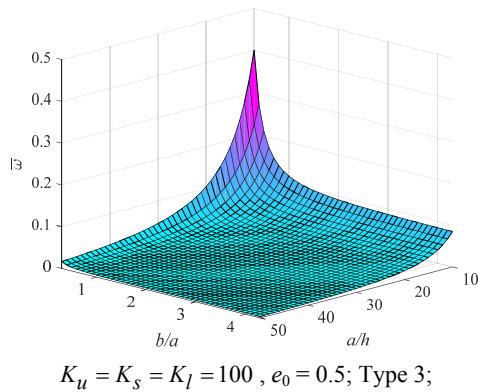


**Fig. 3.** Variation of non-dimensional natural frequency of the FGP plate versus  $b/a$  and  $a/h$  ratios.

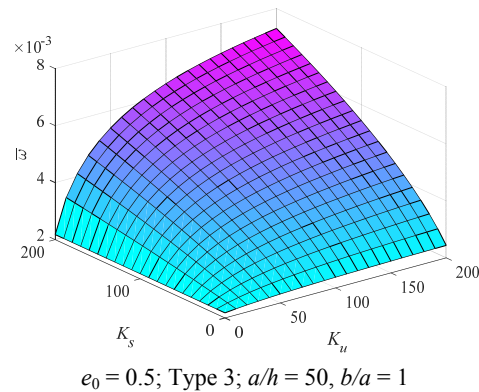


**Fig. 4.** Variation of the non-dimensional natural frequency of the FGP plate versus elastic foundation stiffness.

Fig. 4 depicts the effect of elastic foundation stiffnesses on the non-dimensional natural frequency of the FGP plate. From plots can be seen that non-dimensional fundamental natural frequency increases significantly as elastic foundation stiffness ( $K_u, K_s$ ) increases.

## 5. Conclusion

In this paper, free vibration analysis of a simply supported rectangular FGP plate resting on Kerr's elastic foundation is implemented in the framework of classical plate theory. Navier's solution has been employed to predict the natural frequency. The validation examples are carried out to confirm the accuracy of self-written Matlab code and theoretical model. The significant effect of geometrical parameters ( $b/a$  and  $a/h$  ratios), porosity distribution patterns, porosity coefficient, and elastic foundation stiffness on the natural frequency of FGP plate is indicated through various numerical examples.

## References

1. Chen, D., J. Yang, and S. Kitipornchai, *Free and forced vibrations of shear deformable functionally graded porous beams*. International journal of mechanical sciences, 2016. **108**: p. 14-22.
2. Wattanasakulpong, N. and V. Ungbhakorn, *Linear and nonlinear vibration analysis of elastically restrained ends FGM beams with porosities*. Aerospace Science and Technology, 2014. **32**(1): p. 111-120.
3. Leclaire, P., K. Horoshenkov, and A. Cummings, *Transverse vibrations of a thin rectangular porous plate saturated by a fluid*. Journal of Sound and Vibration, 2001. **247**(1): p. 1-18.
4. Zhao, J., et al., *Three-dimensional exact solution for vibration analysis of thick functionally graded porous (FGP) rectangular plates with arbitrary boundary conditions*. Composites Part B: Engineering, 2018. **155**: p. 369-381.
5. Zhao, J., et al., *Free vibrations of functionally graded porous rectangular plate with uniform elastic boundary conditions*. Composites Part B: Engineering, 2019. **168**: p. 106-120.
6. Demirhan, P.A. and V. Taskin, *Bending and free vibration analysis of Levy-type porous functionally graded plate using state space approach*. Composites Part B: Engineering, 2019. **160**: p. 661-676.
7. Tran, T.T., Q.-H. Pham, and T. Nguyen-Thoi, *Static and free vibration analyses of functionally graded porous variable-thickness plates using an edge-based smoothed finite element method*. Defence Technology, 2021. **17**(3): p. 971-986.
8. Arani, A.G., et al., *Free vibration of embedded porous plate using third-order shear deformation and poroelasticity theories*. Journal of Engineering, 2017. **2017**.
9. Hashemi, S., et al., *Nonlinear free vibration analysis of In-plane Bi-directional functionally graded plate with porosities resting on elastic foundations*. International Journal of Applied Mechanics, 2022: p. 2150131.
10. Benferhat, R., et al., *Effect of porosity on the bending and free vibration response of functionally graded plates resting on Winkler-Pasternak foundations*. Earthquakes and Structures, 2016. **10**(6): p. 1429-1449.
11. Huang, X.-L., et al., *Nonlinear free and forced vibrations of porous sigmoid functionally graded plates on nonlinear elastic foundations*. Composite Structures, 2019. **228**: p. 111326.
12. Shahsavari, D., et al., *A novel quasi-3D hyperbolic theory for free vibration of FG plates with porosities resting on Winkler/Pasternak/Kerr foundation*. Aerospace Science and Technology, 2018. **72**: p. 134-149.
13. Kim, J., K.K. Żur, and J. Reddy, *Bending, free vibration, and buckling of modified couples stress-based functionally graded porous micro-plates*. Composite Structures, 2019. **209**: p. 879-888.
14. Daikh, A.A., *Temperature dependent vibration analysis of functionally graded sandwich plates resting on Winkler/Pasternak/Kerr foundation*. Materials Research Express, 2019. **6**(6): p. 065702.
15. Barati, M.R. and A.M. Zenkour, *Investigating post-buckling of geometrically imperfect metal foam nanobeams with symmetric and asymmetric porosity distributions*. Composite Structures, 2017. **182**: p. 91-98.
16. Banhart, J., *Manufacture, characterisation and application of cellular metals and metal foams*. Progress in materials science, 2001. **46**(6): p. 559-632.
17. Reddy, J.N., *Theory and analysis of elastic plates and shells*. 2006: CRC press.
18. Kneifati, M.C., *Analysis of plates on a Kerr foundation model*. Journal of Engineering Mechanics, 1985. **111**(11): p. 1325-1342.
19. Rezaei, A. and A. Saidi, *Application of Carrera Unified Formulation to study the effect of porosity on natural frequencies of thick porous-cellular plates*. Composites Part B: Engineering, 2016. **91**: p. 361-370.
20. Thang, P.T., et al., *Elastic buckling and free vibration analyses of porous-cellular plates with uniform and non-uniform porosity distributions*. Aerospace Science and Technology, 2018. **79**: p. 278-287.

19. Rezaei, A. and A. Saidi, *Application of Carrera Unified Formulation to study the effect of porosity on natural frequencies of thick porous-cellular plates*. Composites Part B: Engineering, 2016. **91**: p. 361-370.
20. Thang, P.T., et al., *Elastic buckling and free vibration analyses of porous-cellular plates with uniform and non-uniform porosity distributions*. Aerospace Science and Technology, 2018. **79**: p. 278-287.

# Analysis of the role of parameters in 16MND5 steel model considering the radiation effects

Can-Ngon Nguyen

Department of Civil Engineering, Vinh university, Vietnam

Email: [canngon.ng@gmail.com](mailto:canngon.ng@gmail.com)

**Abstract.** This paper focuses on analyzing influence of the role of parameters in the 16MND5 steel model, from which seeks to reflect the radiation impact on steel behaviour through the change of parameters. Thus, respectively article will present the effects of radiation on the Stress-Deformation curve, analysis theoretical significance and role of each parameter, influence together of those parameters. Finally, recommend parameters need to be changed to consider the effects of radiation.

**Keywords:** influence of radiation, plastic flow rule, hardening rule, crystal dislocations, bainite steel microstructure, 16MND5.

## 1. Introduction

At the micro level, the radioactivity generates defects in steel: micropores, dislocation loops, rich copper precipitate. The radioactivity facilitates the process of precipitation, separation of chemicals at steel grains boundary, the separation of phosphorus.

This micro phenomenon that changed almost all the properties of materials at the macro level: increasing the limit elasticity, maximum stress, brittle-plastic temperature transition, resilience, reducing energy plastics.

In the framework of our paper, we focus on the changes of brittle-plastic, particularly reflecting the changes caused by radiation through changing the parameters of the model.

## 2. Effect of radiation on stress-strain curve

Generally, stress-strain curve consists of three main elements: the shape of curve, sensitivity to loading speed, sensitivity to temperature. In order to study the change of stress-strain curve caused by radiation, we present hereafter the changes of three elements caused by radiation.

**The shape of curve:** According to empirical data of the radiation effects (Figure 1), generally macro stress-strain curve tends to shift upward. Limit elasticity and maximum stress are increased.

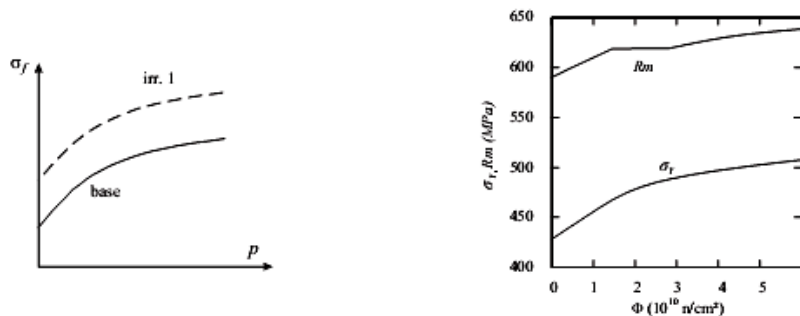


Fig. 1. Effect of radiation on stress-strain curve [1].

**Sensitivity to temperature:** The increase of the limit elasticity is a function of temperature; however, the influence of temperature is quite weak [2]. This is shown by the equation Eq. (1).

$$\sigma_r(\varphi, T) = \sigma_r(\varphi = 0, T) + \Delta\sigma_r(\varphi, T = 300K) \times g(T) \quad (1)$$

where  $g(T) = 1 + 0,83 \exp(-2,81 \frac{T}{T_0}) - 0,616 \exp(-3 \frac{T}{T_0})$

and  $g(-196^\circ C) = 1,111; g(-150^\circ C) = 1,07; g(-50^\circ C) = 1,031$

**Sensitivity to loading speed:** Until now, no experimental data available related to the sensitivity of viscosity stress of irradiated steel material. But the kinematic simulation of crystal defects [3], [4] show that the viscosity stress does not depend on speed when loading speed  $\dot{\gamma} < 10^7 s^{-1}$  (Figure 2). Within the scope of the study, this condition is automatically satisfied.

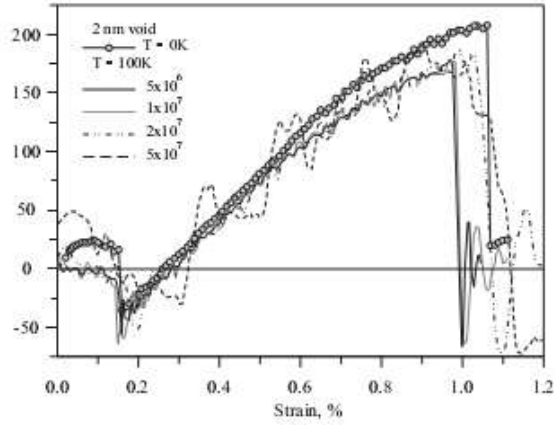


Fig. 2. Viscosity stress and strain speed.

### 3. Equations of the model

We recall here the equations of the model, and physical meaning of parameters.

**Plastic flow law:**

$$\dot{\gamma}^s = \dot{\gamma}_0 \exp\left[-\frac{\Delta G(\tau_{eff})}{k_B T}\right] \text{sign}(\tau_s) = \dot{\gamma}_0 \exp\left[-\frac{\Delta G_0}{k_B T} \left(1 - \left(\frac{\tau_{eff}}{\tau_R}\right)^q\right)^q\right] \text{sign}(\tau_s) \quad (2)$$

**Hardening law:**

$$\tau = \frac{(\alpha s b)^2 \rho}{\tau^s - \tau_0} \int dt$$

$$\tau_{eff}^s = \tau^s - \tau_0 - \tau_{int} \frac{\rho^s (\alpha s b)^2 a}{\tau^s - \tau_0}$$

**Evolution of dislocation density:**

$$\dot{\rho}^s = \frac{|\dot{\gamma}^s|}{b} \left( \frac{1}{D_{grain}} + \frac{\sqrt{\Sigma s \mu} \rho^u}{R(T)} - g_c(T) \rho^s \right) \quad (3)$$

where:

$\Delta G$ : Activation energy;  $k_B$ : Boltzmann constant;  $T$ : absolute temperature;  $\tau_{eff}$ : shear stress apply directly on dislocation;  $\tau_R$ : absolute shear stress to move dislocation at 0 K temperature;  $p, q$ : two

parameters define the shape of the activation energy;  $\dot{\gamma}_0$ : Sliding speed at no thermal depending regime;  $\tau_{int}$ : movement of crystal dislocation is hampered by a forest of other crystal dislocation;  $\tau_0$ : taking into account the role of carbon compounds, precipitates and obstruct at grain boundary and other crystal defects;  $\tau_s$ : projection of shear stress on sliding plane;  $\rho^s$ : the crystal dislocation density of the sliding plane s;  $\alpha_{us}$ : interaction coefficient between two sliding systems u and s;  $\mu$ : shear modulus;  $b$ : vector Burgers;  $\sqrt{\sum_{s \neq u} \rho^s}$ : The average distance between dislocations cutting through sliding plane s;  $D_{grain}$ : the average steel grain size;  $K(T)$ : coefficient characterizing dislocation holding efficiency;  $g_c(T)$ : coefficient characterizing the effectiveness of mutual destruction between dislocations in same sliding system.

#### 4. Theoretical analysis

From the laws of the model, we can change each law:

**Plastic flow law:**

$$\tau_{eff} = \tau_R \left( 1 - \left( -\frac{K_B T}{\Delta G_0} \ln \left( \frac{|\dot{\gamma}^s|}{\dot{\gamma}_0} \right)^{\frac{1}{q}} \right) \right)^{\frac{1}{p}}$$

$$\Rightarrow \tau_{eff} = f(T, \dot{\gamma}^s, \Delta G_0, \dot{\gamma}_0, \tau_R, p, q)$$

**Hardening law:**

$$\tau^s = \tau_0 + \frac{\tau_{eff}}{2} + \frac{1}{2} \sqrt{\tau_{eff}^2 + 4(\alpha \mu b)^2 \rho}$$

**Evolution of dislocation density:**

$$\dot{\rho}^s = \frac{|\dot{\gamma}^s|}{b} \left( \frac{1}{D_{grain}} + \frac{\sqrt{\sum_{s \neq u} \rho^s}}{K(T)} - g_c(T) \rho^s \right)$$

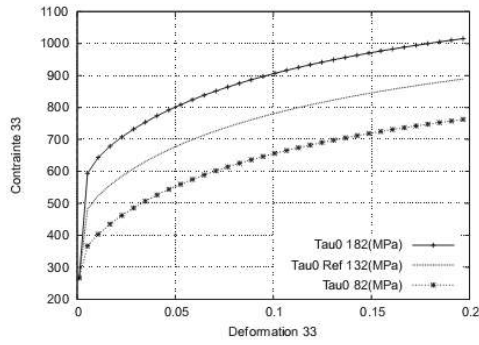
$$\Rightarrow \rho^s = f(\dot{\gamma}^s, \rho^u, K, g)$$

From the change here above, we can draw some methodological rules as follows:

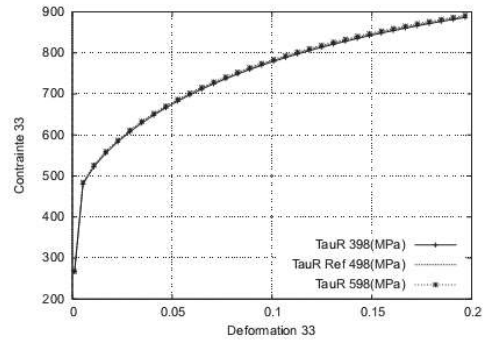
- Changing  $T, \tau, \dot{\gamma}^s, \Delta G_0, \dot{\gamma}_0, \tau_R, p, q$  will change  $\tau_{eff}$  so wil change limit elasticity and the shape of stress-strain curve.
- Changing  $K, g$  only changes the evolution of dislocation density, so it just changes the curvature of stress-strain curve.;
- Changing  $\tau_0$  only change the limit elasticity but the shape of curve remains.

#### 5. The role of each individual parameters and groups of parameters

To understand operation mechanism of the model, we studied systematically influence of individual parameters to stress-strain curve. In each case, we only change one parameter and other parameters remains unchanged. The initial parameters are given in Table 1. The model under simple tension until 20% strain of axis 33, with the speed of strain is  $5 \times 10^{-4} s^{-1}$ . The simulations performed on a Gauss point. The influence of each parameter is shown in Figure 3, 4, 5, 6 at the same temperature 25°C. Figs. 7 & 8 illustrate the combination of p and temperature,  $G_0$  and temperature,  $\tau_0$  and temperature.

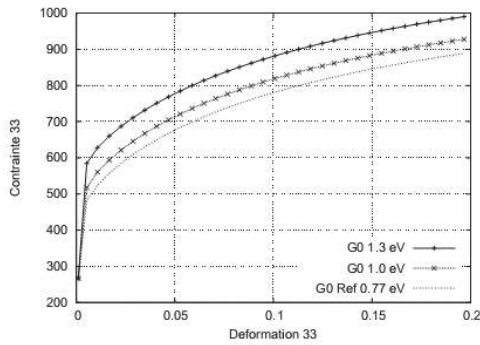


a) Influence of  $\tau_0$

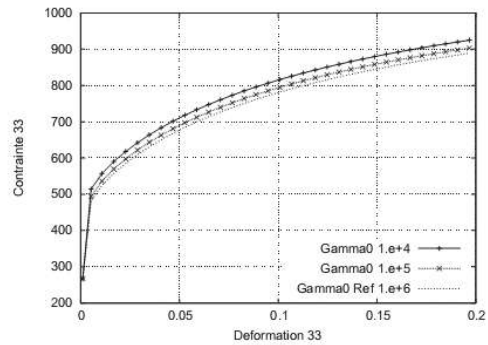


b) Influence of  $\tau_R$

**Fig. 3.**  $\tau_0$  change the limit elasticity but does not change the shape of curve;  $\tau_R$  has a little impact on the curve, almost does not change shape as well as the limit elasticity.

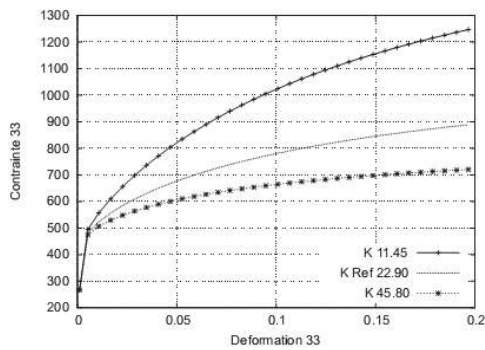


a) Influence of  $\Delta G_0$

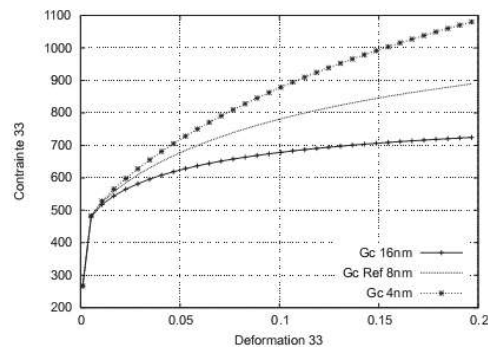


b) Influence of  $\gamma_0$

**Fig. 4.**  $\Delta G_0, \gamma_0$  change the limit elasticity but does not change the shape of curve.



a) Influence of K



b) Influence of  $g_c$

**Fig. 5.** K,  $g_c$  do not change the limit elasticity but change the shape of curve, the smaller K the greater hardening,  $g_c$  is the same.

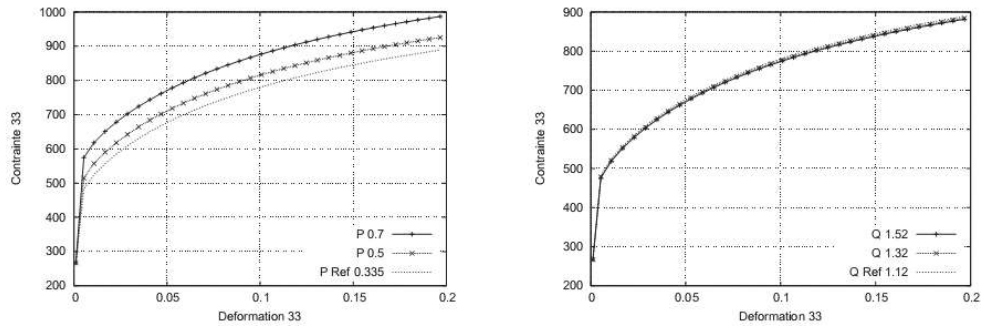


**Fig. 6.** p makes a small change on limit elasticity and q does not.

To be able to bring the influence of radiation on the model (shift upward the stress-strain curve), analysis above shows that we have the following possibilities: change one or group of parameters ( $\tau_0$ ,  $\Delta G_0$ ,  $p$ ,  $q$ ). Also, because of radiation vary with temperature, so we have to investigate combined effect of each parameter and temperature on the change stress-strain curve.

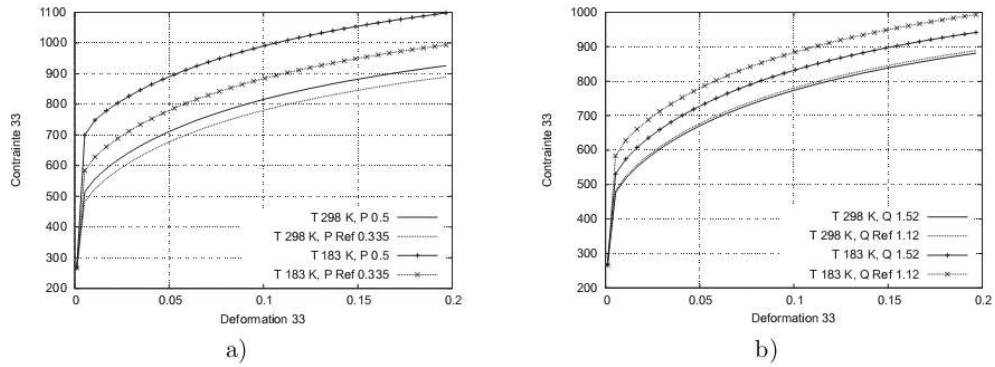


**Fig. 7.** a) Combined effect of p and temperature; b) Combined effect of q and temperature.

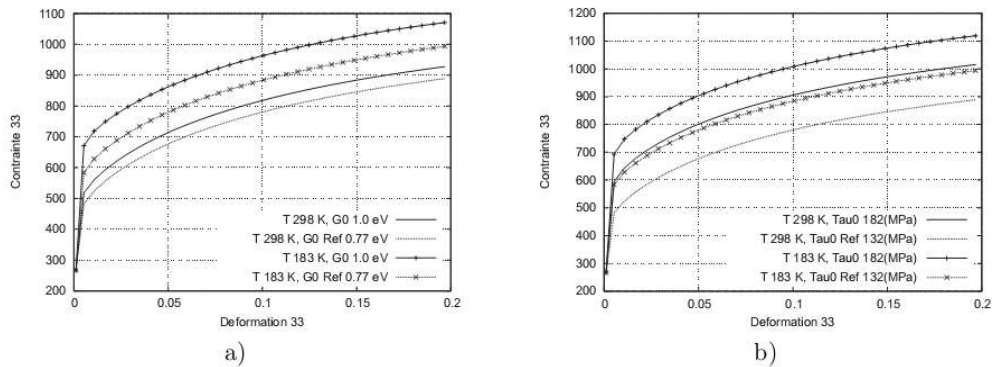


**Fig. 8.** a) Combined effect of  $G_0$  and temperature; b) Combined effect of  $\tau_0$  and temperature.

We can see that the influence of  $\tau_0$  on the stress-strain curve do not dependent on temperature, and  $G_0$ ,  $p$ ,  $q$  change a little the curve at room temperature (25°C). So, to represent

well the change of limit elasticity caused by radioactivity, it is imperative that we have to combine the change of  $\tau_0$  with  $G_0, p, q$ .

**Table 1.** Parameters used for examining the dependence between parameters

C11 (GPa)	C12 (GPa)	C44 (GPa)	$\dot{\gamma}_0$ ( $s^{-1}$ )	$\tau_0$ (MPa)	b(m)	asu
275,2	112,4	81,4	106	77,12	$2,514 \times 10^{-10}$	0,25
K	$r_i, i=1..24$	d(m)	$\Delta G_0$ (eV)	$\tau_R$ (MPa)	P	q
22,9	$2,63 \times 10^{-7}$	$2,5 \times 10^{-6}$	1,0	498	0,25	1,21

## 6. Conclusion

Due to the effects of radiation, the stress-strain curve of steel tends to shift upward, increasing the limit elasticity while the shape of the curve does not change. Through the analysis above, it is shown that we have two ways to take into account of radioactive impact on 16MND5 steel model:

- Change the parameter  $\tau_0$  in hardening law.
- Change  $G_0, p, q$ .
- Combine changing  $\tau_0$  with  $G_0, p, q$ .

## References

1. Tanguy, B., Bouchet, C. Besson, J., and Bugat, S. (2005a). Prediction of the effects of neutron irradiation on the charpy ductile to brittle transition curve of an A508 pressure vessel steel. *Computational Materials Sciences*, 23: 294-300
2. Tanguy, B., Bouchet, C. Besson, J., and Bugat, S. (2005b). Local approach to fracture based prediction of the delta T at 56J and delta T at KIC equal 100 shifts due to irradiation for an A508 pressure vessel steel. *Engineering Fracture Mechanics*, 73:191-206
3. Bacon, D. and Osetsky, Y. (2004). Hardening due to copper precipitates in alpha-iron studied by atomic-scale modelling. *Journal of Nuclear Materials*, pages 1233-1237
4. Bacon, D. and Osetsky, Y. (2007). The atomic-scale modelling of dislocation obstacle interactions in irradiated metals. *Journal of Nuclear Materials*, pages 329-333
5. CN.Nguyen (2010). *Modélisation du comportement en plasticité et à rupture des aciers bainitiques irradiés*. PhD thesis, École Nationale Supérieure des Mines de Paris.
6. Rapport interne de CEA, 2009.

# Using crater eco-city in Op village, Gia Lai Province as a model of planning and developing eco-urban areas in the direction of sustainable development

*Kieu-Vinh Thi Nguyen, Thuy-Huong Thi Doan*

Department of Civil Engineering, Vinh university, Vietnam

*Email: doanhuongdhv@gmail.com*

**Abstract.** The ecological urban system in Vietnam has been formed and developed for years. It is estimated that 755 ecological urban areas are currently classified at different levels from special to grade IV urban areas. Many urban areas are formed based on the principle of creating a quality urban environment and a number of criteria for evaluation stemmed from improving the standard of living in the era of technological advancement. However, protecting the living environment as well as minimizing environmentally harmful activities should be taken into consideration when developing eco-urban areas, in which protecting and promoting natural ecological systems such as seas, rivers, lakes, mountains and hills are very crucial. The problem is to research and integrate solutions for planning and developing ecological urban areas in the direction of sustainable development and the article applies the planning of the old crater eco-city as an example for further research.

**Keywords:** eco-urban areas; sustainable development, the old crater.

## 1. An overview of eco-urban areas

The idea of an eco-urban area was originally known as “Garden-City” at the end of the 19th century. This was an urban planning project introduced to address the environmental problems of the urban areas at the beginning of modernization. It gained constant popularity in the European community as well as other industrialized countries. Moreover, it was a powerful tool to tackle the urban areas’ environmental problems, which result from industrialization. It plays an important role in developing industrialized countries into stably developed urban areas.

The ecological urban areas with the nature balance have been developed worldwide over the past few years. Several eco-urban areas are successfully built such as Portland, Oregon, USA, which is also known as Rose City. It is the first city in the United States to announce a comprehensive plan to reduce CO<sub>2</sub> emissions and actively develop green building initiatives.

Typically, Portland has the most advanced bus, railway, and bicycle system in the world, which helps reduce pollution. Furthermore, it has more than 74 miles of running, biking, and walking trails. Vancouver, Canada is one of the ecological urban areas built between the mountains and beaches and it is home to nature lovers. Significant progress has been made, especially, 99% of electricity has been harnessed from clean and renewable resources since it became an environmentally friendly city. Furthermore, Vancouver is making plans for farms to utilize wind, solar energy, waves, and tidal power to significantly reduce the use of fossil fuel. Nördlingen, Donau-Ries, Bavaria, Germany has successfully built its eco-urban area with the name of Ries Nördlinger despite its harsh natural conditions and unflavourable geographical location, which is in the middle of a complex meteorite crater.

These eco-urban areas are developed with a range of specific criteria aimed at improving the residents’ quality of life despite the urban formation based on natural conditions such as rivers, lakes, seas, and mountains. It is understood in a modern way that “eco-urban area” is an urban area

with the high standard of living, harmony with nature, reasonable construction density, and ecologically guaranteed infrastructure. In addition, it contains beautiful architectural landscapes, eco-friendly industry and successful applications of energy and transportation solutions. The ecological urban areas have not been very familiar in Viet Nam, especially, the ones associated with natural conditions such as seas and mountains are not evaluated based on specific criteria. However, according to researchers on eco-urban areas, the criteria for ecological urban planning can be generalized by building architecture, biodiversity, transportation, urban industry and economy.



**Fig. 1.** The examples of successfully built ecological urban areas all over the world.

- Architecture: works in eco-urban areas must be ensured to optimally explore the sources of sun, wind, and rain to provide energy and meet the users' needs for water. Normally, the ground of high buildings is used for green space.
- Biodiversity: The urban areas must be guaranteed with natural habitat corridors, nurturing biodiversity, and providing access to nature for recreation.
- Transportation: It should be limited by supplying food and goods within urban areas or neighboring areas. Most of the residents in urban areas will live and work within a walking or cycling radius to minimize the need for motorized mobility. Using public transport connected to centers is an efficient solution to meet the residents' demands on moving farther. Additionally, local car-sharing allows people to use it only when needed.
- Industry: The eco-urban areas aim at producing goods that can be reused, reproduced, and regenerated. Industrial processes include the reuse of by-products and the reduction of freight.
- Economy: The Eco-city is a labour-focused economy instead of using raw materials, energy, and water, which aims at maintaining regular jobs and reducing raw materials.

According to Prof. Dr. Le Huy Ba, there are four main principles for building eco-urban areas:

- a. Having minimal encroachment on the natural environment.
- b. Diversifying the use of land, urban functions, and other human activities.
- c. Attempting to keep the urban system self-contained and self-balancing when possible.
- d. Keeping urban population growth and promoting the potential of an optimally balanced environment.

## 2. Sustainable Eco-urban planning and development

In recent years, sustainable development has been a hot issue in which becomes an essential path and a big challenge for many countries because not only is it economically stable, but it also promotes social and environmental sustainability. A number of inseparably close criteria are set for sustainable development, which means it cannot achieve the aim of stability if one of them is not included. Therefore, it is necessary to have constant coordination, balance and integration between economic goals and social and environmental ones to develop sustainably. However, it is quite hard to achieve this goal in the areas where there is little economic development and the residents' life demands are high. In addition, developing urban areas, where there has been an increase in the number of man-made architectural works, is not straightforward compared to surrounding areas.

Currently, sustainable development is not only an urgent need but also an indispensable trend of the social development in Viet Nam as well as in other countries around the world. Vietnamese government has synchronously implemented a number of solutions to promote sustainable development under many challenges in the process of urban development, especially, in big cities. As a result, many achievements have been made, one of which is the development of sustainable urban areas.

To develop urban areas sustainably, it is crucial to have a harmonious and close combination between socio-economic development and environmental protection based on the following fundamental directions:

- Considering “human” to be the center of development:
  - + Balancing between economic development goals and the natural environment.
  - + Balancing between economic and social growth
  - + Developing harmoniously between people and technology.
  - + Developing multiculturalism and moral and spiritual life of different groups of people
  - + Ensuring security, peace, order, and social stability
  - + Ensuring the democratic participation of the people in the urban development
  - + Ensuring social justice in economic life
  - + Ensuring harmony among generations and developing space reasonably
  - + Balancing urban-rural development

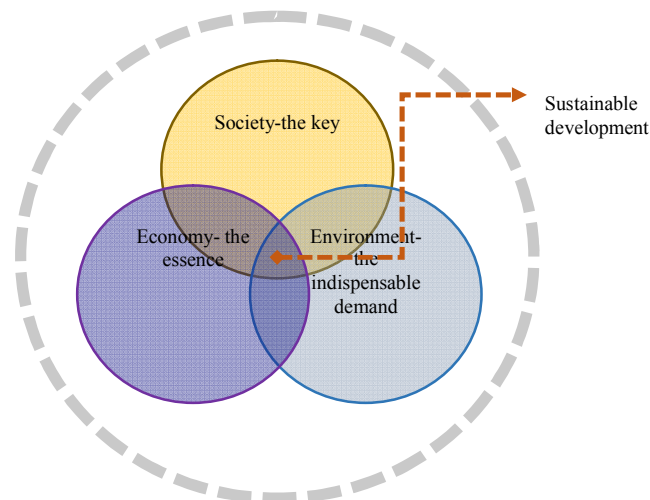


**Fig. 2.** Sustainable Eco-urban planning and development.

In terms of economy, a number of criteria are set to promote sustainable development:

- + Maintaining fast and sustainable economic growth
- + Changing the production and consumption patterns to the direction of being environmentally friendly
- + Implementing a clean industrialization
- + Developing agricultural and rural sustainability
- + Developing local and regional sustainability.

In terms of society, many fields need taking into consideration:

- + Making attempts to deal with hunger eradication, poverty reduction, and promotion of social progress and justice.
- + Maintaining to reduce population growth and create more jobs for workers.

- + Orienting urbanization and migration for sustainable development of urban areas and rationally distributing population and labor by region.
- + Improving the quality of education to raise the people's intellectual level and professional qualifications to meet the requirements of the country's development.
- + Increasing quantity and improving the quality of health care services, working conditions and clean-living environment.

In terms of the environment, the following issues should be considered:

- + Avoiding land degradation and using land resources effectively and stably.
- + Protecting the water environment and using water resources sustainably.
- + Exploring reasonably and having economical and sustainable use of mineral resources
- + Reducing air pollution in urban areas and industrial zones.
- + Managing solid and hazardous waste.
- + Conserving the biodiversity.
- + Implementing measures to mitigate climate change, minimize the effects of climate change and prevent natural disasters.

### **3. Eco-urban planning on the old crater of Op village in the direction of sustainable development**

#### **3.1. Outstanding features and geological and hydrological influences on the old crater**

Volcanoes are formed because the temperature below the Earth's surface is extremely hot, and the temperature increases when going towards the center of the Earth. At a depth of about 20 miles underground, the temperature is so hot that it can melt all kinds of rocks. Molten rocks form magma. The molten rocks are pushed upwards, the higher the mountains are. When the pressure in the lakes of magma is higher than the pressure created by the layers of rock above, the magma will erupt and form a volcano. When volcanoes are active, hot gases and other solids blast through the Earth's surface, which forms a circular hole with a diameter of less than 1 kilometer to erupt. What is erupted by volcanoes' craters will fall down mountainside and foothills, which forms a cone-shaped mountain. The inner or outer process of space objects together with the Earth's crust over old craters will gradually erode by weather. For instance, dust is accumulated to be windblown by the climate on Earth; therefore, the crater's magma can be further accreted by sand, and gravel or it might erode. The craters lie dormant in the ground through time, and they leave rich soil with attractive geology such as clean energy-geothermal energy, hot springs, mineral springs, green industrial materials, basaltic fiber, gems, and other mineral resources.

Volcanoes contain destructive power, but they are the regenerative source of the universe. As molten lava sweeps across the Earth's surface, it powerfully ravages everything in its path. However, it provides a stream of quintessential nutrients on its way to grow new shoots. There have been rich geological heritage and enchanting landscapes thanks to the volcano's powerful eruption millions of years ago. Architectural works' planning and construction inspired by volcano and associated with their sizes and heights aim at preserving the vulnerable heritage and restoring the damaged landscape as well as geological heritages. It is known as an attractive, innovative, and distinctive feature.

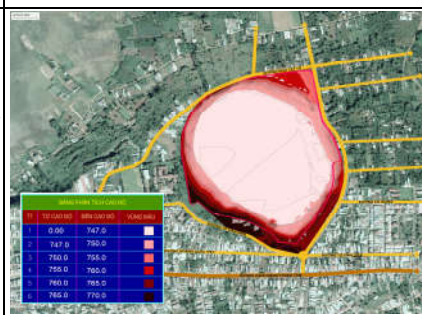
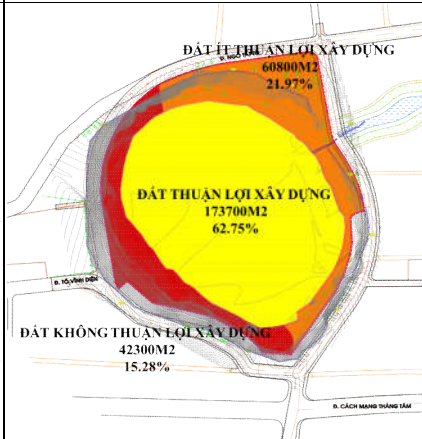
The volcano's crater is located at the cultural center of Pleiku, which is close to urban areas, traffic, and tourism infrastructure. It has potential to develop urban areas, trade, services, and tourism in Gia Lai. Accomplishing the urban development plan as well as promoting tourist attractions based on the general planning construction of Pleiku in the period of 2030 and 2050 is very essential in the favorable context of socio-economic development in general and tourism. The development of eco-urban areas and socio-economic as well as preservation and promotion of regional ethnic identity for tourism can make a great contribution to the economic development and increase the value of heritage as well as regional identity.



**Fig. 3.** Location of the Op village

**Table 1.** General assessment on natural conditions of reasearch area

The area of assessment	Assessment	Analysis and simulation
Terrain	The planning area has uneven terrain, with a basin-shaped topography. The highest point is 752 meters (the area surrounding the crater) the lowest point is 746 meters (the area inside the crater).	
The slope of terrain	+ The western area has a very steep slope of 20%-63% on average. This is an unfavorable area for construction. + The eastern area has an average slope of 4% to 30%. + The basin-shaped area has relatively flat terrain with the average height is from 746.0 to 747.5 meters.	
The topographical condition	The Basaltic soil has characteristics of being porous, loose, low density, high porosity, void coefficient, relative compression coefficient and small cohesive force; therefore, it is essential for construction and technically infrastructural works to avoid subsidence and slippage. For works with a height of 2 floors or more, it is necessary to conduct a specific geological survey to build a suitable foundation.	
Climate	The research area has the general characteristics of Pleiku's climate dominated by tropical monsoon climate, which is cool in the summer, and dry and cold in the winter. However, it has distinctive features because it is strongly influenced by the sub-region climate of the plateau in the west of the mountain range named Truong Son.	

Hydrography	<p>The project has a hydrological regime based on the one of Gia Lai, Pleiku. The largest amount of water in August, September, and October is from 2 to 4 m<sup>3</sup>/s and the lowest flow from March to May is 1.1 m<sup>3</sup>/s;</p> <p>The planning area has a basin-shaped topography of the crater. The main source of water is rainwater. The rainwater system is pumped through the D800, which is across Bui Du Street and connected with Hoi Phu stream. It is the only connection between the planning area and the surrounding area. Hence, it is essential to deal with treatment and drainage at the connection point of this area with other areas with a view to developing the urban environment sustainably during construction.</p>	
The construction elevation	<p>It can be seen from the elevation analysis of the research area that the regions with a height from 765 to 770 have a relatively big difference. Thus, studying the infrastructure based on the elevation is very important. Besides, it is necessary to build houses clinging to the ground, be close to nature and fully explore the urban topography.</p>	
The evaluation of favorable Land Fund for construction	<p>The research area's land, which is favorable, is mainly used for construction accounting for 61%. It belongs to the basin-shaped area of the crater.</p> <p>- The land that is not favorable accounts for about 22% (The Southeast and Northeast areas are at the intersection between the basin-shaped topography and the slope of the crater. Finding solutions to the infrastructure and appropriate architectural form is very crucial for exploitation and construction.</p> <p>+ The unfavorable land is about 17% (the western area, which is adjacent to Pleiku High School, has high sloping terrain). Therefore, it is prioritized for green buffer zone and resorts, which should be constructed, based on natural terrain to provide spaces with views towards the theme park and central air conditioning lake.</p>	

Assessment on the current land use

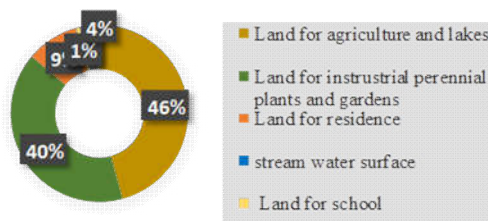


Fig. 4. Assessment on current land.

### 3.2. General assessment

#### 3.2.1. Advantages

The research area for urban construction is located in the center of Pleiku, which is a favorable factor for urban development, commercial services, recreation, and cultural theme park. Eco-urban development can help access and fully explore the regional heritage and cultures.

The research area is mainly agricultural land for perennial crops, but the exploitation is not efficient. It is necessary to find solutions to change the form of production from agriculture to trade and service to provide jobs for local people.

The area's terrain is relatively flat, but there is a difference in the elevation due to the crater's shape. As a result, a number of solutions based on construction elevation should be introduced to the infrastructure to access to the functional areas easily and effectively. Moreover, it is important to be synchronized with the city's general infrastructure system to form a unified whole and easily connect to other areas.

It is favorable for constructing many kinds of high-class eco-villas provided with a wide range of modern public services and facilities. Thanks to the terrain clinging to the mountainside, it is possible to construct semi-subterranean villas to highlight the beauty of the city.

#### 3.2.2. Limitations

The main difficulty is the high cost of construction due to the relatively steep basin-shaped topography. Furthermore, it requires a large amount of investment in complete planning in this area.

### 3.3. Principles for designing (5 sustainable criteria) and Design idea

Ecology: It has low construction density. The priority is given to green areas, parks, and lakes to create green, clean, and beautiful urban areas.

- Tradition (Identity): Creating spaces to introduce the local cultural identity to highlight the beauty of the city.
- Modernity: Synchronizing in technical infrastructure and social infrastructure.
- Comfort: Providing a wide range of public services, commercial service for tourism and daily activities of residents in the urban areas.
- Profit: Promoting provincial urban development and tourism in general and the Op village.



Note:

1. Eco-residential area;
2. Eco-tourism resort.



Fig. 5. Sustainable criteria.

The author proposes to divide the crater's area into two main parts: an eco-residential area and an eco-tourism resort based on the natural topography of the crater's concave shape. Apart from the exploitation of the research area's natural conditions, architectural space and landscape with the crater's structure (the outstanding natural conditions of the crater are exploited) are set to each region to achieve five sustainable development criteria:

1. Being rich and modern
2. Being ecological and fresh
3. Having tradition and identity
4. Having safety and peace
5. Being modern and convenient

The plan of functional zoning based on the crater's special topography is divided into 7 functional areas with a circular structure.



Fig. 5. The proposal for floor-plan of functional zoning.

### 3.4. The proposed criteria for eco-urban planning criteria

Considering the criteria for land use planning, according to QCVN 01: 2019/BXD, it is possible to choose criteria, which are different from those in Table 2.2 in the case of urban planning with specific characteristics. However, they must be suitable and greater than or equal to  $15\text{m}^2$  a person. The authors evaluate the crater's eco-urban area to be a green city, sustainable eco-environmental development, low-rise construction of the large areas and low construction density which is less than or equal to 25%; therefore, the target of civil land can be higher than  $90\text{m}^2/\text{person}$ . The target of land for residence can be higher than  $50\text{m}^2/\text{person}$  and the table of criteria for land use planning and social infrastructure is proposed as follows.

Table 2. Proposed targets for land use

	Soil types	Proposed targets
1	Construction land for the whole urban area	$120 - 150\text{m}^2/\text{person}$
2	Civil land	$80 - 90\text{m}^2/\text{person}$
3	Land for Residential unit	$40-60\text{m}^2/\text{person}$
4	Land for public works	$\geq 8\text{m}^2/\text{person}$
5	Land for green trees and sports	$\geq 10\text{m}^2/\text{person}$
6	Land for traffic (regional roads)	$18-20\text{m}^2/\text{person}$

**Table 3.** The targets for public works (Based on QCVN 01: 2019/BXD)

Types of work	Management unit	Minimum building usage targets		Minimum land use targets	
		Unit	Target	Unit	Target
Kindergartens	Residential unit	seats/1000 people	50	m <sup>2</sup> /seat	15
Primary Schools	Residential unit	seats/1000 people	65	m <sup>2</sup> /1 seat	15
Secondary schools	Residential unit	seats/1000 people	55	m <sup>2</sup> /1 seat	15
Clinics	Residential unit	clinics/1000 people	1	m <sup>2</sup> /clinic	500
Training Grounds	Residential unit			m <sup>2</sup> /person	0,5
Markets	Residential unit	works/residential unit	1	ha/work	0,2

According to the detailed planning project, Vietnam Construction Standards and legal regulations, the fundamentally economic and technical targets for the research area are determined as follows.

**Table 4.** The fundamentally economic and technical targets

	Land use functions	Proposed targets
1	Land for roads and static traffic	≥ 18 % of total land fund
2	Parking	
	- Public works and service	100 m <sup>2</sup> / parking space
3	Water supply	
	- Running water	≥ 180 litres/person – day and night
	- Public and service	≥ 3 litres/m <sup>2</sup> – day and night
	- Kindergartens	≥ 100 litres/person – day and night
	- Flower gardens and parks	≥ 3 litres/m <sup>2</sup> – day and night
	- Road cleaning	≥ 0,5 litres/m <sup>2</sup> – day and night
	- Storing water for leaking	15 % ∑ water supply
4	Electricity supply	
	- Villas	≥ 5 kw/household
	- Public and service	≥ 30 w/m <sup>2</sup>
	- Kindergartens	0,2 kw/person
5	Sewage drainage and environmental sanitation	
	- Sewage drainage	Based on water supply standards
	- Solid waste	1,3 kg/person - day
6	Communication	
	- Houses	2 devices/ household
	- Kindergartens	15 devices/kindergarten
	- Public areas, offices, and sports	1 device/ 100m <sup>2</sup>

### 3.5. Solutions to shape architectural space and landscape of the eco-urban areas.

#### 3.5.1. The layout of architectural landscape and landscape of eco-villa:

These areas are mainly located on the side of a basin-shaped area which is near the lake and the central park, with a cool view of the lake. A three-floor low-rise building which is included basement, rooftop and attic has gardens in the villa connected with open spaces. The architectural form is designed to match the terrain by creating terraces and balconies with views overlooking the theme park and the detention basin.

- The construction density: 50%
- High-rise building: 03 storeys ( Basement, rooftop and Attic are not included) + Area: 300-400 m<sup>2</sup>/plot of land.



An illustration of a single-family villa



An illustration of a single-family villa



Fig. 6. Proposed cross-section of architectural space of residential area.

### 3.5.2. Organizing the architectural space of the eco-tourism area

Service and commercial works are set up at gateway and lakeside locations such as cafes, commercial centers and eateries. The works containing outstanding features of local cultures represent Central Highlands' cultures.

+ Construction density: 40-60%.

+ High building: 3-5 storeys.

The outstanding construction : a nine-floor hotel which leans on the mountainside and has a view towards the park and central detention basin: Construction density: 40%.

Cultural theme park: A park with thematic services, commerce, and entertainment defined by the culture of the investment site exploiting the history and culture of Central Highlands. It aims at exploiting the symbolic constructions of this area such as: communal house, stilt house, gong culture, sinus dance and Jrai village.

The green landscaped park and water landscape are built among the functional areas in the urban area. The green tree and the water surface can not only create a landscape but also make the climate and humidity of the urban area equable. Besides, they help create green and public spaces for residents.



**Fig. 7.** Organizing the architectural space of the eco-tourism area



**Fig. 8.** Organizing the architectural space of the eco-tourism area.

The basic structure to arrange categories: Main gate + reception square + executive office + car park + technical support.

- Commercial area (main street): business, theme-related services combined with interactive minishows.
- Central square combined with interactive activities with the audience.
- Typical Cultural villages represent history (theme of exploitation).
- A 500-seat restaurant + auxiliary.
- Outdoor playground for children and team building.
- Large-scale scene performance area of 3000 seats + auxiliary + stage.
- Commercial shop house.
- Hotels, resorts, and villas.
- International convention center.

#### **4. Conclusion**

Despite any kinds of urban structures including green, compact or ecological urban areas, the process of urban formation and development has to be sustainably developed. In the era of technological advancements, the more advanced the technology is, the more attention the sustainability will be paid. This article introduces the idea of urban planning on the old crater with a view to deeply understanding about the urban construction on special conditions and ensure future sustainable development.

## References

1. GS. TS. Nguyễn Lâm, Tổng thư ký Hiệp hội Các đô thị Việt Nam, *Phát triển đô thị bền vững - những bài học kinh nghiệm của Thủ đô Hà Nội, Thành phố Hồ Chí Minh, Thành phố Huế và hướng tới của các đô thị Việt Nam*. Tạp chí Quy hoạch Đô thị, NXB Trí thức, 2017.
2. ThS. KTS. Nguyễn Hữu Ninh, *Tinh bản sắc trong quy hoạch đô thị, ý tưởng về đô thị sinh thái*, Thông báo Khoa học và Công nghệ số 1.2013.
3. Nguyễn Thế Bá. *Sách Quy hoạch xây dựng phát triển đô thị*, NXB Xây dựng, Hà Nội. 2009.
4. PGS. TS. KTS. Nguyễn Tô Lăng, *Công tác quản lý phát triển đô thị bền vững, một số bài học kinh nghiệm*, Tạp chí ĐH Kiến trúc, Hà Nội. 2018.
5. GS. TSKH. Lê Huy Bá, PGS. TS. Thái Thành Lượm, ThS. Nguyễn Thị Kiều Diễm, *Giáo trình Làng Sinh thái, Đô thị Sinh thái và Khu công nghiệp Sinh thái*, NXB Đại học Công nghiệp Tp.Hồ Chí Minh.
6. Linh Anh, Thành Luân, *Tạo lập hệ thống đô thị quốc gia phát triển bền vững*. Báo Xây dựng, NXB Xây dựng, 2012, 11.07.2012.
7. Phạm Ngọc Sáu, *Quy hoạch Hệ thống hạ tầng kỹ thuật Khu đô thị Sinh thái Vàm Cỏ Đông*, Đồ án quy hoạch, 2007.
8. Lê Hồng Kế, *Đề cập bước đầu đến sinh thái trong quá trình quy hoạch và xây dựng điểm dân cư Việt Nam*”, Luận án PTS, 1989.
9. Nguyễn Thế Chinh, *Kinh nghiệm quốc tế trong công tác bảo vệ tài nguyên môi trường*, Viện Chiến lược Chính sách Tài nguyên, 2012, <http://isponre.gov.vn>.
10. Lê Huy Bá - Lâm Minh Triết, *Giáo trình Sinh thái môi trường học cơ bản*, Nhà xuất bản Đại học Quốc gia TP Hồ Chí Minh. Hồ Chí Minh. 2005.
11. Lưu Đức Hải, *Định hướng chiến lược phát triển đô thị và đô thị hóa bền vững tại Việt Nam*, Diễn đàn phát triển bền vững đô thị. 2016. p.110-123.
12. Tai-Chee Wong, Belinda Yuen, *Understanding the Origins and Evolution of Eco-city Development: An Introduction*, Ebook ISBN: 978-94-007-0383-4, pp 1–14.
13. Simon Joss et al, *Towards the 'ubiquitous eco-city': An analysis of the internationalisation of eco-city policy and practice* Journal of Urban Technology, Volume 6, 2013 - Issue 1.
14. Mark Roseland, *Dimensions of the eco-city Part of special issue Sustainable Urban Development* Volume 14, Issue 4, August 1997, Pages 197-202.
15. Wenhao Xu, *A multi-sectoral decomposition and decoupling analysis of carbon emissions in Guangdong province, China*, Journal of Environmental Management, Volume 298, 15 November 2021, 113485.

# Research solutions to improve the quality of survey, design and construction of private housing works in Ha Tinh

*Tran Van Binh<sup>1</sup> and Luu Thi Thuy<sup>1</sup>*

<sup>1</sup> Faculty of Engineering and Technology, Ha Tinh University, Viet Nam

*Email: binh.tranvan@htu.edu.vn*

**Abstract.** The survey and design work are considered an important step in deciding the economic, technical, and aesthetic content of the project. In this article, the author studies the limitations in the survey and design of individual housing projects in Ha Tinh in recent years. From there, several solutions are proposed to improve the quality of survey and design work, contributing to limiting mistakes in the construction process of individual houses in Ha Tinh.

**Keywords:** Survey, design, individual housing.

## 1. Introduction

The society is developing more and more, the speed of housing construction is faster and faster, beautiful houses are not only happening in the city but also in the countryside because people's lives are getting better and better, concrete houses are growing up day by day. The land with good geology is increasingly scarce, leading to the need to go to the coastal areas with ponds, lakes, and fields to build works.

In our country, the quality management of individual housing construction is not good, the documents focus on key projects, public investment projects [1,2,3,5,7]. For individual houses, although the state has regulations, the responsibility is on the investor and the surveying, designing, supervising and construction units [4,6]. To save costs, the investor often skips the survey stage, or hires a survey unit but does not meet the requirements. leading to many incidents for their own works and neighboring works, causing unsafety to people and properties, affecting economy and labor safety.

Ha Tinh is a province located in the central region of Vietnam. With a population of more than 1.3 million people, the demand for housing construction is increasing, especially when the economy is growing, building a separate house is necessary. Therefore, studying the current situation of survey and design of individual housing projects in Ha Tinh in recent years, thereby proposing solutions to improve the quality of survey and design work, contributing to Limiting mistakes during the construction of individual housing projects is essential.

## 2. Actual situation of survey, design, and construction of individual houses in Ha Tinh

### 2.1. Shortcomings and limitations

Through surveying the survey, design, and construction of separate houses in Ha Tinh, some main shortcomings and limitations are shown as follows:

*About geological survey:* The phenomenon of not carrying out surveys, not setting up survey tasks is quite common in individual housing projects because it is not part of the state budget. The technical plan for geological survey is not reasonable in terms of location, number of holes and drilling depth. There are works with inaccurate survey results, having to re-survey, leading to changing the solution of pile foundation to ice foundation, reducing the cost by about 40% of the

**Editors:**  
**Assoc. Dr. Tran Ngoc Long**  
**Dr. Nguyen Trong Ha - Dr. Nguyen Duy Duan**

---

**ADVANCES IN CIVIL ENGINEERING**  
**Proceedings of the 1<sup>st</sup> Conference on Advances**  
**in Civil Engineering (ICACE 2022)**

**May 21<sup>st</sup>, Vinh University, Vietnam**

*Responsible for publishing:*  
**Director - editor-in-chief BUI MINH CUONG**  
Responsible for the Content NGUYEN HUY TIEN  
Editor and copy editor: Dr. NGUYEN HUY TIEN  
Cover designer: NGUYEN THAC CUONG

**SCIENCE AND TECHNICS PUBLISHING HOUSE**  
70 Tran Hung Dao - Hoan Kiem - Hanoi  
Tel: 024 39423171; Fax: 024 3822 0658  
Website: <http://www.nxbkhkt.com.vn>; Email: [nxbkhkt@hn.vnn.vn](mailto:nxbkhkt@hn.vnn.vn)

**BRANCH OF OFFICE**  
28 Dong Khoi Street - District 1 - Ho Chi Minh City  
Tel: 028 3822 5062

**Affiliate partners:**  
Tando trading and advertising and printing company limited .  
Address: 17/343 Tran Khat Chan - Hai Ba Trung - Ha Noi.

---

Quantity 50 copies, size 17× 24cm, at Tando trading and advertising and printing company limited.  
Address: 17/343 Tran Khat Chan - Hai Ba Trung - Ha Noi.  
Publishing license: 2408-2022/CXBIPH/02-137/KHKT.  
Publication decision No: 158/QĐ-NXBKHKHKT, August 5, 2022.  
ISBN: 978-604-67-2377-6.  
Printed and deposited in 2022.

value of the foundation. Failure to conduct geological survey or improper survey may cause cracking, settlement, tilting of the structure, or may cause collapse of the structure, directly affecting people and neighboring structures.

*About topographic survey:* Many works using cadastral maps do not guarantee elevation or do not comply with regulations on transmission of cores and protection of landmarks; do not use the coordinate system for positioning, causing architectural consequences and deviations in the technical infrastructure system.

In this article, the author surveyed 100 individual housing projects in districts and cities of Ha Tinh province, and obtained some results shown in the following tables:

**Table 1.** Data table of survey results of individual housing projects in Ha Tinh related to geological and topographic survey issues

Number of works the author investigated and surveyed	Number of projects that the investor hires a surveying unit	Number of projects that the investor does not hire a survey unit
100	12	88

Statistics show that the number of individual housing projects that the investor hires a geological and topographic surveying unit accounts for 12%, while the number of projects that do not hire a surveyor account for 88%, this is a large percentage leading to construction problems during construction.

*About design:* During the design process, there are still many errors such as unsafe structure in bearing capacity; too safe structure causes waste; unsafe to use; no structural calculations; incorrect calculation; improper application of regulations and standards.

The quality of architectural design also has problems such as: Many works have not been carefully studied in terms of architectural form, ground, utility and decorative details. This leads to the fact that during the construction process both doing and repairing, the results are not as expected.

**Table 2.** Survey results on actual situation of individual housing projects in Ha Tinh related to design issues

Number of works the author investigated and surveyed	Number of projects without hiring a design unit	The number of projects that hire a design unit, but the company does not register for business, the design is unsafe, wrong with regulations and standards.	The number of projects that hire a design unit that is in favor of safety, causes waste	Number of projects hiring design units, having business registration, good design
100	45	25	15	15

Statistics show that the number of individual housing projects that hire a designer, have a legal seal, have a good design, or design units that are in favor of safety and cause waste accounts for a significant small 15%. Meanwhile, the number of projects that hire a design unit without the company's seal, unsafe design, and non-standard and standard accounts for 25%. Especially, the number of projects that do not hire a design unit account for 45%.

*About the estimate:* Most of the design documents for individual houses without estimates or with estimates are just procedures for getting a bank loan or cannot use the estimates made by the design contractors (lack or excess of volume; wrong unit price, price of materials; improper application of policies and regimes; use of materials not suitable for the work; incorrect calculation).

**Table 3.** Survey results on actual situation of individual housing projects in Ha Tinh related to cost estimation

Number of works the author investigated and surveyed	number of works not estimated	Number of projects that have been estimated but only loaned, in case the authorities check	Number of projects that have been estimated but cannot be used	Number of projects making estimates to meet requirements
100	55	15	20	10

Of the 100 surveyed projects, the number of projects that meet the requirements is only a small percentage of 10%, works that have not been estimated or which have been estimated but fail to meet the requirements account for a relatively large proportion. Especially, the number of projects that do not make estimates accounts for 55% of the total. These constructions make the owner unable to predict the construction cost, causing many unnecessary losses.

**Table 4.** Data table of incident survey results of individual housing projects in Ha Tinh

Number of works the author investigated and surveyed	Number of works with cracked walls, cracked floors, uneven settlement	The number of works affects the surrounding works, causing unsafety for workers	Number of buildings with poor usability and unsecured structure	Number of works built to ensure usability, structure, safety for construction workers and users
100	45	12	18	25

Based on the statistics table, the number of works built to ensure the usability, structure, safety for the construction and use of the works accounts for 25%, out of 100 survey works, the number of unsecured works accounts for a large proportion. In particular, the number of works with cracked walls, floor cracks, and uneven settlement accounts for 45%.

## 2.2. Reason

The causes of the shortcomings and limitations of individual housing projects at the survey and design stage usually stem from the following main reasons:

### *State management agencies:*

For individual housing projects, the state is only interested in works with a floor area larger than 250m<sup>2</sup> or more than 3 floors, with a height of more than 12 [6]. Therefore, other types of separate houses are not taken into account, leading to self-made implementation by investors and contractors, seriously affecting the planning, quality of surrounding works, and labor safety.

### *Investor:*

For individual housing projects, the investor is often subjective, inexperienced, knowledgeable, and listens to the opinions of non-experts, leading to the assignment of the entire project to the construction crews.

Besides, according to state regulations, households are allowed to design separate houses by themselves when the work has a total construction floor area of less than 250 m<sup>2</sup> or less than 3 floors or has a height of less than 12 meters, be consistent with the approved construction planning and take responsibility before law for the design quality, the impact of the construction work on the environment and safety of the neighboring works.

The problem of survey and design accounts for a large part of the economy, individual investors often have the spirit of the crowd, but do not know the geological problem of their house is not like other areas. Some investors hire survey and design units but do not learn carefully about companies, often putting their trust in the wrong place, causing economic losses and labor safety.

**Table 5.** Table of survey data on the reasons why investors do not hire a survey unit

Number of works not surveyed	Number of projects that do not hire surveying units because of funding problems	Number of projects that do not hire a survey because the investor lacks understanding and follows other people's opinions	Number of projects that do not hire a surveyor because they do not trust the surveying unit	Number of projects that do not hire survey for fear of delay
88	20	35	15	18

Of the 100 individual housing projects surveyed by the author, there are 88 works that the author does not hire a survey unit, in which the number of projects that do not hire a survey unit because they do not trust the survey unit accounts for 17%, number of projects not hiring survey

for fear of delay 20.5%, the number of projects that do not hire a surveying agency because of funding problems accounts for 22.73%. Especially, the number of projects that do not hire to survey because the investor lacks understanding and follows other people's opinions accounts for 39.77%.

**Table 6.** Table of survey data on the reasons why investors do not hire a design unit

Number of projects without hiring a design unit	Number of projects that do not hire a design unit because of funding problems	Number of projects that do not hire designers because the investor lacks understanding and follows other people's opinions	The project does not hire a designer because it does not trust the design unit	Number of projects that do not hire designers for fear of delay
45	12	18	10	5

Based on the statistics, it is found that out of 45 projects, the investor does not hire a design unit, the work that does not hire a designer for fear of delay is 5 works, accounts for 11.11%, the percentage of works that do not hire a designer because they do not trust the design unit accounts for 22.22%, rate of works that do not hire a design agency because of funding problems 26.67%. Especially the reason for not hiring a designer is because the investor lacks understanding, following the opinions of others is the most, accounting for 40%.

*Geological and topographic survey unit:*

In the process of data collection, the percentage of projects that investors choose to survey is very low, in survey works, the capacity of the surveying unit is a concern. The unit sending workers is not professionally trained, not properly qualified, the machinery is old, during the survey, there is often no supervision of a geological engineer, leading to different survey results from reality.

**Table 7.** Table of data on the number of survey works

Number of works hired for geological survey	The project hires a qualified geological survey unit	The project hires a geological survey unit without a geological engineer	The project hires a geological survey unit with machinery and equipment that does not meet the requirements
12	3	6	3

Of the 100 works surveyed by the author, only 12 were hired to survey, however, the work hires a capable geological survey unit, or the work hires a geological survey unit with machinery and equipment. rudimentary, expired, do not meet the requirements, accounting for 25%, rate of works hiring geological survey units without geological engineer accounts for 50%, this is the main cause of unsatisfactory geological survey results.

*Construction design unit:*

Currently, design offices are established a lot, without business registration, these offices often design for individual housing projects or receive works from other companies. The headquarters of these units are often located in a place where few people notice, even at home, the main form of business is through social networks, so it is difficult for the authorities to check.

**Table 8.** Data table on number of private housing design offices in Ha Tinh

Number of design units	Number of design units with full capacity, registered as a business	Number of design units that are not registered as businesses but are created by qualified individuals	Number of design units without business registration, created by individuals who are not professional
225	115	64	46

Source: Survey data

Statistics show that, the number of design units is a lot, however, only 51.11% of design companies have full capacity, register their businesses, the percentage of design units that do not register as businesses but are created by qualified individuals accounts for 28.45%, the rate of design units without business registration, made up of non-professional individuals, accounts for 20.45%.

### **3. Proposing some solutions to improve the quality of survey and design of individual houses in Ha Tinh**

#### **3.1. Improve the efficiency of construction quality management by state management agencies**

- ***Capacity building for state management of construction quality:***

Establishing a quality control department for individual housing construction works. At the district level, it is necessary to supplement professional and technical forces by economic measures or sending people to study. At the commune level, professional staff will be arranged, with priority given to wards and townships in the immediate future; Actively encourage the training of people to attend part-time, college and intermediate schools with economic support mechanisms. This solution is highly feasible because the annual number of unemployed youths in the area is large. In parallel with the above measures, it is necessary to organize the assessment and classification of the existing contingent of cadres, civil servants, and public employees to have a plan for professional training.

- ***About mechanisms and policies:***

The construction industry needs to advise the Provincial People's Committee to direct and issue regulations on coordination between specialized agencies; strengthen policies to attract human resources and talents (there are policies to attract talents but not strong enough).

- ***Strengthening the inspection, inspection, and assessment of construction quality:***

Quality assessment activities need to be concerned to evaluate the quality of the works accurately and comprehensively, not to affect the surrounding works or lose the urban beauty. To do so, it is necessary to strengthen the capacity of the appraisal and verification department, the quality control center, planning and urban areas, and at the same time encourage the activities of other independent accrediting organizations.

#### **3.2. Improve the efficiency of investor's construction quality management**

- ***Investors need to hire a quality management unit right from the investment preparation stage:*** The quality of construction works is formed from the stage of survey and design, but most of the works, do not hire a supervisor or only proceed at the end of the investment preparation stage or the beginning of the investment implementation stage. Therefore, the Investor cannot control the survey and design quality.
- ***The investor regularly inspects consulting activities or can hire an individual or a second unit to check:*** This is essential because the supervision consultant is hired by the owner to check the contractors. So, who checks supervision consultants? To do this, the investor or the person hired by the investor needs to have a deep understanding of the profession to understand the responsibilities and order and content of the work that the contractors must perform.
- ***Having plans and measures to select qualified and capable contractors:*** The investor must do a physical check, not just a check on the documents, and at the same time combine many information channels to accurately determine the conditions and capacity of the contractor before, during the bidding and during the implementation process contract.

- *Management by administrative methods and economic contracts*: The administrative method is to communicate the requirements of the investor through "requests" or "check sheets", regularly reported by "votes" instead of mouth-to-mouth family style. Need to manage quality by economic contract. Accordingly, the quality requirements should be detailed in the contract (or contract addendum). This is a mandatory legal requirement. For a long time, the status of economic contracts is just a procedure, especially not used to manage quality, leading to unresolved quality disputes.

### **3.3. Improve the efficiency of construction quality management of contractors**

- *Building a system of quality management apparatus*: consolidating titles according to regulations on capacity conditions; building the apparatus system from the agency to the field; eliminate the phenomenon of total delivery; There is a system of training and retraining to improve professional qualifications and attract human resources and talents.
- *Develop a quality assurance strategy and plan*: Set out the company's goals, roadmap, content and quality management model; have a quality policy in line with the roadmap; at the same time strictly handle the officials who violate the quality. It is necessary to develop a quality assurance plan for each project with quality assurance measures, rather than in an arbitrary and unscientific manner.

## **4. Conclusion**

In this article, the authors present the limitations and causes of the survey and design of individual houses in Ha Tinh. Proposing some solutions to improve the quality management of construction works, contribute to good management and limit risks in survey, design, and construction of individual houses in Ha Tinh. The results of the article are references for investors, businesses, employees, and state management agencies on quality management of individual housing construction.

## **References**

1. Government, Decree No. 15/2021/ND-CP detailing a number of contents on construction investment project management (2021).
2. Ministry of Construction, Circular No. 18/2016/TT-BXD detailing and guiding a number of contents on project appraisal and approval and work construction design and estimate (2016).
3. Ministry of Construction, Circular No. 39/2009/TT-BXD Guidelines on quality management of construction of separate houses (2009).
4. National Assembly, Construction Law No. 50/2014/QH13 (2014).
5. National Assembly, amending and supplementing a number of articles of the Law on Construction, No. 62/2020/QH14 (2020).
6. National Assembly, Consolidated Document No. 02/VBHN-VPQH of the Office of the National Assembly on Construction Law (2020).
7. People's Committee, Decision No. 28/2021/QĐ-UBND Promulgating Regulations on decentralization of some contents on appraisal, organization of construction investment project management and construction quality management built in Ha Tinh province (2021).

**SURVEY QUESTIONS ON SURVEY AND DESIGN OF PRIVATE HOUSING WORKS IN  
HA TINH PROVINCE**

*From the current actual situation, it can be seen that the survey, design and construction of individual houses in Ha Tinh still have many limitations and need to be rectified. Therefore, the research group of Faculty of Engineering and Technology conducted a survey to collect data and evaluate the factors that we hope you can help. The answers and information will be kept confidential and votes will be canceled after completing the topic.*

*Thank you!*

**I. Type of construction:**.....

**II. Address:**.....

**III. Statistics on the number of individual housing projects in Ha Tinh with or without hiring a geological and topographic survey company**

*For item III, please multiply [X] in the appropriate boxes.*

Ordinal number	Survey content	Yes	No	Note
1	When building a project, do you hire a survey company?			

**IV. Quantitative statistics related to the issue of hiring a design company**

*For item IV, please multiply [X] in the boxes according to the actual selection when building the project.*

Ordinal number	Survey content	Yes	No	Note
1	When building a project, you do not hire a design company.			
2	When building a project, you hire a design company but the company does not register for business, the design is unsafe, wrong with standards and standards.			
3	When building a project, you hire a design company, but the design company is too safe, causing waste.			
4	When building a project, do you hire a design company, the company has a business registration, good design.			

**V. Statistics on the number of works related to the issue of estimating (making construction costs)**

*For item V, please multiply [X] in the boxes that match the actual selection when building the project.*

Ordinal number	Survey content	Yes	No	Note
1	When building a project, you do not hire an estimating company.			
2	When building a project, you hire a company to make an estimate, but only to borrow money, in case the authorities check it.			
3	When building a project, you hire a company to make an estimate, but you can't use it.			
4	When building a project, you hire a company to make an estimate to meet the requirements.			

**VI. Statistics on the number of projects having problems***For item VI, please multiply [X] in the boxes if your project has problems while constructing, using.*

Ordinal number	Common problems	Yes	No	Note
1	Does your project have cracked walls, cracked floors, uneven settlement?			
2	Does your work affect the surrounding works, causing unsafety?			
3	Your project has poor usability, the structure is not guaranteed.			
4	Your project is built to ensure usability, structure, and safety for the construction and use of the work.			

**VII. Statistics on the reasons why investors do not hire a survey company***For item VII, please multiply [X] in the appropriate box*

Ordinal number	Reasons for not hiring a survey company	Yes	No	Note
1	Your project does not hire a survey company because of funding problems.			
2	Your project does not hire a survey because I think I understand and do it already, someone else has commented.			
3	Your project does not hire a survey company because it does not trust the survey company.			
4	Your project does not hire a survey for fear of delay.			

**VIII. Statistics on the reasons why investors do not hire a design company***For item VIII, please multiply [X] in the appropriate boxes*

Ordinal number	Reasons for not hiring a survey company	Yes	No	Note
1	Your project does not hire a design company because of funding problems.			
2	Your project does not hire a design company because I think I know and do it, someone else has suggested it.			
3	Your project does not hire a design company because it does not trust the design company.			
4	Your project does not hire a design company for fear of delay.			

**IX. Statistical information about survey company***For item IX, please multiply [X] in the appropriate boxes*

Ordinal number	Survey company capacity	Yes	No	Note
1	Does your project hire a fully qualified geological survey company.			
2	Your project hires a geological survey company but no geoengineer.			
3	Does your project hire a geological survey company whose machinery and equipment do not meet the requirements.			

**X. Statistical information about the design company**

*For item X, please multiply [X] in the appropriate boxes*

Ordinal number	Survey company capacity	Yes	No	Note
1	Does your project hire a design company, have full capacity, register a business.			
2	Your project hires a design company that is not registered as a business but individuals with good expertise.			
3	Your project hires an unregistered design company, made up of unprofessional individuals.			

Your suggestions in the survey, design and construction of individual houses in Ha Tinh:

.....  
.....  
.....

Thank you for helping us with the survey!